1-6-2017

Design Of Genetically-Encoded Ca2+ Probes With Rapid Kinetics For Subcellular Application

Florence Reddish

DESIGN OF GENETICALLY-ENCODED CA^{2+} PROBES WITH RAPID KINETICS FOR SUB-CELLULAR APPLICATION

by

FLORENCE REDDISH

Under the Direction of Jenny Yang, Ph.D.

ABSTRACT

The spatio-temporal attributes of intracellular calcium (Ca^{2+}) transients activate various biological functions. These Ca^{2+} signaling events are triggered extracellularly through different stimuli and controlled intracellularly by the major Ca^{2+} storage organelle and by numerous Ca^{2+} pumps, channels, and Ca^{2+} binding proteins. Ca^{2+} transients can be significantly altered as a result of defects with signal modulation, leading to different diseases. Because of the fragility and intricacy of the Ca^{2+} signaling system, with the endo- and sarcoplasmic reticulum at the center, genetically-encoded Ca^{2+} probes that have been optimized for mammalian expression and fast kinetics are needed to observe global and local Ca^{2+} changes in different cells. Here, we first report

the crystal structure determination of our genetically-encoded Ca^{2+} sensor CatchER which utilizes EGFP as the scaffold protein. Crystal structures of CatchER were resolved in the Ca^{2+}-free, Ca^{2+}-loaded, and gadolinium-loaded forms at 1.66, 1.20, and 1.78 Å, respectively. Analysis of all three structures established conformational changes in T203 and E222 produce the varying ratios of the neutral and anionic chromophore reflected in the absorbance spectrum where Ca^{2+} stabilizes the anionic chromophore and enhances the optical output. Since CatchER has miniscule fluorescence when expressed at 37˚C in mammalian cells, we enhanced its brightness by improving the folding at 37˚C, facilitating better chromophore formation. The resulting mutants are the CatchER-T series of Ca^{2+} sensors with CatchER-T' having the most improvement in brightness at 37˚C. We also introduced the N149E mutation in the binding site to alter the K_d along with the brightness mutations. The resulting mutants were characterized and found to have weaker K_ds compared to wild-type CatchER, similar quantum yields, and altered ratios of the neutral and anionic chromophore in the apo form. Then, CatchER-T' was applied *in situ* to monitor Ca^{2+} changes globally in the ER/SR of C2C12, HEK293, and Cos-7 cells. A new construct consisting of CatchER-T' and JP-45 was created to monitor local Ca^{2+} dynamics in the SR lumen of skeletal muscle cells. The results showed a difference between global and local SR Ca^{2+} release. We also examined the potential and spectroscopic properties to utilize some of our sensors in T cells to monitor the magnesium (Mg^{2+}) flux in immune cells with faulty MagT1 receptors to understand the role of Mg^{2+} in the immune response.

INDEX WORDS: Genetically-Encoded Calcium Indicator, Calcium, Green Fluorescence Protein, Calcium Signaling, Protein Crystallization, JP45

DESIGN OF GENETICALLY-ENCODED CA^{2+} PROBES WITH RAPID KINETICS FOR SUB-CELLULAR APPLICATION

by

FLORENCE REDDISH

A Dissertation Submitted in Partial Fulfillment of the Requirements for the Degree of

Doctor of Philosophy

in the College of Arts and Sciences

Georgia State University

2016

DESIGN OF GENETICALLY-ENCODED CA^{2+} PROBES WITH RAPID KINETICS FOR SUB-CELLULAR APPLICATION

by

FLORENCE REDDISH

Committee Chair: Jenny Yang

Committee: Donald Hamelberg

Giovanni Gadda

Electronic Version Approved:

Office of Graduate Studies

College of Arts and Sciences

Georgia State University

August 2016

DEDICATION

The journey through the Ph.D. program has not been easy by any means. I could not have survived this process without being rooted and grounded in GOD and placing all my faith and trust in Him at all times. I am truly thankful. To my grandmother, Flora Alexander, you were right. I want to thank my parents, Jerome and Sandra Reddish, who have been like my guardian angels here on earth. You all have been there for me through thick and thin, highs and lows, good and bad. I am the woman that you both have watched me grow into because of the love and values you instilled in me at a young age. Thank you for loving me unconditionally. Ma, thank you for being my pastor and my psychiatrist throughout my whole academic career. Thank you both for your emotional and spiritual support throughout this process. Daddy, thanks for being straightforward with me and helping me see how my education would benefit my future family. Thanks for making me breakfast in the mornings too!

To my brothers, Marcus and Chris, and my sister-in-law Kim, thank you all for your encouragement and support throughout this journey. Thanks Marc and Kim for letting me spend the night at your house and feeding me whenever I was there. Chris, you rock! I hope to guide you through this process soon. I love you all very much.

To my nieces Kelise, Jaelyn, and Peyton, I've enjoyed watching the three of you grow up into beautiful and intelligent young ladies. I do apologize for not being able to spend as much time with you all as I wanted. I hope that by watching me achieve this dream, I inspired you all in some way. I love you all! To Charles, I faked all those computer problems just to see you, and it worked lol! I love you. Cheers to us!

ACKNOWLEDGEMENTS

The work completed for this dissertation was done under the direction of Dr. Jenny Yang. I appreciate you, and I thank you for all your help throughout the years. I truly admire you and respect what you have accomplished throughout your years as an educator and researcher. Thank you for believing in me and supporting me. I also want to thank my committee members, Dr. Hamelberg, and Dr. Gadda, for the guidance and helpful suggestions you all have given me throughout this process. Thank you for taking time to read and make corrections to my dissertation. Thank you both for also listening to me and easing my fears. To our collaborators, Dr. Zorzato and Dr. Lenardo, thank you for the data you helped me obtain and/or provided for my dissertation and your analysis.

I also want to thank all my fellow lab members Dr. You Zhuo, Dr. Chen Zhang, Dr. Yanyi Chen, Dr. Jinjiang Quo, Dr. Jie Feng, Dr. Shengui Xue, Dr. Fan Pu, Fantashia Goolsby, Mani Salarian, Corrie Purser, Cassie Miller, Juan Zou, Shanshan Tan, and Rakshya Gorghali for all the good times we have shared together, in and outside of the lab. I would also like to thank Will Lovett for providing a listening ear when I needed to talk. You helped me more than you know.

TABLE OF CONTENTS

LIST OF TABLES

LIST OF FIGURES

1 INTRODUCTION

1.1 Ca^{2+} and extracellular Ca^{2+} regulation

Calcium (Ca^{2+}) is one of the most prevalent minerals in the human body, with ~1 kg found in adults in restricted and unrestricted forms[1]. The major duty and form of bound Ca^{2+} is mineralizing the skeleton[2]. Because the bone environment is dynamic, skeletal Ca^{2+} helps maintain both intra- and extracellular Ca^{2+} levels. The level of unbound Ca^{2+} in adults is ~10 g and can be found in serum (2.2-2.6 mM) as free ions, bound to globulin and albumin, or bound to carbonate, oxalate, and phosphate ions[3]. The physiological level of ionized Ca^{2+} is maintained at 1.0-1.8 mM to prevent toxicity[4]. This ionized portion is utilized for the extracellular and intracellular Ca^{2+} signaling cascade that activates many important functions[5]. The balance of skeletal and free Ca^{2+} is hormonally regulated through the action of parathyroid hormone (PTH), calcitonin (CT), and $1,25(OH)_2D$ (vitamin D) on its receptor targets in the kidneys, intestines, and bone[6]. In addition to hormonal control of extracellular Ca^{2+}, the ion regulates itself through its binding to and activation of the Ca^{2+} sensing receptor (CaSR) in the same tissues and the parathyroid gland[3].

1.1.1 CaSR

The CaSR is a member of the C family of G-protein coupled receptors (GPCR)[7]. Brown and colleagues were the first to clone this receptor from bovine parathyroid gland. Their work showed that the CaSR has structural similarities to metabotropic glutamate receptors (mGluRs), specifically mGluR1 and mGluR5, as well as other members of the GPCR family[8]. The CaSR has four major structural elements: an

approximately 600 residue extracellular domain (ECD) housing the amino-terminal of the receptor, a linker domain composed of cysteine residues that connects the ECD to the first helix in the transmembrane domain, a transmembrane domain comprised of seven helices, and a cytosolic carboxy-terminal tail[9]. The ECD of human CaSR contains 11 potential N-linked glycosylation sites that aid in surface expression of the CaSR. Of the 11 glycosylation sites, eight are glycosylated, and the remaining sites become glycosylated if the other sites are manipulated[10]. The CaSR functions as a homodimer formed by disulfide bonds between cysteine residues located in the ECD[11]. Ray and colleagues performed a series of serine substitutions for the 19 cysteine residues located in the ECD of the CaSR. The resulting mutational analysis in HEK293 cells showed cysteines 129 and 131 are critical for the disulfide bond formation required for dimerization[12]. When both ECDs of the monomer units come together, they take on a venus-flytrap structure with a hinge region that allows the two lobes to open and close upon ligand or Ca^{2+} binding to the hinge region or the ECD[13,7]. Although the CaSR principally detects and is activated by extracellular Ca^{2+}, it also binds other divalent cations such as magnesium (Mg^{2+})[8,14] in addition to aromatic amino acids, such as L-phenylalanine, that help to heighten the sensitivity of the CaSR to Ca^{2+}[15,16]. Direct measurements of Ca^{2+} and other ligands to the ECD have been unsuccessful in the past due to the weak affinity of these sites and the inherent fast release kinetics associated with them. Zhang and colleagues recently expressed and purified the ECD of the CaSR in wild type 293-F cells and HEK293S (GnTI-) cells producing the complex glycosylated form and high mannose form of the ECD, respectively. Their measured Ca^{2+} dissociation constant (K_d), using the ANS binding assay, was 3.8 ± 0.2 mM with a

Hill coefficient of 2.6 ± 0.2, for the wild type form of the ECD[17]. Ca^{2+} generates half-maximal stimulation of the CaSR at 3.2 ± 0.1mM with a Hill coefficient of 3.6 ± 0.3 as measured in tsA cells[18]. The weak affinity and EC_{50} of the ECD for Ca^{2+} would imply that the ion is an impotent agonist for the CaSR since extracellular Ca^{2+} concentration is around 1.3 mM. The positive cooperativity among the Ca^{2+} binding sites and structural organization of the ECD permit the sensitivity of the CaSR to small fluctuations in extracellular Ca^{2+}, aiding its ability to govern serum Ca^{2+} levels through hormonal feedback mechanisms for Ca^{2+} homeostasis[13].

1.1.2 CaSR mediated hormonal regulation of serum Ca^{2+} levels

The systemic balance of Ca^{2+} levels is physiologically sustained through absorption of the ion from the gastrointestinal tract, retention and release of the ion from the kidneys, and its movement in and out of bone. This Ca^{2+} gradient is maintained by the action of the CaSR expressed in these different tissues and the action of the CaSR expressed in the thyroid and parathyroid glands that triggers the release of hormones PTH, CT, and vitamin D3[9]. When the CaSR senses a decrease in extracellular Ca^{2+}, PTH is released from the chief cells of the parathyroid gland. The increase in serum PTH levels blocks CT release from the C-cells of the thyroid gland and hinders bone formation resulting in Ca^{2+} release from the bone microenvironment. PTH also interacts with the PTH receptors on the kidneys, increasing Ca^{2+} reabsorption and onsite production of vitamin D3. The newly synthesized vitamin D3 targets the gastrointestinal tract to increase Ca^{2+} absorption. Prolonged elevation of serum Ca^{2+} levels induces the secretion of CT from the thyroid gland. CT inhibits bone resorption by osteoclast cells and triggers Ca^{2+} excretion by the kidneys[6,19,20]. Figure 1.1.1 depicts the hormonal

regulation of serum Ca^{2+}. Due to the delicate interplay of the subsystems that regulate serum Ca^{2+} levels, small imbalances can lead to many diseases such as hypercalcemia, hypocalcemia, and osteoporosis[6]. The detection of Ca^{2+} by the CaSR, in the tissues responsible for its homeostasis and other tissues expressing the receptor, triggers the release of intracellular Ca^{2+} from the endoplasmic and sarcoplasmic reticulum (ER/SR) inside the cell through the production of inositol triphosphate (IP3)[20]. The Ca^{2+} extruded into the intracellular environment is used as a second messenger in a host of intracellular processes and is regulated by various pumps, channels, receptors, and Ca^{2+} binding proteins (CaBPs)[21].

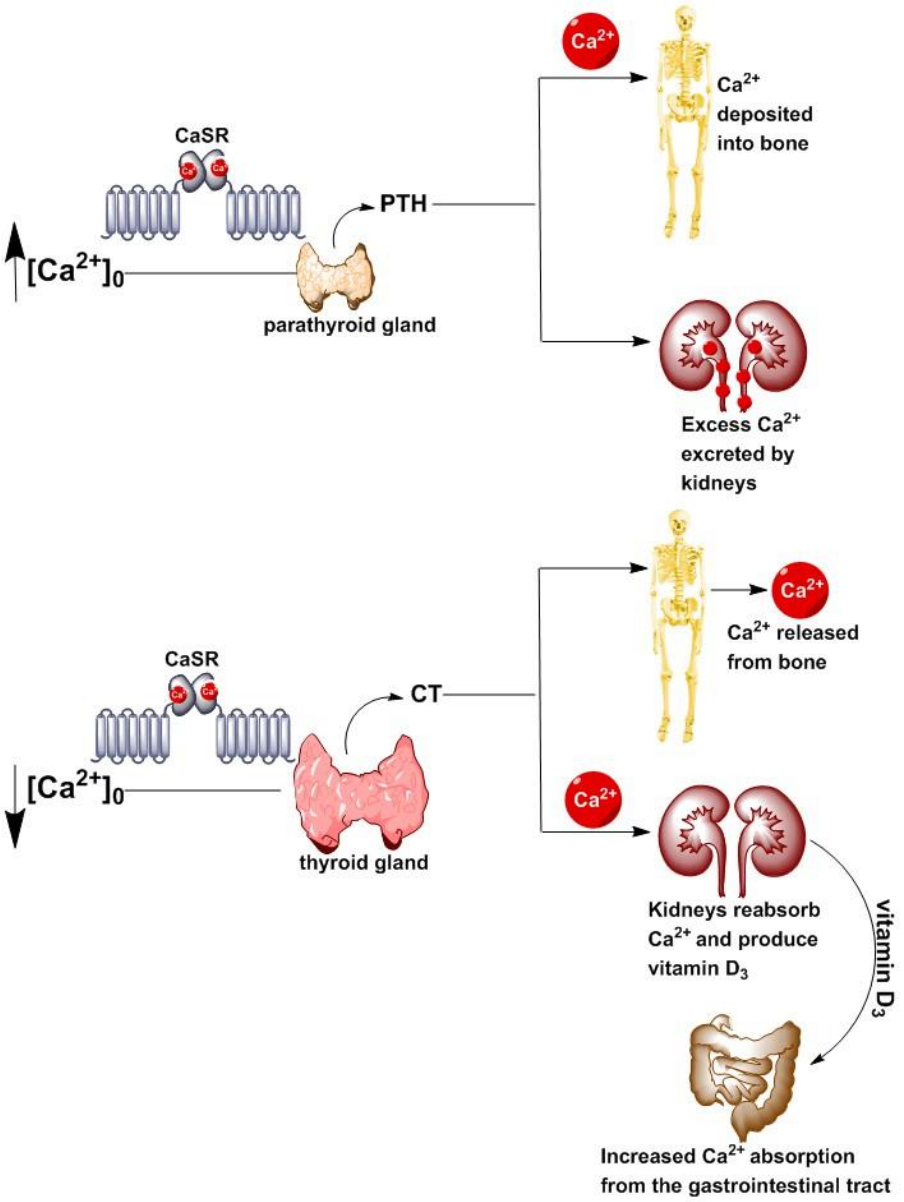

Figure 1.1.1 Hormonal regulation of extracellular Ca^{2+}

Serum Ca^{2+} levels are monitored by the CaSR and hormonally controlled by PTH, CT, and vitamin D3. Increased levels of extracellular Ca^{2+} are sensed by CaSR on the parathyroid gland triggering the release of PTH from chief cells. PTH binds to its receptor on bone and kidneys stimulating bone formation and Ca^{2+} excretion from the kidneys, respectively. Decreased serum Ca^{2+} is sensed by CaSR on the thyroid gland causing CT to be released from C-cells. CT acts on the kidneys increasing Ca^{2+} reabsorption. The kidneys will produce vitamin D3 which acts on the gastrointestinal tract to increase Ca^{2+} reabsorption.

1.2 Intracellular Ca^{2+} regulation and signaling

The efficiency and speed of Ca^{2+} signaling is powered by the ability of cells to maintain the near 20,000-fold gradient between intracellular and extracellular Ca^{2+} concentrations[22]. Resting cytosolic Ca^{2+} concentration in cells is 0.1 µM. When cells are activated, the level of cytosolic Ca^{2+} rises to 1 µM, triggering many downstream processes[5]. This rise in cytosolic Ca^{2+} can control a vast repertoire of cellular functions because of the adaptable nature and organization of the Ca^{2+} signaling system. The Ca^{2+} channels, pumps, and CaBPs expressed in different tissues, i.e. the Ca^{2+} signaling toolkit (Figure 1.2.1), are tailored to yield Ca^{2+} signaling mechanisms that produce varied spatial-temporal patterns for the initiation of slow processes such as gene expression[23] to fast processes such as neurotransmitter release[21,24] shown in Figure 1.2.2.

The intracellular Ca^{2+} signaling system has four major parts: 1.) the initial stimulus that spawns the countless Ca^{2+} mobilizing agents; 2.) the initiation of the ON machinery by the mobilizing agents that cause Ca^{2+} to move into the cytosol; 3.) the action of Ca^{2+} as a messenger molecule prompting processes sensitive to Ca^{2+}; and 4.) restoration of the basal cytosolic and organelle Ca^{2+} concentration through the deactiviation mechanisms that remove the ion from the cytosol. The consistent balance between the two mechanisms maintains the level of intracellular Ca^{2+}. All Ca^{2+} signaling systems will generate different Ca^{2+} transients based on the signaling components used[5].

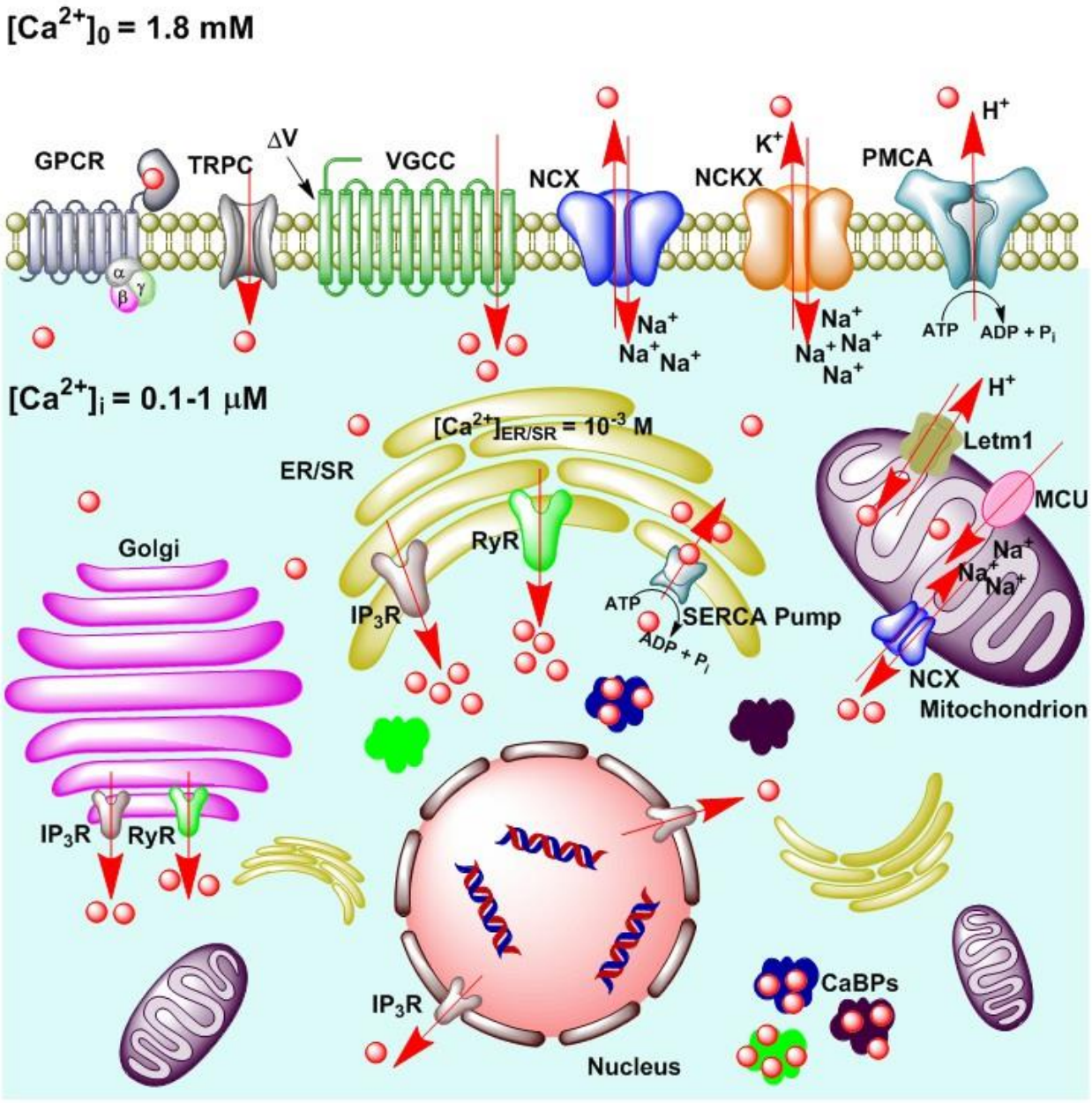

Figure 1.2.1 Components of the intracellular Ca^{2+} signaling toolkit

The various pumps, channels, receptors and CaBPs of the Ca^{2+} signaling toolkit help shape the spatial-temporal elements of the Ca^{2+} signal. Different receptors on the plasma membrane receive the extracellular stimulus triggering Ca^{2+} to flow from the extracellular environment into the cytosol, mobilizing Ca^{2+} from different compartments. Incoming Ca^{2+} triggers the release of more Ca^{2+} from its major storage organelle, the ER/SR, to further shape the Ca^{2+} signal for its activation of downstream processes. Pumps like the PMCA and SERCA extrude Ca^{2+} out of the cell and sequester Ca^{2+} back into the ER/SR and CaBPs bind free Ca^{2+} to maintain cytosolic Ca^{2+} levels at 0.1-1 μM.

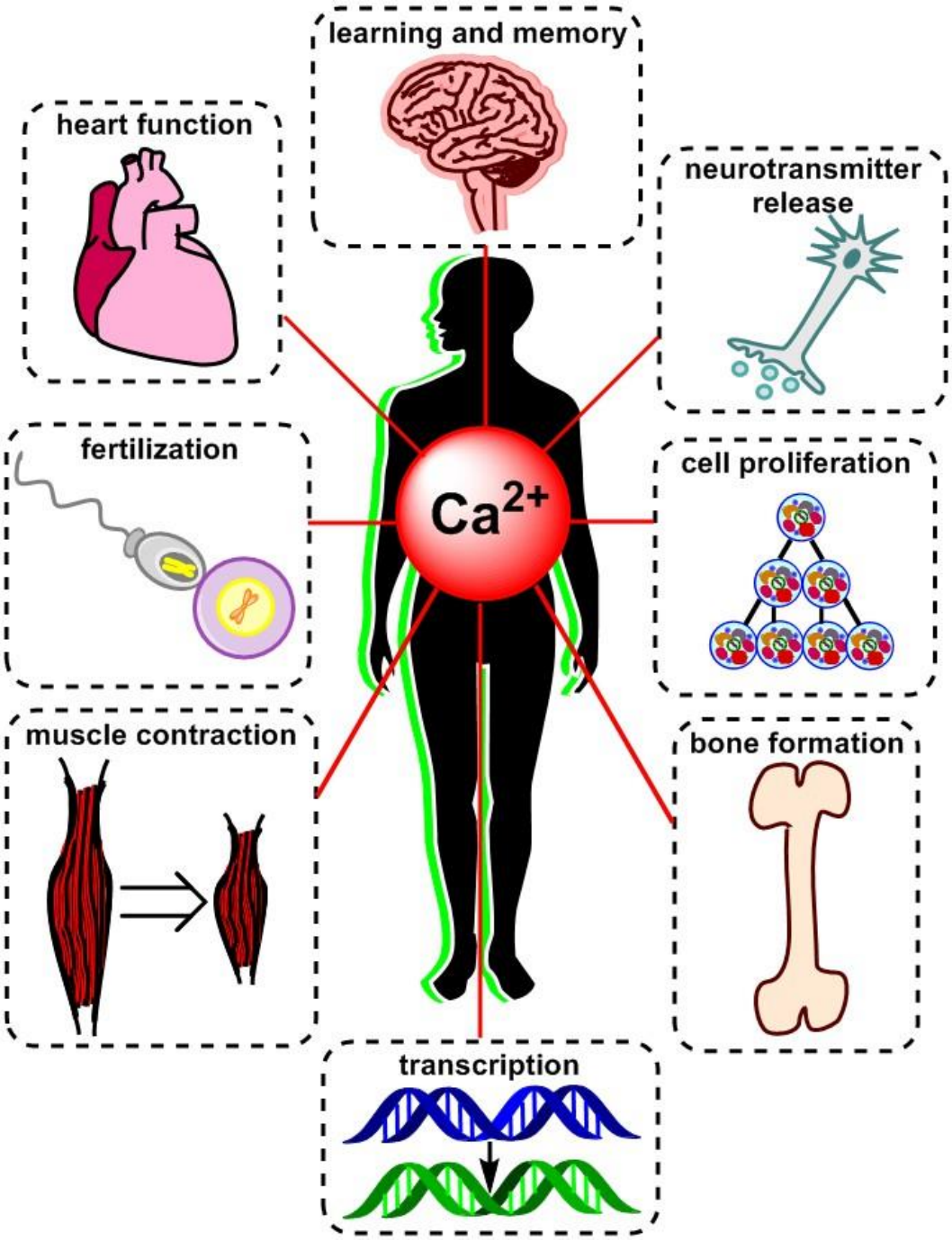

Figure 1.2.2 Biological processes mediated by Ca^{2+}

The varied signal patterns of Ca^{2+} activate diverse processes such as transcription, bone formation, muscle contraction, cell proliferation, fertilization, neurotransmitter release, learning and memory, and cardiac function.

1.2.1 Ca^{2+} pumps and exchangers

The role of Ca^{2+} pumps and exchangers is to direct Ca^{2+} ions out of the cell or back into organelles once the initial stimulus for the signaling event is removed. The major Ca^{2+} pumps are the plasma membrane Ca^{2+} ATPase (PMCA) pump and the sarco-endoplasmic reticulum Ca^{2+} ATPase (SERCA) pump found on the plasma membrane and the ER/SR membrane, respectively. Both pumps are powered by ATP hydrolysis to move Ca^{2+} ions against the concentration gradient. The PMCA and SERCA pumps are defined as P-type ATPases due to the creation of an aspartyl phosphate intermediate in the pumping process. Each pump helps to restore cytosolic Ca^{2+} concentration to 0.1 µM[22,25].

1.2.1.1 Plasma membrane Ca^{2+} ATPase pump

There are four isoforms of the PMCA pump (PMCA1, PMCA2, PMCA3, PMCA4) found in mammals containing 1115 to 1258 amino acids with molecular masses ranging from 125 to 140 kDa. Each isoform is encoded by a different gene. The sequence homology among the isoforms is only 80%, but their global structures are the same containing ten transmembrane segments, two cytosolic loops, and cytosolic amino and carboxy terminal tails[26,27]. Adding to the four basic isoforms, alternative splicing in the first cytosolic loop, site A, and in the calmodulin binding domain (CaM-BD) of the C-terminal, site C, breed an abundance of variants with diverse functions. The PMCA pump is primarily regulated by Ca^{2+}-CaM and the CaM-BD. At rest, the pump is auto-impeded by interaction of the carboxy terminal tail with two primary cytosolic loops. Upon activation, Ca^{2+}-CaM binds to the C-terminal tail causing it to dissociate from the cytosolic loops increasing the Ca^{2+} affinity (K_m) of the pump from 10-50 µM to 0.2-0.3

μM[27,28]. The PMCA pump co-transports protons with one Ca^{2+} ion per ATP consumed to decrease the cytosolic [Ca^{2+}][22].

1.2.1.2 Sarco-endoplasmic reticulum Ca^{2+} ATPase pump

The SERCA pump is another P-type ATPase pump that reduces cytosolic Ca^{2+} and refills the ER/SR by actively pumping the ion into the ER/SR lumen[29]. The pump functions as a monomer with a mass of 110 kDa. Three genes encode SERCA1, SERCA2, and SERCA3 isoforms whose amino acid sequences are highly conserved. From these three genes, alternative splicing generates over 10 variants of the pump adding to the diversity of its function in different tissues[30]. SERCA1 is primarily distributed in fast twitch skeletal muscle. SERCA2 is found in fast twitch and slow twitch muscle, cardiac muscle, smooth muscle, and non-muscle cells. SERCA3 is expressed in non-muscle cells[31]. The crystal structure of rabbit SERCA1a revealed a large cytosolic portion consisting of the Asp 351 phosphorylation site (domain P), the nucleotide binding site (domain N), and the anchor portion (domain A). The transmembrane (domain M) portion of the pump contains 10 α-helices where two Ca^{2+} ions bind[32]. The binding sites are side by side and are formed by M4, M5, M6, and M8 helices. When Ca^{2+} binds to the pump, the large cytosolic head changes from a closed to open conformation to facilitate translocation of the ions. For each ATP molecule consumed, the pump transports two Ca^{2+} ions into the ER/SR lumen[31,33]. Specific inhibitors of the SERCA pump include thapsigargin, from *Thapsia garganica*, and cyclopiazonic acid (CPA), from *Aspergillus* and *Penicillum*. CPA has a low affinity for the pump and reversibly blocks the Ca^{2+} access point[34]. Thapsigargin, on the other

hand, irreversibly binds to the Ca^{2+} free pump at residue F256 in the M3 helix with nanomolar affinity[29].

1.2.1.3 Na^+/Ca^{2+} and $Na^+/Ca^{2+}/K^+$ exchangers

The sodium Ca^{2+} (NCX) and sodium Ca^{2+} potassium (NCKX) exchangers are the predominant machineries used for the extrusion of signal Ca^{2+} across the plasma membrane[35]. The NCX and its three isoforms are a part of the large mammalian solute carrier 8 (SLC8) gene family. NCX1 is the most widely expressed isoform with high expression in heart, brain, and kidney and low levels of expression in other tissues. NCX2 is only abundant in the brain, and NCX3 is only expressed in skeletal muscle and at minimal levels in a few regions of the brain. Only NCX1 and NCX3 can be alternatively spliced in the cytosolic portion of the protein to produce variability among spliced isoforms[36]. The NCX and NCKX share structural similarities that include a cleavable extracellular N-terminal signal peptide, 10 transmembrane α-helices, two hydrophobic α-repeat regions, a large cytosolic loop, and a C-terminal cytosolic tail. The two α-repeat regions have opposing orientations in the plasma membrane and are between TM2 and TM3 (α_1-repeat) and TM7 and TM8 (α_2-repeat). Both areas are crucial for cation binding and transport[36,37]. In the NCX, the large cytosolic loop is located between TM5 and TM6 and contains two Ca^{2+} binding domains (CBD1 and CBD2). Four Ca^{2+} ions bind to CBD1 producing a conformational change activating the Ca^{2+}/Na^+ exchange function of NCX. CBD2 has a seven-fold weaker affinity for Ca^{2+} than CBD1, only binding Ca^{2+} at elevated levels. In the same cytosolic loop resides the XIP domain that is responsible for Na^+-dependent inactivation[37]. The NCX establishes an electrochemical gradient across the plasma membrane by exchanging 3 Na^+ for 1

Ca^{2+} ion. The NCX can also operate in the reverse to allow Ca^{2+} to enter the cytosol, as seen in cardiac cells during depolarization[35].

The NCKX is a part of the SLC24 exchanger gene family with five isoforms[38]. NCKX1 has been researched the most and is highly expressed in the eye. NCKX2 is widely expressed throughout the brain and in cone photoreceptors and ganglion cells of the retina. NCKX3 and NCKX4 are abundantly expressed in the cortex and thalamus of the brain. NCKX5 is broadly expressed in the skin, eye, brain, and thymus showing up at lower levels in other tissues[38]. Structural characteristics of the NCKX are similar to that of the NCX[36]. The α-repeat regions are conserved among the NCKX isoforms and are similar in sequence to the α-repeats of the NCX. The α-repeats are composed of 25 amino acids, primarily acidic, that cause a substantial decrease in cation transport when mutated. Within the α-repeat region, Aspartic acid (Asp) at position 575 is vital for K^+ transport. Glutamic acid (Glu) 188 and Asp548 are considered essential for Ca^{2+} transport[37]. The NCKX transfers $4Na^+$ ions for $1Ca^{2+}$ and $1K^+$ ion. It can be inferred from the transport stoichiometry that Ca^{2+} efflux through the NCKX is controlled by the internal and external Na^+ and K^+ gradients, respectively. Because of its carriage capacity, the NCKX can sustain larger Ca^{2+} gradients and is more reluctant to operate in the reverse mode in response to robust membrane depolarization when compared to the NCX[38].

1.2.2 Ca^{2+} channels

Extracellular and internal store Ca^{2+} are primary sources of signal Ca^{2+} [21]. These two components of the signal event are introduced into the cytosol through different Ca^{2+} channels embedded into the plasma membrane and the membrane of Ca^{2+}

storage organelles[22]. Various stimuli, including changes in membrane potential and ligand binding, activate the opening of these channels spurring cellular changes induced by the accumulation of cytosolic Ca^{2+}[21]. In the following subsections, we will discuss the channels responsible for mobilizing Ca^{2+} into the cytosol.

1.2.2.1 Voltage-gated Ca^{2+} channels

Voltage-gated Ca^{2+} channels (VGCCs or VOCs) allow Ca^{2+} into the cell in response to voltage changes across the plasma membrane[39]. The diverse Ca^{2+} activation currents found in cells can be divided into low voltage currents, with electrical potentials of -60 to -70 mV that are rapidly disabled, and high energy currents, with depolarizing potentials greater than -40 mV and slower inactivation[39]. The high voltage currents are further categorized based on physical properties and antagonists of the current. L-type currents are large conductance currents and are sensitive to 1,4-dihydropyridine. N-type currents are neuronal and can be inhibited by ω-conotoxin GVIA peptide from cone snail. P/Q-type currents were first isolated in Purkinje neurons and are blocked by ω-agatoxin IVA from spider venom. R-type currents are residual or resistant currents and are inhibited by SNX-482. Low voltage currents are designated T-type currents, or transient currents, and show insensitivity to Ca^{2+} blockers. L-type and T-type currents can be detected in many cell types such as cardiac, skeletal, and neuronal; however, the remaining types dominate in neurons[40,39].

Structurally, VGCCs are complexes composed of multiple subunits including the transmembrane α_2 and δ disulfide associated subunit, the cytoplasmic β subunit, the transmembrane γ subunit, and the chief transmembrane $Ca_v\alpha_1$ subunit that forms the channel pore[40,41]. The $Ca_v\alpha_1$ subunit consists of four homologous domains with each

containing six transmembrane segments (S1-S6). The loop that connects S5 and S6 forms the channel pore. In each domain, S1-S4 forms the gating machinery pairing activity with depolarization. S5 and S6 form the inner lining of the pore. Channel deactivation, regulation, and subunit binding occur at the cytosolic N- and C-terminals and loops I-II, II-III, and III-IV that link the domains of the $Ca_v\alpha_1$[40]. Ten isoforms of the $Ca_v\alpha_1$ subunit exist. Due to its importance for channel function, the $Ca_v\alpha_1$ subunit is used to divide VGCCs into three families: Ca_v1, Ca_v2, and Ca_v3[39]. $Ca_v1.1$-$Ca_v1.4$ produce L-type currents and are distributed in cardiac, skeletal muscle, endocrine, neuronal, and retinal cells. $Ca_v2.1$-$Ca_v2.3$ generate P/Q, N, and R-type currents, respectively, and are distributed in nerve terminals and dendrites. $Ca_v3.1$-$Ca_v3.3$ produce T-type currents and are expressed in cardiac muscle, skeletal muscle, and neurons[42]. The β subunit has four isoforms, and its association with the $Ca_v\alpha_1$ leads to increased channel expression and trafficking which increases the Ca^{2+} current. The $\alpha_2\delta$ subunit, like the β subunit, increases channel trafficking to the plasma membrane. The γ subunit aides in the modification of the biophysical properties of the $Ca_v\alpha_1$ subunit[39,40].

1.2.2.2 Transient receptor potential channels

Transient receptor potential channels (TRP) are similar in function to VGCCs in that they are voltage sensitive, but only weakly. TRPs are non-selective ion channels that allow the influx of Ca^{2+} and sodium ions across the plasma membrane into the cytosol leading to depolarization[43]. TRPs and their isoforms are divided into the following six subfamilies based on sequence similarities: TRPC, TRPML, TRPV, TRPM, TRPA, and TRPP. The modeled channel structure includes six transmembrane domains with the ion pore region between transmembrane segments five and six.

TRPs can integrate multiple stimuli that induce activity and signal amplification[44]. These activators include ligands such as 2-APB, DAG, Ca^{2+}, and Mg^{2+}, receptors such as GPCRs, and changes in temperature. Because TRPs are considered signal integrators and amplifiers, they function mainly as cellular sensors and aide in growth cone guidance[43].

1.2.2.3 Ryanodine receptor and the inositol 1,4,5-triphosphate receptor

The Ca^{2+} released from the ER/SR makes up the bulk of the Ca^{2+} signal. The inositol 1,4,5-triphosphate receptor (IP_3R) and the ryanodine receptor (RyR) are the main Ca^{2+} release channels on the ER/SR membrane. Ca^{2+} activates both receptors through a process called Ca^{2+}-induced Ca^{2+} release (CICR), allowing more Ca^{2+} to discharge from the ER/SR to propagate the Ca^{2+} signal[25].

The RyR exists in three isoforms in mammals: RyR1, RyR2, and RyR3. RyR1 and RyR2 are the predominant isoforms found in skeletal and cardiac muscle, respectively, while RyR3 is dominant in the thalamus, hippocampus, corpus striatum, and smooth muscle[45,46]. High resolution cryo-electron microscopy structures of the RyR show it exists as a homotetramer with a total mass over 2 MDa making it the largest ion channel. The large cytosolic portion of the RyR has a mushroom-like shape with the rest of the channel embedded in the SR membrane[47,48]. This large cytosolic portion of the RyR is where many proteins bind to regulate its function such as FKBP12 (RyR1), FKBP12.6 (RyR2), calmodulin, CaMKII, S100A proteins, and DHPRs[49]. Ca^{2+} activates and inhibits RyR1 activity. When Ca^{2+} concentration is ~1μM, the receptor is active, and it is deactivated when the Ca^{2+} concentration reaches 1 mM[50]. Myoplasmic free magnesium is a potent inhibitor of RyR1 in resting skeletal muscle cells. If the

physiological concentration of magnesium is lowered from 1 mmol/L to 0.05 mmol/L, the receptor opens resulting in a steep decrease in SR Ca^{2+}. Cytosolic ATP also triggers the Ca^{2+} release channel activity[51]. Caffeine exerts a stimulatory effect on RyRs by enhancing their affinity for Ca^{2+} without disrupting magnesium binding[52]. 4-chloro-m-cresol (4-CmC) is a potent agonist of the RyR, having a 10 fold higher sensitivity than caffeine for inducing SR Ca^{2+} release with both regularly employed to study RyR-mediated Ca^{2+} release in healthy and diseased cells[53]. RyR1 is highly localized in the terminal cisternae region of the SR membrane facing the t tubules in skeletal muscle cells. The DHPRs, situated on the t tubule membrane, interact directly with RyR1 to activate Ca^{2+} release when membrane depolarization occurs[54]. Residues 1,635-2,636 of RyR1 were shown to interact with the DHPR to mediate Ca^{2+} release and E-C coupling[55]. Later, it was discovered that residues 1-1,680 at the N-terminal portion of RyR1 facilitate E-C coupling[56]. RyR1 also enriches the activity of the DHPR through a backward current[57]. RyR1 and RyR2 are also controlled luminally through interactions with calsequestrin, junctin, and triadin[58]. The process linking depolarization to muscle contraction, E-C coupling, the specialized junction it occurs in, and the associated proteins will be discussed more in section 1.4.1.

The inositol-1,4,5-triphosphate receptor (IP_3R) is the major Ca^{2+} release channel on the ER membrane of non-excitable cells[59]. Its presence in excitable cells servers to amplify the Ca^{2+} signal generated from depolarization[60]. The IP_3R is a member of a vast ion channel superfamily[61]. Like RyR, the IP_3R functions as a tetramer having a large cytosolic domain resembling a mushroom and six transmembrane segments with the Ca^{2+} binding portion homologous to that of the RyR[62]. Three isoforms of the IP_3R

exist with IP_3R1 being well studied[63]. IP_3 is generated as a second messenger from the breakdown of phosphoinositol-4,5-bisphosphate (PIP_2) by phospholipase C (PLC) through activation of GPCRs[59]. Channel opening is activated by both Ca^{2+} and IP_3 where IP_3 increases the response of the channel to Ca^{2+} giving it a bell-shaped response curve similar to RyR[5]. Channel opening allows the release of Ca^{2+} from the ER and other internal stores expressing the receptor[59]. Several molecules interact indirectly or directly with the IP_3R triggering its activation. ATP increases IP_3-mediated Ca^{2+} release through the IP_3R at concentrations of 100 µM[64]. ATP binds to the purinergic receptor P2YR, a GPCR, triggering production of IP_3 that binds to the IP_3R to release Ca^{2+} from the ER[65,66].

1.2.3 Ca^{2+} binding proteins

At the molecular level, Ca^{2+} can influence cellular activity and overall function due to the presence of CaBPs. These binding proteins are responsible for binding free Ca^{2+} during influx acting as shuttles and activators changing the spatial and temporal aspects of the Ca^{2+} signal[67]. CaBPs can be divided into two major subgroups: Ca^{2+} buffer proteins and Ca^{2+} sensors. Ca^{2+} buffer proteins are a small group of the EF-hand family of CaBPs that have Ca^{2+} K_d values in the high nanomolar to low micromolar range, so in resting cells, these binding proteins are primarily in the Ca^{2+} free state. Upon electrical, mechanical, or hormonal stimulation, Ca^{2+} buffer proteins readily bind the influx of Ca^{2+} ions with various affinities[68]. Parvalbumin, for example, is a well-known cytosolic Ca^{2+} buffer primarily found in fast-twitch muscle with 3 EF-hands, two are functional, and one is non-functional. The functional EF-hands are mixed in that they bind Ca^{2+} and Mg^{2+} ions[69]. Parvalbumin has a strong affinity for Ca^{2+} with K_d

values between 4-9 nM with a rapid k_{on} and slow k_{off} of $2.5x10^8$ $M^{-1}s^{-1}$ and 1.01 s^{-1}, respectively. The kinetic properties of parvalbumin allow for fast response to the rapid Ca^{2+} increase in active muscle cells[70]. The second subgroup of CaBPs are the Ca^{2+} sensors which make up the majority of the EF-hand family. Depending on the concentration of this type of CaBP, they may also function as buffer proteins[71]. The ability of the Ca^{2+} sensor proteins to translate the cytosolic Ca^{2+} increase into a mechanical signal, due to the conformational change that takes place, and trigger many downstream processes is attributed to their uniqueness as regulatory proteins. Ca^{2+} controls the action of these proteins[72]. The quintessential example of a Ca^{2+} sensor is calmodulin (CaM)[73]. CaM is composed of 4 EF-hands resembling a dumb bell with two globular domains at either end separated by a helical linker region in the Ca^{2+} bound form. In the Ca^{2+} free form, CaM is in a globular closed conformation. CaM binds four Ca^{2+} ions with positive cooperativity (K_d ~ $5x10^{-7}$- $5x10^{-6}$ M) with the C-terminal domain having a higher affinity than the N-terminal[74]. CaM binds Ca^{2+} at a rate of $1x10^8$ $M^{-1}s^{-1}$ and releases it at 238 s^{-1} [70]. With processes occurring on a timescale of microseconds to hours, from exocytosis to fertilization, CaBPs help to tailor the duration of the signal to accommodate specific cellular events in different cell types[21]. Ca^{2+} probes are needed that can bind and release Ca^{2+} quickly, with low affinity, to monitor these rapid changes in $[Ca^{2+}]$.

1.3 Magnesium

The magnesium (Mg^{2+}) ion plays an important role in physiology[75]. Although magnesium has a smaller ionic radius than Ca^{2+}, it readily binds water molecules increasing its hydration radius[76]. The increased hydration radius allows magnesium to

bind in sites designated for Ca^{2+}. Thus, the magnesium ion must be discussed. The magnesium ion is found in great abundance in the human body. In healthy individuals, serum levels of Mg^{2+} are between 0.7-1.05 mM with tight regulation by absorption and excretion through the intestines and kidneys. Mg^{2+} in serum only accounts for 1% of the 24 g of total Mg^{2+} found in the body with the majority of it residing in muscle, bone, and other tissues[75]. Intracellularly, Mg^{2+} has an almost negligible electrochemical gradient unlike that of its counter ion Ca^{2+}, leaving its speculated role as a second messenger unclear[77,78]. Intracellular levels of Mg^{2+} are maintained between 0.5-1.2 mM with levels at ~1 mM in the ER/SR and the high milli-molar range in the mitochondrion. Cytosolic Mg^{2+} only represents 5-10% of cellular Mg^{2+} [77]. Levels of free cytosolic Mg^{2+} are maintained through different membrane transporters such as TRPM7[79], MRS2[80], and MagT1[81]. The importance of MagT1 will be discussed later in Chapter 5. Mg^{2+} flows into the cell by diffusion. Extrusion of this ion occurs against an electrochemical gradient that is commonly coupled to Na^{+} exchange, where two Na^{+} ions are exchanged for one Mg^{2+} ion. In addition to its structural role in nucleic acids and its role as a cofactor and activator in many enzymatic reactions, Mg^{2+} also binds to ATP to stabilize its charge. Implicated in its function in ATP, the level of free cytosolic Mg^{2+} is effected by the rate of energy production occurring in the mitochondrion, where increases in ATP production lower $[Mg^{2+}]_i$[82]. Along with its function in energy metabolism, Mg^{2+} also plays important role in bone formation and the proper function of the heart, brain, and skeletal muscle[75]. Hypomagnesemia, a clinical state in which serum Mg^{2+} levels fall below 0.5 mM, effects physiological processes involving Mg^{2+} adversely[83]. The pathological results of improper Mg^{2+} regulation include coronary artery disease,

neurological disorders, asthma, vascular calcification, and muscle cramps, to name a few[75]. Magnesium and its role in physiology, with emphasis on the immune response, will be discussed in Chapter 6.

1.4 ER/SR Ca^{2+} signaling

The ER and the sarcoplasmic reticulum (SR), its counterpart in striated muscle cells, are not only the site for protein synthesis inside the cell, but they are also key organelles in most signaling events, being able to receive and transmit signals[84,54]. Stimuli that activate the ER/SR include reactive oxygen species (ROS), inositol 1,4,5-triphosphate (IP_3), sterols, sphingosine-1-phosphate (S-1-P), and Ca^{2+}, just to name a few. The input stimuli are converted to output signals such as stress signals, transcription factors, and Ca^{2+}. The dual role of Ca^{2+} in ER/SR mediated signaling points to its excitatory nature and ability to continue the Ca^{2+} signaling event through Ca^{2+} induced Ca^{2+} release (CICR)[84]. The ryanodine receptor and the inositol 1,4,5-triphosphate receptor (IP_3R) are Ca^{2+} release receptors located on the membranes of the SR and ER, respectively, that are activated by Ca^{2+}[85]. The distribution of these Ca^{2+} release channels, associated proteins, and SERCA pump varies in the ER and SR[86]. The organization of the SR Ca^{2+} release and refilling machinery is highly specific, as is the case in cardiac[87] and skeletal muscle cells[88]. The localized Ca^{2+} domains that arise from the spatial organization of sarcolemmal and SR associated Ca^{2+} channels and CaBPs generate local elevations in Ca^{2+} near the release channels needed for excitation-contraction coupling to occur[88,58,89]. The complex organization of the SR makes analyzing and quantifying the changes involved in Ca^{2+} signaling a challenge. In the following subsections, we will discuss the morphology and organization of the SR

and the implications of the local Ca^{2+} signals generated from this organelle. It is important to have a Ca^{2+} probe that can effectively monitor the fast kinetics of Ca^{2+} release and changes in global and local levels of ER/SR Ca^{2+}. Our work designing a probe for this purpose is addressed in Chapter 5.

1.4.1 Morphology and organization of the SR for E-C coupling

The ER appears as an uninterrupted network with three distinct forms and accompanied specialized functions[90]. The rough ER (RER) appears as flattened sacs and is speckled with ribosomes for protein synthesis. The smooth ER (SER) is an elongated, cylindrical network with key functions in Ca^{2+} storage and release. Surrounding the nucleus is an extension of the ER called the nuclear envelope (NE). The NE is also dotted with ribosomes and supplies the nucleus with Ca^{2+} for gene transcription[90,91]. The SR is a morphologically distinct version of the smooth ER specialized for Ca^{2+} release to fuel muscle contraction[88]. It consists of large sink portions referred to as terminal cisternae (TC) connected to elongated tubes termed the longitudinal SR. RyR1s are located solely in the TC, while SERCA pumps are found exclusively in the longitudinal SR. The distribution of these primary receptors within the SR divide this organelle into two divergent subdomains tasked with the release and the uptake of Ca^{2+} [92]. Within the muscle cell, the TC is distributed to be in proximity to the tubule invaginations of the sarcolemma membrane called the transverse tubules (t tubules). Located on the t tubule membrane are the DHPRs that allow Ca^{2+} to flow into the myoplasm in response to depolarization. The space between the SR TC membrane and the t tubule membrane is referred to as the junctional zone[54]. This extended SR network consisting of the TC, longitudinal SR, and the t tubules surrounds the myofibrils

in repeating units near the sarcomere ensuring delivery of Ca^{2+} for contraction to occur[93]. The immense amount of Ca^{2+} released from the SR in response to the action potential fuels excitation-contraction (E-C) coupling[54,58,94]. This large reservoir of Ca^{2+} required to generate contractile force repetitively from a train of action potentials is maintained by the low affinity, high capacity Ca^{2+} binding and release of CASQ1[95]. CASQ1 is concentrated in the SR TC where it forms long polymers near the opening of RyR1 in a Ca^{2+} dependent manner[96,97]. Polymerized CASQ1 can bind 40-50 mol of Ca^{2+}/mol of CASQ1 with a 10^3 M^{-1} affinity over a high Ca^{2+} concentration range of 0.01-1 M. Its exceptional buffering function makes CASQ1 the sole mechanism for fast Ca^{2+} binding and release from the SR[95]. CASQ1 modulates Ca^{2+} release through the RyR1 by acting as a luminal Ca^{2+} sensor through its association with integral membrane RyR associated proteins junctin and triadin. When junctin and triadin are present, CASQ inhibits RyR function when luminal Ca^{2+} is at 1 mM. As luminal Ca^{2+} increases, CASQ depolymerizes releasing Ca^{2+} and increasing RyR activity[98]. In skeletal muscle cells, an additional protein associated with the junctional zone, having an important role in E-C coupling, was discovered called JP45[99]. JP45 interacts with the DHPR at the cytosolic portion of its N-terminal and with CASQ1 at its C-terminal situated in the SR lumen[100]. Deletion studies of JP45 from young mice resulted in a loss of skeletal muscle strength due to decreased expression of the DHPR which is essential for E-C coupling[101]. These local Ca^{2+} signals that activate the contractile proteins in the junctional zone are fueled by global changes in SR Ca^{2+} and are critical for E-C coupling to occur. Mutations in these junctional zone/RyR1 associated proteins lead to many musculo-skeletal diseases[102]. For this reason, we designed a targeted Ca^{2+} probe called CatchER-T'-

JP45 to understand the local changes in Ca^{2+} occurring in this area of the TC. This work will be discussed in Chapter 5.

1.5 Diseases and disorders associated with disrupted Ca^{2+} signaling

As cells grow and separate into their respective tissue types during the developmental process, diverse elements of the Ca^{2+} signaling machinery will be expressed that will render different properties to the generated Ca^{2+} signal[21, 25]. These components are under continuous modification to adjust to environmental changes and ensure the preservation of the Ca^{2+}-mediated response for the particular cell type. When problems arise with constituents of the signaling network, Ca^{2+} itself will trigger transcription of the defunct components to restore the signal[25]. Many major diseases are attributed to dysfunctional elements in the Ca^{2+} signaling network, primarily the IP_3R and RyR that mediate Ca^{2+} release from the ER/SR[103]. A few of those diseases will be discussed in this section.

1.5.1 Heart disorders

Ca^{2+} is a critical component of the various aspects of the signaling system in cardiomyocytes that work together to generate the contractile force needed to pump blood throughout the body[104]. Some of these areas include the electrophysiological mechanisms used to generate the action potential, E-C coupling, myofilament activation, energy manufacture and metabolism, cell death, and transcriptional control of cardiac machinery[105]. A breakdown or mutation in any of the components in the previously mentioned areas will cause electrical and mechanical problems within the heart[104]. Catecholaminergic polymorphic ventricular tachycardia (CPVT) is a heart disorder that causes abnormal heart rhythm[106]. CPVT is characterized by rapid heart

rate through β-adrenergic receptor stimulation. Commonly occurring in kids and teenagers, CPVT causes fainting and sudden death. When left untreated, CPVT has a 31% mortality rate in patients 30 years of age[107]. The clinical characterization of CPVT is fainting connected to seizures brought on by stress or exercise. Mutations in the cardiac isoform of RyR, RyR2, have been identified in familial cases of CPVT[108]. RyR2 plays a major role in Ca^{2+} regulation and release from the SR in cardiomyocytes[109]. Activation of the L-type Ca^{2+} channel allows Ca^{2+} to flow into the cytosol from the extracellular environment. The circulating Ca^{2+} opens RyR2, through CICR, allowing prompt discharge of Ca^{2+} from the SR. The elevated cytosolic Ca^{2+} level induces contraction and is taken back up into the SR[104, 110]. Improper regulation of this cycle is associated with many heart disorders such as CPVT[107].

1.5.2 Malignant Hyperthermia

Malignant hyperthermia (MH) is a genetic skeletal muscle disease caused by mutations in RyR1[111,112]. Commonly induced by certain anesthetics, MH is the underlying cause of anesthesia-related deaths in patients who are seemingly healthy. The anesthetics known to initiate MH include isoflurane, sevoflurane, haloethane, desflurane, enflurane, and the muscle relaxer succinylcholine[113]. In some reported cases of MH, abrupt changes in temperature and stressors triggered the disease. Clinical hallmarks of MH include rapid heart rate, high blood pressure, sustained muscle contractions, increased CO_2 levels, trouble breathing, and severe increase in core temperature. Untimely diagnosis of MH leads to death. The hypermetabolic state mirrored in MH is attributed to escalated Ca^{2+} release from the SR caused by defects in RyR1 situated on the SR membrane[112,113]. Hundreds of mutations to human RyR1

have been linked to MH, thus far, with research still ongoing. The majority of these mutations are confined to three locales in RyR1: C35-R614 in the N-Terminal, D2129-R2458 in the central region, and I3916-G4942 in the carboxy terminal, but several mutations still exist outside of these areas[114]. MH mutations have also been identified in the human CACNL1A3 gene coding the α_1 subunit of the DHPR located on the sarcolemma[115]. The DHPR and the RyR1 are in close contact with one another. When skeletal muscle cells are depolarized, the DHPR converts the voltage change to a conformational change that triggers SR Ca^{2+} release through the RyR1 leading to muscle contraction in a process known as excitation-contraction coupling (E-C coupling). In MH, mutations in RyR1 and the DHPR prevent communication between the two causing a breakdown in E-C coupling[112]. The abnormal handling of SR Ca^{2+} leads to muscle rigidity caused by elevated myoplasmic Ca^{2+} and increased glycogen and glucose breakdown sparked by phosphorylase kinase galvanization by Ca^{2+} [114]. These frenzied metabolic reactions consume O_2, ATP, and glycogen reserves and create exorbitant amounts of metabolic waste products, leading to an eventual disturbance in ion levels and ensuing cellular destruction[116]. Clinical treatment of MH involves the administration of the muscle relaxer Dantrolene, the only pharmacological agent known to treat the disease[117]. Dantrolene imposes a hindrance on the DHPR, blocking L-type currents and diminishing Ca^{2+} release from the SR; however, expression of RyR1 was found necessary for Dantrolene to exert an inhibitory effect on the DHPR through modification of the coupling between these channels[118].

1.5.3 Alzheimer's Disease

Alzheimer's disease (AD) is medically defined as the continuous deterioration of mental capacity leading to noticeable declines in behavior and memory associated with aging[119]. Currently, the prevalence of AD is ranked highest among all other neurological maladies and has no cure. The majority of AD cases that arise are late onset or sporadic AD (SAD). Familial AD (FAD), or early onset AD, constitutes a small percentage of cases and has genetic origins. In both cases, AD manifests in the brain as lesions of amyloid-beta (Aβ) protein, fibrous tangles of tau (τ) protein, and cell death resulting in the reduction of brain mass and ultimately death[120,121]. Amyloid plaque formation is caused by the improper cleavage of the neuroprotective amyloid precursor protein (APP) by secretase enzymes resulting in copious amounts of the cytotoxic, 42 residue fragment Aβ[122]. Mutations in APP and presenilins 1 and 2 (PS1 and PS2), which are located in the ER membrane of neurons, lead to a buildup of Aβ in cases of FAD. A common denominator in all cases of AD is the mishandling of neuronal intracellular Ca^{2+}, primarily IP_3R and RyR-mediated Ca^{2+} release from the ER[119,123]. Resting free intracellular Ca^{2+} levels were dramatically increased in the neurons of transgenic mice exhibiting AD compared to normal neurons. This increase was due to the influx of Ca^{2+} through voltage gated channels and its release from the ER through the IP_3R and RyR[124]. PS1 and PS2 mutants of FAD were shown to excite IP_3R activity causing amplified Ca^{2+} signaling from the ER which increased Aβ production[125]. Injection of Aβ aggregates into Xenopus oocytes alone elicited IP_3R stimulation through GPCR production of IP_3 resulting in vigorous Ca^{2+} release from the ER and cytotoxicity[126]. Reduction in IP_3R levels and blocking of RyR activity was shown to

alleviate AD symptoms in AD mouse models solidifying IP_3R and RyR-mediated Ca^{2+} release from the ER in neurons as therapeutic targets for AD[127,128].

1.6 The inception of Ca^{2+} imaging with synthetic dyes

As detailed in the preceding sections, the movement of Ca^{2+} outside and inside the cell is central to many functions in living organisms. When the flow of Ca^{2+} is impeded, various pathologies will ensue[25]. A popular tool used for understanding the Ca^{2+} signaling pathways in different functions is Ca^{2+} indicators. Two groups of Ca^{2+} indicators exist: synthetic and genetically-encoded[129,130]. The latter will be discussed in a later section. Organic Ca^{2+} dyes are highly sought after for Ca^{2+} imaging because of their broad emission spectra and ease of use in cells[129]. A drawback to using synthetic indicators is their lack of targeting specificity to different organelles. Ca^{2+} dyes compartmentalize in cells, making it difficult to measure Ca^{2+} in one specific organelle. Another disadvantage to using synthetic indicators is their leakage from the cell during long experiments[131]. Introducing dextran tags on the dyes allows them to stay in cells longer[129]. The origin of Ca^{2+} dyes and a few of the commonly used indicators will be discussed in this section.

The first Ca^{2+} chelator dyes were designed by Roger Tsien in the 1980s[132,133]. Quin2, located in Figure 1.6.1A, is a fluorescent quinolone Ca^{2+} dye that binds Ca^{2+} in a 1:1 ratio. Its excitation and emission wavelengths are 339 nm and 492 nm, respectively. Quin2 has a Ca^{2+} K_d of 60 nM, in the absence of magnesium, and a K_d of 115 nM in the presence of 1 mM magnesium. The AM ester form of Quin2 was used to measure the resting intracellular Ca^{2+} concentration in mouse and pig lymphocytes which was determined to be 120 nM[134].

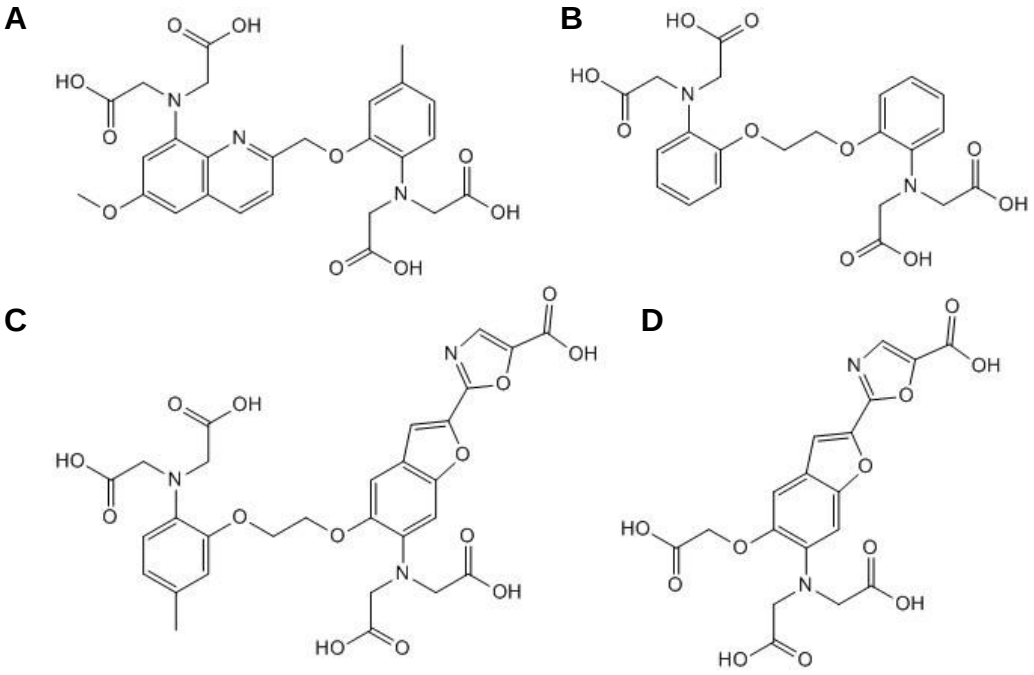

Figure 1.6.1 Structures of the first and commonly used synthetic Ca^{2+} dyes

Structures of quin2 (A), BAPTA (B), fura-2 (C), and Mag-fura-2 (D). Quin2 was the first Ca^{2+} dye created with a Ca^{2+} K_d of 60 nM. Poor fluorescence makes Quin2 less suitable for monitoring Ca^{2+} flux in situ. BAPTA (B) is a derivative of EGTA and is more selective for Ca^{2+} over magnesium. Fura-2 (C) is the most commonly used, ratiometric Ca^{2+} imaging dye derived from BAPTA and EGTA. Mag-fura-2 (D) is a weaker affinity Ca^{2+} dye originally created to detect magnesium.

Depicted in Figure 1.6.1B, 1,2-bis(o-aminophenoxy) ethane-N,N,-N',N'-tetraacetic acid (BAPTA) is a synthetic Ca^{2+} dye that was derived from the Ca^{2+} chelator ethylene glycol bis(β-aminoethyl ether)-N,N,N',N'-tetraacetic acid (EGTA). BAPTA has an excitation maximum of 254 nm and emits at 363 nm. Compared to EGTA, BAPTA has a higher selectivity for Ca^{2+} than magnesium with a K_d of 1.1 x 10^{-7} M for Ca^{2+} and 17 mM for magnesium in the presence of 0.1 M KCl. BAPTA is also less sensitive to fluctuations in pH and has faster kinetics with an off rate of 60 s^{-1} [132,135].

The most widely used synthetic Ca^{2+} indicator, thus far, is fura-2 (Figure 1.6.1C) with a stilbene chromophore containing tetracarboxylate ligands similar to its predecessors EGTA and BAPTA[133]. The Ca^{2+} K_ds of fura-2 in cytosolic buffer conditions are 135 nM without magnesium and 224 nM in the presence of 1 mM magnesium. Fura-2 has a better selectivity for Ca^{2+} over magnesium, compared to Quin2, with a magnesium K_d of 9.8 mM. A key feature of fura-2 is that it is a ratiometric indicator. Fura-2 has an absorbance peak at ~380 nm. As Ca^{2+} is added and the complex forms, the 380 nm peak decreases and a new peak at ~340 nm forms and continues to increase. It has single wavelength emission at ~512 nm. The ratiometric property of fura-2 allows for the correction of dye variability and instrument inefficiency[129,133]. Fura-2 has been used extensively in different cell types and tissues to monitor changes in cytosolic Ca^{2+}. It has been applied in mast cells where emptying of intracellular Ca^{2+} stores was found to stimulate a steady inward current of Ca^{2+} termed Ca^{2+}-release activated Ca^{2+} (I_{CRAC})[136]. Fura-2 has also been used in MCF-7 cancer cells to identify the contribution of increased Orai1 expression and store operated Ca^{2+} entry to activation of membrane androgen receptors[137]. Because of the high affinity of fura-2 for Ca^{2+}[133], it cannot be applied to Ca^{2+} storage organelles containing millimolar amounts of Ca^{2+}. A different Ca^{2+} indicator, such as mag-fura-2, that can detect Ca^{2+} levels in organelles is preferred.

Mag-fura-2 (Figure 1.6.1D), previously known as FURAPTRA, was created from the *O*-aminophenol-*N,N,O*-triacetic acid chelator APTRA by Robert E. London and colleagues[138]. Mag-fura-2 was initially used and created to measure free magnesium in the cytosol. The magnesium K_d of mag-fura-2 is 1.5 mM. Consequently, mag-fura-2

also binds Ca^{2+} with a K_d of 53 µM. Like fura-2, mag-fura-2 is also ratiometric having an absorbance max at ~380 nm in the absence of metal with a peak shift and increase at 340 nm as the dye-metal complex forms. Mag-fura-2 fluoresces at 510 nm, and like fura-2, it exhibits 1:1 binding stoichiometry. It is a pH insensitive Ca^{2+} dye with a pK_a of 5.0[139]. It was first used to measure a cytosolic magnesium concentration in rat hepatocytes of 0.59 mM[139], and was later applied in cultured embryonic chicken heart cells where the resting $[Mg^{2+}]_i$ was 0.48 mM[140]. Hofer and colleagues were the first to take advantage of the proclivity of mag-fura-2 AM to compartmentalize in cells to investigate the effect of Cl^- on the release and reuptake of Ca^{2+} in an IP_3-sensitive organelle[141].

In addition to the indicators discussed above, several other organic Ca^{2+} dyes are available for the study of Ca^{2+} and Mg^{2+} flow inside the cell. A listing of these dyes, K_ds, and other properties can be found in Table 1.6.1.

Table 1.6.1 Properties of commonly used Ca^{2+} and Mg^{2+} dyes

Indicator	Ca^{2+} K_d (µM)	Mg^{2+} K_d (mM)	Λ_{ex} and λ_{em} (nm)	Quantum Yield
BAPTA[132,135]	0.11	17	254, 363	0.027
Quin2[134]	0.060	0.000115	339, 492	---
Fura-2[133]	0.135	9.8	340/380, 512	0.49
Mag-fura-2[139]	53	1.5	340/380, 512	---
Fluo-4[142]	0.345	---	494, 516	0.14
Mag-fluo-4[142]	22	4.7	493, 516	---
Rhod-2[143]	1.0	---	553, 576	0.102

*K_d – dissociation constant; λ_{ex} – excitation wavelength; λ_{em} – emission wavelength; quantum yield – ratio of photons emitted to photons absorbed
*/ separates excitation wavelengths of ratio metric dyes
*Ca2+ and magnesium K_ds were determined at room temperature. Buffer conditions are found in the provided references for each dye.

1.7 The discovery of GFP and fluorescent proteins

The isolation of green fluorescent protein (GFP) from the *Aequorea victoria* jellyfish gave light to and revolutionized the field of cell imaging[144,145]. In 2008, Osamu Shimomura, Martin Chalfie, and Roger Tsien were awarded the Nobel Prize in chemistry for their work contributing to the discovery and development of GFP, which will be discussed in detail later in this section. While studying bioluminescence in jellyfish, Shimomura isolated and identified Aequorin and GFP as the light generating moieties in *Aequorea victoria* and the fluorescence resonance energy transfer (FRET) mechanism by which the two create bioluminescence[146]. Aequorin emits blue light when it binds four Ca^{2+} ions and its cofactor coelentrazine[147,148]. The emitted blue light serves as excitation light for GFP that emits the green light observed[146]. Shimomura showed GFP fluorescence came from its unique, integrated chromophore and not cofactors[149]. Douglas Prasher was the first to clone and sequence the GFP gene[150], but he was not included in the Nobel Prize. Chalfie was the first to express the cloned GFP DNA in *E. coli* and *C. elegans*, beginning its use as a marker for gene expression and pointing to its future use in various aspects of biological imaging[151]. The work of Roger Tsien made GFP a more effective tool for visualizing physiological elements and processes. Tsien determined the mechanism of fluorophore formation in GFP[152], and was able to solve the crystal structure of the S65T mutant, enhanced GFP (EGFP)[153]. The structure of wild type GFP was determined, prior to the structure of EGFP, by Yang and colleagues[154]. Tsien's mutagenesis work targeting the GFP chromophore and surrounding residues revealed key mutations that produced different emission wavelength variants of GFP capable of FRET[152,155]. By initiating the early research

elucidating the biochemistry[156] and chromophore[157] of the red tetrameric protein DsRed from *Discosoma sp.*, Tsien was able to produce a monomeric form of DsRed called mRFP1[158]. From mRFP1, Tsien produced mutants, called mFruits, with red-shifted emission wavelengths extending the color palette of available FPs[159,160]. The advancements made with *Aequorea victoria* GFP led researchers to identify GFP-like proteins in other sea animals, such as coral and crustaceans, which cover the visible spectrum. GFP variants and GFP-like proteins are continuously used not only as fluorescent tags, but as biological sensors of physiological elements and compounds such as Ca^{2+} which will be discussed in the next section[161].

GFP, located in Figure 1.7.1, is a single chain of 238 amino acids with a molecular mass of 27 KDa[150]. The tertiary fold of the protein is that of a beta barrel consisting of 11 beta strands where each contains 9-13 residues. Central to the protein fold is a greek key motif connecting the second half of the beta barrel (strands 7-11)[162]. The beta barrel is a virtually impeccable cylinder at 42 Å long with a 24 Å diameter. The top of the barrel is covered by three short alpha helices, with another at the bottom. GFP has two characteristic absorption peaks at 395 nm and 475 nm corresponding to the neutral and anionic forms of the chromophore. Inside the solvent-inaccessible beta barrel is a central alpha helix, primarily composed of hydrophobic residues[154,153]. Within the central helix is the chromophore formed by the autocatalytic cyclization of residues S65, Y66, and G67. Formation of the *p*-hydroxybenzylideneimidazolinone chromophore is as follows: 1). the protein folds into its tertiary structure; 2). the nucleophilic amide group of G67 attacks the carbonyl group of S65 forming the imidazolinone ring; 3). dehydration of the imidazolinone ring; 4). dehydrogenation of the α-β bond of Y66

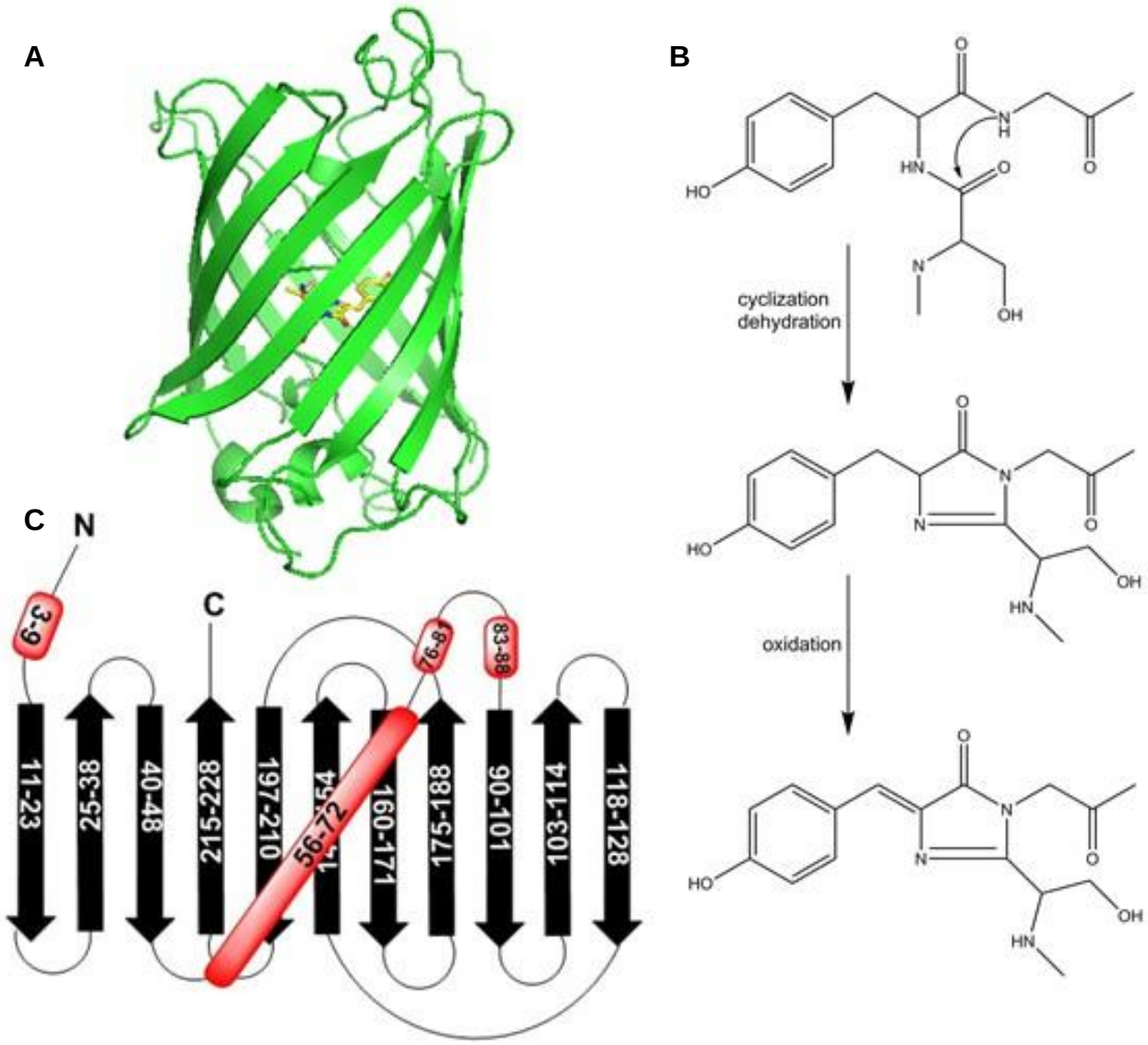

Figure 1.7.1 Structure and chromophore formation of GFP

A) Crystal structure of GFP containing the S65T mutation created in pymol (PDB: 1ema). The chromophore is in yellow. B) Reaction scheme for chromophore formation in GFP. After the protein folds into the β-barrel, the chromophore forms through an autocatalytic cyclization where the amide group of G67 attacks the carbonyl group of S65 forming the imidazolinone ring with the loss of water and a final dehydrogenation of the α-β bond of Y66 by molecular oxygen producing the conjugated chromophore. C) Representation of the overall fold of GFP. The numbers correspond to the residues found in each of the secondary structure elements. N and C mark the amino and carboxy terminals of the protein. Adapted from Ormo, et al., *Science*,1996 and Reid, et al., *Biochemistry*, 1997.

by molecular oxygen producing the final conjugated chromophore[162]. The oxidation step has a rate constant (k_{ox}) of 1.51 x $10^{-4}s^{-1}$ making it the rate limiting step for chromophore formation[163].

As stated previously, the 395 nm and 475 nm absorbance peaks correspond to the neutral and anionic ground states of the GFP chromophore that emit light at ~510 nm[164]. The absorbance spectrum of GFP depicting its dual excitation peaks is located in Figure 1.7.2A. The amplitude of the 395 nm absorbance peak is three times larger than that of the 475 nm peak making more of the neutral chromophore present in wild type GFP[162]. When the chromophore absorbs 395 nm light, the pK_a of the chromophore is reduced causing dissociation of the phenolic proton in a process termed excited state proton transfer (ESPT)[165] which is depicted in Figure 1.7.2B. In a 0.9 Å resolution structure of GFP, two proton wires, or extensive hydrogen bond networks, were revealed on either side of the chromophore. One is involved in chromophore formation and the other, called the active site wire, is responsible for shuttling the photodissociated proton during ESPT. The active site wire is formed by hydrogen bonds from many residues with key residues being N146, Y66, E222, S72, T203, H148, and E5[166].

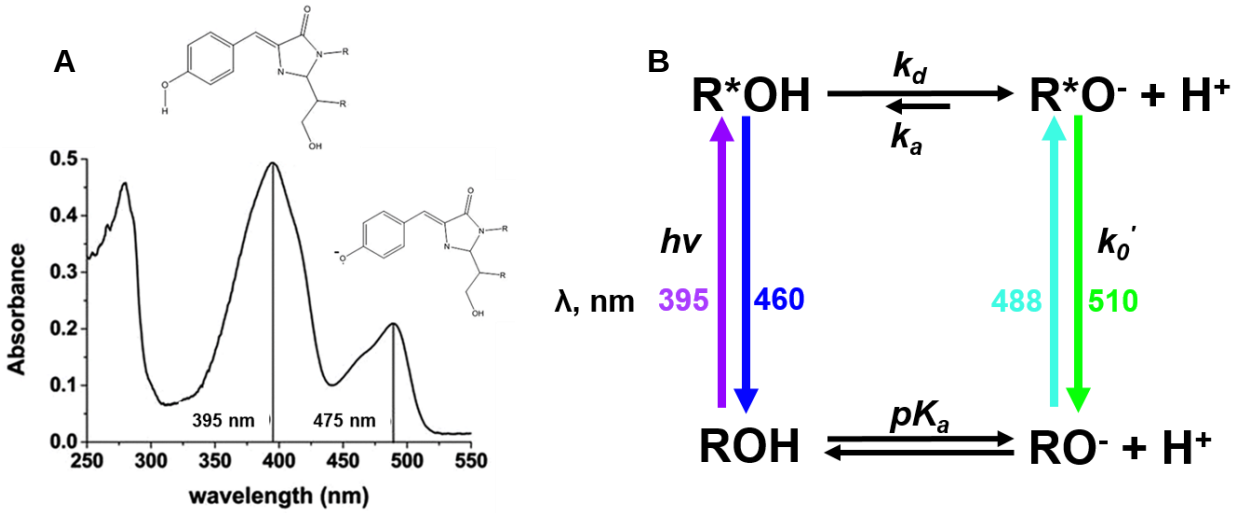

Figure 1.7.2 UV absorbance spectrum of GFP and scheme for ESPT

A) Absorbance spectrum of GFP reflecting the two ionization states of the chromophore. The neutral chromophore corresponds to the 395 nm peak and the anionic chromophore corresponds to the 475 nm peak. In EGFP, the S65T and F64L mutations make the anionic chromophore dominant with a large peak occurring at 488 nm in the absorbance spectrum. B) During ESPT, the hydroxyl group of the tyrosine residue in the chromophore will lose its proton after being excited with 395 nm light or return back to the ground state and emit light at 460 nm. If the proton dissociates, the anionic species will return to the ground state, emitting light at 510 nm. The anionic chromophore can be directly excited at 475 or 488 nm and will also fluoresce at 510 nm. The ionization state of the GFP chromophore is also heavily dependent on the pH of the solvent. Modified from Wineman-Fisher, et al., *Phys.Chem.Chem.Phys.,* 2014 and Zhuo, et al., *J. Phys. Chem. B*, 2015.

Mutational analysis of GFP has identified the amount of tolerable deletions the beta barrel can withstand before fluorescence is lost and mutations that improve the folding of the protein[162]. Residues 7-229 are required to maintain GFP fluorescence, which means only six residues from the N-terminal and nine residues from the C-terminal can be deleted without disrupting the folding of the protein[167]. Many mutations have been identified to help improve expression of GFP at 37˚C such as F99S, F64L, V163A, M153T, S175G, I167T, and S72A. However, implementing these mutations

have only improved the folding ability of the protein and not its overall brightness[162]. In superfolder GFP, the S30R Y39N mutations yielded a four-fold increase in the actual brightness at 37˚C compared to the commonly used cycle 3 GFP folding variant[168,169]. The F64L and S65T mutations were made to GFP to produce its brightest and most widely used mutant, EGFP[170]. EGFP only contains the anionic form of the chromophore with a single excitation peak at 488 nm and emission at 510 nm. The F64L mutation improves the folding efficiency of the protein at 37˚C by improving the packing of hydrophobic residues V29, L18, and F27 around the chromophore and reducing the solvent accessible area. The S65T mutation suppresses the neutral chromophore and promotes the formation of the anionic chromophore by disrupting the hydrogen bond between E222 and S65[170,171].

In the quest to improve the fluorescence and utility of expressed GFP, key mutations were found that shifted the emission spectrum and subsequent perceived color of the protein[162]. Substituting a Histidine residue for the Tyrosine in the chromophore at position 66 shifts the GFP emission from green to blue creating blue fluorescent protein (BFP). BFP has excitation and emission maxima at 383 nm and 445 nm. Although this new chromophore mutation produced a different color variant of GFP, it made the chromophore more flexible, which made it more prone to photobleaching, and reduced the quantum yield[165,172]. Substituting a Tryptophan at position 66 in the GFP chromophore shifts the emission from green to cyan producing cyan fluorescent protein (CFP) with excitation and emission wavelengths of 433 nm and 475 nm respectively. When the M153T, V163A, N146I, and N212K mutations were introduced to CFP, the quantum yield increased to 0.67 which is similar to wild-type

GFP[155]. Mutating serine to glycine at position 65 and the threonine at position 203 to tyrosine in GFP creates a π-π stacking interaction that stabilizes the dipole moment of the chromophore produced in the excited state, generating yellow fluorescent protein (YFP). YFP excites at ~514 nm and emits at ~527 nm. The new chromophore environment in YFP rearranges the internal hydrogen bond network and packing interactions within the β-barrel making the protein sensitive to photobleaching and chloride ions[165]. Citrine, an improved version of YFP consisting of the S65G/V68L/Q69M/S72A/T203Y mutations, has a more stable pK_a of 5.7, improved photostability, and reduced chloride sensitivity due to the Q69M mutation. The methionine side chain fills the once open halide binding cavity[173]. Additional mutations F46L/F64L/V163A/M153T/S175G were introduced into EYFP, S65G/S72A/T203Y, to produce Venus[174]. The F46L mutation increases the speed of chromophore maturation while the other mutations improve the folding of the protein, making the fluorescence more visible at 37°C expression in mammalian cell application[175,174]. Variants of BFP, CFP, and YFP are commonly used in the construction of forster resonance energy transfer (FRET) pair Ca^{2+} sensors. The emitted light from BFP or CFP (donor) is used to excite YFP (acceptor). CFP and YFP have been optimized for use in FRET pair Ca^{2+} sensor design[176]. Camelons, designed by Miyawaki and colleagues, are FRET pair Ca^{2+} sensors containing BFP or CFP at the N-terminal fused to CaM and the M13 binding peptide with a YFP variant at the C-terminal[177]. The various fluorescent protein-based Ca^{2+} probes with advantage of targeting to specific organelles will be discussed in the next section.

1.8 Genetically-encoded Ca^{2+} indicators

In the past 30 years, the Ca^{2+} imaging world has been revolutionized by the discovery and manipulation of fluorescent proteins[145]. Using site-directed mutagenesis, circular permutation, and fused FP constructs, a variety of Ca^{2+} probes have been created to monitor cytosolic and organellar Ca^{2+}[130]. GECIs fall into two major categories: single fluorophore and FRET pair. Single fluorophore sensors are non-ratiometric and experience a change in fluorescence intensity when Ca^{2+} binds. Most of the single fluorophore sensors are large chimeras of a FP connected to CaM and M13, the CaM binding peptide. Chelation of Ca^{2+} by CaM induces a conformational change that rearranges the chromophore environment, inducing fluorescence change[178,179]. Our Ca^{2+} sensor CatchER, and its variants, do not use CaM as the chelator. A Ca^{2+} binding site, consisting of five negatively charged residues, was mutated on the surface of the cycle 3 variant of GFP in a chromophore sensitive location that altered the protonation of the chromophore[180]. The addition of Ca^{2+} stabilizes the charge on the chromophore, increasing the fluorescence intensity[181]. For single fluorophore sensors, Ca^{2+} binding produces changes either in absorbance or the quantum yield that lead to the change in fluorescence intensity. Single fluorophore sensors are commonly referred to as intensiometric because the fluorescence intensity change at only one wavelength is measured[130]. FRET pair, or ratiometric, sensors involve the fusion of two FPs with CaM and M13 in the center of the construct. In these indicators, the emission energy of one FP (donor) is used as the excitation energy for the other FP (acceptor). The fluorescence change is measured by exciting the donor FP and measuring the emission of the donor and acceptor to calculate the ratio[182]. The efficacy of energy transfer is

dependent on the distance between the two FPs and the extent of overlap between the emission and excitation of the donor and acceptor, respectively[130]. The conformational change that occurs between CaM and M13 when Ca^{2+} binds brings the FPs closer together for FRET to occur[130,183]. The two previously mentioned categories can be divided further into four subcategories: bioluminescent indicators, single fluorophore indicators utilizing a CaBP in the construct, grafted single fluorophore indicators, and FRET pair indicators[179]. Figure 1.8.1 shows examples of the Ca^{2+} sensors from each of the subcategories. Examples of each sensor type and their targeting ability for measuring Ca^{2+} transients in subcellular environments such as the ER/SR will be discussed in this section.

The first GECI used was the bioluminescent protein aequorin isolated from *Aequorea victoria* where it acted as the FRET pair donor to GFP[147]. Aequorin is a 21 kDa globular protein containing four E-F hand motifs where only three actively bind Ca^{2+} with a K_d of 1 µM. At the center of the protein exists a hydrophobic pocket where its cofactor coelenterazine binds, acting as the chromophore[148]. Aequorin is excited at 403 nm and emits light at 470 nm. The chelation of Ca^{2+} ions by the three binding sites induces a conformational change converting coelenterazine to coelenteramide and CO_2 with light emission[184]. Recombinant aequorin has been used to monitor changes in cytosolic Ca^{2+} in mammalian cell lines such as HeLa, ins-1, and L929 and cultured myocytes and neurons[185]. It has also been targeted to the mitochondria of CHO.T cells to monitor Ca^{2+} concentration[186]. Aequorin has also been used as a chimera fused to GFP to sense cytosolic Ca^{2+} in mouse neuroblastoma cells[187]. Longer emission

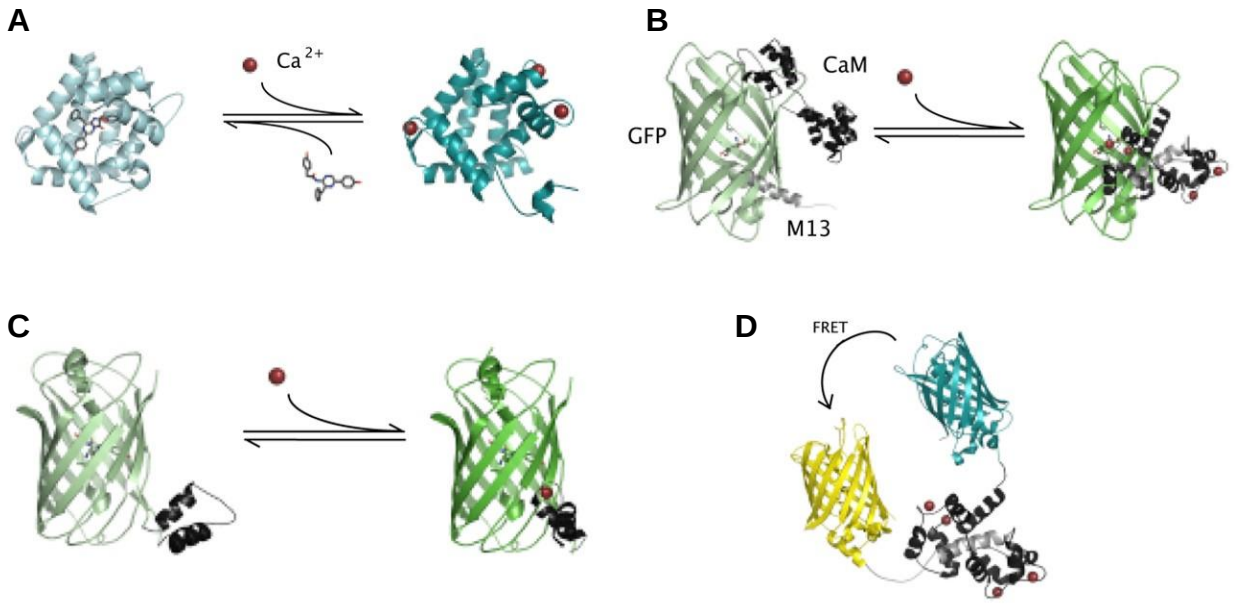

Figure 1.8.1 Four categories of genetically-encoded Ca^{2+} indicators

A) Aequorin is a type of single fluorophore Ca^{2+} sensor and is also a bioluminescent indicator. Aequorin binds three Ca^{2+} ions and the cofactor coelenterazine to produce emission at 470 nm. B) GCaMP is considered a single fluorophore sensor since only one FP is used in the construct, but GCaMP and GCaMP like sensors use a native CaBP, like CaM or TnC, as the Ca^{2+} binding moiety. GCaMP utilizes cpGFP, CaM, and the M13 binding peptide. When CaM binds Ca^{2+} and M13, the conformational change triggers closing of the cavity created in cpGFP and fluorescence increases. C) Grafted, single fluorophore sensors, such as Ca-G1, fuse an EF-hand from a CaBP to a chromophore sensitive area in a FP. D) FRET pair, or ratiometric, sensors involve the fusion of two FPs with CaM and M13 in the center of the construct. Cameleons, a type of FRET sensor, use CYP as the donor and YFP as the acceptor. The Ca^{2+} induced conformational change in CaM brings the two FPs closer together for FRET to occur. Modified from McCombs, et al., *Methods*, 2008.

constructs of aequorin have been produced using Venus and mRFP1, making Ca^{2+} imaging in deep tissues with aequorin possible[188]. Because aequorin-based Ca^{2+} probes use the luminescent cofactor coelenterazine to produce fluorescence, intensity measurements can vacillate with cofactor depletion[130]. Recently, a new aequorin-GFP fusion probe called GAP was created that does not require recombination with coelenterazine[189]. GAP is a ratiometric Ca^{2+} sensor with excitation maxima at 403 nm

and 470 nm and emission at 510 nm. GAP has a Ca^{2+} K_d of 200 nM, which is suitable for measuring cytosolic Ca^{2+}, with a Hill coefficient of 1. It has good selectivity for Ca^{2+} over magnesium and a large dynamic range. The ER-targeted low affinity version of GAP, erGAP1, has a K_d of 12 µM with a Hill coefficient of 1. In HeLa cells, erGAP1 detected ATP+carbachol stimulated Ca^{2+} release from the ER which yielded a 20% decrease in the intensity ratio and a 58.8 ± 7.5% intensity decrease with ATP+histamine stimulation. erGAP1 had a two to threefold reduction in the intensity ratio with caffeine stimulated ER Ca^{2+} release in dorsal root ganglia neurons. No data was provided for Ca^{2+} binding and release kinetics. Constructs were also created to target the nucleus, Golgi, and the mitochondria[189].

The creation of Camgaroo and Pericam Ca^{2+} sensors were the first attempts in the GECI field to use native CaBPs in the construct either by grafting or fusion[178]. Xenopus CaM, without the M13 binding peptide, was inserted between residues 144 and 146 of EYFP, ECFP, and EGFP to produce these new Ca^{2+} sensors. The EYFP grafted Camgaroo, termed Camgaroo-1, had the largest Ca^{2+} response and a Ca^{2+} K_d of 7 µM. Camgaroo-1, however did not fold properly at 37°C, was pH sensitive, and could not be targeted to organelles[190]. Exposing Camgaroo-1 to error-prone PCR resulted in Camgaroo-2 with similar Ca^{2+} affinity and fluorescence change to its predecessor. Camgaroo-2 folded well in HeLa cells and was easily targeted to the mitochondria[173]. Using a similar grafting strategy, our lab created the Ca-G series of GECIs with the insertion of an EF-hand or Ca^{2+} binding loop between residues 144-145, 157-158, and 172-173 of EGFP[191]. Ca-G1, the most promising variant, has EF-hand III of CaM inserted into EGFP between residues 172 and 173. Ca-G1 is ratiometric with excitation

peaks at 398 nm and 490 nm and single wavelength emission at 510 nm. With its single EF-hand, Ca-G1 has a weak Ca^{2+} affinity of ~0.4 mM. Its weak affinity made it suitable to measure ER Ca^{2+} changes in HeLa and BHK cells with the addition of the ER retention sequence and tag. Although its affinity makes it suitable for measuring ER/SR Ca^{2+}, Ca-G1 is pH sensitive with a pK_a of 7.5[191].

Cameleons are genetically encoded FRET pair sensors consisting of two fluorescent proteins, normally cyan and yellow FPs, with calmodulin and M13, from myosin light chain kinase, in the center of the construct. These sensors have been applied in different cell lines to monitor Ca^{2+} dynamics from the ER/SR and cytosol[177] but primary application is cytosolic due to their strong affinity for Ca^{2+}. Recently, ER-targeted cameleons with a red hue were developed based off of the optimal cameleon D1ER. The new red shifted cameleon called D1ERCmR2 has the fluorescent proteins Clover positioned at the N-terminal acting as the FRET pair donor and mRuby2 at the C-terminal acting as the FRET pair acceptor. D1ERCmR2 has two *in vitro* K_ds of 0.8 µM and 60 µM with an *in situ* K_d of 220 µM determined in HeLa cells. D1ERCmR2 can be used in tandem with fura-2 to measure ER and cytosolic Ca^{2+} concentrations[192]. As for the kinetics of cameleon sensors, not much data has been reported. Cameleons YC2.0, one of the first yellow cameleons, has a dissociation time constant (T_{rt}) of 83 ms. YC-Nano140 has a T_{rt} of 303 ms[130].

Because of the large size of FRET pairs and limited signal intensity, new probes, called GCaMP, were developed using a single circularly permuted EGFP (cpEGFP) fused to calmodulin and M13. The use of cpEGFP increased the signal intensity of the probes for use in cells but their affinities for Ca^{2+} are high with K_d values in the

nanomolar range[193,194]. The original GCaMP indicator, published in 2001, has a Ca^{2+} K_d of 235 nM with a dissociation time constant of ~200 ms[193]. The Ca^{2+} induced fluorescence change mechanism was discovered from crystal structure analysis of GCaMP2. The Ca^{2+} induced conformational change in CaM creates new contacts between CaM and cpGFP. CaM residues change the chromophore environment of cpGFP, preventing solvent access to the chromophore aiding fluorescence increase[194]. Since its unveiling, several variants of GCaMP have been created and used to monitor Ca^{2+} transients in different environments such as mouse cardiac cells *in vivo* (GCaMP2)[195], chemosensory neurons of *C. elegans* and *D. melanogaster* (GCaMP3)[196], and in the brain cells of mice, *Caenorhabditis*, *Drosophila*, and zebra fish (GCaMP5s)[197]. GCaMP6f is a newer construct in the GCaMP family with the ability to sense Ca^{2+} nanosparks that initiate EC coupling in the junctional zone dyad space in rat cardiomyocytes. By targeting the sensor to the junctional zone using resident proteins junctin and triadin, Ca^{2+} nanosparks that are 50 times smaller than standard sparks were seen[198]. All of the initial GCaMP variants mentioned have strong affinities for Ca^{2+} that limit their use to cellular environments with minimal Ca^{2+} concentrations like the cytosol, and only use cpGFP. None of the initial GCaMPs have Ca^{2+} affinities low enough to target to organelles like the ER/SR[193,195,197]. A new subfamily of GCaMPs was created, from random mutations to GCaMP3, termed genetically encoded Ca^{2+} indicators for optical imaging (GECOs). Green (G-GECO), red (R-GECO), and ratiometric blue-green (GEM-GECO) variants were created. Although the color palette was expanded, the new GECO variants still have high Ca^{2+} sensitivity[199]. Robert Campbell and colleagues created low affinity red GECOs, LAR-GECO1 and LAR-

GECO1.2, with Ca^{2+} K_ds of 24 µM and 12 µM, respectively. LAR-GECO1 was used to monitor thapsigargin inhibition of ER refilling in HeLa, HEK293, and U2-OS cells co-transfected with CatchER. LAR-GECO had larger decreases in intensity over all three cell lines[200]. In 2014, new low affinity, GECO-type indicators were created based on cfGCaMP2. The lead variant, from a library of 58 mutants, had a Ca^{2+} K_d of 368 µM and a large dynamic range. This new variant termed Ca^{2+}-measuring organelle-Entrapped Protein IndicAtor 1 in the ER (CEPIA1*er*) was able to monitor ER Ca^{2+} dynamics in HeLa cells with thapsigargin and histamine treatment[201]. Variants of CEPIA were also created with different emission wavelengths such as red (R-CEPIA*er*), green (G-CEPIA*er*), and ratiometric blue-green (GEM-CEPIA*er*) with Ca^{2+} affinities of 565 µM, 672 µM, and 558 µM, respectively[201]. Table 1.8.1 lists some of the current indicators, their affinities, the organelle they are suited for, and the area of the color palette they fill.

Although the CaM-based biosensors are the most widely used, earlier versions had some drawbacks such as the lack of Ca^{2+} response when targeted to particular regions of the cell and reduced dynamic range when expressed *in vivo*[178]. To combat the interference of CaM-based biosensors with regulatory processes in the cell, Heim and Griesbeck began designing ratiometric GECIs based on the skeletal muscle and cardiac variants of troponin C (TnC) with part of their binding peptide, troponin I, used as the linker[202]. The best variant, TN-L15, utilized TnC from chicken skeletal muscle with 14 amino acids deleted from the N-terminal. TN-L15 has CFP as the donor FP at

Table 1.8.1 Ca^{2+} K_ds and subcellular targets of current GECIs

Subcellular compartment	CYAN/Yellow	GREEN	Yellow	RED
Intracellular (0.1-1 μM Ca^{2+})	**GEM-GECO**[199] (K_d = 0.3 μM) [a]**YC3.6**[204] (K_d = 0.3 μM) [a]**TN-XL**[205] (K_d = 2.5 μM)	**GCaMP**[193] (K_d = 0.5 μM) **G-GECO**[199] (K_d = 0.6-1.2 μM)	**Flash pericam**[203] (K_d = 0.7 μM)	**R-GECO**[199] (K_d = 0.5 μM)
Mitochondria/ Nuclear envelope (1-10 μM Ca^{2+})	[a]**Cameleon-2**[206] (K_d = 0.07; 11 μM) [a]**YC4.6**[204] (K_d = 0.06, 14.4 μM)		**Ratiometric pericam**[203] (K_d = 1.7 μM) **Camgaroo-2**[173] (K_d = 5.3 μM)	
ER/SR (0.2-1 mM Ca^{2+})	[a]**D1ER**[207] (K_d = 0.8, 60 μM) [a]**Cameleon-4**[206] (K_d = 0.08, 700 μM) [a]**GEM-CEPIA1*er***[201] (K_d = 558 μM)	**CatchER**[180] (K_d = 190 μM) **G-CEPIA1*er***[201] (K_d = 672 μM)		**R-CEPIA1*er***[201] (K_d = 565 μM)

*K_d – dissociation constant.
*Colors correspond to characteristic emission wavelength of each indicator.
*All K_ds were obtained at room temperature. Additional conditions can be found in the provided references. [a]Ratiometric containing Cyan and Yellow FPs.

the N-terminal and Citrine as the acceptor FP at the C-terminal with the truncated TnC in between. TN-L15 exhibited a 140% increase in ratio change *in vitro* with a K_d of 1.2 μM for Ca^{2+} and a K_d of 2.2 mM for magnesium. Because of its high affinity for Ca^{2+}, TN-L15 was targeted to the cytosolic side of the plasma membrane in primary hippocampal neurons and HEK293 cells to monitor Ca^{2+} flux from the membrane to the cytosol[202]. By replacing Citrine in TN-L15 with the circularly permutated variant Citrine cp174 and mutating residues in EF-hand III and IV of TnC, the improved variant TN-XL

was produced. TN-XL has a 400% change in its fluorescence ratio when Ca^{2+} saturation is reached *in vitro* with a Ca^{2+} K_d of 2.5 µM and a Hill coefficient of 1.7. Off rate kinetics from stopped-flow experiments showed TN-XL had time constants of 142 ms and 867 ms[205].

Thus far, current genetically encoded Ca^{2+} probes have a significant disadvantage in their use of native CaBPs or other functional domains that bind Ca^{2+}. In this case, the reporter construct can potentially interfere with cellular processes that involve the native protein since high expression levels of the indicator are needed for Ca^{2+} imaging[144,179].

1.9 Previous work leading to CatchER and questions to be addressed

In the past, our lab has demonstrated our knowledge and skill for designing novel CaBPs using non-native CaBPs as the scaffold[208,209], and manipulating the binding affinity of these designed CaBPs by altering the number of charged residues in the metal binding site[210,211]. Using our previously published results and subsequent statistical analysis of coordination chemistry in native CaBPs[212,213], we designed two novel EGFP-based sensors Ca-G1 and CatchER (Ca^{2+} sensor for detecting high concentration in the ER)[191,180]. Ca-G1 was created using the grafting approach to incorporate EF-hand III of CaM into EGFP at residue 172. Ca-G1 has two excitation peaks at 398 nm and 490 nm with single wavelength emission at 510 nm. Ca-G1 is advantageous as a ratiometric sensor, with a Ca^{2+} K_d ranging from 0.4-0.8 mM, but has a small dynamic range and slow kinetics[191]. CatchER has a similar absorption profile as Ca-G1 with 395 nm and 488 nm excitation peaks and single wavelength emission at 510 nm, but it is not ratiometric. CatchER has a large fluorescence intensity change induced by Ca^{2+} binding and a K_d between 120-180 µM with a Ca^{2+} off rate of 700 s^{-1}

which makes it capable of measuring Ca^{2+} release from the ER/SR in various cell types[180]. CatchER also has a 44% in fluorescence lifetime with Ca^{2+} bound[214]. We have also applied this strategy to mCherry with our red sensor MCD1 having faster release kinetics than CatchER but a smaller fluorescent dynamic range upon Ca^{2+} binding (unpublished results). All of our designed sensors have the advantage of being easily targeted to cellular compartments containing high concentrations of Ca^{2+} like the ER/SR, fast kinetics and affinities to cover the wide range of $[Ca^{2+}]$ in different organelles, and a Ca^{2+} response that is not transduced by a native CaBP.

Although CatchER has been highly requested and used by various labs, a common issue is its unsatisfactory fluorescence at 37°C in mammalian cells which is the temperature mammalian cells grow efficiently. The absorbance spectrum of CatchER also resembles that of wtGFP with two excitation peaks even though EGFP, having a single excitation peak, is the scaffold for CatchER. Through this research, there were several questions we wanted to address: 1) What structural elements cause the optical property changes seen in CatchER? 2) Can we make mutations to the sensor to broaden the K_d range and improve the fluorescence intensity at 37°C for mammalian cell studies? 3) Can we use the sensor to quantify drug-induced Ca^{2+} release and kinetics in different receptor mediated signaling pathways? and 4) Can we target the sensor to measure local Ca^{2+} changes near channels to further compare the local and global changes that occur during signaling events?

1.10 Overview of this dissertation

To determine the structural basis for the fluorescence enhancement of CatchER upon Ca^{2+} binding and other key residues that can improve the optical properties and

binding affinity, crystals of CatchER were grown and the structure was determined and analyzed. Various mutations were made to CatchER to generate different variants with different K_ds and fluorescence enhancement. Some of the variants have been used *in situ* in different cell types to monitor Ca^{2+} release in the presence and absence of receptor agonists and blockers. The majority of the Ca^{2+} imaging work done was carried out with an improved variant, CatchER-T'. CatchER variants were also used to monitor magnesium transients in T lymphocytes.

Chapter two will discuss the materials and methods used to carry out the research for this dissertation. Chapter three will go over the crystallization and structure determination of CatchER. Chapter four will discuss the effects of adding an additional negatively charged residue to the binding site of CatchER and monitoring the drug effects in situ using variants containing the S30R and/or Y39N mutations. Chapter five will discuss the optimization of CatchER to CatchER-T' using the S30R Y39N mutations from superfolder GFP that were shown to improve the folding and subsequent brightness of the protein at 37˚C. Chapter six will discuss the use of CatchER variants for the *in situ* monitoring of Mg^{2+} in T cells. Chapter seven will go over the major conclusions and significance of the research put forth in this dissertation.

2 MATERIALS AND METHODS

2.1 Primer design and PCR

Primers were designed based on the segment of DNA containing the residue to be mutated. Primers were between 18-34 base pairs in length. Mutations, deletions, or insertions were placed within or near the complimentary portion of the primer pair. Non-overlapping segments of each primer complimented the template DNA to insure hybridization with the template and mutation success. Tm values of the non-overlapping segments for each primer pair were made to match one another[215]. The PCR reaction was set up using pfu DNA polymerase (GBioscience). To the PCR tube, 2 µL of dNTPs, 1 µL of template DNA (20-50 ng), 5 µL of 10X pfu buffer, 1 µL of pfu DNA polymerase, and 2 µL each of the forward and reverse primer was added and brought to a final volume of 50 µL. The contents of the tube were mixed by pipetting. The tube(s) was then placed in the thermocycler, and the following program was run: step 1: 95˚C for 1 min., step 2: 95˚C for 1 min., step 3: -5˚C the T_m of the non-overlapping region for 1 min, step 4: 72˚C for 13 min., repeat steps 2-4 for 12 cycles, step 5: -5˚C the Tm of the complimentary region for 1 min, step 6: 72˚C for 30 min, repeat steps 5 and 6 for one cycle, and step 7: hold at 4˚C. After completion, 1 µL of Dpn1 enzyme and 5 µL of 10X CutSmart buffer were added to the PCR product and incubated for 1-2 h at 37˚C. After incubation, 2-8 µL of the PCR product was transformed into DH5α cells, grown in 10 mL of LB, and extracted using the Qiagen Mini Prep Kit. The concentration of the purified DNA was determined using the absorbance peak at 260 nm and calculated using a web-based DNA concentration calculator. Samples were then sent to GENEWIZ for sequencing.

2.2 Transformation

For this procedure, 50 µl of BL21 DE3 cells and 0.5 µl of the protein DNA was mixed in an eppendorf tube and allowed to sit on ice for exactly 30 minutes. The DNA/bacteria mixture was then placed in a 42°C water bath for exactly 90 seconds and then placed back on ice for 2 minutes. Fifty micro-liters of Lurea Bertani (LB) media was added and mixed into the DNA/bacteria mixture and allowed to incubate at 37°C for 30 minutes. After incubation, 50 µl of the solution was streaked onto an agar plate containing the antibiotic kanamycin near a lighted Bunsen burner. A control plate was made with only the BL21 DE3 cells. The plates were then placed upside down in the 37°C incubator overnight.

2.3 Inoculation

The next day, one colony of bacteria was chosen for expression. Operating next to a lighted Bunsen burner, one healthy colony of bacteria from the transformation plate was retrieved using an inoculating loop. The colony was then added to 10 mL of autoclaved LB media and 6 µl of kanamycin in a 50 mL falcon tube. In the case of mCherry and its variants, 1 µL of ampicillin is used for every 1 mL of LB in inoculation and expression. The bacteria mixture was allowed to grow in the shaker at 37°C overnight at 200-230 rpm.

2.4 Expression

A full diagram of the expression procedure can be found in Figure 2.4.1. To 1 L of autoclaved LB media in a 2.8 L flask, 600 µl of 50 mg/ml kanamycin was added for a final concentration of 0.03 mg/ml for kanamycin. One milliliter of this solution was placed into two disposable cuvettes to be used as optical density (OD) references in the

UV-VIS spectrophotometer. Fifty milliliters of the 250 mL inoculate was added to each flask containing 1 L of LB+kanamycin or LB+ampicillin. The flask was then placed in the shaker and allowed to shake at 37°C at 200-230 rpm. In a labeled disposable UV cuvette, 1 ml aliquots of the bacteria mixture were taken at 1hr intervals for OD determination at 600 nm. Once the UV absorbance of the mixture reached 0.6, the bacteria were induced with 200 µl of 1 M IPTG with a final concentration of 0.2 mM once added to the mixture. As the absorbance approached 0.6, 1 ml aliquots were taken at decreased time intervals. After the addition of IPTG, the flask(s) were then allowed to shake at 25°C overnight, taking 1 ml samples of the mixture for OD analysis at 1-2 hr intervals and a final sample from overnight. One sample before induction (BI), and after induction overnight (AI/ON) were taken and centrifuged for 1 min at 6,000 rpm to collect the cell pellets for sodium dodecyl sulfate polyacrylamide gel electrophoresis (SDS-PAGE) analysis.

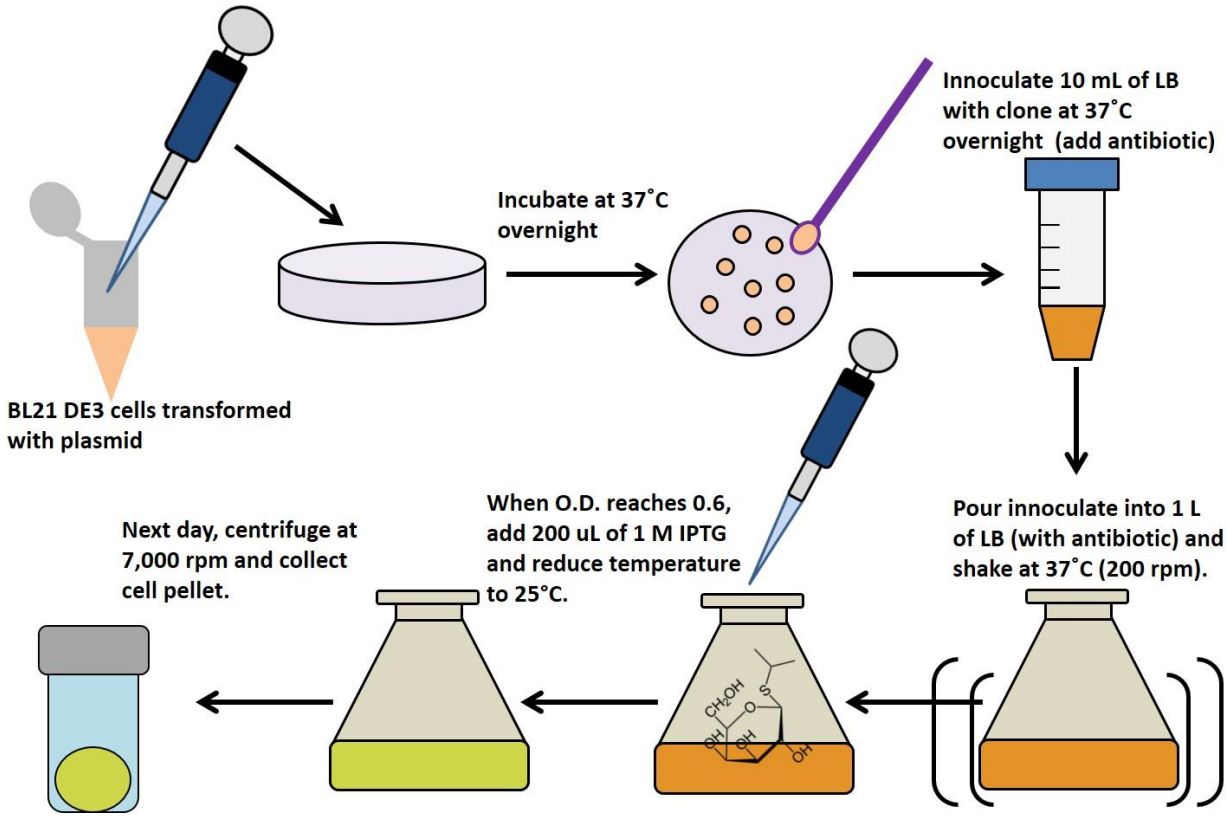

Figure 2.4.1 Expression procedure for Ca^{2+} sensors

To overexpress our Ca^{2+} sensors, the plasmid DNA for the selected sensor is transformed into BL21 (DE3) cells or a different bacteria cell strain. The transformed cells are plated onto LB agar and allowed to grow overnight at 37°C. The next afternoon, a colony from the dish is selected and inoculated into 10 mL of LB, with the appropriate amount and type of antibiotic, and allowed to shake overnight at 37°C. The next day, the inoculate is poured into 1 L of LB with the antibiotic and allowed to shake at 200 rpm at 37°C while monitoring the O.D. every hour or every two hours. Once the O.D. reaches 0.6, 200 µL of 1 M IPTG is added to the flask to induce overexpression of the desired protein and the temperature is reduced to 25°C to ensure correct folding of the sensor and chromophore formation. The next day, the content of the flask is centrifuged at 7,000 rpm to collect the cell pellet for purification.

For fluorescence analysis before and after expression, the same samples were used before gel electrophoresis with three additional samples taken after induction.

For the SDS gel samples, 200 µl of the SDS gel sample buffer was added to each cell pellet in an eppendorf tube and vortexed until mixed. The samples were then

boiled for 10 min at 95°C to 100°C. Around 6-10 µl of each sample was loaded onto a 15% SDS gel and allowed to run at 118 volts for 1 hr 20 min or until the samples neared the bottom of the gel. The gel was then stained with the coomassie blue staining buffer and microwaved for 45 sec. The gel was then placed into destaining buffer overnight to allow the protein bands to develop.

For fluorescence analysis, the cell pellets from each sample were re-dissolved in 200 µl of 10 mM Tris pH 7.4. The samples were then placed on a 96 well plate and were analyzed.

2.5 Collecting the cell pellet

Once the absorbance reached 1.2-1.5, the flasks were removed from the shaker. The content of the flasks were poured into the large centrifuge containers. For 1 L of LB/bacteria, three centrifuge containers were used. The bottles were then balanced in pairs: the two centrifuge bottles containing the bacteria mixture and the final container containing the bacteria was balanced against water. The balanced pairs were placed across from each other in the large centrifuge and allowed to run at 7,000 rpm for 35 min. The cell pellet was then collected and placed in the -20°C freezer.

2.6 Cell lysis

Sonication is a technique used to lyse cells using sound waves. Inside a falcon tube the cell pellet from expression was re-dissolved in 10ml of extraction buffer with a pH of 8 and vortexed. The tube was then kept on ice for sonication. Before placing the sonication rod inside the falcon tube, it was cleaned with ethanol and water. The cells were sonicated with 30 pulses for a total of six times with 2 to 5 min cooling breaks in

between. After sonication, the solution of lysed cells and protein was placed into a small centrifuge tube and balanced with water. The tubes were placed across from each other in the small centrifuge and were allowed to run for 40 min on 17,000 rpm. After centrifugation, the supernatant was poured into a beaker and syringe filtered for a total of 3 times into a clean falcon tube using a 0.45 µm filter. The filtrate was then stored in the 4°C refrigerator if it was not being purified the same day. A sample of the cell pellet after sonication was taken for SDS gel analysis along with 20 µl of the filtered supernatant.

The sonication technique is primarily employed when large amounts of protein are not required. However, for crystallization purposes, the French press was used to lyse the bacterial cells. The French press instrument uses large amounts of pressure to burst bacterial cells, releasing all the contents inside[216]. The shear force exerted upon the cells when the pressure is released causes the cells to burst. Another advantage to this technique is that less heat is produced. The French press cell is kept cold to minimize temperature increases that could damage the protein of interest.

2.7 Purification using Immobilized Metal Ion Affinity Chromatography (IMAC) and gel filtration chromatography

In order to get pure samples of the EGFP-based Ca^{2+} sensors, a form of IMAC called HisTag purification, outlined in Figure 2.7.1, was utilized using a 5 mL HiTrap chelating column on a Fast Protein Liquid Chromatography system (FPLC). Gel filtration chromatography was also implemented, using a 100 mL Hi Load Superdex 75 16/60 column as an extra purification step. The Ca^{2+} probes contain a 6X Histidine sequence that will interact with 0.1 M $NiSO_4$ when loaded onto a 5 mL HiTrap chelating

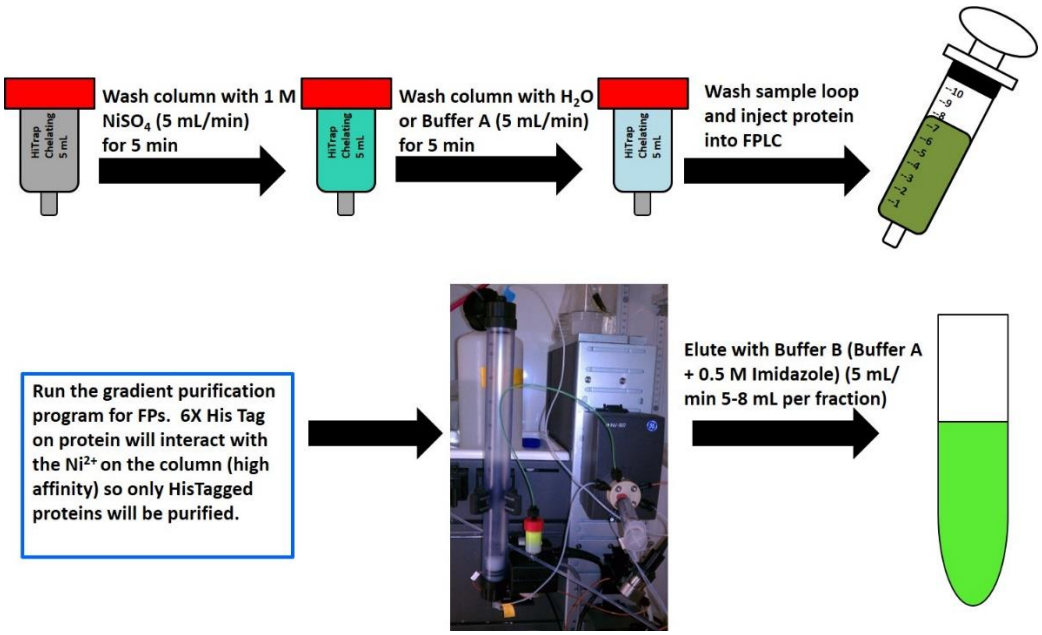

Figure 2.7.1 HisTag purification procedure for Ca^{2+} sensors

A form of IMAC called HisTag purification is implemented to purify the Ca^{2+} probes containing a 6X histidine tag at the N-terminal of the protein. A 5 mL HiTrap NTA chelating column is washed with 1 M nickel sulfate that interacts with the NTA molecules in the column, turning the column a blue-green color. Following column charging with nickel sulfate, the excess is washed away with Buffer A, leaving the column a light blue color. After column washing, the sample loop is washed manually, and the protein is loaded into the sample loop. Using the designated gradient purification program, the sample is injected and bound onto the column through the nickel-HisTag interaction and eluted using an imidazole gradient where the protein of interest elutes out at 37% Buffer B.

column. Once the $NiSO_4$ solution was loaded onto the column (blue color), the protein sample was then injected into the FPLC and loaded onto the column (green color) using 50 mM phosphate and 250 mM sodium chloride at pH 7.4 (Buffer A). After the protein was loaded onto the column, the sample was eluted using a gradient of Buffer B containing Buffer A and 0.5 M imidazole. After the protein was eluted, the fractions containing the protein (green color) were collected. Twenty micro-liters of each protein containing fraction were placed into eppendorf tubes for SDS gel analysis to determine

the fractions with the highest concentration of protein and purity. The chelating column was then washed with a solution of 100 mM EDTA and 1 M NaCl at pH 8, to remove the nickel sulfate, until the column was free of blue color. For gel filtration, two column volumes of 10 mM Tris pH 7.4 were washed through the column at 1 mL/min. The gel filtration program was run, after 2 mL sample injection, using 10 mM Tris pH 7.4 at 0.5 mL/min, to minimize the pressure in the column, to elute the pure protein in 2 mL fractions. The protein was collected and 10 uL samples of each fraction were taken for SDS-PAGE analysis. The protein was re-concentrated if it was for protein crystallization.

2.8 Dialysis

After HisTag purification, the fractions containing the most protein were combined and placed into dialysis bags and placed into 2 L of 10 mM Tris at pH 7.4. This technique helps to remove the imidazole salt from the protein and change the protein buffer from Buffer B to 10 mM Tris pH 7.4. The protein was allowed to dialyse 5 times changing the buffer every 2-3 h monitoring the absorbance at 280 nm for complete removal of imidazole. After dialysis, protein samples were concentrated to 1-5 mL using the Amicon concentrator with N_2 gas and a 10 kDa membrane. Protein samples were then stored with/without the addition of 20-25% glycerol in -20˚C for later use.

2.9 Crystallization using the hanging drop vapor diffusion method

Using the hanging drop method of vapor diffusion, screening of crystal growth conditions for the free and Ca^{2+} loaded form of sensor variants was carried out. Five micro-molar EGTA was added to the protein samples for apo form crystallization. A 24

well crystallization plate was used. Around the top of each well, vacuum seal grease was added to prevent air from entering inside the well and to promote vapor diffusion. To each well, the calculated amount of each mother liquor component was added to make up 1 mL in each well. The pH value of the mother liquor changed for each horizontal row. Different amounts of PEG were added to each vertical row of the 24 well plate using the stock solutions of PEG. In a 2:2 ratio, 2 µl of protein was placed on a round siliconized glass cover slip (Hampton Research, Laguna Niguel, CA) and 2 µl of the well solution was added to the drop. This process was repeated for each well. The cover slips were then carefully inverted and placed on top of each well with applied pressure to ensure the wells were sealed. Observations were recorded immediately after and then every few days following crystallization.

Crystals of Ca^{2+} free and Ca^{2+} loaded CatchER were obtained via the hanging drop method of vapor diffusion using 2 µL protein: 2 µL reservoir solutions at room temperature in 24-well VDX plates (Hampton Research, Aliso Viejo, CA). Ca^{2+} free CatchER crystals (0.9 mM protein, 5 µM EGTA) grew in solutions containing 53 mM HEPES pH 7.0, 1 mM β-mercaptoethanol, 50 mM $(NH_4)_2SO_4$, and 16% PEG 4000 or 51 mM HEPES pH 7.0, 1 mM β-mercaptoethanol, 50 mM NaOAc, and 17% PEG 4000. The Ca^{2+} loaded CatchER complex was created by adding 50 mM $CaCl_2$ to a 0.9 mM protein solution (final concentration of 0.45 mM). Crystals grew in mother liquors containing 51-53 mM HEPES

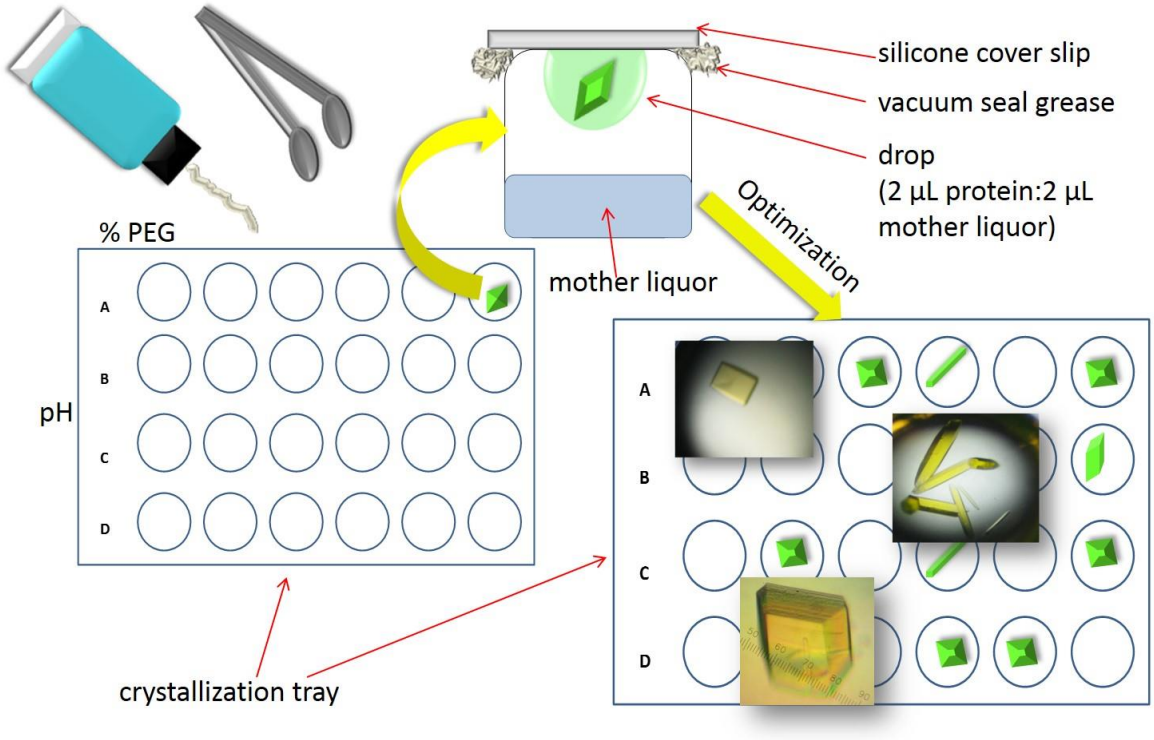

Figure 2.9.1 Crystallization via hanging drop vapor diffusion

A literature review of crystal conditions for FPs was done prior to setting up a crystal screening tray to narrow down the screening conditions. Utilizing a 24 well crystallization plate, prescreening of crystal conditions was done by varying the %PEG used by column and the pH by row at room temperature. The concentration of salt and other additives was held constant. Concentrations of salt, PEG, buffer, and other additives were calculated for 1 mL, filtered, and added to each well using filtered ddH_2O to make the final volume 1 mL. Two microliters of the protein sample was placed onto round glass coverslips and mixed with 2 µL of well solution taken from the corresponding well. The slides were placed over the well, encircled with vacuum seal grease, using some pressure to ensure a good seal. A mother liquor was created from the conditions that produced well formed crystals and was used to setup a whole tray of the optimized conditions to grow as many crystals for X-Ray crystallography. This procedure was followed to obtain the Ca^{2+} free and Ca^{2+} loaded crystals of CatchER. Ca^{2+} free CatchER crystals were soaked in mother liquor containing gadolinium to get gadolinium loaded CatchER crystals.

pH 6.9-7.4, 1 mM β-mercaptoethanol, 50 mM NaOAc, and 16-17% PEG 3350. Crystals of CatchER-Gd^{3+} were obtained via the soaking technique. Crystals of apo CatchER were

soaked for 1 to 2 days in a solution of mother liquor with the final concentration of $GdCl_3$ ranging from 1 mM to 4.5 mM. The crystals were mounted in liquid nitrogen with 20-30% (v/v) glycerol as cryoprotectant. X-ray diffraction data for the crystals were collected on the SER-CAT beamline of the Advanced Photon Source, Argonne National Laboratory, Argonne, IL.

2.10 Crystal structure determination

X-ray data collection was done by Dr. Irene Weber's group at Georgia State University. The crystal structures of CatchER were determined by Ying Zhang in Dr. Irene Weber's group. Crystals of CatchER were sent to the Advanced Photon Source at Argonne National Laboratory, Argonne, Illinois, USA. X-ray diffraction data was collected using the SER-CAT beamline. Structural data for the Ca^{2+} free, Ca^{2+} bound, and Gd^{3+} bound crystal structures were deposited into the Protein Data Bank (PDB) with codes 4l13, 4l1i and 4l12 respectively. A detailed protocol for the X-ray data collection and the molecular replacement done to obtain each structure is in the published article[181].

2.11 CatchER-Gd^{3+} stoichiometry via Job Plot

The method of continuous variations (Job Plot)[217] was used to confirm 1:1 binding of CatchER to Gd^{3+}. Duplicate samples of 40, 35, 30, 25, 20, 15, and 10 µM CatchER (actual concentrations were 38, 35, 30, 24, 20, 15, and 10.5 µM based on absorbance at 280 nm) were prepared in 20 mM PIPES pH 6.8. The absorbance and fluorescence spectra of each sample was recorded before and after adding 10, 15, 20, 25, 30, 35, and 40 µM of Gd^{3+} respectively to keep the total [CatchER + Gd^{3+}] equal to

50 µM. The relative amount of Gd^{3+} bound CatchER was calculated using the following derived equation:

$$\frac{F_{Ca^{2+}\,bound}}{F_{Ca^{2+}\,free}} = \frac{S_f \times C_f + S_b \times C_b}{S_f \times C_T} = \frac{S_f(C_T - C_b) + S_b \times C_b}{S_f \times C_T} \quad \text{Equation 2.1}$$

$$= 1 + \frac{C_b(S_b - S_f)}{S_f \times C_T} \quad \text{Equation 2.2}$$

$$a = \frac{S_b - S_f}{S_f} \quad \text{Equation 2.3}$$

$$\frac{C_b}{C_T} \times a = \frac{F_{Ca^{2+}\,bound}}{F_{Ca^{2+}\,free}} - 1 \quad \text{Equation 2.4}$$

$$C_b \times V = \left(\frac{F_{Ca^{2+}bound}}{F_{Ca^{2+}free}} - 1\right) \times \frac{C_T}{a} \quad \text{Equation 2.5}$$

where Cb is the amount of CatchER bound to Gd^{3+}, FGd^{3+} bound/FGd^{3+} free is the ratio of the fluorescence intensity with and without Gd^{3+}, C is the concentration of CatchER, and a is a constant of the difference between the quantum yields of the bound and free forms of CatchER divided by the quantum yield of the free form. S_f and S_b are the coefficients of the Ca^{2+} free and Ca^{2+} bound CatchER, respectively, and C_f and C_b are the concentrations of Ca^{2+} free and Ca^{2+} bound CatchER, respectively. C_T is the total concentration.

2.12 Optical property determination of CatchER variants

The quantum yield is a measure of the ratio of photons emitted to photons absorbed (Figure 2.12.1) that tells the efficiency of fluorescence[218]. In this experiment, protein variant samples were prepared in triplicate in different concentrations (within the sensitive range for absorbance readings) in 10 mM Tris pH 7.4 with 5 µM EGTA. Samples of wild type protein (EGFP) were also prepared in different concentrations

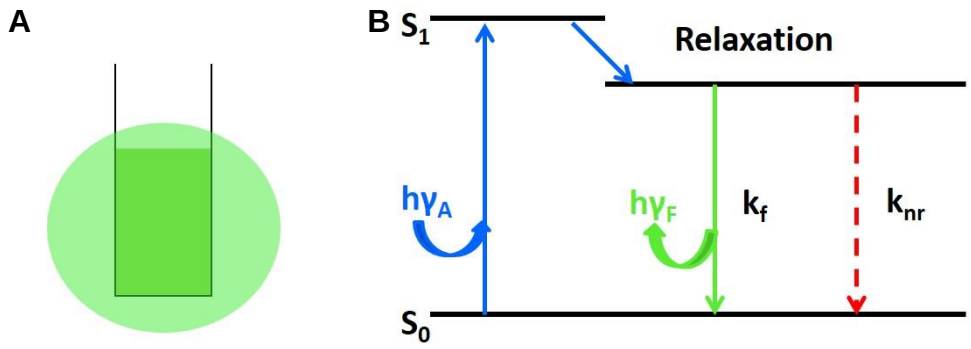

Figure 2.12.1 Perceived brightness of protein sample (A) and scheme for quantum yield (B)

A) The brightness of the fluorescent protein is the perceived intensity of its fluorescence. Brightness is a product of the extinction coefficient and the quantum yield. B) Simplified jablonski diagram of the absorbance and emission of light. When light is absorbed, electrons will move from the ground state (S_0) to the excited state (S_1). At this point, relaxation will occur to the lowest unoccupied molecular orbital where the electron will then fall back to ground state emitting a photon (k_f). Emission, however, is also effected by non-radiative decay processes (k_{nr}). The quantum yield is a ratio of k_f to the sum of all the k_{nr} processes.

in the same buffer because EGFP was used as the internal standard and needed in the final calculation. Fluorescence and absorbance of each sample was taken with and without 10 mM Ca^{2+}. Slit widths for the fluorescence measurements were adjusted based on the most concentrated sample and were 0.15 mm and 0.60 mm for excitation and emission, respectively. The fluorescence and absorbance values from each concentration point at each respective excitation wavelength were then plotted against each other (fluorescence vs. absorbance) in K-graph and fit using a linear equation for both apo and holo-form. The slope of the line for the variant and for EGFP were used in the final calculation using the following formula,

$$\phi = \phi_r(F_p/A_p)/(F_r/A_r) \qquad \text{Equation 2.6}$$

where F_p/A_p is the slope of the line for the variant, F_r/A_r is the slope of the line for EGFP, and ϕ_r is the quantum yield of the internal standard which is 0.6 for EGFP.

The extinction coefficient is a measure of how strongly a compound absorbs light at a given wavelength as a function of concentration and cell path length. It is constant at a specific wavelength. The extinction coefficient was measured by absorbance using the alkali denaturation assay (Figure 2.12.2) which is a standard assay for fluorescent proteins. This experiment is done after data has been collected from the quantum yield sample set (same day). To denature the samples, 0.1 M NaOH was added to each, and samples were mixed by inversion. The absorbance of each denatured sample was taken at the new absorbance peak which is ~447 nm for fluorescent proteins that have been denatured by this standard method. The absorbance of native to denatured protein was plotted in K-graph and fit using a linear equation. The slope of the line was used in the final calculation.

The perceived brightness was determined by multiplying the extinction coefficient and quantum yield. The following formula was used to calculate the extinction coefficient:

$$\varepsilon_{p,395/488\ nm} = \varepsilon_{p,447\ nm}(A_{p,395/488\ nm}/A_{p,447\ nm}) \qquad \text{Equation 2.7}$$

where $A_{p,395/488}/A_{p,447}$ is the slope of the line and $\varepsilon_{p,447}$ is the extinction coefficient of denatured wild-type GFP at 447 nm which is 44,000 $M^{-1}cm^{-1}$.

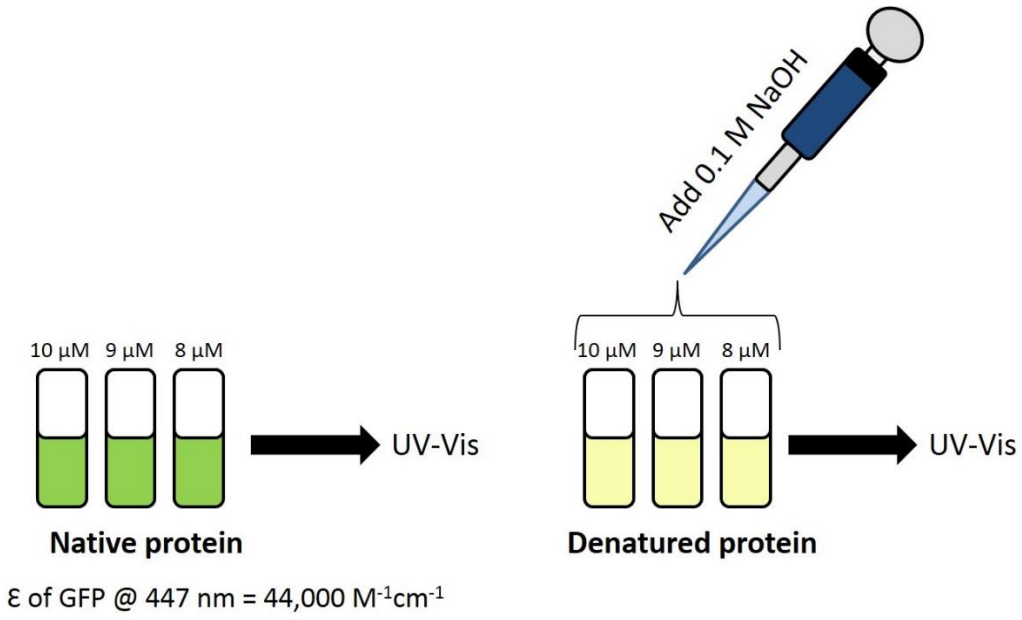

Figure 2.12.2 Measurement of the extinction coefficient of Ca^{2+} probes via the Alkali denaturation assay

The extinction coefficient of fluorescent proteins reflects how well the chromophore absorbs light. The Alkali denaturation assay is the established method used to determine the extinction coefficient of the chromophore of fluorescent proteins at their maximum absorbance wavelength by taking the absorbance ratio of the native protein to the denatured protein. Native protein samples are prepared at different concentrations, within the sensitive range of the UV-Vis spectrophotometer, and the absorbance spectrum of each is collected. Then, 10 µL of 0.1 M NaOH is mixed into each sample to unfold the protein and the absorbance spectrum of each is collected. The absorbance maximum of each folded sample is plotted against the new absorbance maximum of the denatured sample at 447 nm. The resulting line is fitted and the slope is used in the final calculation.

2.13 Apparent pK_a determination of CatchER variants

The apparent pK_a of the sensor variants was determined in order to know the pH sensitivity of the chromophore. Ten duplicate samples containing 10 µM protein and 5 µM EGTA were prepared in each of the buffers listed in Table 2.13.1 below. After preparation, samples were allowed to incubate at 4°C overnight. The next day, the actual

Table 2.13.1 Buffer concentrations and pH values used for pK_a measurement

Buffer	pH
0.5 M NaOAc	1.0
10 mM NaOAc	3.1
10 mM NaOAc	4.1
10 mM NaOAc	4.5
10 mM NaOAc	5.1
10 mM MES	5.5
10 mM MES	6.3
10 mM PIPES	7.2
10 mM Tris	8.0
10 mM Tris	9.2

pH of each sample was measured and recorded before beginning the analysis (pH of apo-form). Samples were analyzed using the fluorimeter without Ca^{2+} and with the addition of 5 mM Ca^{2+}. Once the experiment was completed, the pH of each sample was measured and recorded again (pH of holo-form). Fluorescence intensity was then normalized and plotted vs. pH to obtain the pK_a via curve fit in K-graph. The proposed reaction scheme and derivation of the pK_a equation was used to fit the normalized data,

$$HP \leftrightarrow H^+ + P^- \qquad \text{Equation 2.8}$$

$$pH = pK_a + \log\frac{[P]}{[HP]} \qquad \text{Equation 2.9}$$

$$f = \frac{F - F_{min}}{F_{max} - F_{min}} \qquad \text{Equation 2.10}$$

$$F_{min} = [P]_T c_1 \qquad \text{Equation 2.11}$$

$$F_{max} = [P]_T c_2 \qquad \text{Equation 2.12}$$

$$F = ([P]_T - [P])c_1 + [P]c_2 \qquad \text{Equation 2.13}$$

$$f = \frac{[P]_T c_1 - [P] c_1 + [P] c_2 - [P]_T c_1}{[P]_T c_2 - [P]_T c_1} = \frac{[P]}{[P]_T} \qquad \text{Equation 2.14}$$

$$\frac{[P]}{[HP]} = \frac{1}{1/f - 1} \qquad \text{Equation 2.15}$$

$$f = \frac{1}{1 + \exp\left(\frac{pK_a - pH}{c}\right)} \qquad \text{Equation 2.16}$$

where H^+ is the proton; P is the protein; f is the normalized ΔF change; $[P]_T$ is the total protein concentration; c_1 or c_2 is the extinction coefficient of HP or P fluorescence, respectively; F is the real-time fluorescence intensity; F_{min} is the fluorescence at the lowest pH; F_{max} is the fluorescence at the highest pH; and c is a constant for adjustment. The value theoretically equals log e.

2.14 *In vitro* K_d of CatchER variants via Fluorescence Spectroscopy

Samples of 10 µM sensor with 5 µM ethylene glycol tetraacetic acid (EGTA) were prepared in triplicate in 1 mL volumes in 10 mM Tris, pH 7.4. The samples were placed in quartz fluorescence cuvettes, and 0-15 mM Ca^{2+} or Mg^{2+} was added to each sample using 0.1 M and 1 M Ca^{2+} stock solutions or Mg^{2+} solutions . The fluorescence response of the sensor to increasing Ca^{2+} concentrations was monitored using a fluorescence spectrophotometer (Photon Technology International, Canada) with the *Felix32* fluorescence analysis software. Slit widths were set at 0.3 mm for excitation and emission. The samples were excited at 395 nm and 488 nm with emission collected from 410-600 nm for 395 nm excitation and from 500-600 nm for 488 nm excitation. The absorbance spectrum before and after titration was obtained using a Shimadzu UV-1601 spectrophotometer. Fluorescence and absorbance traces were

plotted using Kalidegraph (KGraph). The data was normalized to show the relative change in relation to the basal fluorescence using the following equation,

$$y = \frac{(F - F_{min})}{(F_{max} - F_{min})} \qquad \text{Equation 2.17}$$

where F is the fluorescence intensity at any point, F_{min} is minimum fluorescence intensity, and F_{max} is the maximum fluorescence intensity. The normalized data was then plotted and fitted in KGraph to obtain the dissociation constant (K_d) using the following equation for 1:1 binding,

$$\frac{[PM]}{[P_T]} = \frac{[M_T]}{K_d + [M_T]} \qquad \text{Equation 2.18}$$

where [PM] is the concentration of protein-metal complex, $[P_T]$ is the total protein concentration, $[M_T]$ is the total metal concentration, and K_d is the dissociation constant. $[PM]/[P_T]$ represents the change in complex formation. A complete derivation of the 1:1 binding equation was done in previous work[181]. To determine the Ca^{2+} K_d at physiological concentrations of salt, enough KCl was weighed and dissolved in Tris buffer used to prepare the protein samples to make the final concentration of KCl 150 mM. The pH of the buffer was adjusted to be 7.4 after addition of KCl. The subsequent titrations proceeded as previously outlined.

2.15 *In vitro* K_d of CatchER variants via equilibrium dialysis and ICP-OES spectrometry

2.15.1 Equilibrium dialysis

The absorbance spectrum of each equilibrium dialysis sample was collected using a Shimadzu UV-1601 spectrophotometer before and after equilibration. In 15 mL falcon tubes, 20 uM samples of the EGFP-based sensors were prepared with a final volume of 5.5 mL. 5.5 mL of 10 mM Tris pH 7.4 was used as the blank. As a positive control, 5.5 mL of 20 µM of alpha-lactalbumin was prepared along with EGFP and myoglobin as negative controls. Absorbance spectra were taken of each sample to confirm that each was ~20 µM. Sample concentrations were adjusted accordingly. An accurate concentration of each calculated at 280 nm was used in the final K_d calculation. After collecting the absorbance spectra, 4 L of 10 mM Tris pH 7.4 was prepared and 3.8 L was placed in a 4 L beaker with a magnetic stir bar. To the 3.8 L buffer, 20 µM of Ca^{2+} was added and allowed to mix for a few minutes, then 6 mL of the buffer/Ca^{2+} mixture was placed in a 15 mL falcon tube and labeled t = 0. The samples were then placed in 18 mm wide Spectra/Por dialysis bags (Spectrum Labs) with a 3.5 kDa molecular weight cutoff (bags were pre-soaked in water for 30 min before use). The dialysis samples were then placed in the beaker on a stir plate and allowed to equilibrate for 48 h at room temperature, shown in Figure 2.15.1, taking two more 6 mL samples of the buffer after 24 h (t = 1) and after 48 h (t = 2). After setting up the equilibrium dialysis experiment, Ca^{2+} standards were prepared to obtain the Ca^{2+} standard curve from ICP-OES. The standards and volumes associated are found in Table 2.15.1.

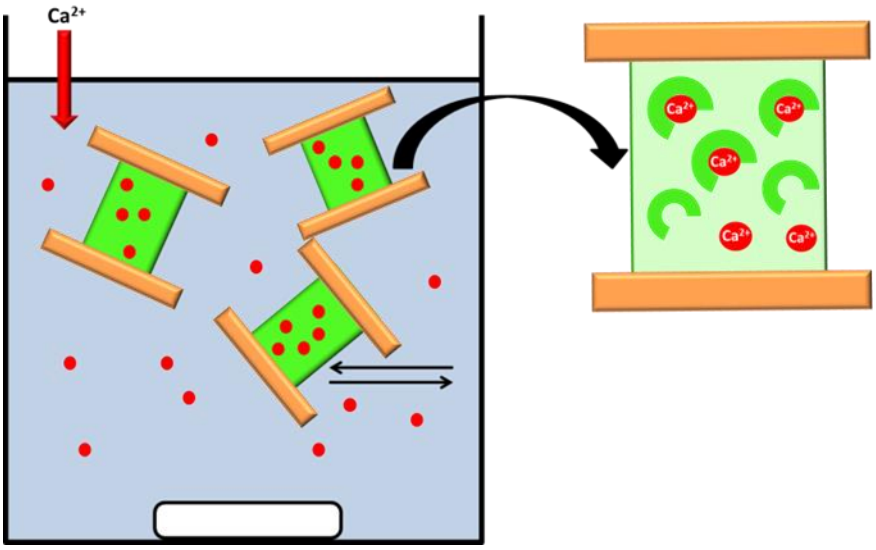

Figure 2.15.1 Schematic of equilibrium dialysis of CatchER variants

Protein samples in dialysis bags are allowed to equilibrate against a buffer solution containing a certain concentration of Ca^{2+} for 48 h. At the end of 48 h, samples are analyzed for Ca^{2+} content using ICP-OES. The concentration of protein and final amount of Ca^{2+} in each sample is used to calculate the K_d.

Table 2.15.1 Prepared Ca^{2+} standards for ICP-OES standard curve

Standard	Total volume (mL)	Volume of Ca^{2+} needed (mL)	Volume of ICP-OES H_2O needed (mL)	Volume of 70% HNO_3 needed (mL)
10 ppm	30	0.30	28.843	0.857
4 ppm	15	6.0 from 10 ppm	8.571	0.429
3 ppm	15	4.5 from 10 ppm	10.071	0.429
2 ppm	15	3.0 from 10 ppm	11.571	0.429
500 ppb	15	0.75 from 10 ppm	13.821	0.429
100 ppb	15	0.15 from 10 ppm	14.421	0.429
Blank	10	0	9.714	0.286

2.15.2 ICP-OES

After 48 h equilibration, the samples were analyzed using the Varian 720-ES ICP-OES. Before using the instrument, 1 L of 2% HNO_3 and 500 mL of 2 ppm yttrium internal standard were prepared. Before turning on the instrument, the Argon (Ar) gas was opened and the water bath was turned on. The pump lines were tightened placing both the white line (for sample) and orange line (for internal standard) into the 2% HNO_3 (orange line was placed in internal standard solution before beginning the analysis). The ICP worksheet computer program was then opened. In the program, go to 'instrument' to turn on the pump. After 5 min the plasma was turned on. Once the plasma flame ignited, the instrument was allowed to stabilize for 30 min. While the instrument stabilized, the samples were collected (with clean gloves) from the dialysis bags and placed in labeled 15 mL falcon tubes. Sample tubes were then placed in a holder along with the standard curve solutions to allow for easy access during the analysis. In the ICP program, a new worksheet was created as follows: go to 'worksheet', 'new', and select VAIMDB_Varian ICP-OES Data (000); choose an old file for this type of analysis, then click 'method' and 'worksheet'; rename the worksheet and click 'ok'; go to 'method', 'edit method', then 'standards' and update concentrations for standard curve in ppb; go to 'tools' and 'standard names' to change names of standards; go to 'sequence editor' and enter the # of samples (excluding the metal standards) changing the name of the samples under the 'sequence' tab (put them in the order you want them analyzed in). After organizing the worksheet, seven Ca^{2+} emission wavelengths were chosen to collect intensity data at: 396.847, 317.933, 219.779, 370.602, 643.907, 220.861, and 373.690. Once the worksheet setup was complete, the

analysis was started by pressing start (play button). Between samples, the white line was placed in the 2% HNO_3 solution to clean the line for each sample measurement. At the end of the analysis, the plasma was turned off and then the Ar gas. The pump was allowed to run for 10 min to clean the instrument of any residue then turned off. After 15-20 min, the water bath was turned off. The intensity data was exported to an Excel file. The standard curves were plotted for each wavelength (intensity vs. ppb) to obtain the $[Ca^{2+}]$ in ppb for each sample at each wavelength. Parts per billion concentrations were then converted to micro-molar concentrations. Calculation of the K_d is based on the following formulas,

$$K_d = \frac{[Ca^{2+}]_{free}[P]_{free}}{[P\text{-}Ca^{2+}]} \qquad \text{Equation 2.19}$$

$$[P\text{-}Ca^{2+}] = [Ca^{2+}]_{variant} - [Ca^{2+}]_{free} \qquad \text{Equation 2.20}$$

$$[P]_{free} = [P]_{total} - [P\text{-}Ca^{2+}] \qquad \text{Equation 2.21}$$

where $[Ca]_{free}$ is the concentration of Ca^{2+} found in the buffer after equilibration is reached (t = 0 sample) determined by ICP-OES, [Ca-P] is the concentration of Ca^{2+} found inside the dialysis bag of each sample ($[Ca]_{variant}$) determined by ICP-OES minus $[Ca]_{free}$, and $[P]_{free}$ is the 280 nm concentration of protein sample ($[P]_{total}$) minus the concentration of [Ca-P]. All calculations were done in Excel. Concentrations of Ca^{2+}, in µM, found in each sample and K_d values are tabled in the results section along with standard curves, absorbance spectra, and bar graphs comparing the concentrations of Ca^{2+} found in each sample at each wavelength.

2.16 Ionic strength effect on Ca^{2+} binding kinetics via stopped flow spectrofluorometry

To determine the electrostatic nature of Ca^{2+} binding to our sensors, we used stopped flow spectrofluorometry to determine the Ca^{2+} binding kinetics at increased salt concentrations with the help of Dr. Gadda. The kinetics of our probes were investigated using an SF-61 stopped-flow spectrofluorometer (10-mm path length, 2.2-ms dead time at room temperature; Hi-Tech Scientific) at room temperature. Fluorescence intensity changes were recorded with a 455-nm long-pass filter with excitation at 395 nm. Protein samples were prepared at 40 µM in 5-10 mL from a concentrated protein stock and diluted with the Tris-KCl buffer to be mixed with. A list of the buffers used can be found in Table 2.16.1. The buffers were prepared at 2X concentration so the final dilution in the mixing chamber would be the desired concentration. In the stopped flow instrument, buffer and protein were loaded into separate syringes, shot against each other, and the fluorescence intensity trace was recorded. Because the contents of both syringes were mixed together, the concentrations of each were diluted by half with a final protein concentration of 20 µM. Approximately five shots were recorded for each point, and the best three were averaged. The raw data was fitted using the following equations,

$$F = F_\infty - \Delta F \exp(-k_{obs} \cdot t) \qquad \text{Equation 2.22}$$

$$F = F_\infty + \Delta F \exp(-k_{obs} \cdot t) \qquad \text{Equation 2.23}$$

which describes F, the fluorescence intensity, at any given time; F_∞, the fluorescence at infinite time; ΔF, the amplitude of the fluorescence change; k_{obs}, the observed rate constant; and t, the time.

Table 2.16.1 Buffers used to measure Ca^{2+} binding kinetics of CatchER variants

Protein	Ca^{2+} buffers (10 mM Tris, pH 7.4) (mM)	
CatchER	0 mM KCl	0, 0.16, 0.4, 0.8, 1.6, 4
	150 mM KCl	0, 0.8, 2, 4, 8, 20
149E	0 mM KCl	0, 0.1, 0.25, 0.5, 1, 2.5
	150 mM KCl	0, 0.2, 0.5, 1, 2, 5, 10, 20
CatchER-T	0 mM KCl	0, 0.12, 0.3, 0.6, 1.2, 3
	150 mM KCl	0, 0.34, 0.85, 1.7, 3.4, 8.5, 15, 20

2.17 Creating CatchER-JP45 construct using restriction enzyme digest and ligation

In the pcDNA3.1+ vector, CatchER resides between the BamH1 and EcoR1 restriction enzyme sites. After the EcoR1 site, there is an additional Not1 cleavage site. JP45 resides in the pDsRed2-N3 vector containing the fluorescent protein DsRed between the BamH1 and Not1 restriction sites. To make the CatchER-JP45 construct, an enzyme digest was done using BamH1 and Not1 on both plasmids. To an Eppendorf tube, 2-20 µL of plasmid was added along with 1 µL of both enzymes, 2 µL of 10x reaction buffer N3 which both enzymes were most efficient at, and water to make the final reaction volume 20 µL. The reaction was placed in the 37°C incubator for 3 h or overnight. All samples were loaded onto an agarose gel and ran at 80 v. The gel was analyzed for the presence of two bands: plasmid vector by itself (higher bp amount) and the fragment excised by the restriction enzymes (lower bp amount). The bands

representing CatchER and the JP45 vector were cut, and the DNA was extracted using a gel extraction kit (Qiagen) using an elution volume of 30 µL for CatchER and 50 µL for the JP45 vector. The fragments were then ligated together, and the DNA was used to transform XL10 Gold cells following the normal transformation procedure implementing a 45 s heat shock and an hour 37°C incubation period with 100 µL of NZY media containing 25 µL of 20% glucose, 12.5 µL of 1 M MgSO4 and 12.5 µL of 1 M $MgCl_2$. Plates were analyzed for clones the next day. To easily sequence the insertion of CatchER into the C-terminal of the construct, the JP45 red-forward primer 5'-GAGAAGCCAAGTAAAGGGGAGAAACTGAAG-3' was designed using a small sequence of DNA at the end of JP45.

2.18 Mammalian cell culture and transfection

Human Embryonic Kidney (HEK293), Cos-7, and C2C12 myoblast cells (all from ATCC) were cultured in Dulbecco's Modified Eagle's Medium (DMEM) (Sigma-Aldrich), high glucose with 10% Fetal Bovine Serum (FBS) and optional 100 µg/mL penicillin-streptomycin, in a humidified incubator at 37˚C with 5% CO_2. HEK293 and Cos-7 cells were trypsinized and seeded onto 22 mm x 40 mm glass microscope slides (Fisherbrand®) where they were allowed to grow for 2 days. Cells were then transiently transfected with 2 µg of CatchER-T' DNA in the pcDNA+3.1 vector using Lipofectamine 2000 (Life Technologies) in a 1:3 w/v ratio for DNA:Lipofectamine, following the manufacturer protocol, in 3 mL of OPTI-MEM for 4-6 h at 37˚C. Due to the difficulty of transfecting adherent cell lines, a different transfection procedure and reagent was used that has been shown to improve the transfection efficiency of C2C12 cells[219]. C2C12 myoblast cells were trypsinized and seeded onto glass slides, as previously mentioned.

The cells were then transiently transfected with 2 µg of variant pcDNA+3.1 using the transfection reagent Effectene at a fixed1:8 w/v DNA:Enhancer ratio and a 1:4 w/v DNA:Effectene ratio in 3 mL of DMEM and 2 mL of OPTI-MEM for 24 h at 37˚C. After transfection of all cell lines, the media was replaced with fresh DMEM, and cells were incubated for 48 h at 37˚C to ensure expression of the sensors. Differentiated C2C12 cells were transfected using the same method, changing the media to DMEM supplemented with 2% FBS. Cells were allowed to differentiate for 4-6 days, changing the media every other day, then imaging was done.

2.19 Fluorescence microscopy

Live cell fluorescence imaging was done using a Leica DM6100B inverted microscope with a cooled EM-CCD camera (C9100-13, Hamamatsu). CatchER-T' and its constructs were excited at 488 nm using a Till Polychrome V Xenon lamp (Till Photonics) with an HQ480/20× excitation filter, a D535/25 emission filter, and a 515DCXR dichroic mirror (Chroma Technology Corp.). Slides were viewed through a 40X oil immersion objective. One frame was taken every 5 s. Fura-2 AM was excited at 340/380 nm with the same light source utilizing the D340xv2, D380xv2, and D510/80 excitation and emission filter set with a 400DCLP dichroic mirror. Rhod-2 AM was excited at 550 nm. Slides were mounted using vacuum seal grease to the bottom of a bath chamber with a ~1 mL capacity. Solutions were exchanged using a vacuum perfusion system. All imaging was done at room temperature. Intensity measurement data and pictures were collected using Simple PCI software (Hamamatsu).

2.20 Monitoring response to agonists and antagonists of ER/SR Ca^{2+} release and reuptake channels

Slides containing attached cells were mounted onto the bath chamber with vacuum seal grease. The fluorescence response of CatchER variants to ryanodine receptor agonists caffeine and 4-cmc, IP_3R and purinergic receptor agonist ATP, and SERCA pump antagonists thapsigargin and CPA were carried out in Ringer's Buffer (121 mM NaCl, 2.4 mM K_2HPO_4, 0.4 mM KH_2PO4, 1 mM $MgCl_2$,10 mM HEPES, 10 mM glucose, pH 7.25) with or without 1.8 mM $CaCl_2$. To monitor $[Ca^{2+}]_i$, 4 µM Rhod-2 AM was mixed with pluoronic F-127 in a 1:1 v/v ratio and added to slides in 6 cm dishes containing 2 mL of Ringer's buffer. Slides were incubated for 30 min to 1 h at room temperature and allowed to de-esterify for 10 min in the dark. The fluorescence data was normalized by dividing all fluorescence values (F) by the basal or Ca^{2+} free fluorescence value (F_0). A list of all the agents commonly used in Ca^{2+} imaging, preparation details, their targets and affects are located in Table 2.20.1.

Table 2.20.1 Agents used to stimulate or inhibit Ca^{2+} release for cell imaging

Agents	Stock [Agent]	Solvent	Applied [Agent]	Target	Anticipated effect
IP_3	10 mM	DMSO	10 µM	IP_3R	$[Ca^{2+}]_{ER}\downarrow$; $[Ca^{2+}]_{cyt}\uparrow$
Histamine	50 mM	Steril H_2O	200 µM	IP_3R	$[Ca^{2+}]_{ER}\downarrow$; $[Ca^{2+}]_{cyt}\uparrow$
Caffeine	40 mM	Steril H_2O	10 mM	RyR	$[Ca^{2+}]_{ER}\downarrow$; $[Ca^{2+}]_{cyt}\uparrow$
4-cmc	20 mM	Steril H_2O	200 µM	RyR	$[Ca^{2+}]_{ER}\downarrow$; $[Ca^{2+}]_{cyt}\uparrow$
CPA	50 mM	DMSO	15 µM	SERCA	$[Ca^{2+}]_{ER}\downarrow$; $[Ca^{2+}]_{cyt}\uparrow$
Thapsigargin	1 mM	DMSO	2 - 5 µM	SERCA	$[Ca^{2+}]_{ER}\downarrow$; $[Ca^{2+}]_{cyt}\uparrow$
Digitonin	25 mg/mL	Steril H_2O	25 µM	plasma membrane	permeablize membrane irreversibly
Saponin[a]	10% (w/v)	Steril H_2O	0.001 - 0.005%	plasma membrane	permeablize membrane irreversibly
Ionomycin	10 mM	DMSO	2-10 µM	membranes	shuttles Ca^{2+} across membranes

Multiple stocks of each agent are prepared and stored at -20°C. [a]Saponin is sensitive to freeze thaw cycles and will lose its permeablization ability over time.

2.21 *In situ* K_d and calibration

Cells were permeabilized for 15-30 s with 0.002% saponin in intracellular buffer (125 mM KCl, 25 mM NaCl, 10 mM HEPES, 0.5 mM Na_2ATP, 0.2 mM $MgCl_2$, 200 µM $CaCl_2$, 500 µM EGTA, pH 7.25). The final amount of free Ca^{2+} was 100 nM. Cells were then washed with KCl rinse buffer (140 mM KCl, 10 mM NaCl, 1 mM $MgCl_2$, 20 mM HEPES, pH 7.25). Ca^{2+} and EGTA solutions were prepared in KCl buffer at 0.3, 0.6, 2, 5, 10, 20, 50, 100, and 200 mM Ca^{2+} and 1 mM EGTA. The Ca^{2+} ionophore ionomycin was added to each solution at a final concentration of 10 µM. The intensity plateaus

from each Ca^{2+} point and the EGTA addition (0 point) were averaged, normalized, and fitted using Equations 2.17 and 2.18. The F_{max} and F_{min} values were obtained from the highest Ca^{2+} concentration (100 or 200 mM) and the lowest Ca^{2+} concentration (EGTA) and were put into the following calibration equation to determine the basal $[Ca^{2+}]_{ER/SR}$,

$$[Ca^{2+}] = K_d[(F - F_{min})/(F_{max} - F)] \qquad \text{Equation 2.24}$$

where F is the basal fluorescence intensity at the start of the experiment, F_{min} is the minimum fluorescence after depletion of Ca^{2+} and F_{max} is the maximal fluorescence after the addition of Ca^{2+}.

3 STRUCTURAL BASIS FOR A HAND-LIKE SITE IN THE CA^{2+} SENSOR CATCHER WITH FAST KINETICS

(This chapter has been published in Zhang, Y., Reddish, F., Tang, S., Zhuo, Y., Wang, Y. F., Yang, J. J., and Weber, I. T.,(2013), *Acta Crystallographia D*, D69, 2309-2319.) The second author performed the protein expression, purification, crystal screenings, crystallization, metal binding experiments using absorbance and fluorescence spectroscopy, and writing the results and discussion for the manuscript.

3.1 Introduction

The Ca^{2+} ion (Ca^{2+}) acts as a ubiquitous signaling molecule in the regulation of numerous biological functions including heartbeat, muscle contraction, cell development and proliferation[220,105]. Ca^{2+} signals exhibit different amplitudes and durations as the ions flow between subcellular compartments. Ca^{2+} functions as a first messenger in the central nervous system and works as an extracellular ion source for postsynaptic ligand-gated channels[24]. The endoplasmic reticulum (ER) functions as an intracellular Ca^{2+} store and the release of ER Ca^{2+} triggers a series of biological processes via binding to intracellular Ca^{2+}-sensing proteins such as calmodulin (CaM) and troponin C (TnC)[221]. The Ca^{2+}-signaling events are controlled by the basal ER/SR (sarcoplasmic reticulum) Ca^{2+} level, as well as the amplitude and the kinetics of Ca^{2+} release from the Ca^{2+} stores. Hence, determination of the concentration of free Ca^{2+} in the ER is of extensive interest and has stimulated the development of tractable intracellular Ca^{2+} sensors.

Many efforts have been devoted to green fluorescent protein (GFP)-based Ca^{2+}-fluorescent indicators such as the cameleons[177,206], pericams[222], TN-XL[205] and TN-XXL[223]. Their detection is based on either fluorescence resonance energy transfer (FRET) between two different GFP variants or the pH-dependent change in ionization

state of the chromophore in circularly permutated GFP[177,224,203,190]. One common property of these sensors is that they involve the insertion of naturally occurring Ca^{2+}-sensing proteins such as CaM and its target binding peptide and are capable of sensing cytosolic Ca^{2+} responses in the nanomolar to micromolar range[225,226,162]. Several ER/SR sensors with lower metal-binding affinities have been developed by modifying the Ca^{2+}-binding loops or the peptide-interaction surface of CaM[227,177,207,228,229]. These sensors exhibit some limitations such as off-rates which are not fast enough to detect the Ca^{2+} release during action potentials. In addition, only ~50% of the skeletal muscle cells show a response to Ca^{2+} stimulation. For the FRET-pair involved sensors, their highly variable basal CFP (cyan fluorescent protein)/YFP (yellow fluorescent protein) ratio and poor signal-to-noise ratio also limit quantitative determination of Ca^{2+} concentration and Ca^{2+} release[230,231]. Therefore, there is a pressing need for new Ca^{2+} sensors targeted to cellular compartments with putative high Ca^{2+} concentration, as in the ER/SR, to overcome these limitations. In a previous attempt to meet this urgent need, our laboratory engineered a Ca^{2+} sensor, ‘G1’, by grafting an EF-hand motif into enhanced green fluorescent protein (EGFP)[191]. Unlike GFP, which can be excited at 395 and 475 nm, EGFP contains two mutations F64L and S65T and has one absorption maximum at 488 nm[162,232]. The F64L mutation is responsible for the improved folding efficiency at 310 K, while S65T is a critical mutation for suppressing the 395 nm absorbance peak[162,232,233]. This G1 sensor has an apparent K_d of 0.8 mM and responds to Ca^{2+} with a ratiometric fluorescence change, but with a slow kinetic response.

Recently, we reported a new strategy for creating Ca^{2+} indicators by introducing a Ca^{2+}-binding site into EGFP via site-directed mutagenesis of selected residues in the

fluorescence-sensitive location[180]. The single EGFP based Ca^{2+} biosensor termed CatchER was generated by the substitutions S147E, S202D, Q204E, F223E and T225E in the designed Ca^{2+}-binding site of EGFP (Fig. 3.1.1). CatchER provides multiple advantages for reliably monitoring Ca^{2+} signaling in high [Ca^{2+}] environments. (i) It exhibits a unique Ca^{2+}-induced change in optical properties. Ca^{2+} binding results in ratiometric changes in absorption, while fluorescence emission at 510 nm is increased when excited at either 398 or 490 nm (Fig. 3.2.3A); the

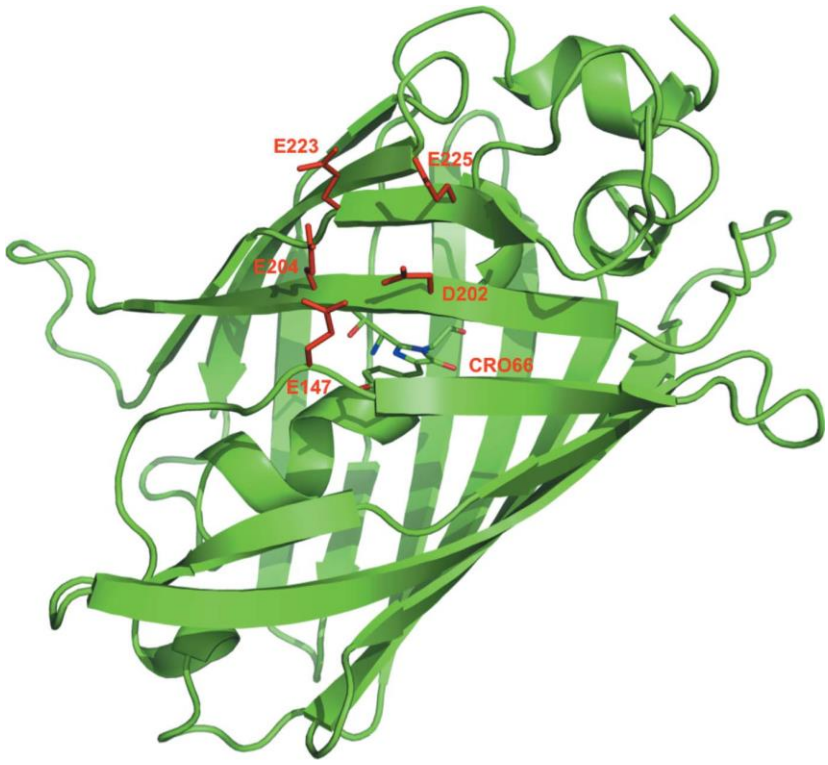

Figure 3.1.1 Structure of CatchER

Structure of CatchER (green cartoon) indicating the locations of the mutated residues (red sticks) S147E, S202D, Q204E, F223E and T225E; the chromophore CRO66 is shown in green sticks with CPK atom colors.

high signal-to-noise ratio for fluorescent change in response to Ca^{2+} as well as the avoidance of cooperativity associated with multiple binding sites allows accurate detection of Ca^{2+} both in vitro and in vivo. (ii) CatchER exhibits unprecedented dissociation kinetics, with an off-rate of >100 s^{-1} and a fast kinetic response to Ca^{2+} changes within milliseconds; recent work has also shown that CatchER is able to detect multiple Ca^{2+} spikes during muscle contraction and relaxation[234]. (iii) The K_d of CatchER (around 1 mM) allows the accurate calibration of SR Ca^{2+} signaling; CatchER is able to report considerable differences in SR/ER Ca^{2+} concentration between epithelial HeLa, kidney HEK293 and muscle C2C12 cells. (iv) No invasive methods are required for CatchER detection in living organelles compared with current Ca^{2+} dyes. Such cumulative advantages, especially the fast kinetic properties, allowed us to monitor SR luminal Ca^{2+} in flexor digitorum brevis (FDB) muscle fibers to understand the mechanism of diminished SR Ca^{2+} release in aging mice[235,236].

In this report, we describe the crystallographic analysis of CatchER to understand the structural basis for the Ca^{2+} induced fluorescent and absorption changes and fast response. Crystal structures were determined of CatchER in the absence of Ca^{2+} (CatchER(apo)), in the presence of Ca^{2+} (CatchER-Ca^{2+}) and from crystals soaked with Gd^{3+} (CatchER-Gd^{3+}). To overcome the challenges in visualizing Ca^{2+}-binding sites in the proteins owing to the weak Ca^{2+}-binding affinity and the high off-rate and the difficulty in distinguishing Ca^{2+} from water in the crystal structure, we used the heavier Gd^{3+} ions with similar metal-binding coordination properties to Ca^{2+} to identify the position of the metal ion. These X-ray crystal structures of CatchER and its complexes

may assist the future development of protein–ligand interaction-based biosensors for the detection of various physiological molecules.

3.2 Results and discussion

3.2.1 Expression and purification of CatchER

Our GECI CatchER has been created to monitor Ca^{2+} transients in the ER/SR and measure Ca^{2+} concentration in said organelles through a novel mechanism where the binding of Ca^{2+} on the surface of the protein induces an increase in fluorescence intensity. To visualize the possible structural rearrangement involved around the chromophore in CatchER, protein crystallography was employed. In order to obtain diffraction quality crystals of CatchER, a large amount of the sensor needed to be expressed and then purified with high yield. Figure 3.2.1A shows the optical density of the BL21 (DE3) cells during overexpression of CatchER from all three flasks using the method outlined in Chapter 2 section 2.4. The region of the graph circled in purple indicates the point of IPTG addition to induce overexpression of the probe. Figure 3.2.1B shows the expression gel of the sensor with samples taken from all three flasks. SDS-PAGE gel analysis shows a clear increase in the amount of protein expressed after induction with IPTG.

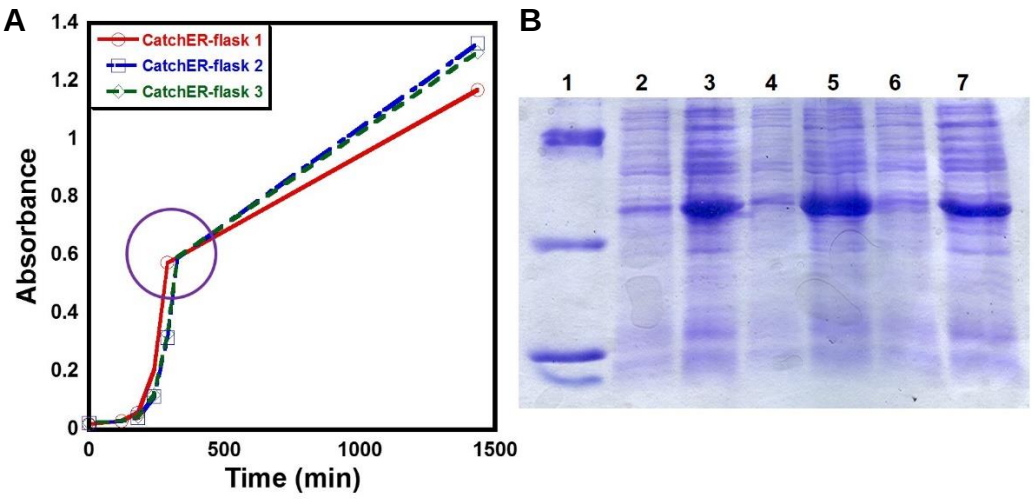

Figure 3.2.1 Overexpression of CatchER in BL21 (DE3) cells.

A) CatchER DNA was transformed into BL21 (DE3) cells and plated onto kanamycin resistant LB agar plates. One colony was selected from the plate, after overnight growth, and placed into a 50 mL falcon tube containing 30 mL of LB medium with 18 µL of kanamycin and shook overnight at 37°C at 200 rpm. The next day the inoculated was split between three 2.8 L flasks containing 1 L of autoclaved LB medium with 600 µL of kanamycin added to each. The flasks were shaken in a 37°C incubator at 220 rpm. One milliliter samples were taken every hour to check the optical density of each flask. Once the optical density reached 0.6, 200 µL of 1 M IPTG was added to the flask and the temperature was reduced to 25°C for proper expression of CatchER to occur. Samples were taken the next day to obtain the final optical density reading. B) SDS-PAGE gel of CatchER expression samples from each flask. Lane 1 is the marker; lanes 2 and 3 are before and after induction from flask 1; lanes 4 and 5 are before and after induction from flask 2; and lanes 6 and 7 are before and after induction from flask 3.

After overexpression of the sensor, the cell pellet was collected and sonicated in 20-30 mL of extraction buffer to break the cells and release the protein. After centrifugation of the cell lysate, the supernatant containing CatchER was purified using HisTag purification on a Ni^{2+}-NTA column using an imidazole gradient outlined in Chapter 2 section 2.7. The HisTag chromatogram and SDS-PAGE gel for CatchER are shown in Figure 3.2.2A. SDS-PAGE analysis of the fractions collected from HisTag

purification show the purity of CatchER compared to the cell pellet (lane 1) and the supernatant (lane 3). Since the purified protein would be used for crystallization, gel filtration was employed as an additional purification step to ensure a quality protein sample that would produce diffraction quality crystals (Chapter 2 section 2.7). Figure 3.2.2B shows the pure protein peak, circled in red, on the gel filtration chromatogram and the SDS-PAGE gel showing the purity of the fractions collected.

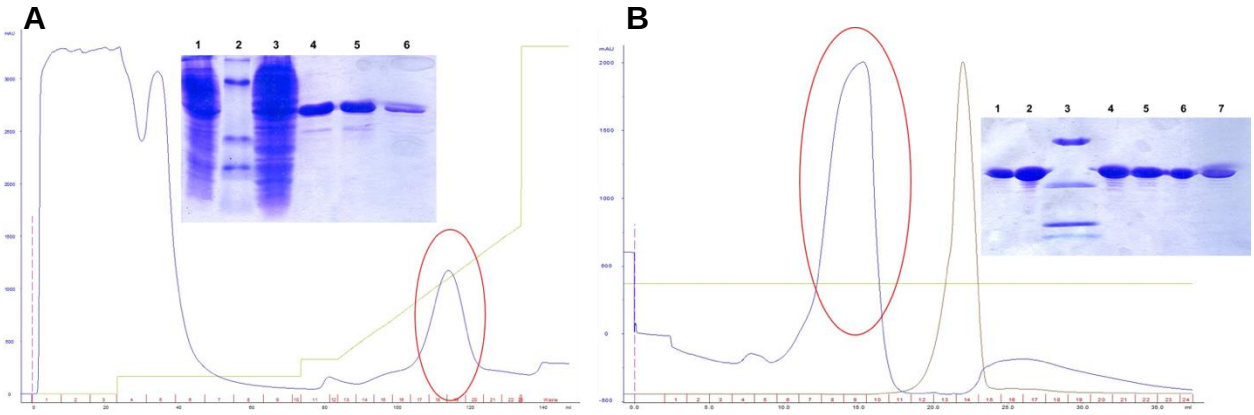

Figure 3.2.2 HisTag purification (A) and gel filtration (B) of CatchER.

A) CatchER was purified using an FPLC system. The supernatant containing CatchER was loaded onto a 5 mL HiTrap Ni^{2+}-NTA chelating column where the 6X Histidine tag on the N-terminal of CatchER interacted with the Ni^{2+} on the column. The protein began eluting at ~36% imidazole (150 mM). Samples were collected for SDS-PAGE gel analysis of protein purity (inset). Lane 1 is the cell pellet; lane 2 is the marker; lane 3 is the supernatant; and lanes 4-6 are fractions 17, 18, and 19. The pure protein fractions were collected and concentrated down to 1-2 mL. B) The concentrated protein was injected into a Superdex 75 gel filtration column using 10 mM Tris, pH 7.4, as the eluting buffer. The flow rate was set at 0.5 mL/min. The inset SDS-PAGE gel of the fractions collected from gel filtration show their purity.

3.2.2 Metal binding properties of CatchER

The absorption and fluorescence response of CatchER to Ca^{2+} and Gd^{3+} is shown in Figure 3.2.3A-F with the fluorescence monitored at 510 nm upon excitation at 488 nm. The normalized response shows an excellent fit to the 1:1 binding equation.

From these results, the K_d of CatchER for Gd^{3+} is 53.0 ± 4.0 and 177.0 ± 13.6 µM when excited at 395 and 488 nm, respectively. The K_d of CatchER for Ca^{2+} was determined to be 315.4 ± 40.0 and 227.0 ± 3.3 µM when excited at 395 and 488 nm, respectively. The addition of Ca^{2+} or Gd^{3+} greatly enhances the fluorescence emission of CatchER at 510 nm when excited at 395 or 488 nm. The protocol used is found in Chapter 2 section 2.14.

Because the structure of the binding site was difficult to elucidate from the crystal structure of the Ca^{2+} load form of CatchER, alternative methods were used to improve the diffraction in that area. Crystals of Ca^{2+} free CatchER were soaked in the mother liquor solution containing 2 mM of $GdCl_3$. Structural analysis of Gd^{3+}-loaded CatchER revealed double occupancy for Gd^{3+} within the metal binding site. To ensure 1:1 binding of CatchER to Gd^{3+}, the stoichiometric interactions of CatchER with Gd^{3+} was investigated and determined using the Job Plot method (Figure 3.2.3F) as outlined in Chapter 2 section 2.11. Table 3.2.1 lists the calculated relative amounts of Gd^{3+} loaded CatchER from the plot in Figure 3.2.3F that were determined using Equation 2.5 in Chapter 2 section 2.11. The largest amount of Gd^{3+} bound CatchER was obtained at equi-molar amounts of CatchER and Gd^{3+} (25 µM, highlighted in red). Along with determining the stoichiometric interaction of CatchER with Gd^{3+}, we determined the binding affinity of CatchER to Gd^{3+} found in Figure 3.2.3D. The Gd^{3+} K_d of CatchER was calculated to be 53.0 ± 4.0 µM (395 nm) and 177.0 ± 13.6 µM (488 nm).

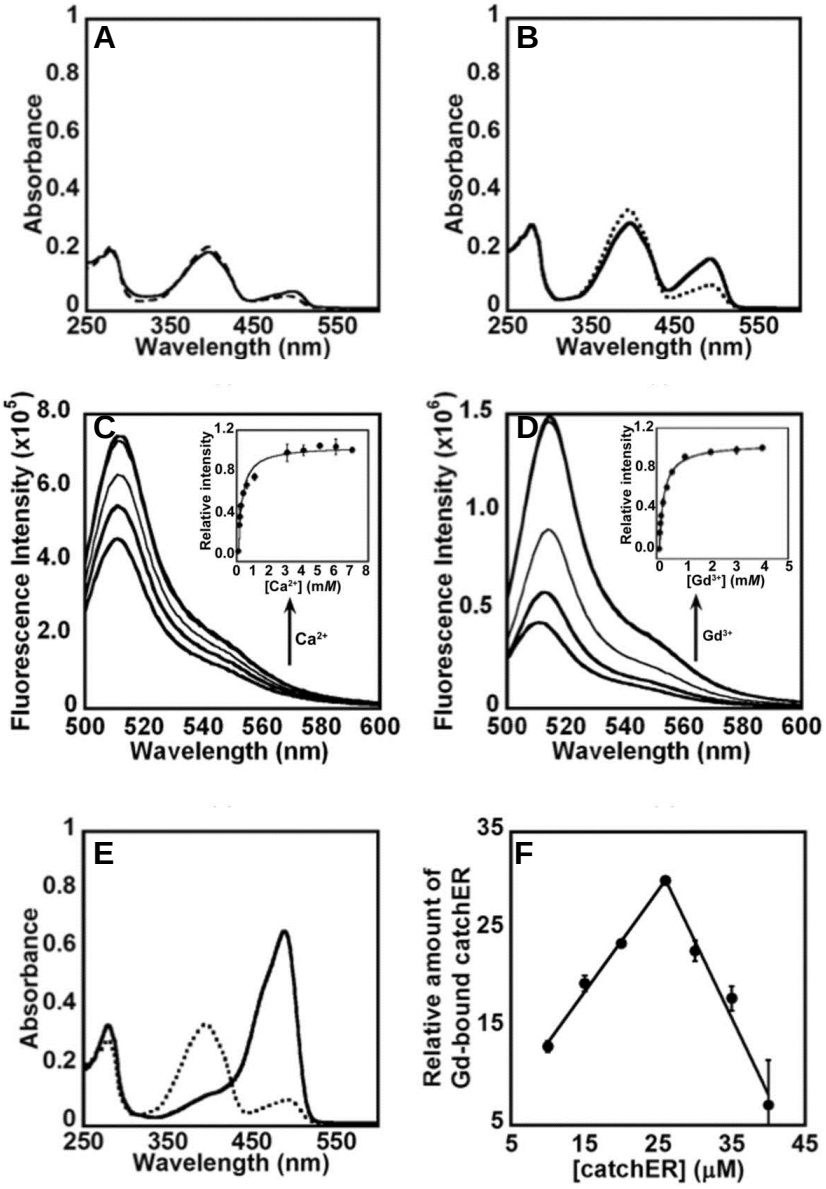

Figure 3.2.3 Absorbance spectra of CatchER and metal binding analysis via fluorescence spectroscopy

A) Absorbance response of CatchER to 5 mM Ca^{2+}: 20 μM CatchER with 5 mM EGTA (dashed line) in 10 mM Tris pH 7.4 and the same CatchER sample with 5 mM Ca^{2+} added (solid line). Addition of Ca^{2+} produces more of the anionic chromophore (increase in the 488 nm absorbance peak) and less of the neutral chromophore (decrease in the 395 nm absorbance peak). B) Absorbance response of CatchER to 200 μM Gd^{3+}. A 20 μM sample of CatchER was prepared in 20 mM PIPES pH 6.8. The dashed line represents the sample with 5 mM EGTA and the solid line is the same sample with 200 μM Gd^{3+} added. C) and D) Fluorescence response of CatchER to Ca^{2+} and Gd^{3+} excited at 488 nm with emission at 510 nm with inset binding curves. The normalized fluorescence response for Ca^{2+} and Gd^{3+} was fitted with a 1:1 binding equation,

producing K_d values of 227.0 ± 3.3 and 177.0 ± 13.6 µM for Ca^{2+} and Gd^{3+}, respectively. E) Overlay of the absorbance spectrum of 20 µM CatchER with 5 mM EGTA (dashed line) and 20 mM EGFP (solid line) in 10 mM Tris pH 7.4. F) Binding stoichiometry of CatchER to Gd^{3+} via a Job plot. The relative amount of CatchER bound to Gd^{3+} was determined using fluorescence and absorbance intensity changes in the absence and presence of Gd^{3+}. The concentrations of CatchER were 40, 35, 30, 25, 20, 15 and 10 µM (the actual concentrations determined via the 280 nm absorbance peak were 38, 35, 30, 24, 20, 15 and 10.5 µM). The total molar ratio was held constant at 50 mM. The plot represents fluorescence data of complex formation from 395 nm excitation. Figure taken from Zhang, et al., *Acta Cryst*., 2013.

Table 3.2.1 Relative amounts of CatchER-Gd^{3+} complex formation with corresponding ratios

[CatchER] (µM)	[Gd^{3+}] (µM)	[Gd-CatchER] (µM) Abs 493 nm	[Gd-CatchER] (µM) Fluo 395 nm	[Gd-CatchER] (µM) Fluo 488 nm	[CatchER]/[Gd^{3+}] Ratio
40	10	11.1± 2.3	6.7 ± 4.4	6.5 ± 3.7	4.0
35	15	18.0 ± 1.4	17.5 ± 1.2	16.4 ± 1.0	2.3
30	20	23.0 ± 0.3	22.8 ± 1.0	20.5 ± 0.7	1.5
25	25	30.8 ± 3.5	32.7 ± 0.5	20.0 ± 1.7	1.0
20	30	15.7 ± 2.2	23.6 ± 0.0	14.4 ± 0.5	0.6
15	35	10.4 ± 0.3	19.5 ± 0.8	11.4 ± 0.5	0.4
10	40	7.2 ± 0.0	13.7 ± 0.6	7.8 ± 0.3	0.2

*[Gd-CatchER] – concentration of complex formed when Gd^{3+} binds to CatchER. Abs 493 – absorbance wavelength used to calculate complex formation; Fluo 395 and 488 - fluorescence was monitored at 510 nm and 395 nm and 488 nm were the excitation wavelengths used to calculate complex formation. Data was collected at room temperature. CatchER samples prepared in 20 mM PIPES pH 6.8 with 10 µM EGTA. Data for 1:1 binding is highlighted in red. Table taken from Zhang, et al., *Acta Cryst*., 2013.

3.2.3 Crystallographic analysis of CatchER structures

To find the best crystal growth conditions that would yield well-formed crystals for X-ray analysis and structure determination, a literature review for the crystal growth conditions of different fluorescent proteins and sensors was done and summarized in Table 3.2.2. The protein concentration, protein buffer, crystallization method, temperature, precipitant concentration, salt concentration, crystal buffer concentration,

additives used, structure resolution, and length of time required for crystals to grow were charted for each of the proteins listed in Table 3.2.2. Crystallization was perfomed as outlined in Chapter 2 section 2.9. Crystal structures of CatchER in the apo form, Ca^{2+} form and Gd^{3+} loaded form were determined to identify and analyze the Ca^{2+} binding site in the designed sensor. The crystallographic data collection and refinement statistics are summarized in Table 3.2.3. and the data statistics versus resolution for each CatchER are listed in Table A.1 located in Appendix A. The crystal structures of CatchER(apo), CatchER-Ca^{2+}, and CatchER-Gd^{3+} were refined to R factors of 19.6%, 15.8% and 19.6% at resolutions of 1.55, 1.20 and 1.78 Å, respectively. These three structures are in different space groups: CatchER(apo) structure is in space group *C*2, CatchER-Ca^{2+} in $P2_12_12_1$ and CatchER-Gd^{3+} in $C222_1$. Structure validation are performed and shown in the Ramachandran plots (Appendix A, Figure A.2A-C). Figure 3.2.4A and B shows pictures of the Ca^{2+} free and Ca^{2+} loaded crystals. The *p*-hydroxylbenzylideneimidazolidinone chromophore (CRO66) is clearly visible in the electron density for all structures, as shown in Figure 3.2.4C for CatchER-Ca^{2+}. The three crystal structures have very similar backbone conformations, as demonstrated by the low r.m.s.d. values of 0.09–0.20 A ° for each pair of structures. Slightly more variation is seen relative to the EGFP structure (PDB entry 4eul), with r.m.s.d. values of 0.39–0.41Å.

Because of the high resolution of the diffraction data, the solvent was fitted with 167 water molecules for CatchER(apo), 197 water molecules for CatchER-Ca^{2+} and 138 water molecules for CatchER-Gd^{3+}. One acetate molecule was refined with an

occupancy of 1.0 in CatchER(apo), two Ca^{2+} ions with relative occupancy of 0.5 each in CatchER-Ca^{2+} and two Gd^{3+} ions with relative occupancies of 0.7 and 0.3 in CatchER-Gd^{3+}. These molecules were identified by the shape and peak height in the electron-density maps, B factors and potential interactions with other molecules, as described in the next section. The occupancies were calculated with SHELX for CatchER-Ca^{2+} and were estimated with REFMAC5 for the other structures.

Alternative conformations were modeled for a total of 19, 23 and 13 residues in the CatchER(apo), CatchER-Ca^{2+} and CatchER-Gd^{3+} structures, respectively. The surface loop of residues 155–159 shows two alternative conformations with about 0.5/0.5 relative occupancy in all three structures (Appendix A, Fig. A.3), while most other reported structures have a single conformation of these residues. This disordered loop is located on the opposite side of the protein to the designed metal-binding site. Notably, Glu222 consistently shows two alternate conformations in the CatchER-Ca^{2+} and CatchER-Gd^{3+} structures (Fig. 3.2.4D) and a single conformation in CatchER(apo). Among the five designed mutations located on three neighboring β-strands, the side chain of Glu225 has two alternate conformations in CatchER(apo) and CatchER-Ca^{2+} that interact with the two alternative conformations of the Arg73 side chain. Owing to the surface location of the five mutated residues and the potential for radiation damage to the carboxylate side chains, Glu204, Glu223 and Glu225 showed relatively poor electron density in the different CatchER complexes.

Table 3.2.2 Summary of crystal growth conditions for select fluorescent proteins and Ca^{2+} sensors

	EGFP[153]	BFP[172]	[a]Y66L 237	[b]GCaMP2[194]	DsRed 238	[c]dsFP483[239]	mCherry 160	mOrange 160	mStrawberry 160	mPlum 240	[d]Dronpa 241
[Protein] mg/mL	NA	12 mg/mL	15 mg/mL	10-30 mg/mL	15 mg/mL	NA	NA	NA	NA	25 mg/mL	23 mg/mL
Protein buffer	20 mM HEPES pH 7.5	10 mM HEPES pH 7	20 mM HEPES pH 7.9, 300 mM NaCl	100 mM NaCl, 25 mM HEPES pH 7.4	20 mM Tris pH 7.4, 300 mM NaCl, 2 mM B-mercaptoe thanol	50 mM HEPES pH 7.9, 300 mM NaCl, 1 mM EDTA	50 mM HEPES pH 7.9	50 mM HEPES pH 7.9	NA	50 mM HEPES pH 7.9	20 mM Tris-HCl pH 7.5, 120 mM NaCl
Crystallization method	hanging drop	hanging drop	hanging drop	hanging drop	hanging drop	NA	hanging drop	hanging drop	hanging drop	hanging drop	sitting drop
Temperature	25° C	4° C	4° C	20° C	NA	4° C	NA	NA	NA	NA	22°C
[Precipitant]	22-26% PEG 4000	10-12% PEG 3400	15-20% PEG 8000	20 % PEG 8000	16% PEG 1550	16% PEG 4000	30%PEG 4000	28% PEG 1550	NA	30% PEG 3400	22% PEG 3350
[Salt] (mM)	50 mM $MgCl_2$	NA	200 mM CaOAc	1.6 M $(NH_4)_2SO_4$ 1 mM $CaCl_2$	NA	300 mM NaCl, 200 mM CaOAc	100 mM NaOAc	200 mM $MgCl_2$	1.1 M Citrate	200 mM NaCl	140 mM Mg $(NO_3)_2$
[Crystal buffer], pH	50 mM HEPES pH 8-8.5	100 mM NaOAc pH 4.5, 4.6	100 mM Cacodylic acid pH 6.5	100 mM HEPES pH 7.5	100 mM Tris pH 7.4	100 mM HEPES pH 7.9	100 mM Tris pH 8.5	100 mM Tris pH 8.2	75 mM Glycine pH 10.5	100 mM Tris pH 8.5	NA
Additive	10 mM B-mercaptoe thanol	NA	NA	NA	1 µL B-mercapto/ well	NA	NA	NA	NA	NA	NA
Resolution	NA	2.1 Å	1.5 Å	2.0 Å	2.0 Å	2.1 Å	1.36 Å	1.08 Å	1.6 Å	1.34 Å	1.8 Å
Time	5 days	2-6 days	3-5 days	NA	1-2 weeks	NA	overnight	1 week	1-2 months	1 week	2 days

References provided for each protein. [a]Variant of GFP. [b]GFP and CaM-based Ca^{2+} probe. [c]Cyan fluorescent protein from *Discosoma striata*. [d]Reversibly switchable fluorescent protein isolated from the coral *Pectiniidae*. NA –data not available.

Table 3.2.3 Statistical analysis of CatchER crystal structures

Complex Name	CatchER (apo)	CatchER-Ca^{2+}	CatchER-Gd^{3+}
X-ray source	APS_22ID	APS_22ID	APS_22BM
Wavelength (Å)	0.8	0.8	1.0
Temperature (K)	100	100	100
Space group	C2	$P2_12_12_1$	$C222_1$
a (Å)	61.16	54.24	61.06
b (Å)	88.79	61.06	88.33
c (Å)	118.54	67.40	118.17
β (°)	90.31	90.00	90.00
Unique reflections	89,647	70,349	30,260
R_{merge} (%) overall‡	9.6% (27.0%)	8.1% (39.2%)	8.5% (18.5%)
<I/б> overall‡	6.9 (4.2)	19.9 (6.1)	14.2 (8.7)
Resolution range (Å)	30.99 – 1.55	10 – 1.20	27.13 – 1.78
Completeness (%) overall[a]	98.6% (96.9%)	99.2% (100%)	98.3% (93.8%)
R_{work}	0.182	0.148	0.202
R_{free}	0.207	0.182	0.226
No. of solvent atoms (total occupancies)	340 (293.2)	288 (229)	141 (136.5)
RMS deviation from ideality			
Bonds (Å)	0.008	0.014	0.012
Angle distance	1.384[a]	0.031[b] (Å)	1.565[a]
Average B-factors ($Å^2$)			
Main chain atoms	20.11	16.19	20.40
Side chain atoms	24.40	21.05	21.86
Solvent	27.46	27.75	27.86
Occupancy of metal ion	-	0.5/0.5	0.7/0.3

‡Values in parentheses are for the highest resolution shell. Total occupancies are the sum of calculated occupancies of all the atoms or ions. [a]The angle r.m.s.d. in REFMAC5.2 is indicated by angle in degrees. [b]The angle r.m.s.d. in SHELX-97 is indicated by distance in Å. Table taken from Zhang, et al., *Acta Cryst*., 2013.

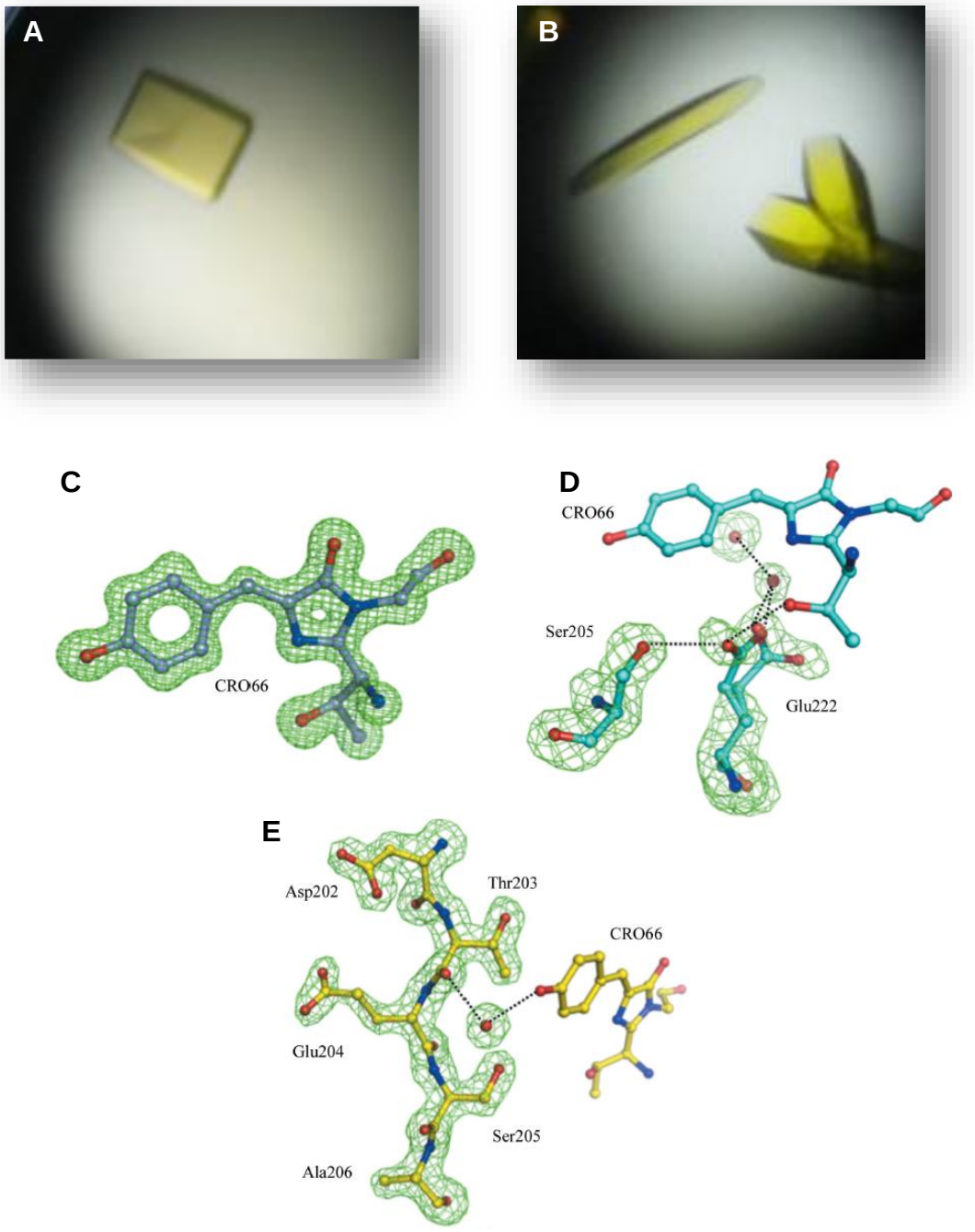

Figure 3.2.4 CatchER crystals and structural analysis of the chromophore

Crystals of Ca^{2+} free (A) and Ca^{2+} loaded CatchER (B). Gadolinium loaded crystals of CatchER were obtained through soaking the crystals in the crystal growth solution containing 2 mM of $GdCl_3$. C) Electron density map of the chromophore from CatchER-Ca^{2+}. D) Electron density maps showing two conformations of Glu222 from CatchER-

Gd^{3+} and two water molecules. E) Electron density map showing residues Asp202–Ala206 of CatchER (apo) and one water molecule with chromophore (CRO66). The dotted lines represent hydrogen-bond interactions. Taken from Zhang, et al., *Acta Cryst*., 2013.

3.2.4 Identification of metal ions in the designed binding site of CatchER

CatchER was designed with five mutated residues, S147E, S202D, Q204E, F223E and T225E, compared with EGFP. The mutations are located on three β-strands, pointing out of the protein β-barrel to form a penta-carboxylate ionic environment suitable for binding Ca^{2+} (Fig. 3.1.1). In CatchER(apo), one of the carboxyl O atoms of Glu147 forms close interactions with the carboxylate of Asp202, suggesting possible protonation of the carboxylates (Fig. 3.2.5A). Protonated carboxylates have been reported in other protein crystal structures[242]. The Glu147 and Asp202 carboxylates are further apart with no direct interaction in the CatchER structures with Ca^{2+} and Gd^{3+}, and additional solvent peaks were observed in this region of the electron-density maps.

The identification of Ca^{2+} in the designed binding site of CatchER was not trivial partly because of the fast off-rate related to its weak Ca^{2+}-binding affinity. Crystals of CatchER were grown in high concentrations of 50 mM Ca^{2+} to ensure saturation of the CatchER molecules; however, the non-protein peaks in the electron-density maps near the mutated residues were indistinguishable from those assigned to water elsewhere (Fig. 3.2.5B). Therefore, the presence of Ca^{2+} was deduced from the interactions with nearby protein residues and water molecules. Two possible locations for Ca^{2+} were identified, mostly by the presence of shorter distances of 1.8–2.5 Å to interacting O atoms of Glu147 and water molecules and further interactions with Asp202 and other water molecules in the designed site (Fig. 3.2.5B; Table 3.2.4). These interatomic

distances are within the range observed in high resolution crystal structures of proteins[243]. The two locations were fitted with Ca^{2+} ions refined at partial occupancy

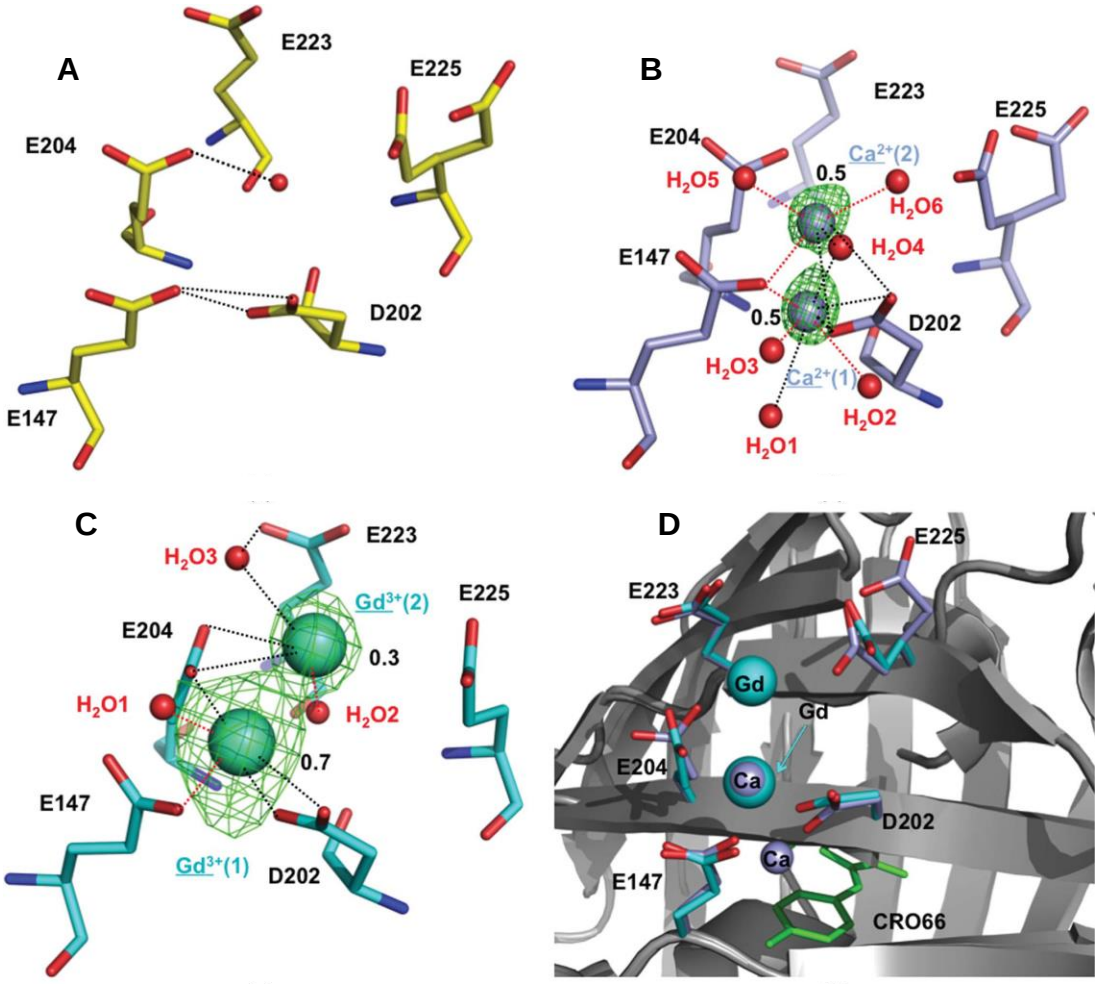

Figure 3.2.5 The hydrogen bond interactions around the designed binding site in CatchER crystal structures

(A-C) The protein is represented as yellow, light blue and cyan sticks in CatchER(apo), CatchER-Ca^{2+} and CatchERGd^{3+}, respectively. Ca^{2+}, Gd^{3+} and water molecules are represented as spheres. The numbers (0.5/0.5, 0.7/0.3) give the relative occupancy of the alternate positions of the Ca^{2+} and Gd^{3+} ions, respectively. The interatomic (non-H) distance range of 2.6–3.2 Å was used for hydrogen bonds (black dotted lines). Shorter distances in the range 2.0–2.4 Å (red dotted lines) suggest coordination to a metal ion. The coordinating waters are numbered as in Table 3.2.4. D) Superposition of CatchER-Ca^{2+} and CatchER-Gd^{3+}; the protein backbones are shown as gray cartoons and the chromophore (CRO66) is represented as green sticks. The five mutated residues and ions are shown in sticks and spheres in light blue for CatchER-Ca^{2+} and cyan for

CatchER-Gd^{3+}. The cyan arrow points to the major site for Gd^{3+}. Taken from Zhang, et al., *Acta Cryst*., 2013.

Table 3.2.4 CatchER-metal interactions within the proposed coordination site

A) Ca^{2+}

		Distance (Å)	
CatchER atom	**B factor (Å²)/occupancy**	**Ca^{2+}(1)**	**Ca^{2+}(2)**
Glu147 OE2	30.76/1.0	1.9	2.1
Asp202 OD1	18.84/1.0	3.0	3.2
Asp202 OD2	27.29/1.0	2.6	2.8
H_2O1	35.36/1.0	3.1	---
H_2O2	31.95/1.0	2.5	---
H_2O3	25.38/1.0	1.8	---
H_2O4	44.32/0.5	2.5	3.0
H_2O5	25.02/1.0	---	2.1
H_2O6	42.44/1.0	---	2.7

B) Gd^{3+}

		Distance (Å)	
CatchER atom	**B factor (Å²)/occupancy**	**Gd^{3+}(1)**	**Gd^{3+}(2)**
Glu147 OE2	30.51/1.0	2.2	---
Asp202 OD1	22.52/1.0	2.6	---
Asp202 OD2	30.51/1.0	2.5	---
Glu204 OE1	32.69/1.0	2.6	3.1
Glu204 OE2	29.53/1.0	---	3.1
H_2O1	33.89/1.0	2.1	---
H_2O2	24.74/1.0	---	2.3
H_2O3	33.62/1.0	---	2.9

Tables taken from Zhang, et al., *Acta Cryst*., 2013.

(0.5/0.5). However, this deduction for Ca^{2+} cannot exclude the possible binding of Na^+ or water molecules from the crystallization solution. No significant electron density was present in the apo structure at the positions assigned to Ca^{2+} near Glu147 and Asp202.

In order to pinpoint the metal binding site more definitively, the structure of CatchER-Gd^{3+} was obtained from apo crystals soaked in high concentrations of $GdCl_3$.

Ca^{2+} has 18 electrons orbiting the nucleus, while Gd^{3+} has 61 orbital electrons. Therefore, it is easier to locate Gd^{3+} with increased diffraction over Ca^{2+} since the X-ray atomic scattering factor increases with atomic number. The major 0.7 occupancy Gd^{3+} ion was identified unambiguously from the very high peak at 22б in the electron density indicative of a heavy-metal ion (Fig. 3.2.5C). This Gd^{3+} ion is located between the side chains of Glu147, Asp202 and Glu204, forming four ionic interactions with these three residues at distances of 2.2, 2.5, 2.6 and 2.6 Å and one with a nearby water molecule at 2.1 Å (Fig. 3.2.5C and Table 3.2.4). The second Gd^{3+} ion with 0.3 occupancy was deduced from positive difference density observed in (Fo - Fc) maps when a water molecule or a partial occupancy Na^{+} ion was refined at this site. Overall, the Gd^{3+} ions coordinate with the side chains of residues Glu147, Asp202 and Glu204 of the designed Ca^{2+}-binding site as well as the water molecules.

Superposition of the CatchER-Ca^{2+} and CatchER-Gd^{3+} structures revealed that the major occupancy site for the Gd^{3+} ion is identical to one of the sites deduced for the Ca^{2+} ion (Fig. 3.2.5D). This Ca^{2+} ion coordinates with the side chains of Glu147 and Asp202 and three water molecules. No Gd^{3+} ion was visible at the other site, where the Ca^{2+} ion coordinates with the carboxylate side chains of Glu147 and Asp202 and four water molecules (Fig. 3.2.5B). It is possible that the presence of the high-occupancy Gd^{3+} ion at the adjacent site precludes binding to the inner site occupied by a Ca^{2+} ion in the CatchER-Ca^{2+} structure.

The extended binding site formed by the carboxylate side chains of the mutated residues Glu147, Asp202, Glu204, Glu223 and Glu225 traps metal ions at three possible positions, as shown by superposition of CatchER-Ca^{2+} and CatchER-Gd^{3+} (Fig.

3.2.5D). The metal ions mainly interact with side chains of Glu147, Asp202 and Glu204. No direct interactions of designed metal-ligand residues Glu223 and Glu225 with the metal ions are visible and their side chains are not well defined in the electron-density maps, possibly owing to radiation damage. Nevertheless, both Ca^{2+} and Gd^{3+} ions are well situated at the designed Ca^{2+}-binding site in CatchER, which suggests that these X-ray structures provide snapshots of steps in the likely dynamic metal-binding process.

3.2.5 Structural changes around the chromophore

The chromophore interactions were compared in the CatchER structures, EGFP (PDB entry 4eul)[170] and GFP (PDB entry 1emb)[244]. The chromophore is buried centrally in the protein molecule and is well protected from solvent. It can exist as neutral and anionic forms, which are responsible for the absorbance at 395 and 475 nm, respectively[154] (Fig. 3.2.6). The spectroscopic characterization of CatchER and its response to Ca^{2+} shows two absorption maxima with a major peak at 398 nm and a smaller peak at 490 nm; it thus resembles GFP with two similar excitation wavelengths,

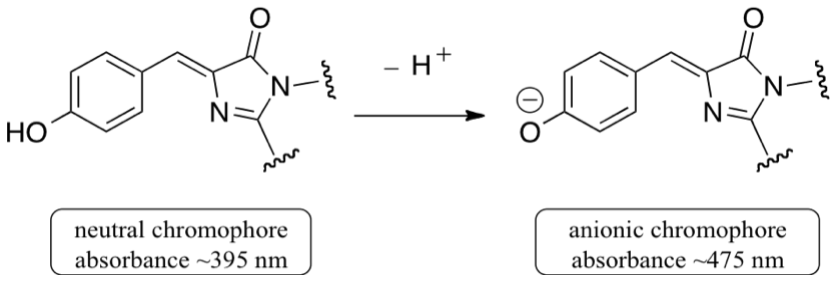

Figure 3.2.6 Protonation states of the GFP chromophore with the corresponding absorbance wavelengths

Taken from Zhang, et al., *Acta Cryst*., 2013.

unlike EGFP with one single excitation peak at 488 nm[162] (Fig. 3.2.3E). Comparisons of the chromophore environment in the three CatchER structures and the currently solved EGFP and GFP structures have shed light on the relationship between the spectroscopic properties and the structures. The intricate hydrogen-bond networks around the chromophores of CatchER(apo), CatchER-Ca^{2+} or CatchER-Gd^{3+}, EGFP[170] and GFP[244] are shown in Figs. 3.2.7A-D. Most hydrogen-bond interactions are conserved in the vicinity of the carbonyl group of the imidazolidinone ring of the chromophore[170,244,153]. Two residues, Thr203 and Glu222, show a critical role in the chemical environment of the chromophore. Thr203 has been observed with two different conformations: in one the side chain of Thr203 can make direct contact with the tyrosyl group of the chromophore, while in the other the side chain of Thr203 rotates away from the tyrosyl group and the main chain moves towards the chromophore, resulting in the elimination of direct hydrogen-bond interactions but permitting a water-mediated interaction between the main-chain carbonyl group and the chromophore tyrosyl group. In addition, the side chain of Glu222 has shown two alternate conformations in some EGFP structures[170, 245].

In our structural analysis and comparisons, CatchER-Ca^{2+} and CatchER-Gd^{3+} have similar interactions around the chromophore, as shown schematically in Fig. 3.2.7B, while CatchER(apo) has different interactions for Glu222 (Fig. 3.2.7A). In all three of the CatchER structures Thr203 formed a water-mediated hydrogen bond with the chromophore tyrosyl via the second type of conformation mentioned above. The representative OMIT map of Asp202–Asp206 adjacent to CRO66 and the mediating water for a hydrogen bond in CatchER(apo) is shown in Fig. 3.2.4E. This type of

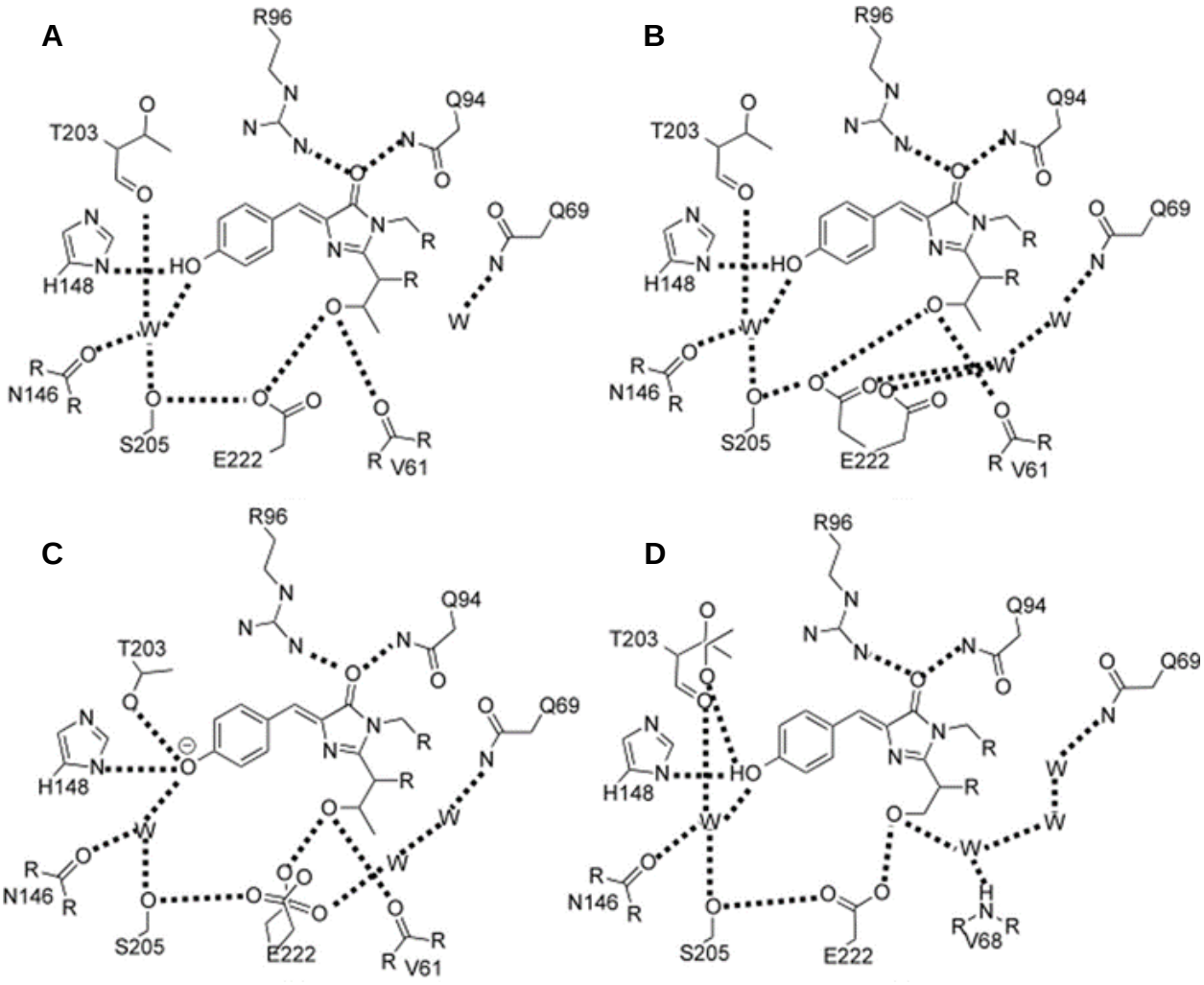

Figure 3.2.7 Scheme of the hydrogen bond interactions between the chromophore and surrounding residues and water molecules (W) in CatchER(apo) (A), CatchER-Ca^{2+} or Gd^{3+} (B), EGFP (C), and GFP (D).

Hydrogen bonds are shown as dashed lines. The interatomic (non-H) distance range of 2.6–3.2 A ° was used for hydrogen bonds. Taken from Zhang, et al., *Acta Cryst*., 2013.

interaction between the carbonyl group of Thr203 and chromophore was also found in the GFP structure (PDB entry 1emb; Fig. 3.2.7D), even though it also has an alternate side-chain conformation with 0.15 occupancy which can form direct hydrogen bonding to the chromophore[244]. In contrast, in the EGFP structure (PDB entry 4eul) Thr203 only forms the first type of interaction (Fig. 3.2.7C). Regarding the side chain of Glu222, the

conformational population differs in the three CatchER structures: only one conformation of Glu222 was observed in CatchER(apo) and its side chain is considered to be deprotonated and forms a hydrogen bond to Ser205 and another to the hydroxyl group of the chromophore (Fig. 3.2.7A); in CatchER-Ca^{2+} and CatchER-Gd^{3+} one additional alternative conformation of Glu222 was determined which lacks interactions with the chromophore; instead, it participates in interactions with a network of water molecules linking to Gln69 (Fig. 3.2.7B). Recent crystallographic study of EGFP has revealed two alternate conformations for Glu222 not only in the EGFP structure (PDB entry 4eul) used here for comparison but in another reported structure (PDB entry 2y0g)[245]. In both published structures Glu222 shows similar interactions with the chromophore and the surrounding environment as in Fig. 3.2.7C, which is quite similar to the arrangement in CatchER-Ca^{2+} and CatchER-Gd^{3+}. However, in the GFP structure (PDB entry 1emb), one conformation of Gly222 was defined that forms hydrogen-bond interactions as in CatchER(apo).

Previously, profound but opposite effects of residues Thr203 and Glu222 were reported from mutagenesis and analysis of crystal structures[152,246,244]. Introduction of a T203I mutation in GFP retains the 395 nm peak but eliminates the 475 nm peak, whereas GFP with an E222G mutation retains the 475 nm peak but lacks the 395 nm peak[152,246]. The crystal structures of GFP and EGFP revealed that the side chain of Thr203 can stabilize a negative charge on the chromophore (anionic form chromophore) as a hydrogen bond donor through a direct hydrogen bond to the chromophore tyrosyl residue, but the carboxylate of charged Glu222 can maintain the neutral form of the chromophore through electrostatic repulsion and the hydrogen-bonding network via

water and Ser205[244]. In the CatchER structures the conformation of Thr203 preferred the proposed protonated form of the chromophore. The hydrogen-bond network via water and Ser205 is achieved by one conformation of Glu222 in deprotonated or negatively charged states and helps to maintain the neutral form of the chromophore. In CatchER-Ca^{2+} and CatchER-Gd^{3+}, even though the other conformation of Glu222 does not interact with the chromophore threonine as in EGFP[232,245,170], this alternate conformation with almost half occupancy is proposed to be protonated and can no longer maintain the neutral form of the chromophore. Therefore, although there is only one conformation of Glu222 in CatchER(apo), we suggest that the chromophore of CatchER has a mixture of neutral and negatively charged states, as observed in wild-type GFP, which has two conformations of Thr203[244]. The ratio of neutral and negatively charged chromophore can differ in the CatchER structures based on their spectroscopic properties. In the absorbance spectra, addition of Ca^{2+} results in a concurrent increased intensity around 490 nm (increase in deprotonated chromophore) and a decreased absorption intensity around 398 nm (decrease in the protonated chromophore state), exhibiting an optical spectral feature that more closely resembles that of EGFP, as shown in Fig.3.2.3E. Tang and coworkers also reported that the presence of Ca^{2+} results in a decrease in the pK_a value of the chromophore of CatchER[180], suggesting that the chromophore in CatchER is more deprotonated upon Ca^{2+} binding. This change could be related to the observed equilibrium shift in conformational populations of Glu222 in CatchER: the increase of deprotonated chromophore on Ca^{2+} binding is likely to be owing to the stabilizing capability of Glu222 as a hydrogen-bond donor with the hydrogen-bond acceptor of deprotonated Thr65 in

the chromophore (Fig. 3.2.7B). Such a stabilizing effect is manifested by the changes in the proton wire network between apo and Ca^{2+}-loaded forms of CatchER and EGFP, as shown in Figs. 3.2.7A–C. Thus, binding of Ca^{2+} induces an equilibrium shift in conformational populations of the Glu222 side chain and its network of interactions through two water molecules to Gln69. Overall, the crystal structures of CatchER have reinforced support for the proposed excited-state photon-transfer pathway for the photoisomerization of GFP which was based on structural and spectroscopic studies[247,244]. A similar observation and proposed interpretation apply to Gd^{3+}-induced change (Fig. 3.2.3B and Fig. 3.2.7B). No significant difference was observed for Leu42, Thr43, Tyr143 and Thr153 in the structural comparison of CatchER(apo) with CatchER-Ca^{2+}, despite the chemical shift changes related to Ca^{2+} binding[235] shown in dynamic NMR. The addition of Ca^{2+} leads to the gradual splitting of one resonance into two for Gln69, which is buried inside the protein[180]. In both CatchER-Ca^{2+} and CatchER-Gd^{3+}, Gln69 forms a hydrogen-bond network through two water molecules with Glu222 and this network was also found in EGFP (PDB entry 4eul; Fig. 3.2.7B). However, this network was interrupted owing to a missing water molecule in CatchER(apo) (Fig. 3.2.7A). Therefore, we propose here that the Ca^{2+}-induced change in optical properties could also be associated with the Gln69 hydrogen-bond network.

3.2.6 Relationship between mutations of the novel metal-binding site and optical properties

CatchER was selected from a series of Ca^{2+} sensors designed by introducing different mutations around the desired Ca^{2+}-binding site, designated D8, D9, D10, D11 (CatchER) and D12[235]. These mutants all show an increase in the peak at 398 nm and

a decrease at 490 nm to different extents. D8 contains only two mutations, S202D and F223E, while the other variants have additional mutations, which indicated that the S202D and/or F223E mutations might play an important role in the conserved absorbance changes for the designed proteins. Based on the structural changes around the chromophore, Thr203 and Glu222 are two key residues that account for the altered chemical environment of the chromophore. The effects of these two residues might be modified by mutations of adjacent residues: S202D and F223E. However, the F223E mutation makes no direct interaction with Ca^{2+} in CatchER-Ca^{2+}, although it forms a water-mediated hydrogen bond with one Gd^{3+} in the CatchER-Gd^{3+} structure. Instead, the S147E mutation appears to function as the anion for interacting with metal cations, while the S202D mutation is also involved in metal coordination based on our crystal structures. The main chain of residues 202–206 has shifted by 0.7–0.9 Å in association with the rotation of Thr203 in CatchER relative to EGFP, which leads to the ionization change of the chromophore (Fig. 3.2.8).

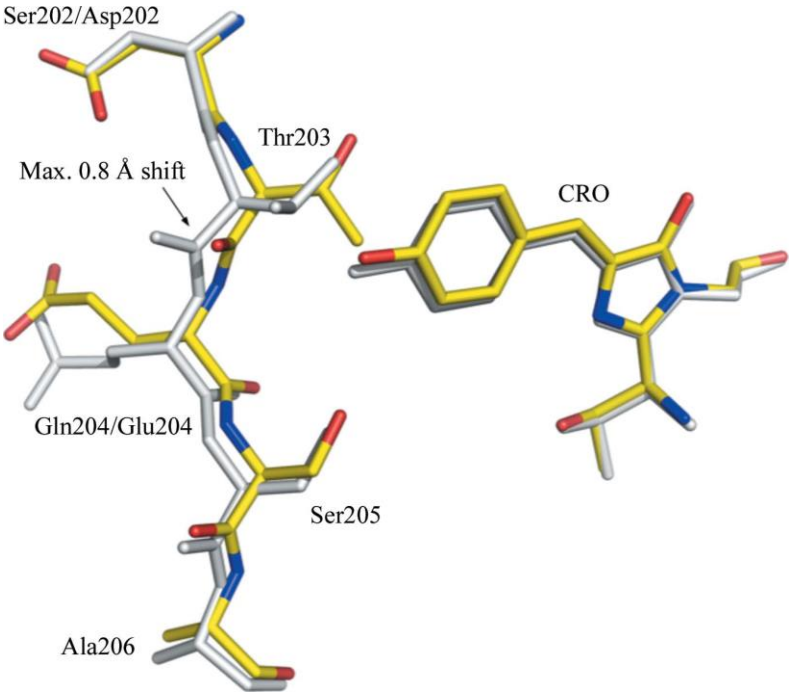

Figure 3.2.8 Comparison of EGFP and CatchER(apo) at the chromophore and nearby residues

Residues 202–206 of EGFP and CatchER(apo) are shown as sticks in gray and yellow, respectively. Ser202/Asp202 and Gln204/Glu204 label mutated residues in EGFP/CatchER(apo). The main chain from residues 202–206 shifts with a maximum value of 0.8 Å as indicated by the arrow. Taken from Zhang, et al., *Acta Cryst*., 2013.

3.3 Conclusion

The binding of the metal ions Ca^{2+} and Gd^{3+} to the designed Ca^{2+} sensor CatchER has been investigated by spectroscopic methods and X-ray crystallography. Both the kinetic assays and the structures demonstrated the binding of the two types of metal ions to CatchER; however, there were unexpected differences. The crystal structures of CatchER in the apo form and in its complexes with Ca^{2+} and Gd^{3+} reveal snapshots of the dynamic binding of metal ions to the designed site comprising five carboxylate side chains. Both Ca^{2+} and Gd^{3+} ions were observed in two locations within the designed binding site. The high (millimolar) concentrations of Ca^{2+} and Gd^{3+} used to

obtain the crystal structures of their CatchER complexes resulted in two alternative binding sites for each metal ion with one central common binding site. In solution, however, these two metal ions bind CatchER with a 1:1 stoichiometry and micromolar affinity. These structures suggest that the ability of Ca^{2+} ions to jump between two possible binding sites may be partly responsible for the fast kinetics of metal-ion binding to CatchER.

4 BIOPHYSICAL CHARACTERIZATION OF CATCHER VARIANTS

4.1 Introduction

As discussed in Chapter 1, calcium (Ca^{2+}) is an activator of many cellular processes such as cell proliferation, fertilization, embryonic pattern formation, apoptosis, and muscle contraction[5]. The activation of these biological events, occurring on different time scales, is due to the kinetic action of various receptors, channels, and CaBPs that shape each Ca^{2+} signaling event[5]. The endoplasmic reticulum (ER) and the sarcoplasmic reticulum (SR), its counterpart in muscle cells, are the major intracellular Ca^{2+} storage organelles and act as Ca^{2+} sinks that help to amplify the Ca^{2+} signal[21]. The ER/SR is an integral part in Ca^{2+} signaling with dual roles as a transmitter and receiver of signals[84]. The ryanodine receptor and the inositol 1,4,5-triphosphate receptor (IP_3R) are Ca^{2+} release receptors located on the membranes of the SR and ER, respectively, that are activated by Ca^{2+} [22]. Analyzing and quantifying the changes involved in Ca^{2+} stimulated events has been and remains a challenge. Because the ER/SR is the major subcellular Ca^{2+} containing compartment with a central function in the propagation of the Ca^{2+} signal, much work has been focused on understanding ER/SR Ca^{2+} signaling[84].

The creation of synthetic Ca^{2+} dyes helped to advance the field and practice of Ca^{2+} imaging. Although dyes, such as Mag-fura-2, have been widely used to measure compartmentalized Ca^{2+} in different cells,[138,248,141] they have limitations such as uneven dye loading, photobleaching, and the inability to be targeted to specific organelles. The discovery of GFP and the advancement of fluorescent protein-based Ca^{2+} probes has propelled the field of Ca^{2+} imaging forward[162]. Some of the current genetically-encoded

Ca^{2+} probes are FRET pairs involving YFP, CFP, calmodulin and the M13 binding peptide[177]. Others, such as GCaMP2, R-GECO, and troponin-based sensors are single fluorophore sensors involving Ca^{2+} binding proteins calmodulin and troponin c[249,250,251]. These chimera probes have been applied in various cell types thus far to monitor Ca^{2+} dynamics; however, these probes are faced with limited tuning of K_ds and cooperativity among the multiple Ca^{2+} binding sites found in their Ca^{2+} binding domains[130]. Single fluorophore sensors using EGFP have been designed with a Ca^{2+} binding site created from mutating residues on the surface of the beta barrel in a chromophore sensitive location or grafting in an EF-hand or EF-hand loop into a flexible region of EGFP[180,191]. Our highly touted sensor CatchER has a K_d of ~0.18 mM, a k_{on} rate resembling the diffusion limit, and a k_{off} of $700s^{-1}$ [180]. Single fluorophore sensors, such as CatchER, have been designed by mutating residues on the surface of EGFP to create the Ca^{2+} binding site with better tuning ability to accommodate high Ca^{2+} concentration environments with fast kinetics making the probes suitable for monitoring the rapid Ca^{2+} transients that occur in processes like muscle contraction[180,252].

Here we report the analysis of CatchER variants containing the N149E mutation in the binding site (Figure 4.1.1). Our hypothesis is that the N149E mutation will strengthen the affinity for Ca^{2+} with the additional negative charge acting as an additional coordination ligand. These variants, referred to as 149E, have a weaker affinity for Ca^{2+} compared to CatchER with a slightly lower quantum yield but higher extinction coefficient. We also analyze the biophysical properties of CatchER variants containing the S175G, S30R, and Y39N mutations that improve the brightness of the probes at 37°C. The purpose of the modifications is discussed in detail in Chapter 5.

Spectroscopic methods were used to elucidate the effect that the addition of these mutations had on the intrinsic properties of each variant. Select variants were also transfected into mammalian cells to monitor Ca^{2+} release from the ER/SR.

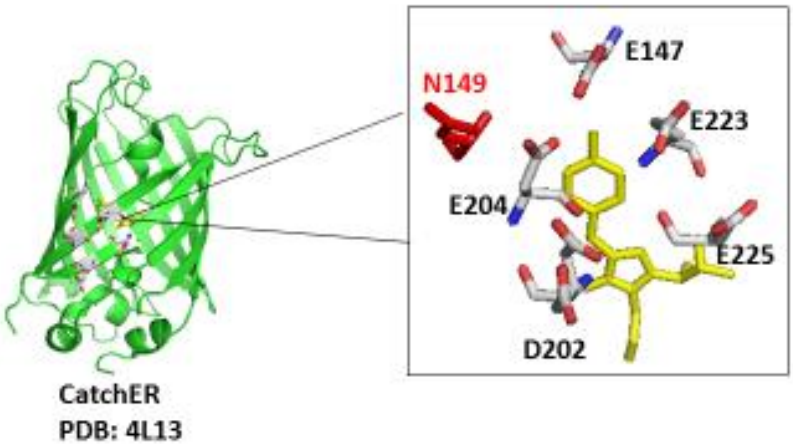

Figure 4.1.1 Location of N149 residue in the binding site of CatchER

The designed metal binding site of CatchER contains five negatively charged residues located a chromophore sensitive region of EGFP. Residue N149 was mutated to glutamate (E) to create a sensor with a different affinity for Ca^{2+}.

4.2 Results

4.2.1 Expression and purification of CatchER variants

The CatchER mutants were overexpressed and purified in preparation for biophysical studies to determine and quantify the effects of these mutations on their biophysical properties in response to Ca^{2+}. All of the sensor variants were expressed in BL21 (DE3) cells using the method outline in Chapter 2 section 2.4. The growth curves and SDS-PAGE gels for expression are shown in Figure 4.2.1. for the 149E variants.

The expression data for the CatchER-T variants is located in Chapter 5, Figure 5.2.2. The bacteria containing each of the mutants grew well. The SDS-PAGE gel confirms expression of each protein after induction with IPTG.

After expression, the cell pellets were collected and sonicated to yield a cell lysate containing the proteins of interest. Centrifugation of the cell lysate yielded the supernatant containing the protein of interest. The protein was separated and purified from the supernatant using affinity chromatography exploiting the strong association of the 6X Histidine tag, found on each protein, with Ni^{2+} immobilized on the 5 mL HiTrap chelating column. Figures 4.2.2A-H shows the chromatograms and SDS-PAGE gels for the HisTag and gel filtration purification of 149E CatchER variants. The protein was injected onto the column using Buffer A with a 5 mL/min flow rate. The protein eluted from the column using Buffer B (Buffer A with 500 mM imidazole) at the same flow rate. After HisTag purification, the protein samples were concentrated to 2 mL and injected onto a Superdex 75 100 mL column at 1 mL/min with 10 mM Tris pH 7.4 (Figures 4.2.2B, D, F, and H). The SDS gel of 149E' gel filtration was not run due to the low amount of protein obtained from the two purification steps.

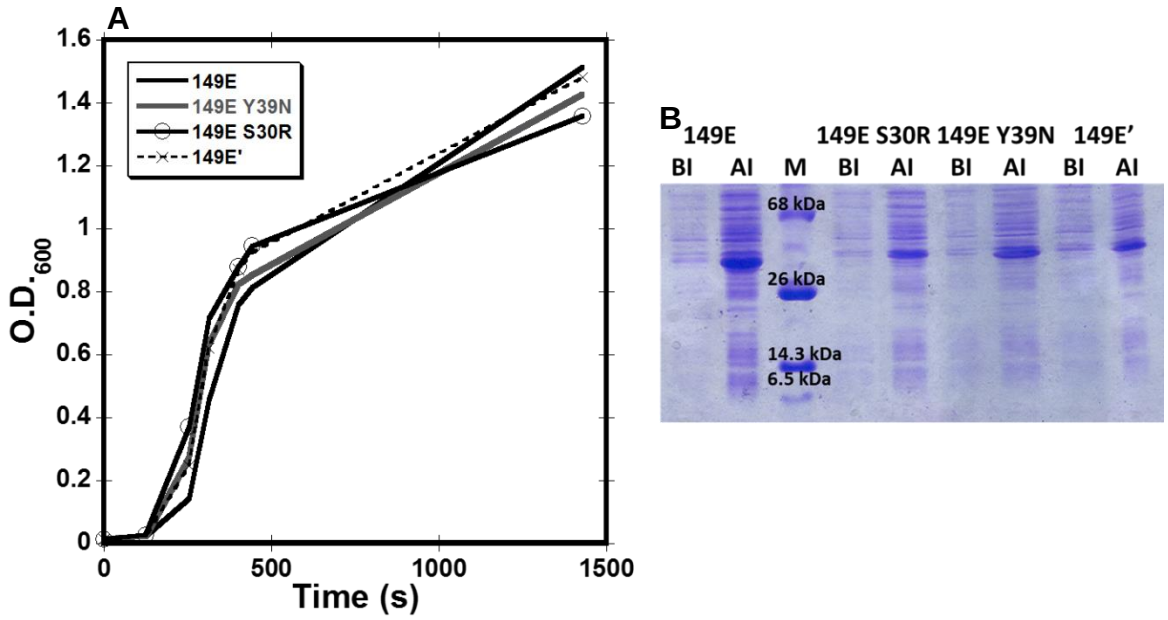

Figure 4.2.1 Expression of 149E variants in BL21(DE3) cells

The DNA for each of the plasmids in the pET28a bacterial expression vector was transformed into BL21 (DE3) cells. One colony from each of the four plates was taken to inoculate 10 mL of LB media. The pre-culture was added to 1 L of LB with 600 uL of kanamycin and allowed to grow in a shaker at 37°C until the O.D. reached 0.6 (A) when cells were induced with 200 µL of 1 M IPTG, reducing the temperature to 25°C. The bacteria grew well for each of the four mutants. B) Expression samples taken before induction (BI) and after induction (AI) were used to run the SDS-PAGE gel confirming the proteins were expressed. The marker is labeled as M.

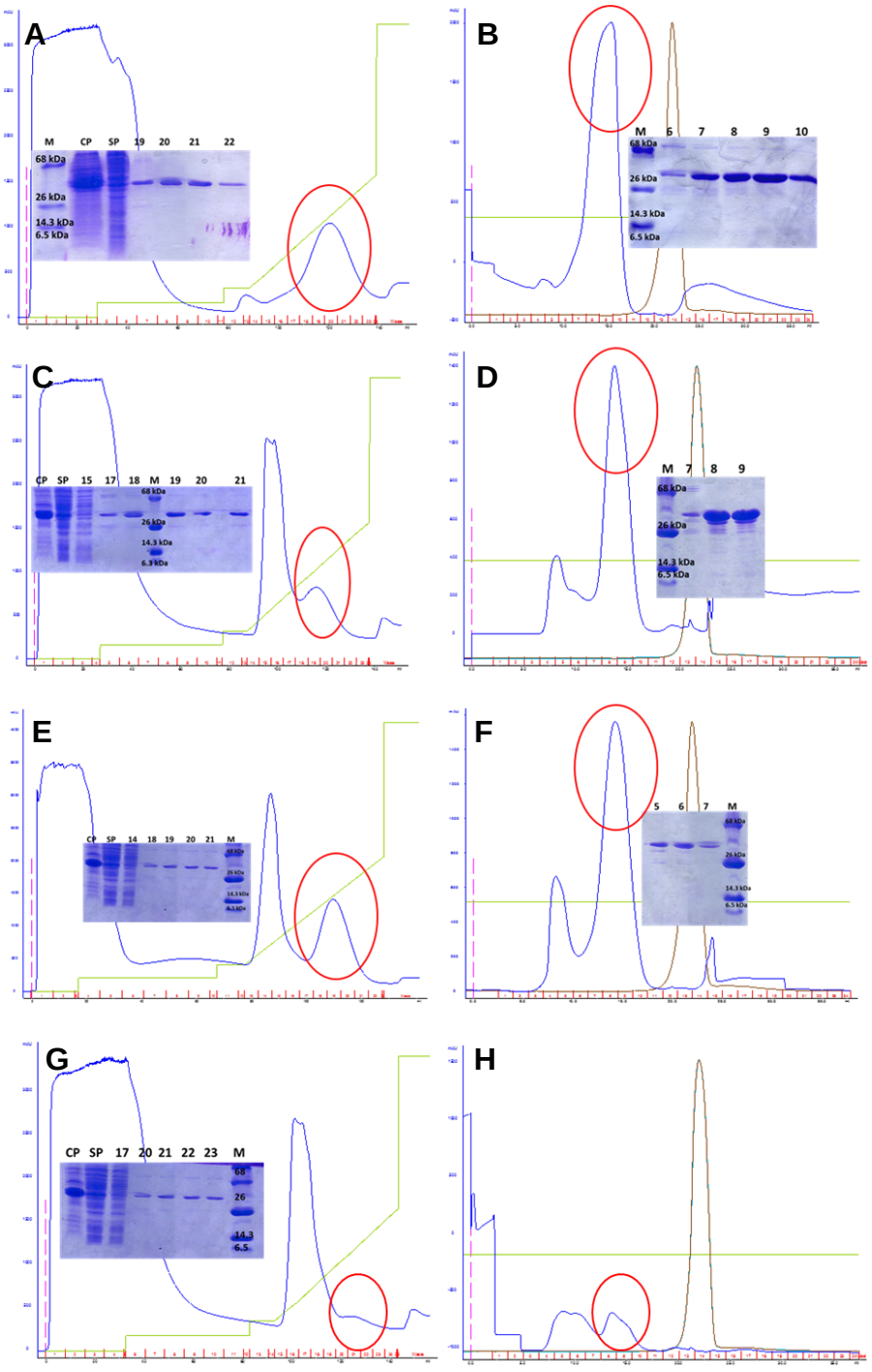

Figure 4.2.2 Purification of 149E CatchER variants

Representative purification data for 149E (A, HisTag; B, gel filtration), 149E S30R (C, HisTag; D, gel filtration), 149E Y39N (E, HisTag; F, gel filtration), and 149E' (G, HisTag; H gel filtration). The supernatant obtained from the sonicated BL21 (DE3) cells was syringe filtered and loaded onto a 5 mL HiTrap chelating column containing immobilized Ni^{2+} using Buffer A at a 5 mL/min flow rate. The protein was eluted at the same rate using Buffer B containing 500 mM imidazole. The first peak in the chromatograms is the

cell debris being washed away during loading. The peaks containing the sensor proteins are circled in red. Inset SDS gel analysis shows clear protein bands for the sensors near the 26 kDa marker. Purified CatchER-T variants were concentrated to 2 mL and loaded onto a Superdex 75 column using 10 mM Tris pH 7.4 at 1 mL/min. The protein was eluted out in 2 mL fractions, all of which were not depicted in the SDS gel. The resulting inset SDS-PAGE gels show pure protein. (G and H) 149E' does not have high expression, so the amount of protein shown in the chromatograms is low. An SDS gel was not done for the gel filtration fractions of 149E' due to the low yield.

4.2.2 Metal binding of CatchER variants via fluorescence spectroscopy

The first property that we need to know about our sensors is their affinity for Ca^{2+}. The K_d of CatchER variants was determined using fluorescence spectroscopy, outlined in Chapter 2 section 2.14, at both excitation wavelengths, 395 and 488 nm, with emission monitored from 410-600 and 500-600 nm, respectively, using 10 µM of protein in triplicate with 10 µM EGTA added to the samples to get the basal fluorescence (0 mM Ca^{2+}). The absorbance spectrum of each protein was collected before and after titration with Ca^{2+}. The absorbance spectrum for all the variants analyzed shows a decrease in the 395 nm excitation peak and an increase of the 488 nm excitation peak with saturating levels of Ca^{2+} compared to without Ca^{2+} (Figure 4.2.3). The inset binding curves fit a 1:1 binding equation (Equation 2.18) after the data was normalized using Equation 2.17. The Ca^{2+} K_ds, in the absence and presence of 150 mM KCl, of most of the variants and their dynamic ranges are listed in Table 4.2.1. Fluorescence titration spectra for 149E and 149E S30R in the presence of 150 mM KCl are located in Appendix B, Figure B.1.

Table 4.2.1 Ca^{2+} K_ds and dynamic ranges of 149E variants

		No KCl		150 mM KCl	
	λ_{ex} (nm)	**K_d (mM)**	**F_{max}/F_{min}**	**K_d (mM)**	**F_{max}/F_{min}**
CatchER	**395**	0.3 ± 0.1	1.7 ± 0.1	1.8 ± 0.2	1.2 ± 0.1
	488	0.2 ± 0.1	1.6 ± 0.1	0.9 ± 0.2	1.1 ± 0.2
149E	**395**	0.4 ± 0.1	1.3 ± 0.1	NR	NR
	488	0.8 ± 0.1	1.5 ± 0.1	2.2 ± 0.4	-------
149E S30R	**395**	0.1 ± 0.0	1.4 ± 0.2	NR	NR
	488	0.3 ± 0.1	2.0 ± 0.1	1.6 ± 0.2	1.5 ± 0.1
149E Y39N	**395**	0.4 ± 0.1	1.4 ± 0.1	-------	-------
	488	1.1 ± 0.1	1.6 ± 0.1	-------	-------
149E'	**395**	1.2 ± 0.5	1.4 ± 0.1	-------	-------
	488	2.8 ± 0.5	1.6 ± 0.1	-------	-------

* Data presented is mean ± stdev. K_d – dissociation constant, λ_{ex} – excitation wavelength, F_{max}/F_{min} – dynamic range in response to Ca^{2+} calculated using the fluorescence at maximal saturation divided by the fluorescence with no Ca^{2+} present. Data collected at room temperature. Samples prepared in 10 mM Tris pH 7.4 with or without 150 mM KCl. Fluorescence slit widths were 0.25 mm for excitation and emission. Dashed lines indicate data not collected. NR – no response to Ca^{2+}.

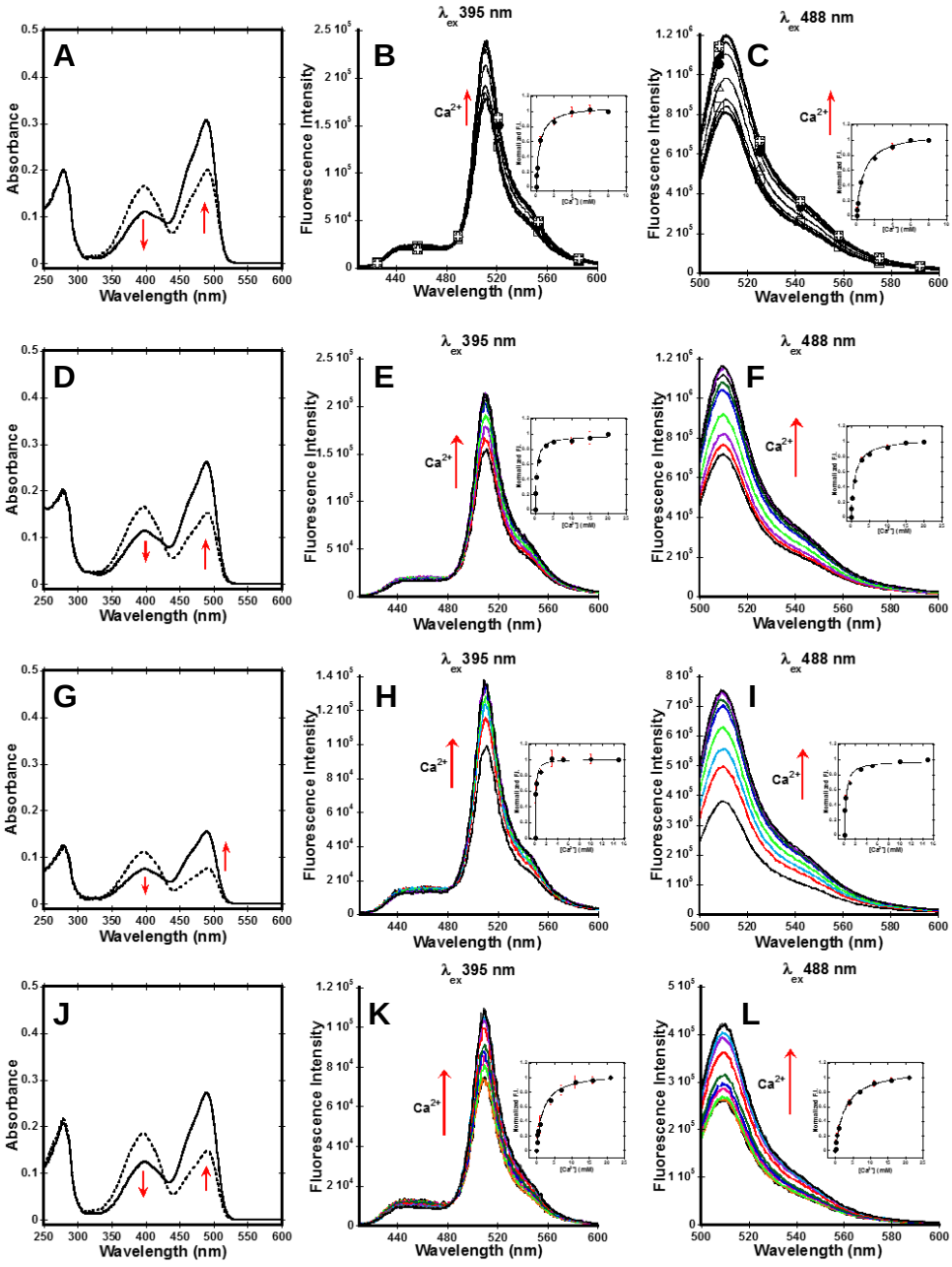

Figure 4.2.3 *In vitro* K_d of 149E (A-C), 149E Y39N (D-F), 149E S30R (G-I), and 149E' (J-L) in 10 mM Tris pH 7.4

(A, D, G, J) Absorbance spectra of 10 µM of the protein sample before titration with 5 uM EGTA (dashed line) and after with a saturating amount of Ca^{2+} (solid line). The population of the anionic chromophore, corresponding to the 488 nm peak, increases and the amount of neutral chromophore, corresponding to the 395 nm peak, decreases with increasing Ca^{2+}. (B and C). Fluorescence increase of 149E in response to 0, 0.05, 0.15, 0.5, 2, 4, 6, and 8 mM Ca^{2+}. (E and F) Fluorescence increase of 149E Y39N in

response to 0, 0.1, 0.3, 1, 3, 5, 10, 15, and 20 mM Ca^{2+}. (H and I) Fluorescence increase of 149E S30R in response to 0, 0.1, 0.3, 1, 3, 5, 10, and 15 mM Ca^{2+}. (K and L) Fluorescence increase of 149E' in response to 0, 0.05, 0.15, 0.3, 0.5, 1, 4, 7, 11, 16, and 21 mM Ca^{2+}. All samples were excited at 395 nm and 488 nm with emission scanned from 410-600 nm for 395 nm excitation and from 500-600 nm for 488 nm excitation. Slit widths for excitation and emission were 0.25 mm. Inset curves show the normalized fluorescence intensity data fit to a 1:1 binding equation to get the K_d.

4.2.3 Optical properties of CatchER variants.

The apo (Ca^{2+} free) and holo-form (Ca^{2+} bound) quantum yields (Φ) of CatchER, CatchER-T, 149E, 149E Y39N, and 149E S30R were determined using fluorescence data obtained from 488 nm excitation with emission at 510 nm and from absorbance values at 488 nm. The detailed protocol is found in Chapter 2 section 2.12. Table 4.2.2 lists all optical property values for 149E, 149E Y39N, 149E S30R, CatchER, and CatchER-T. The quantum yields were calculated using Equation 2.6. The apo and holo-form quantum yield of 149E is 0.6 ± 0.1 and 0.5 ± 0.1, respectively. The apo-form quantum yield of CatchER is 0.8 ± 0.1 and 0.6 ± 0.1 in the holo-form. Figures 4.2.4C-D, 4.2.5C-D, 4.2.6C-D, 4.2.7C-D, and 4.2.8C-D show the raw absorbance and fluorescence data for CatchER, CatchER-T, 149E, 149E Y39N, and 149E S30R used to calculate the quantum yield and extinction coefficient for each variant. The addition of 10 mM Ca^{2+} decreases the quantum yields for CatchER, 149E, 149E Y39N and 149E S30R (Table 4.2.2).

The molar absorptivity, also known as the extinction coefficient (ε), tells how well a compound absorbs light at a given wavelength. Brightness is a product of ε and Φ. A detailed protocol is located in Chapter 2 section 2.12. Both the extinction coefficient and brightness were calculated for the variants, using Equation 2.7, and are listed in

Table 4.2.2. 149E has extinction coefficients of 26.1 ± 0.1 $mM^{-1}cm^{-1}$ (apo) and 33.0 ± 0.5 $mM^{-1}cm^{-1}$ (holo) at 488 nm. The brightness of 149E is 18.0 ± 0.1 $mM^{-1}cm^{-1}$ (apo) and 22.5 ± 0.1 $mM^{-1}cm^{-1}$ (holo) at 488 nm.

Table 4.2.2 Optical properties of CatchER variants

Variant	Quantum Yield		Extinction Coefficient ($mM^{-1}cm^{-1}$)		Brightness ($mM^{-1}cm^{-1}$)	
	Apo	Holo	Apo	Holo	Apo	Holo
CatchER	0.8 ± 0.1	0.6 ± 0.1	7.1 ± 0.1	15.0 ± 0.1	5.5 ± 0.1	8.5 ± 0.1
149E	0.6 ± 0.1	0.5 ± 0.1	25.4 ± 0.1	40.0 ± 0.1	15.0 ± 0.1	20.3 ± 0.2
CatchER-T	0.8 ± 0.1	0.8 ± 0.1	11.0 ± 0.1	14.1 ± 0.1	8.7 ± 0.1	11.8 ± 0.1
149E Y39N	0.6 ± 0.1	0.5 ± 0.1	22.7 ± 0.1	37.3 ± 0.2	13.3 ± 0.2	19.5 ± 0.3
149E S30R	0.7 ± 0.1	0.6 ± 0.1	17.6 ± 0.3	34.7 ± 0.1	12.0 ± 0.2	20.3 ± 0.2

Data presented is mean ± stdev. Samples prepared in 10 mM Tris pH 7.4. Experiments conducted at room temperature. Excitation and emission slit widths were 0.1 mm and 0.6 mm, respectively. EGFP quantum yield of 0.6 was used as the reference in the calculation. The 44 $mM^{-1}cm^{-1}$ extinction coefficient at 447 nm absorbance peak for all FPs was used to calculate the extinction coefficient of the variants.

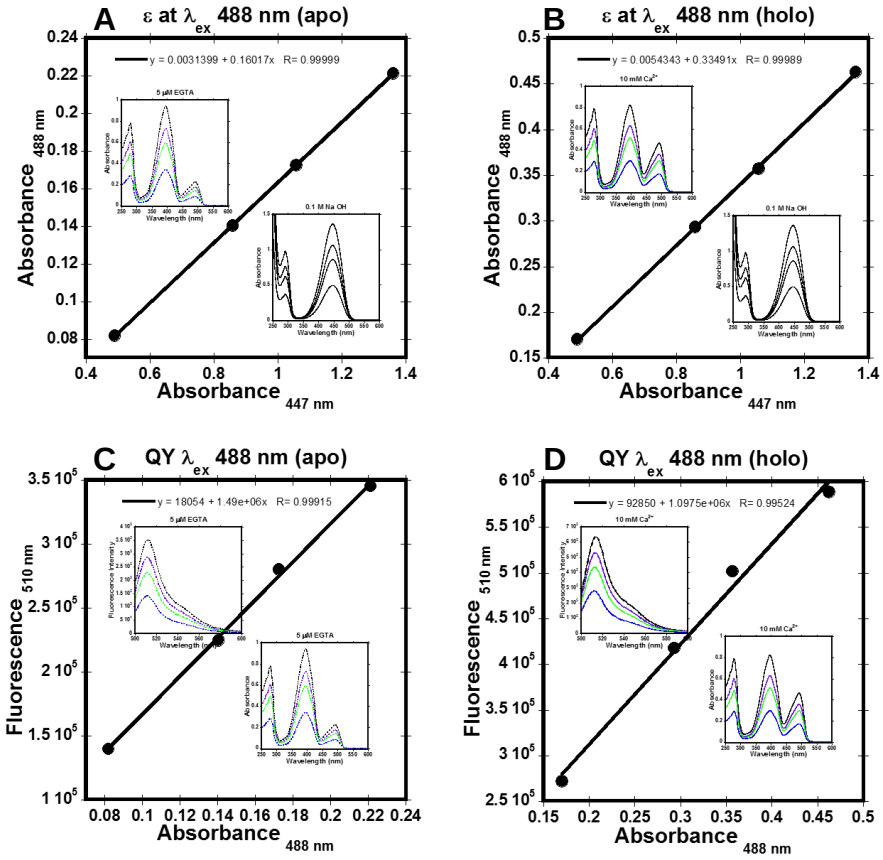

Figure 4.2.4 Extinction coefficient (A and B) and Quantum yield (C and D) measurement of CatchER with and without 10 mM Ca^{2+}.

A and B) Linear scatter plot of the absorbance at 488 nm plotted against the absorbance at 447 nm of CatchER samples at different concentrations without Ca^{2+} containing 5 µM EGTA (A) and with Ca^{2+} (B). Inset curves are the raw absorbance data. C and D) Linear scatter plots of the fluorescence intensity at 510 nm from 488 nm excitation plotted against the absorbance at 488 nm of CatchER samples at different concentrations without Ca^{2+} (C) and with Ca^{2+} (D). Fluorescence slit widths were 0.15 mm and 0.60 mm for excitation and emission, respectively. Experiments were done at room temperature with samples prepared in 10 mM Tris pH 7.4. 0.1 M NaOH was added to each sample after all fluorescence and absorbance spectra were collected to get the absorbance spectra of the denatured samples with the major absorbance peak occurring at 447 nm. The absorbance data for the denatured samples was used to calculate the extinction coefficient.

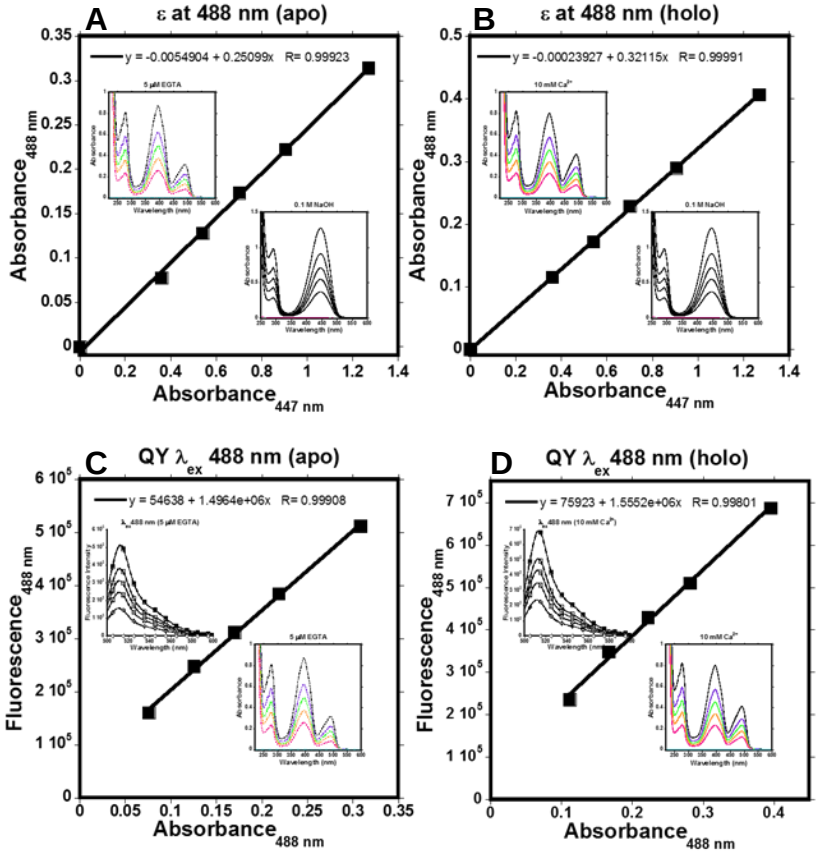

Figure 4.2.5 Extinction coefficient (A and B) and Quantum yield (C and D) measurement of CatchER-T with and without 10 mM Ca^{2+}.

A and B) Linear scatter plot of the absorbance at 488 nm plotted against the absorbance at 447 nm of CatchER-T samples at different concentrations without Ca^{2+} containing 5 µM EGTA (A) and with Ca^{2+} (B). Inset curves are the raw absorbance data. C and D) Linear scatter plots of the fluorescence intensity at 510 nm from 488 nm excitation plotted against the absorbance at 488 nm of CatchER-T samples at different concentrations without Ca^{2+} (C) and with Ca^{2+} (D). Fluorescence slit widths were 0.15 mm and 0.60 mm for excitation and emission, respectively. Experiments were done at room temperature with samples prepared in 10 mM Tris pH 7.4. 0.1 M NaOH was added to each sample after all fluorescence and absorbance spectra were collected to get the absorbance spectra of the denatured samples with the major absorbance peak occurring at 447 nm. The absorbance data for the denatured samples was used to calculate the extinction coefficient.

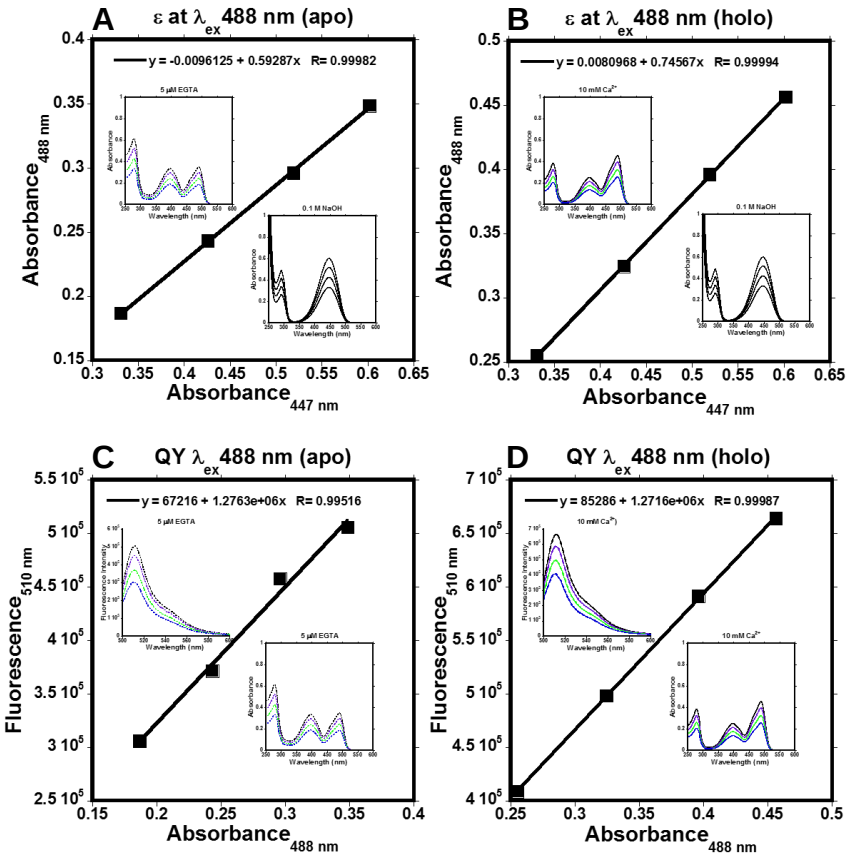

Figure 4.2.6 Extinction coefficient (A and B) and Quantum yield (C and D) measurement of 149E with and without 10 mM Ca^{2+}

A and B) Linear scatter plot of the absorbance at 488 nm plotted against the absorbance at 447 nm of 149E samples at different concentrations without Ca^{2+} containing 5 μM EGTA (A) and with Ca^{2+} (B). Inset curves are the raw absorbance data. C and D) Linear scatter plots of the fluorescence intensity at 510 nm from 488 nm excitation plotted against the absorbance at 488 nm of 149E samples at different concentrations without Ca^{2+} (C) and with Ca^{2+} (D). Fluorescence slit widths were 0.15 mm and 0.60 mm for excitation and emission, respectively. Experiments were done at room temperature with samples prepared in 10 mM Tris pH 7.4. 0.1 M NaOH was added to each sample after all fluorescence and absorbance spectra were collected to get the absorbance spectra of the denatured samples with the major absorbance peak occurring at 447 nm. The absorbance data for the denatured samples was used to calculate the extinction coefficient.

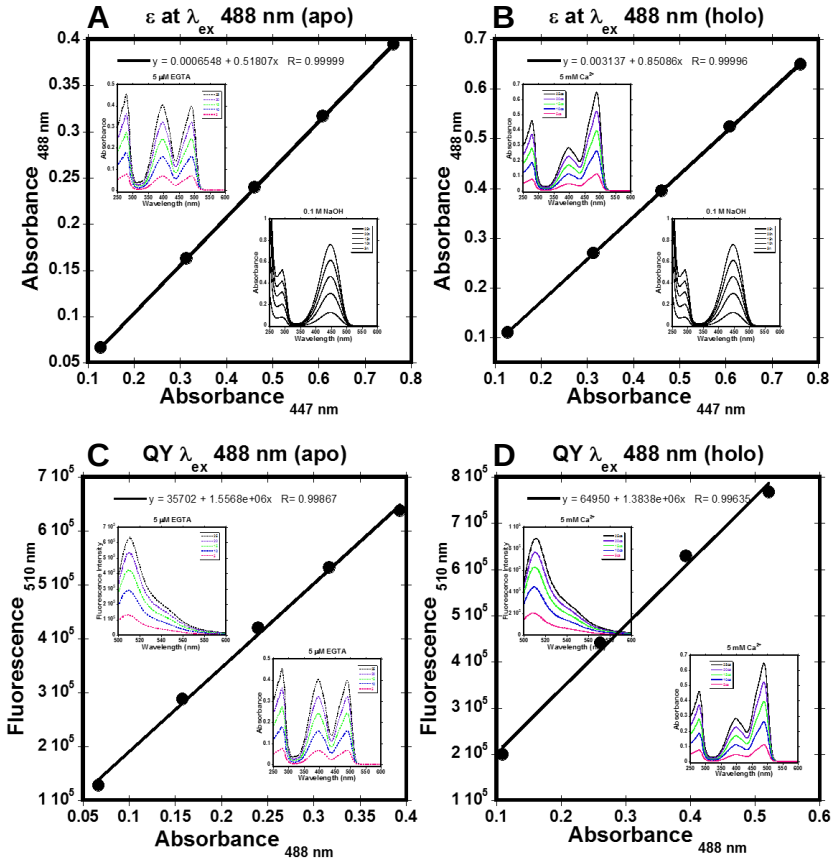

Figure 4.2.7 Extinction coefficient (A and B) and Quantum yield (C and D) measurement of 149E Y39N with and without 10 mM Ca^{2+}

A and B) Linear scatter plot of the absorbance at 488 nm plotted against the absorbance at 447 nm of 149E Y39N samples at different concentrations without Ca^{2+} containing 5 μM EGTA (A) and with Ca^{2+} (B). Inset curves are the raw absorbance data. C and D) Linear scatter plots of the fluorescence intensity at 510 nm from 488 nm excitation plotted against the absorbance at 488 nm of 149E Y39N samples at different concentrations without Ca^{2+} (C) and with Ca^{2+} (D). Fluorescence slit widths were 0.15 mm and 0.60 mm for excitation and emission, respectively. Experiments were done at room temperature with samples prepared in 10 mM Tris pH 7.4. 0.1 M NaOH was added to each sample after all fluorescence and absorbance spectra were collected to get the absorbance spectra of the denatured samples with the major absorbance peak occurring at 447 nm. The absorbance data for the denatured samples was used to calculate the extinction coefficient.

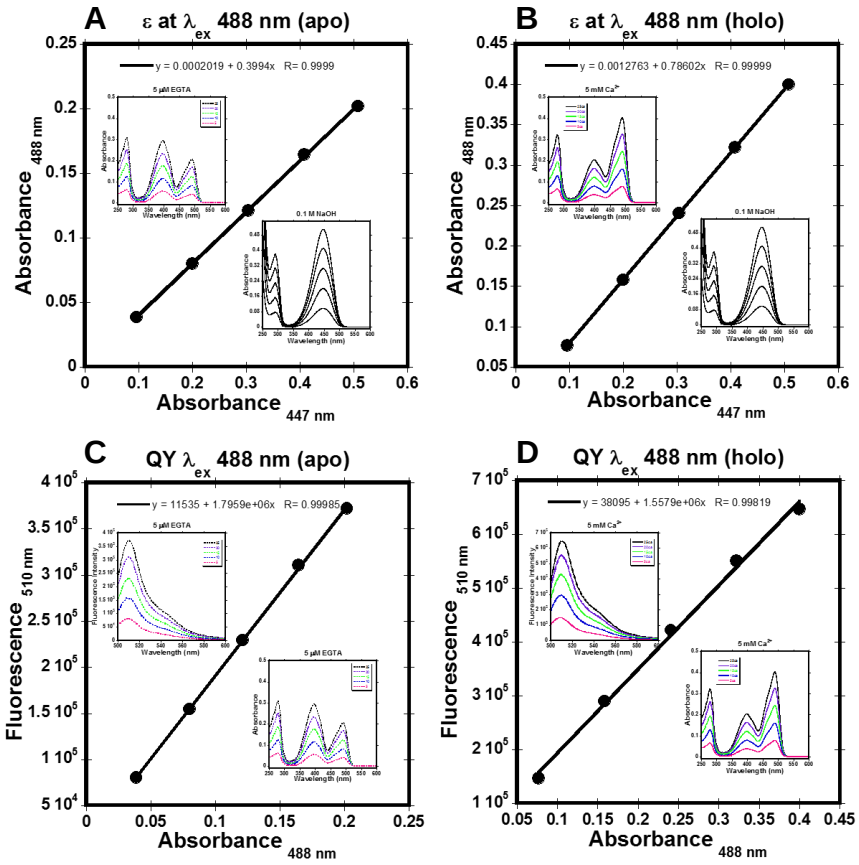

Figure 4.2.8 Extinction coefficient (A and B) and Quantum yield (C and D) measurement of 149E S30R with and without 10 mM Ca^{2+}

A and B) Linear scatter plot of the absorbance at 488 nm plotted against the absorbance at 447 nm of 149E S30R samples at different concentrations without Ca^{2+} containing 5 μM EGTA (A) and with Ca^{2+} (B). Inset curves are the raw absorbance data. C and D) Linear scatter plots of the fluorescence intensity at 510 nm from 488 nm excitation plotted against the absorbance at 488 nm of 149E S30R samples at different concentrations without Ca^{2+} (C) and with Ca^{2+} (D). Fluorescence slit widths were 0.15 mm and 0.60 mm for excitation and emission, respectively. Experiments were done at room temperature with samples prepared in 10 mM Tris pH 7.4. 0.1 M NaOH was added to each sample after all fluorescence and absorbance spectra were collected to get the absorbance spectra of the denatured samples with the major absorbance peak occurring at 447 nm. The absorbance data for the denatured samples was used to calculate the extinction coefficient.

4.2.4 pK_a of Ca^{2+} probes.

The pK_a of CatchER-T (Figure 4.2.5) and 149E (Figure 4.2.6) was measured via fluorescence in the presence and absence of 5 and 10 mM Ca^{2+} as outlined in Chapter 2 section 2.13. Each probe had its highest fluorescence at pH 8 or 9 with added Ca^{2+} and the lowest fluorescence intensity occurred at pH 1.1. Table 4.2.3 lists the pK_a values for 149E, CatchER-T, and CatchER obtained using Equation 2.16. The CatchER pK_a values are from published data[180]. CatchER-T has a pK_a of 7.3 ± 0.2 and 7.8 ± 0.5 without Ca^{2+} excited at 395 and 488 nm respectively and 6.7 ± 0.1 and 6.8 ± 0.3 with Ca^{2+} excited at 395 and 488 nm, respectively. Of the sensors whose pK_a was determined, 149E has the lowest pK_a values of 6.4 ± 0.1 and 6.5 ± 0.1 without Ca^{2+} excited at 395 and 488 nm and 6.4 ± 0.3 and 6.4 ± 0.1 with Ca^{2+}.

Table 4.2.3 pK_a of select CatchER variants

Protein	**149E**		**CatchER-T**		**CatchER[180]**	
Excitation Wavelength	**395 nm**	**488 nm**	**395 nm**	**488 nm**	**395 nm**	**488 nm**
Apo	6.4 ± 0.1	6.5 ± 0.1	7.3 ± 0.2	7.8 ± 0.5	7.1 ± 0.1	7.6 ± 0.1
Holo	6.4 ± 0.3	6.4 ± 0.1	6.7 ± 0.1	6.8 ± 0.3	6.9 ± 0.1	6.9 ± 0.1

Data presented is mean ± stdev. Ten micromolar protein samples were prepared in different buffers from 1-9 pH with overnight incubation at 4°C. pH values were recorded before and after data collection. Samples were warmed to room temperature before experiment. Reported values of CatchER are from the cited reference.

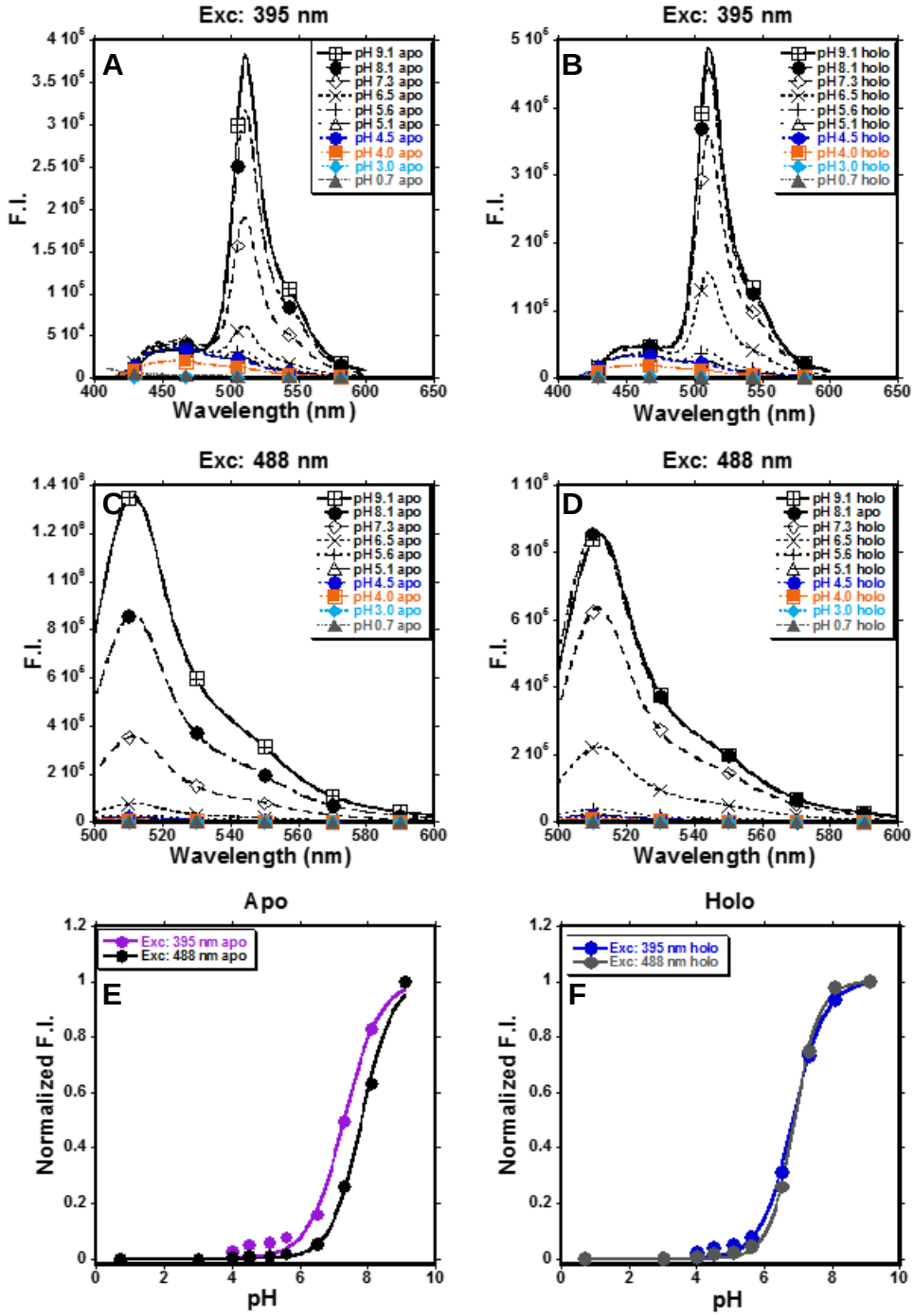

Figure 4.2.9 pK_a of CatchER-T with and without 5 mM Ca^{2+}

(A and B) 10 uM CatchER-T excited at 395 nm in apo and holo-form from pH 9.1 to pH 1.0. (C and D) Same protein samples excited at 488 nm and monitored from 500-600 nm. E and F) Fluorescence data of the apo (E) and holo (F) samples was normalized and fitted using the Henderson-Hasselbalch equation translated for K-graph. The pK_a

of CatchER-T in apo-form was 7.3 ± 0.2 and 7.8 ± 0.5 at 395 and 488 nm excitation and the pKa in the holo-form was 6.7 ± 0.1 and 6.8 ± 0.3 at 395 and 488 nm excitation.

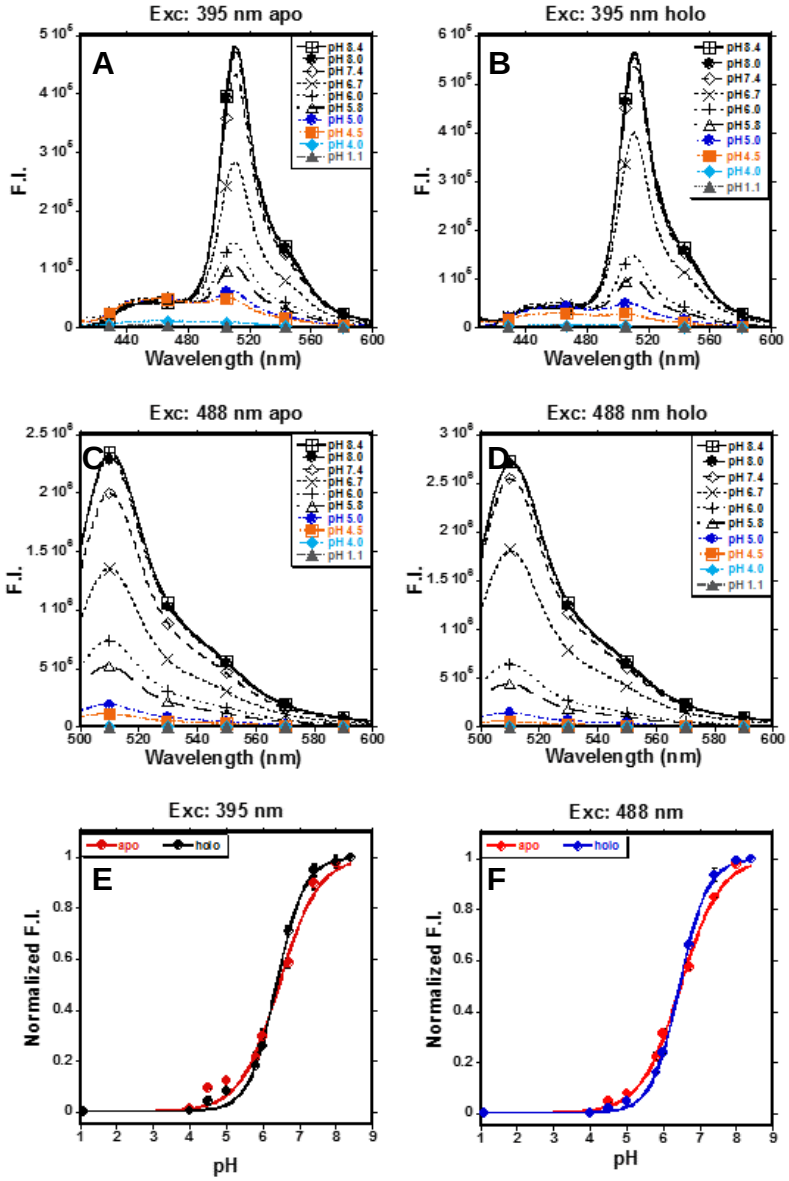

Figure 4.2.10 pK_a of 149E with and without 5 mM Ca^{2+}

(A and B) 10 uM 149E excited at 395 nm in apo and holo-form from pH 8.4 to pH 1.1. (C and D) Same protein samples excited at 488 nm and monitored from 500-600 nm. E and F) Fluorescence data was normalized and fitted using the Henderson-Hasselbalch equation translated for K-graph. The pK_a of 149E in apo-form was 6.4 ± 0.1 and 6.5 ±

0.1 excited at 396 and 488 nm, and the pKa of the holo-form was 6.4 ± 0.3 and 6.4 ± 0.1 at 396 and 488 nm excitation.

4.2.5 K_d determination via equilibrium dialysis/ICP-OES

Equilibrium dialysis is a commonly used method in the pharmaceutical industry for determining the affinity of a receptor for its ligand or a drug for its target[253]. As shown in Chapter 2 Figure 2.15.1, the technique involves placing samples in dialysis bags or chambers and allowing the sample to equilibrate against buffer, containing the ligand of interest, for a sufficient period of time. The experiment was done as described in Chapter 2 section 2.15. K_d values were calculated using Equation 2.19. Twenty microliters of protein is placed into cellulose dialysis bags and allowed to equilibrate for 48 h against 4 L of buffer plus a certain concentration of Ca^{2+}. α-lactalbumin and myoglobin were used as positive and negative controls, respectively. EGFP was used as an additional negative control. The absorbance spectra of the samples were taken before and after dialysis. After 48 h, the samples were collected and analyzed using ICP-OES. The ICP-OES spectrometer has the ability to detect metal concentrations as low as 0.1-100 ng/mL in various matrices[254]. This instrument involves the use of an RF induced white plasma fueled by Argon (Ar) gas[255]. Samples for analysis are converted to aerosol where the metals in solution collide with Ar gas particles forcing electrons into excited states causing the emission of a photon upon relaxation to ground state[256]. Results of the Ca^{2+} K_d of CatchER variants using this method are found in Figure 4.2.7. The data was compiled from different ICP-OES experiments. Standard curves used to calculate Ca^{2+} concentrations from each Ca^{2+} emission wavelength are in Appendix B

Figure B.2. Examples of [Ca^{2+}] calculated from ICP-OES are located in Appendix B Tables B.1, B.2, and B.3.

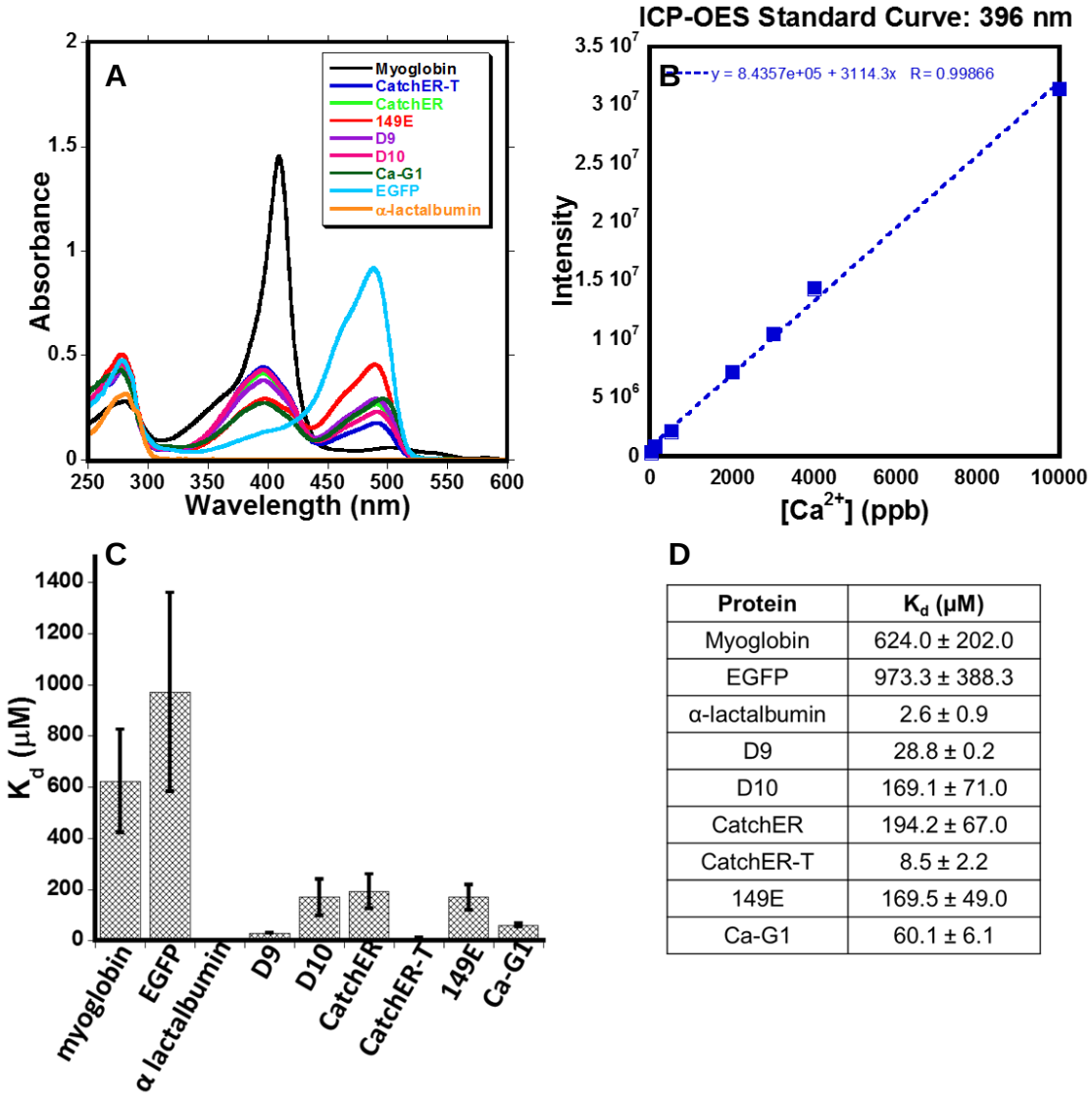

D

Protein	K_d (μM)
Myoglobin	624.0 ± 202.0
EGFP	973.3 ± 388.3
α-lactalbumin	2.6 ± 0.9
D9	28.8 ± 0.2
D10	169.1 ± 71.0
CatchER	194.2 ± 67.0
CatchER-T	8.5 ± 2.2
149E	169.5 ± 49.0
Ca-G1	60.1 ± 6.1

Figure 4.2.11 Ca^{2+} K_d determination of CatchER variants using equilibrium dialysis and ICP-OES

A) Absorbance spectrum overlay of samples prepared for equilibrium dialysis. Protein samples were prepared at ~20 μM. B) Representative ICP-OES standard curve obtained from prepared Ca^{2+} standard solutions. Data was collected from the 396 nm emission wavelength of Ca^{2+}. C and D) Calculated K_d values of the CatchER variants tested from different equilibrium dialysis experiments in 10 mM Tris pH 7.4.

4.2.6 Stopped-flow analysis of CatchER variants

CatchER, whose *in vitro* and *in situ* data has been published, is able to detect Ca^{2+} changes in the cell because of its weak affinity (K_d = 180 µM) and its rapid k_{off} of ~700 s^{-1} [180]. Because CatchER reacts quickly with Ca^{2+}, a large percentage of its binding process is not seen during stopped-flow fluorescence analysis. The Ca^{2+} binding site in CatchER has a -5 charge due to the concentration of Asp and Glu residues. The electrostatic nature of Ca^{2+} binding to CatchER in addition to the negatively charged surface of EGFP is proposed to contribute to the fast binding and release kinetics we see in CatchER. To probe the role of electrostatics in Ca^{2+} binding to CatchER and other variants, stopped-flow kinetics measurements were done at the physiological [KCl] of 150 mM as outlined in Chapter 2 section 2.16. Table 4.2.4 lists the k_{off} values for 149E, CatchER, and CatchER-T with and without 150 mM KCl present in the buffer along with the stopped-flow and fluorescence K_ds for each. Values for k_{off} were obtain using a single exponential fit for the stopped-flow data. Figure 4.2.12 shows the k_{off} traces and inset k_{on} traces for the previously mentioned variants in the absence and presence of 150 mM KCl.

Table 4.2.4 Stopped flow analysis of CatchER variants

	k_{off} (s^{-1})[a]		sf K_d (mM)[b]		Fluo K_d (mM)[c]	
	0 mM KCl	**150 mM KCl**	**0 mM KCl**	**150 mM KCl**	**0 mM KCl**	**150 mM KCl**
149E	124 ± 3	142 ± 2	0.1 ± 0.01	1.2 ± 0.2	0.2 ± 0.1	0.9 ± 0.2
CatchER	68 ± 1	308 ± 7	0.3 ± 0.1	2.5 ± 0.8	0.3 ± 0.1	2.0 ± 0.4
CatchER-T	137 ± 2	491 ± 11	0.2 ± 0.01	1.9 ± 0.1	0.4 ± 0.1	1.7 ± 0.1

Data represents mean ± stdv. Fluorescence data collected at room temperature with a 455 nm long pass filter with 395 nm excitation. [a]Rate of dissociation of Ca^{2+} from the protein calculated using a single exponential decay fit of the sf data. [b]sf K_d is the dissociation constant calculated from the fluorescence stopped-flow traces with increasing Ca^{2+}. [c]Fluo K_d is the dissociation constant calculated from fluorometric titration.

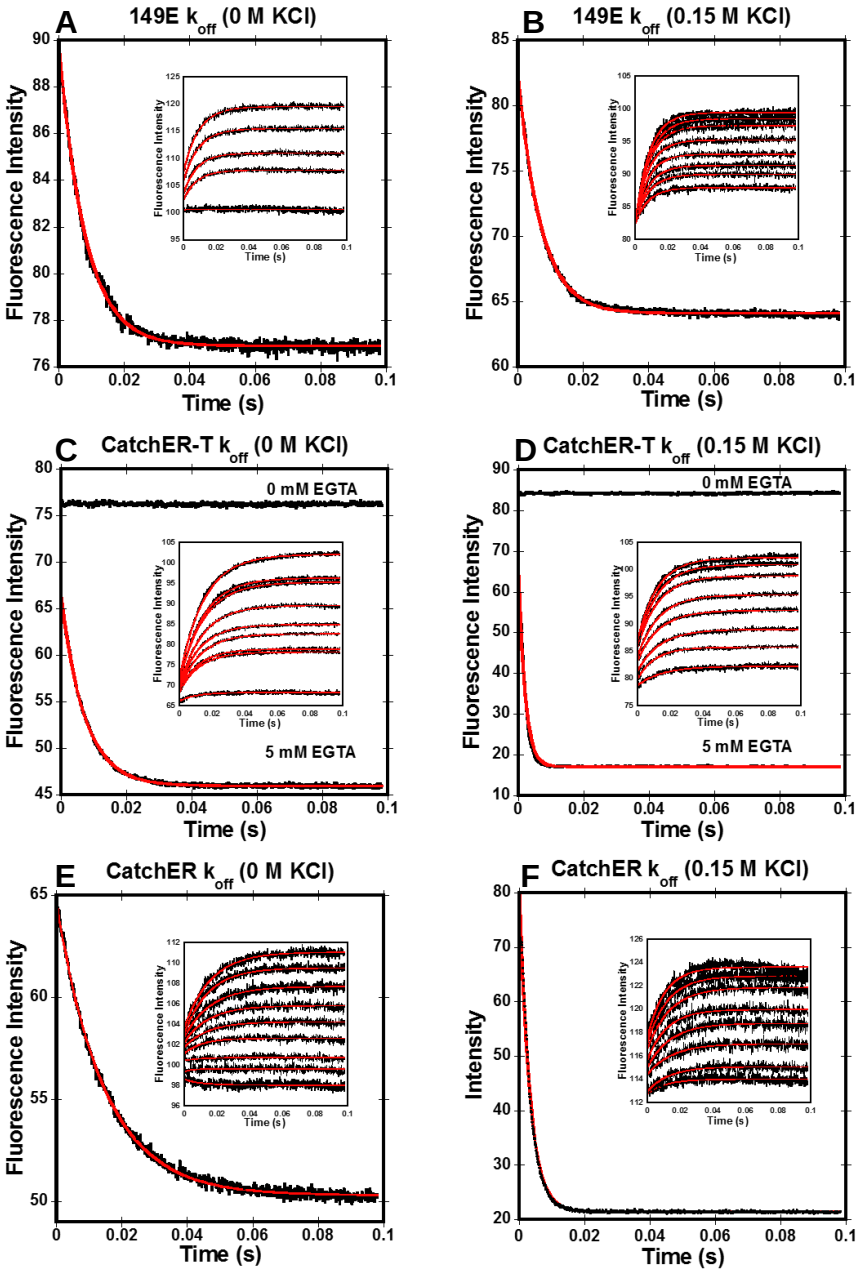

Figure 4.2.12 Stopped-flow kinetics analysis of 149E (A and B), CatchER-T (C and D), and CatchER (E and F) in the absence and presence of 150 mM KCl

k_{off} fluorescence traces from 395 nm excitation with rapid mixing of 149E (A), CatchER-T (C), and CatchER (E) at a final concentration of 20 µM saturated with 250-300 µM Ca^{2+} shot against EGTA. Inset curves are k_{on} traces at increasing Ca^{2+} concentrations. Samples are in 10 mM Tris pH 7.4 without KCl. B, D, F) k_{off} traces of each protein in 10 mM Tris 150 mM KCl pH 7.4 with 1 mM Ca^{2+} added to each. Data was collected at room temperature.

4.2.7 Monitoring ER/SR Ca^{2+} release using CatchER variants

We examined the response of select CatchER variants to changes in $[Ca^{2+}]_{ER/SR}$ in mammalian cells. Since CatchER contains the calreticulin signal peptide and the KDEL ER/SR retention sequence for ER/SR localization, all the variants made from CatchER are targeted to the ER/SR. C2C12 myoblast cells were transfected with the variant DNA using Effectene outlined in Chapter 2 section 2.18. The imaging experiments were carried out as detailed in Chapter 2 section 2.20. Figure 4.2.13A shows the response of 149E Y39N to 200 µM 4-cmc in C2C12 myoblast cells. The response was collected from five cells. Although the intensity baseline before and after treatment was not stable, there is a clear decrease in the intensity with the addition of 4-cmc, indicating the probe is sensing the decrease in SR Ca^{2+} in response to RyR channel activation by 4-cmc. Figures 4.2.13B and C show the response of CatchER-T and CatchER-T S30R to Ca^{2+} in the presence of 10 µM ionomycin after permeabilization with 25 µM digitonin. Data from one C2C12 myoblast cell was collected for each.

In collaboration with Dr. Heping Cheng at Peking University in China, CatchER, CatchER-T', and our mCherry-based probe R-CatchER were used to monitor Ca^{2+} release in neonatal rat ventricular myocytes. Senor DNA was inserted into the adenovirus vector for easy transfection of ventricular myocytes. Figure 4.2.14A and B show the expression of CatchER and CatchER-T' in these cells. R-CatchER expression is not pictured. The sensors have good expression in this cell type. RyR2-mediated SR depletion was triggered using caffeine with simultaneous monitoring of cytosolic Ca^{2+}

with rhodamine 2 (Figure 4.2.14D-F). The green Ca^{2+} dye Fluo 4 was paired with R-CatchER to prevent spectral overlap and mixing of fluorescence signals. Fluorescence intensity changes for CatchER, CatchER-T', and R-CatchER, in response to caffeine depletion, are minimal compared to changes seen with the dyes. CatchER had a 15% decrease in fluorescence intensity while CatchER-T' had a 20% decrease in fluorescence. R-CatchER experienced a 5% decrease in intensity.

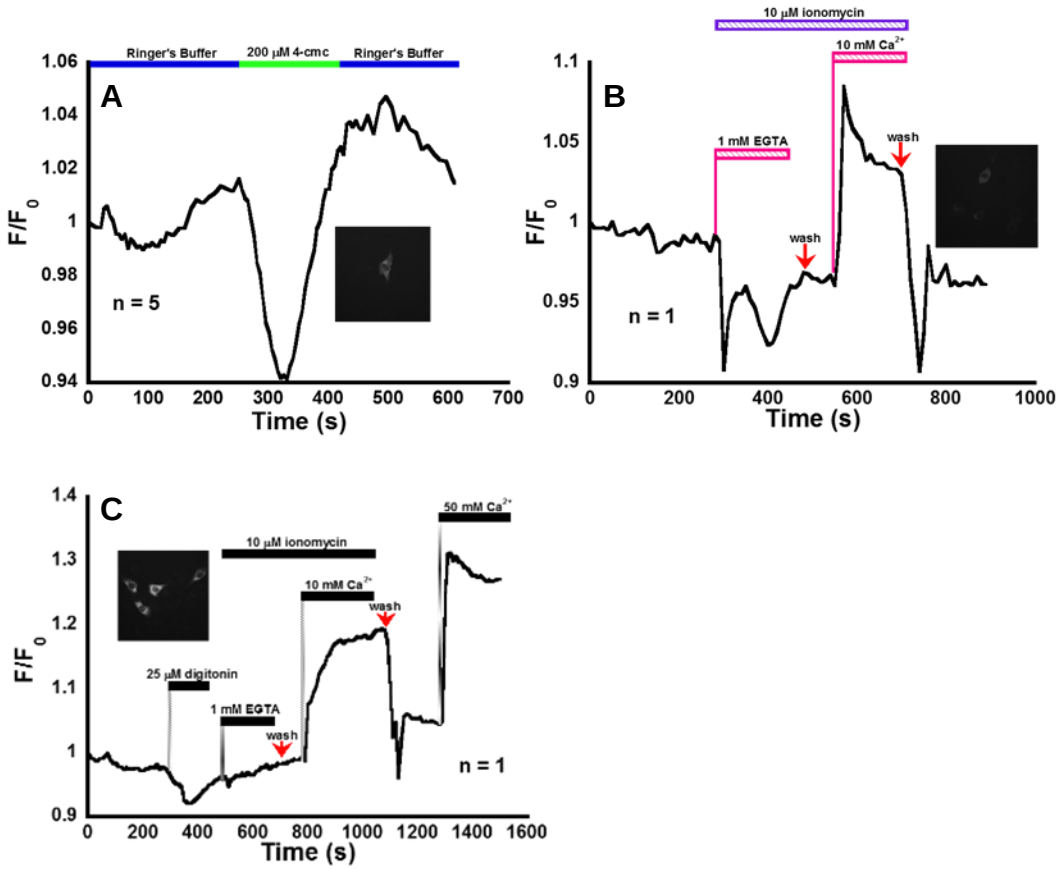

Figure 4.2.13 Monitoring changes in SR Ca^{2+} in C2C12 myoblast cells using 149E Y39N (A), CatchER-T (B), and CatchER-T S30R (C)

(A) Ca^{2+} release from the SR through activation of RyR1 with 200 µM 4-cmc in Ringer's buffer containing 1.8 mM Ca^{2+}. Cells were imaged using a Leica DM6100B inverted microscope with a cooled EM-CCD camera. Cells were viewed through a 40X oil immersion objective with and exposure time of 0.07 s and a gain of 175. The fluorophore was excited at 488 nm with emission monitored at 510. B and C) Permeablization of C2C12 myoblast cells with 25 µM digitonin expressing CatchER-T and CatchER-T S30R. Cells were permeablized in intracellular buffer, pH 7.2, then washed with 1 mM EGTA containing 10 µM ionomycin in KCl buffer, pH 7.2. 10 or 50 mM Ca^{2+} in KCl buffer containing 10 µM ionomycin was added to the cells to see the intensity increase. Red arrows refer to wash with KCl buffer containing 10 µM ionomycin. N refers to the number of cells. B) Digitonin was perfused through the chamber permeablizing all the cells on the slide. Cell shown is from a different region of the slide after testing a cell that had no response.

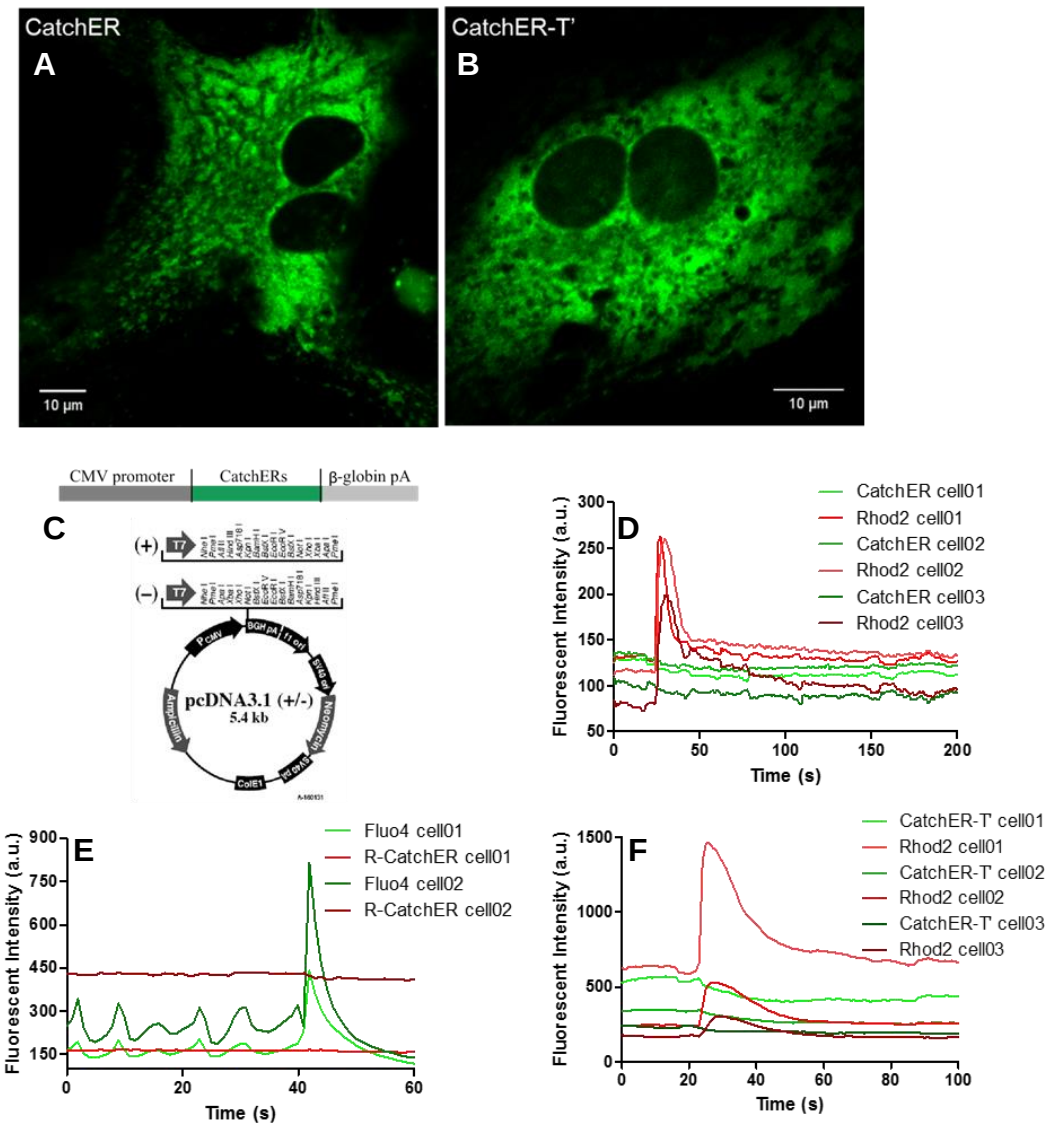

Figure 4.2.14 Application of CatchER variants in neonatal rat ventricular myocytes

A-C) The DNA for CatchER, CatchER-T', and R-CatchER was inserted into an adenovirus vector. Neonatal rat ventricular myocytes were transfected with the variant DNA for expression of the sensors (expression of R-CatchER not shown). D-F) Ventricular myocytes expressing CatchER (D), R-CatchER (E), and CatchER-T' (F) were treated with caffeine triggering RyR2-mediated Ca^{2+} release from the SR. Changes in cytosolic Ca^{2+} were monitored using rhodamine 2 (Rhod2) and Fluo4 for R-CatchER. CatchER saw a 15% decrease in fluorescence intensity while CatchER-T' saw a 20% decrease in fluorescence. R-CatchER had a 5% decrease in intensity. Data collected by Dr. Heping Cheng and colleagues in China.

4.3 Discussion

The current class of genetically encoded Ca^{2+} sensors available today rely on the incorporation of a native CaBP into a fluorescent protein fusion construct using one or two fluorescent proteins. The CaBP acts as the Ca^{2+} binding site that transmits the binding energy to the fluorescent proteins converting the energy into a measureable fluorescence response. These sensors have K_d values in the nanomolar range for Ca^{2+}. The high affinity these sensors experience for Ca^{2+} cannot be altered easily due to the high cooperativity intrinsic to natural Ca^{2+} binding sites[194,177,72]. For this reason, Ca^{2+} sensors are needed with tunable K_ds to target the various spatio-temporal [Ca^{2+}] changes that occur intracellularly.

4.3.1 Metal binding of CatchER variants

Through analysis of the coordination chemistry and associated ligands in CaBPs, it is well understood that Ca^{2+} is coordinated in proteins with pentagonal bipyramidal geometry[212]. The binding site of CatchER was designed using this knowledge with site directed mutagenesis. 147E, 202D, 204E, 223E, and 225E are the acidic residues that create the binding site in CatchER. The Ca^{2+} and Gd^{3+} bound crystal structures reveal that the dynamic nature of the metal ion in the binding site is responsible for the weak K_d and fast kinetics of the sensor[181]. Creation of the binding site gives E222, which is important for charge stabilization of the chromophore[245], two conformations in the Ca^{2+} loaded crystal structure. As Ca^{2+} is added to CatchER, E222 rotates to stabilize the negative charge of the anionic chromophore being produced, noted by the increase in the 488 nm absorbance peak[181]. Based on the spectral properties of 149E, this mutation increases the amount of the anionic chromophore present in the protein. The

N149E mutation may influence the conformation of E222 which could be the reason for the absorbance spectrum changes seen that are similar to CatchER. Incorporation of the N149E mutation to CatchER weakens the Ca^{2+} K_d. The CatchER Ca^{2+} crystal structure shows that the primary chelating ligands are 147E, 202D, and 204E. The decrease in the affinity may be attributed to disruption of the metal coordination geometry and charge repulsion from the added negative charge.

Although the S30R and Y39N mutations are far from the metal binding site, they impact the affinity of the variants for Ca^{2+}. These mutations improve the global stability and fold of the β-barrel[169] which seems to have an indirect effect on the binding site. Compared to 149E, 149E S30R has a stronger affinity for Ca^{2+} and an increase in the dynamic range when excited at 488 nm (Table 4.2.1). The 149E Y39N mutant has a weaker Ca^{2+} affinity than 149E and 149E S30R. The double mutant, 149E', has the lowest affinity for Ca^{2+} because of the overall effect the mutations have on the stability of the protein.

Because our sensors are targeted to the ER/SR it is important to know how physiological concentrations of salts, like KCl, will influence the affinity of the sensors for Ca^{2+}. In Table 4.2.1, it is clear that the addition of 150 mM KCl during Ca^{2+} titration weakens the affinity of the sensors for Ca^{2+}. In some cases, the Cl^- ion quenched fluorescence from one excitation wavelength (Appendix B, Figure B.1). At this salt concentration, the dynamic range of the sensors was reduced. Cl^- ions have been reported to quench the fluorescence of GFP proteins[173]. When applied *in situ*, our probes will likely experience a reduced dynamic range from the other physiological ions in solution.

4.3.2 Optical properties of CatchER variants

Table 4.2.2 lists all the optical property values calculated at the 488 nm excitation peak. The optical properties of the variants were determined with 488 nm excitation because this excitation wavelength is used for cell imaging. EGFP has a single excitation peak at 488 nm[170], and it is the scaffold protein used for these variants. Because EGFP was used as the reference in these experiments, only the optical properties at 488 nm excitation could be calculated. The quantum yield of CatchER-T does not change with Ca^{2+}, so Ca^{2+} does not improve the efficiency of fluorescence. The quantum yield of 149E and CatchER, on the other hand, experiences a slight decrease with the addition of Ca^{2+}. The calculated extinction coefficients of the variants were consistent with the observed absorbance spectrum changes with and without Ca^{2+}. Without Ca^{2+}, the absorbance peak at 395 nm is large and the peak at 488 nm is small. When Ca^{2+} is added, a ratiometric change is seen where the 395 peak decreases and the 488 peak increases. The ratio change is small, but the increase is observed in the extinction coefficient values. Compared to CatchER, 149E has a 3.7 fold increase in its extinction coefficient in the apo form, which is the largest increase of all the mutants analyzed. CatchER-T, containing the S175G mutation, also experiences an increase in its extinction coefficient in the apo form, 11.0 ± 0.1 $mM^{-1}cm^{-1}$ compared to 7.1 ± 0.1 $mM^{-1}cm^{-1}$ of CatchER. Through analysis of the 149E variants, the S30R and Y39N mutations decrease the extinction coefficients in the apo form. 149E is the brighter variant with a brightness of 15.0 ± 0.1 $mM^{-1}cm^{-1}$. Only the quantum yield of 149E S30R has a slight increase over that of 149E, 0.7 ± 0.1 compared to 0.6 ± 0.1.

Comparing the optical properties of all the variants with Ca^{2+}, metal binding increases the extinction coefficient and brightness, while slightly decreasing the quantum yield.

4.3.3 pK_a of Ca^{2+} probes.

GFP-based Ca^{2+} probes are inundated with pH sensitivity issues. This problem is primarily caused by the alternate protonation states of the chromophore[244]. Several Ca^{2+} probes utilizing GFP have been applied in mammalian cells to monitor Ca^{2+} changes in real-time[193,196]. In the work presented, 149E is the most pH insensitive CatchER variant with pK_a values around 6.5 for both apo and holo-form. CatchER and CatchER-T have comparable pK_a values above neutral pH. Research has shown the pH of the ER remains neutral during stimulated Ca^{2+} release[257]. This information supports the use of our probes for monitoring ER Ca^{2+} release with minimal pH effects. Because 149E is more resistant to pH changes, it could be applied to other organelles in the cell that contain Ca^{2+} but have a pH below neutral such as the Golgi or early endosomes[258]. Through analysis of the different GFP proteins, several mutations were discovered that made the protein less sensitive to pH, such as the T203I mutation[259,173,260]. This knowledge can be used to implement the necessary point mutations in our sensors to lower the pK_a values further, ensuring the fluorescence of the probe will remain intact in lower pH environments.

4.3.4 Equilibrium dialysis/ICP-OES of CatchER variants

Using the equilibrium dialysis method, we were able to confirm that our sensors are binding Ca^{2+}. The amount of Ca^{2+} found in the buffer samples for each experiment showed that the dialysis system did reach equilibrium and the amount of Ca^{2+} added to the buffer was similar to the amount found in the buffer after equilibration (Appendix B

Tables B.1, B.2, and B.3). The calculated equilibrium dialysis K_d values for D9, D10, CatchER, CatchER-T, and 149E are found in Figure 3.2.5.1D. The K_d calculated for CatchER-T is 8.5 ± 2.2 µM which is much stronger than the 0.3 ± 0.1 mM K_d from the steady state fluorescence titration. The K_d calculated for CatchER is 194.2 ± 67.0 µM which is similar to the published fluorescence K_d[180], but the standard deviation is high which suggests an error in the measurement. In Appendix B Tables B.1, B.2, and B.3, the amount of Ca^{2+} found in the blank dialysis bags were consistently around 1-2 µM higher than the equilibrated buffer 2. The difference between the blank and the equilibrated buffer is the Ca^{2+} that associates with the dialysis bag. Cellulose has been shown to bind Ca^{2+} non-specifically[261]. This finding may suggest that the background Ca^{2+} is 1-2 µM. This error may be due to the purity of the protein or the intensity fluctuation among the different Ca^{2+} emission wavelengths monitored. Binding of Ca^{2+} to the negative controls is occurring even though neither EGFP nor myoglobin have a Ca^{2+} binding site.

Equilibrium dialysis and ultrafiltration are the two most commonly used methods in the pharmaceutical industry to study drug-protein binding. Because of their simplicity, these two approaches can be applied to various organisms for *in vitro* or *in vivo* analysis. Equilibrium dialysis, however, is referred to as the standard method for studying ligand binding. The foundation of the equilibrium dialysis method is centered on forming a balance between a protein and a buffer, containing the ligand, which is separated by a membrane with an appropriate molecular weight cutoff[262]. There are several limitations to the equilibrium dialysis method that can cause an error in the resulting calculated K_d. Equilibration times over 12 h can increase the amount of

sample lost and degraded[253]. Because of the oncotic pressure differences created across the membrane, sample volume can shift between 10-30%[263,264]. Another issue that effects accurate measurements from equilibrium dialysis is the Donnan effect. The Donnan effect arises when two liquid sections containing a mixture of permeable and impermeable charged ions are separated by a semi-permeable membrane. The effect emerges because of the unequal charge distribution of impermeable ions across the membrane[265]. This distorted electrical gradient created across the membrane can alter the measurement. The Donnan effect can be accounted for using various calculations and by increasing the ionic strength of the buffer if the binding event is not electrostatic in nature[266].

4.3.5 Stopped-flow analysis of CatchER variants

The binding kinetics of CaBPs has prominent influence on the shape and duration of the Ca^{2+} signal. CaBPs such as parvalbumin and calretinin have fast on rates and slow off rates with K_d values around 100-200 nM[68]. In order to understand how our sensors will associate with Ca^{2+} inside the cell, we must obtain specific kinetic parameters that directly relate to Ca^{2+} binding. Intracellularly, a large [K^+] helps maintain the resting voltage of the cell at ~70 v. Along with K^+, other monovalent ions such as Na^+, divalent ions such as Mg^{2+}, and small molecules such as ATP exist inside the cell. Fluorescence spectroscopy will be used to measure the binding affinity and metal selectivity of our sensors. To confirm whether or not electrostatic interactions impact the fast release kinetics of CatchER, we used stopped-flow spectroscopy to determine the k_{off} and K_d of CatchER in the absence and presence of 150 mM KCl along with the kinetics of 149E and CatchER-T located in Figure 4.2.12. The k_{off} for

CatchER in 0 M KCl was calculated to be ~67 s^{-1} (Figure 4.2.12E, Table 4.2.4) which is a 10 fold decrease from the reported value[180]. However, the addition of KCl increased the k_{off} of CatchER from 68.3 ± 1.2 s-1 to 308.5 ± 6.7 s-1, a ~4.5 fold increase in the off rate in the presence of 150 mM KCl (Table 4.2.4). There is a possibility that the CatchER sample used to get the published data contained high amounts of salt since after HisTag purification, which elutes the bound protein of interest using an imidazole gradient, only dialysis was performed to remove the imidazole, not gel filtration. All the protein samples used for the kinetics experiments completed for this dissertation were subjected to two steps of purification, HisTag and gel filtration chromatography, to ensure removal of all contaminants and salts. The addition of 150 mM KCl reduced the fluorescence response range of the sensors to Ca^{2+}. The kinetics of 149E and CatchER-T are reported for the first time. Determining the k_{off} of 149E in the presence of KCl increases the value slightly from the value obtained without KCl (Figure 4.2.12A and B, Table 4.2.4). On the other hand, 150 mM KCl increases the k_{off} of CatchER-T by ~3.6 fold compared to the koff with no KCl present (Figure 4.2.12C and D, Table 4.2.4). The stopped-flow Ca^{2+} K_ds for each variant are similar to those calculated from the static fluorescence titrations. The k_{obs} values obtained from fitting the k_{on} traces for each protein could not be fit to a straight line (data not shown) indicating the presence of an intermediate as was seen with Ca-G1[191].

4.3.6 Monitoring ER/SR Ca^{2+} release using CatchER variants

To test the response of some of the new variants in situ, we transfected them into C2C12 myoblast cells. The cells containing CatchER-T and CatchER-T S30R were permeablized with digitonin then exposed to Ca^{2+} to see the response range of the

sensor (Figure 4.2.13). CatchER-T and CatchER-T S30R do respond to Ca^{2+} but not enough cells were analyzed to confirm the response. RyR-mediated SR Ca^{2+} release was triggered with 200 µM 4-cmc and monitored with 149E Y39N (Figure 4.2.13A). Data from five cells was collected. A 6% decrease in SR Ca^{2+} content was seen.

In collaboration with Dr. Heping Cheng, CatchER, CatchER-T', and our mCherry-based probe R-CatchER were used to monitor Ca^{2+} release in neonatal rat ventricular myocytes. RyR2-mediated SR depletion was triggered using caffeine with simultaneous monitoring of cytosolic Ca^{2+} with rhodamine 2 and Fluo 4 (Figure 4.2.14D-F). Fluorescence intensity changes for CatchER, CatchER-T', and R-CatchER, in response to caffeine depletion, are minimal compared to changes seen with the dyes. CatchER had a 15% decrease in fluorescence intensity while CatchER-T' had a 20% decrease in fluorescence. R-CatchER experienced a 5% decrease in intensity. The small changes in Ca^{2+} release are due to the small dynamic range of the sensors.

4.4 Conclusion

The biophysical properties of CatchER variants containing the N149E mutation and brightness mutations S175G, S30R, and Y39N have been reported using spectroscopic methods. The N149E mutation, located in the metal binding site, decreased the affinity for Ca^{2+} of the resulting probe. This data disproved our hypothesis. Errors in the equilibrium dialysis measurement prevented accurate calculation of the Ca^{2+} K_d for the different variants analyzed. 149E variants had large increases in their extinction coefficients compared to CatchER with 149E having the most substantial increase. Compared to CatchER, 149E has a 3.7 fold increase in its extinction coefficient in the apo form, which is the biggest increase of all the mutants

analyzed. CatchER-T, containing the S175G mutation, also experiences an increase in its extinction coefficient in the apo form compared to CatchER. Through analysis of the 149E variants, the S30R and Y39N mutations decrease the extinction coefficients in the apo form. Only the quantum yield of 149E S30R has a slight increase over that of 149E. Comparing the optical properties of all the variants with Ca^{2+}, metal binding increases the extinction coefficient and brightness, while slightly decreasing the quantum yield. Compared to CatchER, 149E has less pH dependence. Kinetic analysis of 149E revealed slower kinetics compared to CatchER. Select variants were also analyzed *in situ* in C2C12 myoblast cells and neonatal rat ventricular myocyte cells. Although the amplitude changes *in situ* were small, we have shown that our sensors can be targeted and expressed in the ER/SR of mammalian cells. As a result of this work, a less pH sensitive CatchER variant was made with a weaker affinity for Ca^{2+} and increased absorption ability, providing another tool that can be used to monitor Ca^{2+} dynamics in the ER/SR in normal and disease states.

5 OPTIMIZATION OF CATCHER AND ITS TARGETED SUBCELLULAR APPLICATION

5.1 Introduction

Ca^{2+} (Ca^{2+}) is an activator of a multitude of cellular processes necessary for the formation and survival of organisms[5]. Initiation of these events is dependent on all the components of the Ca^{2+} signaling toolkit consisting of Ca^{2+} pumps, Ca^{2+} channels, receptors and Ca^{2+} binding proteins (CaBPs) that all respond on different timescales to create the varied Ca^{2+} transients that govern biological function[21]. Inside the cell, Ca^{2+} is primarily stored in the endoplasmic reticulum (ER) or the sarcoplasmic reticulum (SR), its counterpart in muscle cells[84,54]. The ER is the site of protein synthesis and folding inside the cell and is central to Ca^{2+} signaling. The task of converting the extracellular stimulus received into a coded intracellular Ca^{2+} signal, wave or oscillation, lies with the ER/SR and the non-uniform distribution of CaBPs, the sarco-endoplasmic reticulum Ca^{2+} ATPase uptake pump (SERCA), and inositol 1,4,5-triphosphate receptor (IP_3R) and ryanodine receptor (RyR) Ca^{2+} release channels. These modulators of the Ca^{2+} signal create spatially diverse compartments with different Ca^{2+} concentrations within the ER/SR lumen[267]. The morphology of the ER appears as flattened sacs or as a tubule network in the cell. Although the ER can rapidly remodel itself, it often maintains a fixed, complex arrangement that allows it to carry out various tasks in different areas of the cell. In skeletal muscle cells, the SR has a highly specialized arrangement to deliver quickly the Ca^{2+} needed for muscle contraction in response to membrane depolarization[268,84].

The SR forms an elongated meshwork around each myofibril inside the skeletal muscle cell. T tubules are invaginations of the sarcolemma that extend into the myoplasm and surround each myofibril. The T tubules allow rapid diffusion of the sarcolemma depolarization into the muscle fibers. In the muscle fibers, T tubules are situated near the enlarged portions of the SR called the terminal cisternae (TC) in the cytoplasm[54]. The portion of the TC membrane facing the T tubule is called the junctional SR membrane with the space in between termed the junctional zone. Localized in the junctional SR membrane is RyR isoform 1 (RyR1). Protein modulators of RyR1 function include the luminal SR CaBP calsequestrin isoform 1 (CASQ1) and SR integral membrane proteins like junctin and triadin[58]. It is here where the L-type voltage gated Ca^{2+} channels (VGCC), or dihydropyridine receptors (DHPR), organized in tetrads on the portion of the T tubule membrane facing the junctional SR membrane, open in response to membrane depolarization and mechanically activate Ca^{2+} release from the SR through its direct interaction with RyR1s[88,102]. The immense amount of Ca^{2+} released from the SR in response to the action potential fuels excitation-contraction (E-C) coupling[94,269]. The large reservoir of Ca^{2+} required to generate contractile force repetitively from a train of action potentials is maintained by the low affinity, high capacity Ca^{2+} binding and release of CASQ1[95]. CASQ1 is localized in the lumen of the TC where it forms long polymers near the opening of RyR1 in a Ca^{2+} dependent manner[96,97]. Polymerized CASQ1 can bind 40-50 mol of Ca^{2+}/mol of CASQ1 with a 10^3 M^{-1} affinity over a high Ca^{2+} concentration range of 0.01-1 M. Its exceptional buffering function makes CASQ1 the sole mechanism for fast Ca^{2+} binding and release

from the SR. CASQ polymers interact directly with the luminal opening of the RyR or through interactions with junctin and triadin[96,98].

Since these indigenous junctional zone proteins are directly involved in generating contractile force in this highly specialized location of the cell, their dysfunction negatively affects intracellular and SR Ca^{2+} regulation causing various muscle pathologies[116]. Malignant hyperthermia (MH) is a genetic skeletal muscle disease caused by mutations in the gene encoding RyR1[111]. Clinical hallmarks of MH include rapid heart rate, high blood pressure, sustained muscle contractions, increased CO_2 levels, trouble breathing, and a rapid and often fatal rise in core body temperature[113]. Untimely diagnosis of MH leads to death. The hypermetabolic state seen in MH patients is attributed to escalated Ca^{2+} release from the SR caused by defects in mutated RyR1 situated on the junctional SR membrane[112,113]. Hundreds of mutations in the human RyR1 have been identified so far and causally linked to MH with research still ongoing. The majority of these mutations are confined to three locales in RyR1: C35-R614 in the N-Terminal, D2129-R2458 in the central region, and I3916-G4942 in the carboxy terminal, but more recently mutations have been identified outside of these domains[114]. MH mutations have also been identified in the human CACNL1A3 gene coding the α_1 subunit of the DHPR located on the sarcolemma[115]. The DHPR and the RyR1 are in close contact with one another. When skeletal muscle cells are depolarized, the DHPR converts the voltage change to a conformational change that triggers SR Ca^{2+} release through the RyR1 leading to muscle contraction in a process known as excitation-contraction coupling (E-C coupling)[270]. In MH, mutations in RyR1 and the DHPR cause a gain of function in E-C coupling[112]. Mutations in RyR1,

however, are not found in all cases of MH which implies dysfunction in other associated proteins. Deletion of the CASQ1 gene in mice prompts increases in sudden death from MH and environmental heat stroke (EHS) events in reaction to volatile anesthetics and heat exposure[271,272]. Missense mutations D244G and M87T in CASQ1 significantly modify its Ca^{2+} dependent functions in SR Ca^{2+} release[273].

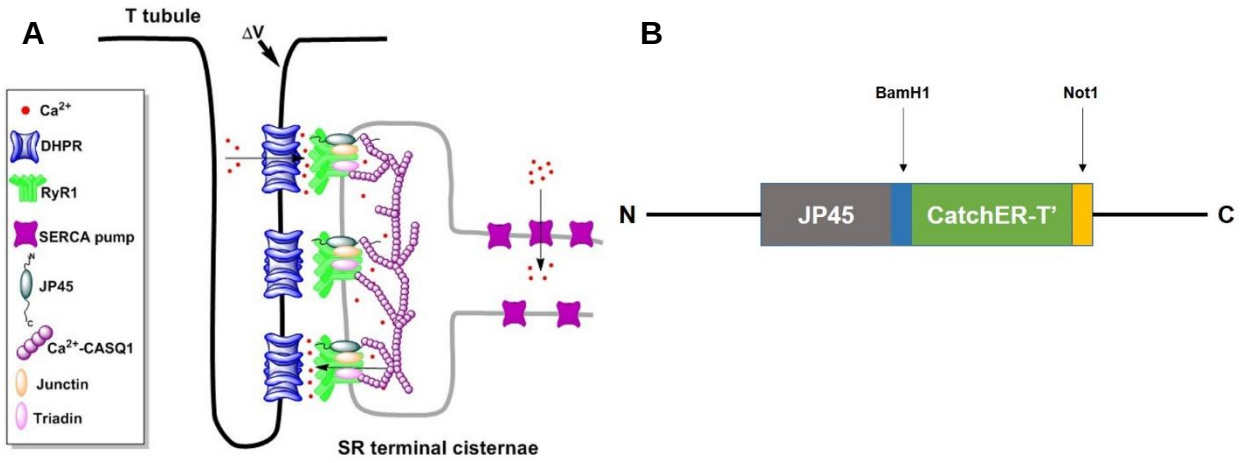

Figure 5.1.1 Design of a targeted CatchER probe to monitor local Ca^{2+} in the junctional SR lumen

A) Representation of the organization of the junctional zone and the channels, receptors, pumps, and proteins involved in the E-C coupling process in skeletal muscle cells. Modified from Divet, et al., *Journal of Muscle Research and Cell Motility*, 2005. B) CatchER and CatchER-T' is located at the C-terminal of JP45 in the pDsRed2-N3 vector between the BamH1 (blue) and the Not1 (orange) restriction enzyme sites.

As shown in Figure 5.1.1A, an additional protein in skeletal muscle called JP45 was found associated with the junctional zone and plays a major role in E-C coupling. JP45 is a 45 kDa transmembrane protein found in the SR junctional face membrane. Francesco Zorzato and colleagues were the first to identify JP45 from TC fractions isolated from skeletal muscle tissue of New Zealand White rabbits. Through Western blot, immunoprecipitation, and immunoblotting experiments, JP45 was shown to be

localized in the junctional SR membrane of fast and slow twitch skeletal muscle. Its presence in the same fraction where other junctional proteins such as RyR and triadin were found eluded to the association of JP45 with these proteins and subsequently E-C coupling[99]. Later, Ayuk Anderson et al. showed that JP45 interacts with the α1 subunit of the DHPR via its N-terminal cytosolic domain and with calsequestrin (CASQ1) via its C-terminal situated in the SR lumen, of which both are found in the junctional face membrane[100]. Because the junctional zone and the associated proteins are needed to store and release large amounts of Ca^{2+} from the SR to facilitate E-C coupling and abnormalities in these proteins can result in neuromuscular diseases, it is important to have a probe that can monitor the rapid fluxes in Ca^{2+} in these subcellular microdomains, to dissect the molecular and physiological basis of neuromuscular diseases linked to abnormal E-C coupling. Since the architecture and arrangement of proteins and receptors in this area of the SR are different compared to the rest of the organelle, changes in local Ca^{2+} near the junctional face SR membrane might be different in comparison to Ca^{2+} changes in the global SR lumen. The questions to be answered are can we create a probe with good fluorescence at 37°C to monitor the fast changes in Ca^{2+} concentration that occur during E-C coupling? Can we use this new probe to see the difference in local and global Ca^{2+} signaling events?

The goals of the research outlined here are to identify mutations that can be made to the GFP scaffold of CatchER to improve its fluorescence *in situ* at 37˚C and to use the optimized sensor to look at Ca^{2+} flux in the global and local environment of the SR in skeletal muscle cells. Here, we report the improved version of our Ca^{2+} probe CatchER called CatchER-T'. Although CatchER has fast kinetics with a k_{off} of ~700 s^{-1}, it does

not fluoresce when expressed at 37°C in mammalian cells[180]. To improve its fluorescence at 37°C, we incorporated two key mutations from superfolder GFP that were deemed important for improving the folding and subsequent fluorescence at 37°C: S30R and Y39N. S30R had the most profound effect on refolding kinetics and brightness after urea denaturation due to its involvement in the creation of a five residue ionic network that increases the overall stability of GFP because of the energetic advantage of organized ion pair networks. Y39N introduces a new hydrogen bond in the β-turn it resides in, converting the turn into a more stable 3_{10} helix[169]. We hypothesize that incorporating these two mutations into CatchER would improve its fluorescence for mammalian cell imaging and not alter the K_d of the probe since these mutations are distant from the metal binding site. We also hypothesize that the Ca^{2+} transient produced from local Ca^{2+} release near the luminal opening of the RyR1, monitored by our targeted construct CatchER-T'-JP45, would be strongly buffered by CASQ1 and would appear vastly different in comparison to the global decrease in Ca^{2+} that occurs when monitoring Ca^{2+} changes with CatchER-T'.

5.2 Results

5.2.1 Design of CatchER-T' and CatchER-T'-JP45

Although our highly touted sensor CatchER has fast binding kinetics and a K_d weak enough to accurately sense Ca^{2+} in the high Ca^{2+} environment of the ER/SR, it does not express well at ambient temperature which hinders *in situ* application in some cell lines[180]. The S30R and Y39N mutations were made to CatchER based on a review of superfolder GFP. In the study of superfolder GFP, the S30R and Y39N mutations were shown to have the largest effect on the brightness of the protein at 37°C by

improving folding and stabilization. S30R had the most profound effect on refolding kinetics and brightness after urea denaturation due to its involvement in the formation of an intramolecular electrostatic network comprised of residues E32-R30-E17-R122-E115. This system produced by the S30R mutation improves the overall stability of the protein due to the energetic advantage of organized ion pair networks. Y39N is located in one of two type 1 beta turns in superfolder GFP between strands 2 and 3. Making the Y39N mutation converts both turns into a 3_{10} helix. The additional H-bond alters the dihedral angles of the backbone making the turn tighter to boost helix formation[169]. The S175G mutation was also introduced into the sensor to improve the thermostability[274]. Mutations were made using Pfu DNA polymerase using 5'-AAGTTCAGCGTGCGCGGCGAGGGCGAG-3' and 5'-CTCGCCCTCGGCGCGCACGCTGAACTT-3' for S30R, 5'-GGCGATGCCACCAACGGCAAGCTG-3' and 5'-CAGCTTGCCGTTGGTGGCATCGCC-3' for Y39N, and 5'-GAGGACGGCGGCGTGCAGCT-3' and 5'-AGCTGCACGCCGCCGTCCTC-3' for S175G.

JP45 was received in the pDsRed2-N3 vector. DsRed was located at the C-terminal of JP45 between the BamH1 and Not1 restriction enzyme sites. The pDsRed2-N3 vector was digested with BamH1 and Not1 to remove DsRed. In the pcDNA3.1+ vector, CatchER is between the BamH1 and EcoR1 restriction enzyme sites. There is an additional Not1 cleavage site after the EcoR1 site in the CatchER plasmid. After treatment of both plasmids with BamH1 and Not1 restriction enzymes, the products were subjected to DNA agarose gel electrophoresis (Figure 5.2.1). The JP45 vector

cleavage product and the excised CatchER fragment were extracted and purified from the DNA gel and ligated together using T4 DNA ligase. The forward primer 5'-GAGAAGCCAAGTAAAGGGGAGAAACTGAAG-3' taken from the C-terminal DNA sequence at the end of JP45 was used to confirm the successful addition of CatchER in the JP45 vector. To create CatchER-T'-JP45, PCR was done using the CatchER-JP45 plasmid to make the S30R, Y39N, and S175G mutations. The sequence was confirmed using the JP45 forward primer.

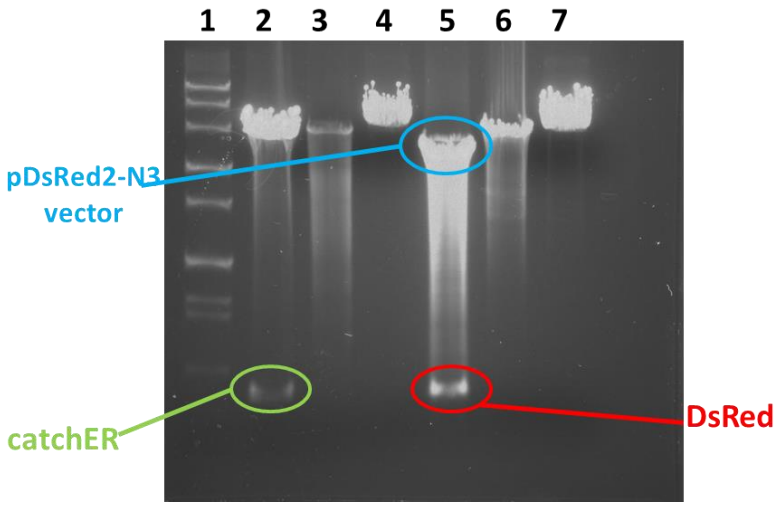

Figure 5.2.1 Double digestion of CatchER pcDNA+3.1 vector and JP45 pDsRed2-N3 vector using BamH1 and Not1 restriction enzymes.

The pDsRed2-N3 vector containing JP45 and the CatchER pcDNA3.1+ vector were both subjected to restriction enzyme digest with BamH1 and Not1 enzymes. Lane 1 is the DNA marker, lane 2 is the CatchER pcDNA3.1+ vector digest with the excised CatchER fragment circled in green, lane 3 is the CatchER plasmid treated with BamH1, lane 4 is the CatchER plasmid treated with Not1, lane 5 is the JP45 pDsRed2-N3 vector digest with the excised DsRed fragment circled in red and the cleaved vector circled in blue, lane 6 is the pDsRed2-N3 vector treated with BamH1, and lane 7 is the pDsRed2-N3 vector treated with Not1. T4 DNA ligase was used to fuse the cut CatchER fragment from lane 2 and the cut JP45 vector from lane 5 to create CatchER-JP45.

5.2.2 Expression and purification of CatchER-T variants

Our GECI CatchER was created to monitor Ca^{2+} transients in the ER/SR and measure Ca^{2+} concentration in said organelles through a novel mechanism where the binding of Ca^{2+} on the surface of the protein induces an increase in fluorescence intensity. Because of the poor performance of CatchER at 37°C in mammalian cells, the probe was optimized to improve the fluorescence at 37°C resulting in the CatchER-T series of variants. To obtain large amounts of the probes for *in vitro* analysis, the sensors needed to be expressed and purified with high yield. Figure 5.2.2A shows the optical density of the BL21 (DE3) cells during overexpression of CatchER-T variants from all four flasks. Figure 5.2.2B shows the expression gel of the sensors. SDS-PAGE gel analysis shows a clear increase of protein expressed after induction with IPTG.

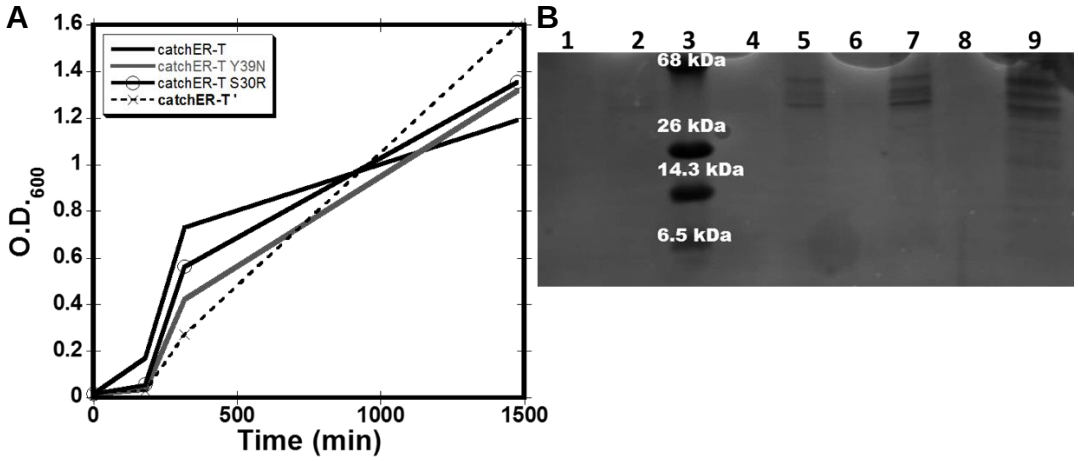

Figure 5.2.2 Overexpression of CatchER-T' and its variants in BL21(DE3) cells

The DNA for each of the plasmids in the pET28a bacterial expression vector was transformed into BL21 (DE3) cells. One colony from each of the four plates was taken to inoculate 10 mL of LB media. The pre-culture was added to 1 L of LB with 600 uL of kanamycin and allowed to grow in a shaker at 37°C until the O.D. reached 0.6 (A) when cells were induced with 200 µL of 1 M IPTG, reducing the temperature to 25°C. The

bacteria grew well for each of the four mutants. B) Expression samples taken before and after induction were used to run the SDS-PAGE gel confirming the proteins were expressed. Lanes 1 and 2 are CatchER-T before and after induction, lane 3 is the protein marker, lanes 4 and 5 are CatchER-T Y39N before and after induction, lanes 6 and 7 are CatchER-T S30R before and after induction, and lanes 8 and 9 are CatchER-T' before and after induction.

After overexpression of the new variants, the cell pellets were collected. For protein purification, the selected pellet was sonicated in 20-30 mL of extraction buffer to break the cells and release the protein. After centrifugation of the cell lysate, the supernatant containing the protein of interest was purified using HisTag purification on a Ni^{2+}-NTA column using an imidazole gradient. The HisTag chromatogram and SDS-PAGE gel for CatchER-T' is shown in Figure 5.2.3A. SDS-PAGE analysis of the fractions collected from HisTag purification show the purity of CatchER-T' compared to the cell pellet (CP) and the supernatant (SP). Gel filtration was employed as an additional purification step to ensure a quality protein sample. Figure 5.2.3B shows the pure protein peak, circled in red, on the gel filtration chromatogram, and the inset SDS-PAGE gel shows the purity of the fractions collected. CatchER-T, CatchER-T S30R, and CatchER-T Y39N were also purified with results located in Figure 5.2.4.

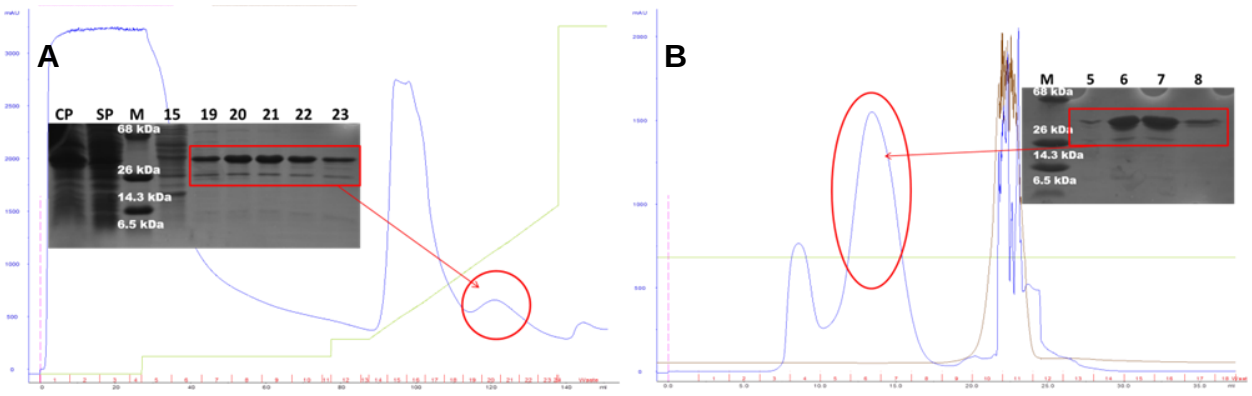

Figure 5.2.3 HisTag purification and gel filtration of CatchER-T'

A) The supernatant obtained from the sonicated BL21 (DE3) cells was syringe filtered and loaded onto a 5 mL HiTrap chelating column containing immobilized Ni^{2+} using Buffer A at a 5 mL/min flow rate. The protein was eluted at the same rate using Buffer B containing 500 mM imidazole. The first peak in the chromatograms is the cell debris being washed away during loading. The peaks containing the sensor proteins are circled in red. SDS gel analysis shows clear protein bands for the sensors near the 26 kDa marker. B) Purified CatchER-T' was concentrated to 2 mL and loaded onto a Superdex 75 column using 10 mM Tris pH 7.4 at 1 mL/min. The protein was eluted out in 2 mL fractions. The resulting SDS-PAGE gel shows a high concentration of pure protein. Protein peak in the gel filtration chromatogram is circled in red.

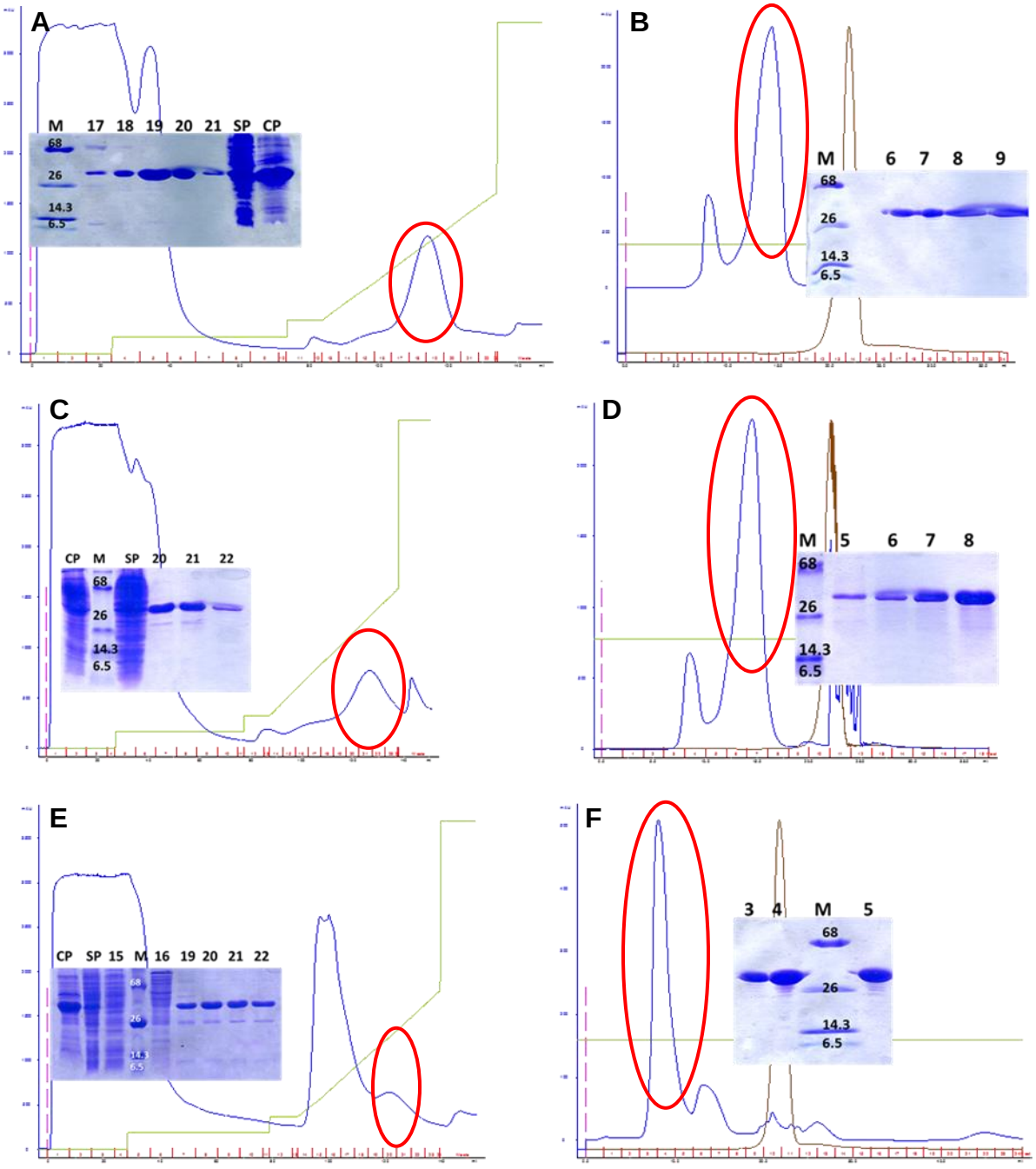

Figure 5.2.4 HisTag purification and gel filtration of CatchER-T variants

Representative purification data for CatchER-T (A, HisTag; B, gel filtration), CatchER-T S30R (C, HisTag; D, gel filtration), and CatchER-T Y39N (E, HisTag; F, gel filtration). The supernatant obtained from the sonicated BL21 (DE3) cells was syringe filtered and loaded onto a 5 mL HiTrap chelating column containing immobilized Ni^{2+} using Buffer A at a 5 mL/min flow rate. The protein was eluted at the same rate using Buffer B containing 500 mM imidazole. The first peak in the chromatograms is the cell debris being washed away during loading. The peaks containing the sensor proteins are circled in red. Inset SDS gel analysis shows clear protein bands for the sensors near

the 26 kDa marker. B) Purified CatchER-T variants were concentrated to 2 mL and loaded onto a Superdex 75 column using 10 mM Tris pH 7.4 at 1 mL/min. The protein was eluted out in 2 mL or 8 mL fractions. The resulting inset SDS-PAGE gels show a high concentration of pure protein.

The S175G mutation is known to improve the folding at 37°C for GFP proteins, reducing their thermosensitivity[274]. The S30R and Y39N mutations were incorporated in succession into CatchER to improve the fluorescence of the sensor for 37°C expression in mammalian cells (Figure 5.2.5A). To see if the mutations did improve the thermostability and brightness of the sensor at 37°C, each variant, including CatchER, was expressed in C2C12 myoblast cells at 37°C. C2C12 cells were seeded and transfected on glass microscope slides in 6 cm dishes. The slides were mounted and viewed under a fluorescence microscope. Images were taken from 8 fields of view on each slide. The intensity of the cells from each area was quantified using Image J and plotted with error using K-graph. The bar graph of the intensity measurement for each variant expressed in C2C12 myoblast cells is located in Figure 5.2.5B. Of the variants created, CatchER-T' containing all three mutations, was the brightest at 37°C expression compared to CatchER. Because CatchER-T' was the brightest variant, subsequent cell imaging studies were done using this variant.

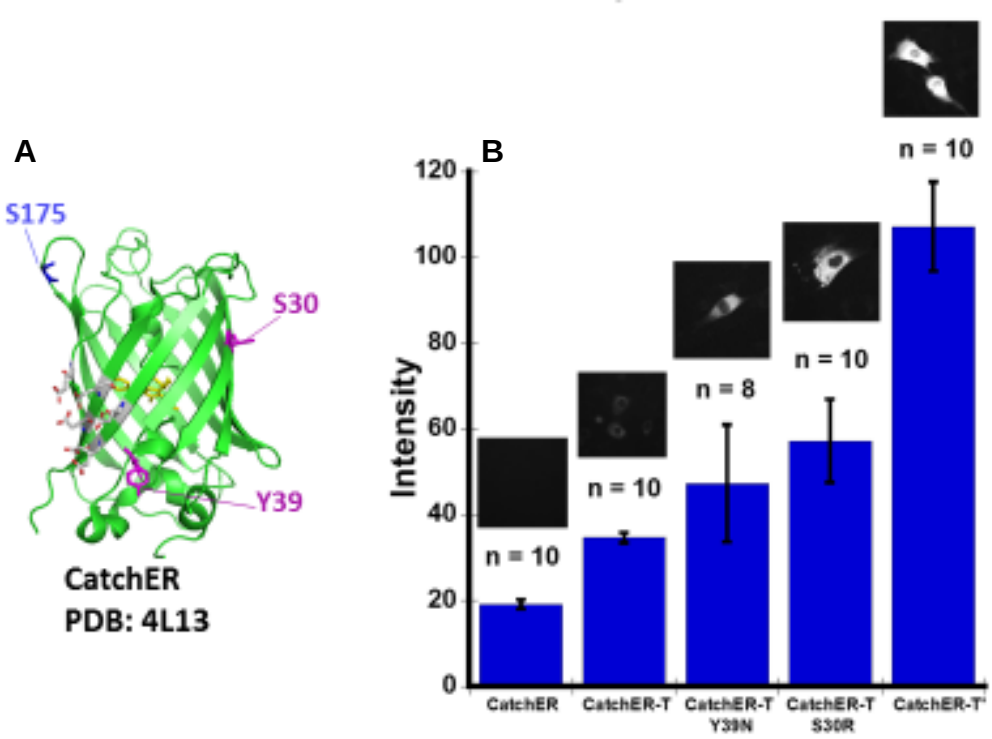

Figure 5.2.5 Brightness of CatchER-T variants expressed in C2C12 myoblast cells at 37°C

A) Position of brightness mutations S175G, S30R and Y39N in relation to the Ca^{2+} binding site in CatchER created in Pymol. B) DNA from CatchER and CatchER-T variants was transfected into C2C12 myoblast cells for 24 h, using a 1:4 DNA:Effectene ratio, at 37°C. Variants were expressed in C2C12 myoblast cells at 37°C for 48 h and imaged using a Leica DM6100B inverted microscope with a cooled EM-CCD camera. Cells were viewed through a 40X oil immersion objective with and exposure time of 0.07 s and a gain of 175. The fluorophore was excited at 488 nm with emission monitored at 510.fluorescence microscope with a 0.7 s exposure time and a gain of 175. Images from eight fields of view were taken from each slide. The intensity of the cells from each image was measured using ImageJ subtracting the background from each. The error was calculated from all the cells analyzed for each variant where n equals the number of cells.

5.2.3 In vitro and in situ Ca^{2+} K_d of CatchER-T'

Fluorescence measurements of CatchER-T' with increasing Ca^{2+} concentrations were done in order to obtain the affinity of the sensor for Ca^{2+} *in vitro* (Figure 5.2.6) as detailed in Chapter 2 section 2.14. Triplicate samples of 10 µM CatchER-T' were

prepared and titrated with 0.15, 0.3, 0.4, 0.5, 0.7, 1, 3, 5, 8, 10, and 15 mM Ca^{2+} with 10 µM EGTA added to the samples to get the basal fluorescence (0 mM Ca^{2+}). The absorbance spectrum from one sample reveals the decrease in the 395 nm excitation peak and the increase of the 488 nm excitation peak with saturating levels of Ca^{2+} (solid line) compared to without Ca^{2+} (dashed line) observed in Figure 5.2.6A. CatchER-T' has an incremental increase in fluorescence intensity corresponding to the addition of Ca^{2+} when excited at both 395 nm and 488 nm with emission monitored at 510 nm for both. The data was normalized using Equation 2.17. The inset binding curves fit to a 1:1 binding equation (Equation 2.18) with K_d values of 1.1 ± 0.1 mM and 1.3 ± 0.2 mM at 395 nm and 488 nm excitation, respectively (Figures 5.2.6B and C). Figure 5.2.7 shows the in vitro Ca^{2+} K_d data for CatchER (Figure 5.2.7A-C), CatchER-T (Figure 5.2.7D-F), CatchER-T Y39N (Figure 5.2.7G-I), and CatchER-T S30R (Figure 5.2.7J-L). Fluorescence spectra for Ca^{2+} titrations done in the presence of 150 mM KCl are located in Appendix C Figure C.1.

Table 5.2.1 *In vitro* Ca^{2+} K_d data for CatchER-T variants

		No KCl		150 mM KCl	
	λ_{ex} (nm)	**K_d (mM)**	**F_{max}/F_{min}**	**K_d (mM)**	**F_{max}/F_{min}**
CatchER	**395**	0.3 ± 0.1	1.7 ± 0.1	1.8 ± 0.2	1.2 ± 0.1
	488	0.2 ± 0.1	1.6 ± 0.1	0.9 ± 0.2	1.1 ± 0.2
CatchER-T	**395**	0.4 ± 0.1	2.1 ± 0.1	NR	NR
	488	0.3 ± 0.1	2.1 ± 0.1	1.7 ± 0.1	1.3 ± 0.1
CatchER-T S30R	**395**	0.8 ± 0.2	1.9 ± 0.1	2.4 ± 0.2	1.4 ± 0.1
	488	1.0 ± 0.2	1.5 ± 0.1	5.1 ± 1.2	1.1 ± 0.1
CatchER-T Y39N	**395**	1.7 ± 0.3	1.9 ± 0.1	3.4 ± 0.3	1.4 ± 0.1
	488	2.0 ± 0.6	1.5 ± 0.1	0.8 ± 0.1	1.2 ± 0.1
CatchER-T'	**395**	1.1 ± 0.1	1.8 ± 0.1	-------	-------
	488	1.3 ± 0.2	1.6 ± 0.1	-------	-------

*Data represents mean ± stdev. K_d – dissociation constant, λ_{ex} – excitation wavelength, F_{max}/F_{min} – dynamic range in response to Ca^{2+} calculated using the fluorescence at maximal saturation divided by the fluorescence with no Ca^{2+} present. Data collected at room temperature. Samples prepared in 10 mM Tris pH 7.4 with or without 150 mM KCl. Fluorescence slit widths were 0.25 mm for excitation and emission. Dashed lines indicate data not available. NR – no response.

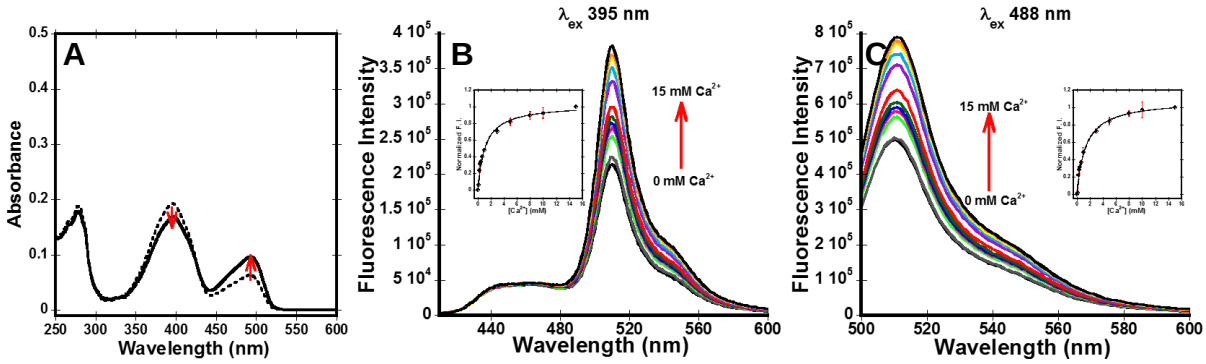

Figure 5.2.6 *In vitro* Ca^{2+} K_d of CatchER-T' via fluorescence spectroscopy

A) Absorbance spectra of 10 µM CatchER-T' sample before titration with 10 µM EGTA (dashed line) and after titrating up to 10 mM Ca^{2+} (solid line). Red arrows indicate the increase and decrease in the 488 nm and 395 nm excitation peaks with the addition of Ca^{2+}. B and C) Fluorescence increase of CatchER-T' in response to the stepwise addition of Ca^{2+} excited at 395 nm and 488 nm, respectively, and monitored at 510 nm. Slit widths for excitation and emission were 0.25 mm. The fluorescence intensity was normalized and plotted against [Ca^{2+}] to get the inset K_d curves for each excitation wavelength. The average K_d from all three trials for each excitation wavelength were 1.1 ± 0.1 mM and 1.3 ± 0.2 mM, respectively.

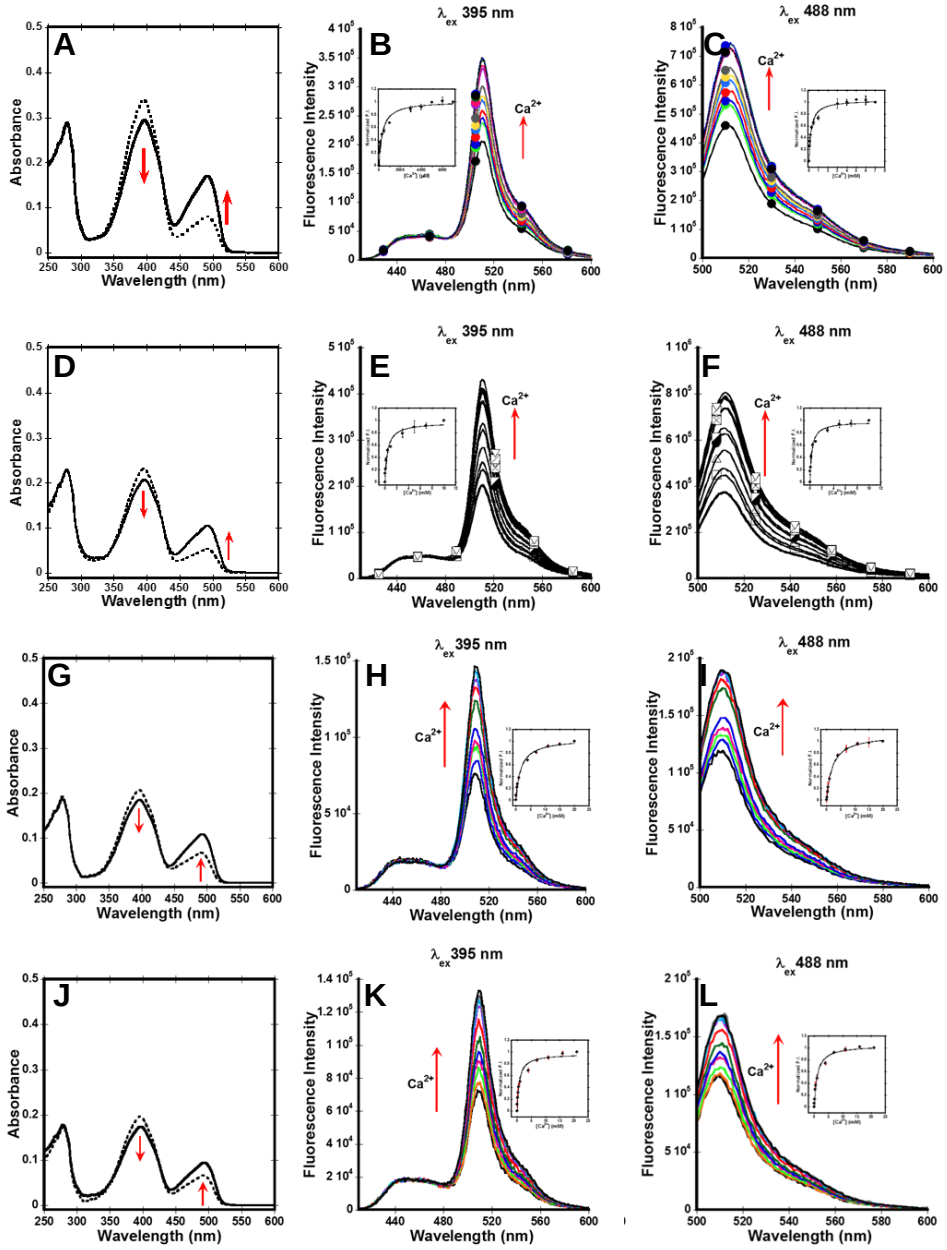

Figure 5.2.7 *In vitro* Ca^{2+} K_d of CatchER (A-C), CatchER-T (D-F), CatchER-T Y39N (G-I), and CatchER-T S30R (J-L) via fluorescence spectroscopy

(A, D, G, J) Absorbance spectra of 10 µM of the protein sample before titration with 5 µM EGTA (dashed line) and after with a saturating amount of Ca^{2+} (solid line). The population of the anionic chromophore, corresponding to the 488 nm peak, increases and the amount of neutral chromophore, corresponding to the 395 nm peak, decreases with increasing Ca^{2+}. (B and C). Fluorescence increase of CatchER in response to 0-7 mM Ca^{2+}. (E and F) Fluorescence increase of CatchER-T in response to 0-10 mM Ca^{2+}. (H and I) Fluorescence increase of CatchER-T Y39N in response to 0-20 mM Ca^{2+}. (K

and L) Fluorescence increase of CatchER-T S30R in response to 0-21 mM Ca^{2+}. All samples were excited at 395 nm and 488 nm with emission scanned from 410-600 nm for 395 nm excitation and from 500-600 nm for 488 nm excitation. Slit widths for excitation and emission were 0.25 mm. Inset curves show the normalized fluorescence intensity data fit to the 1:1 binding equation to get the K_d.

In order to understand how effective our sensor is for sensing ER/SR Ca^{2+} levels, we determined the K_d *in situ* in C2C12 and HEK293 cells. Ions such as, Mg^{2+}, Na^+, K^+, and small physiological molecules exist in the ER/SR concurrently with Ca^{2+} [275]; therefore, the *in situ* K_d is more accurate than the *in vitro* K_d since it reflects its value in a physiological system. The data was collected as outlined in Chapter 2 section 2.21. C2C12 myoblast cells were permeabilized with 0.005% saponin for ~15 s then washed with 1 mM EGTA in KCl buffer containing 10 µM ionomycin. Ca^{2+} concentrations were added in a stepwise manner. The data was normalized using Equation 2.17 and fitted using Equation 2.18. The average K_d was 3.1 ± 1.4 mM for 7 cells (Figure 5.2.8A). The same protocol was followed for HEK293 cells permeabilized with 0.002% saponin for 30 s to get an average K_d of 3.2 ± 1.4 mM for 11 cells (Figure 5.2.8B).

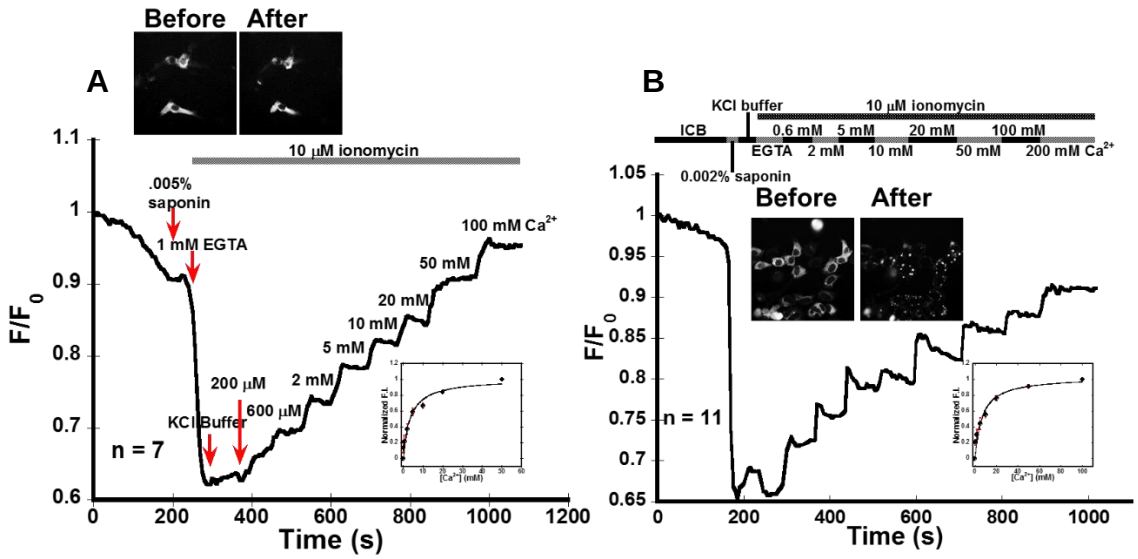

Figure 5.2.8 *In situ* Ca^{2+} K_d of CatchER-T'

Measurement of the *in situ* K_d of CatchER-T' in C2C12 myoblasts (A) and HEK293 cells (B). Cells were imaged using a Leica DM6100B inverted microscope with a cooled EM-CCD camera. Cells were viewed through a 40X oil immersion objective with and exposure time of 0.07 s and a gain of 175. The fluorophore was excited at 488 nm with emission monitored at 510. Cells were permeabilized with 0.005% or 0.002% saponin in intracellular buffer for 15-30 s. EGTA and Ca^{2+} solutions were prepared in KCl buffer. n refers to the number of cells imaged. Inset fluorescence images are representative of cells before and after treatment. A). 0.3, 0.6, 2, 5, 10, 20, 50, and 100 mM Ca^{2+} was added to permeabilized C2C12 myoblast cells in the presence of 10 µM ionomycin to get a K_d of 3.1 ± 1.4 mM. B). 0.6, 2, 5, 10, 20, 50, 100, and 200 mM Ca^{2+} was added to permeabilized HEK293 cells in the presence of 10 µM ionomycin to get a K_d of 3.2 ± 1.4 mM.

5.2.4 Monitoring drug effects on receptor-mediated ER/SR Ca^{2+} signaling pathways with CatchER-T'

We examined the ability of CatchER-T' to monitor changes in $[Ca^{2+}]_{ER/SR}$ in mouse skeletal muscle cells (C2C12 myoblasts), African green monkey kidney cells (Cos-7), and human embryonic kidney (HEK293) cells. Figure 5.2.9 shows the response of CatchER-T' in C2C12 myoblast cells to application of 2 µM thapsigargin (Figure 5.2.9A), 10 mM caffeine (Figure 5.2.9B), 100 µM ATP with cytosolic Ca^{2+} monitored with Rhod-2

AM (Figure 5.2.9C), 200 µM 4-cmc (Figure 5.2.9D), 100 µM ATP (Figure 5.2.9E), and 15 µM CPA (Figure 5.2.9F). 4-cmc addition produced a 30.0 ± 7.0% change in the fluorescence intensity of CatchER-T' which directly correlates with a 30% decrease in $[Ca^{2+}]_{ER/SR}$ (Table 5.2.2). After treatment with caffeine (Figure 5.2.9B), 4-cmc (Figure 5.2.9D), ATP (Figure 5.2.9E), and CPA (Figure 5.2.9F), fluorescence intensity returned to baseline by washing with 6 mL of Ringer's buffer containing 1.8 mM Ca^{2+}, indicating refilling of the SR through the SERCA pump. Because thapsigargin is an irreversible inhibitor of the SERCA pump, no recovery occurred after washing with Ringer's buffer (Figure 5.2.9A). No SR refilling was seen in cells treated with 100 µM ATP loaded with rhodamine 2 after washing with Ringer's buffer. Cytosolic $[Ca^{2+}]$ does increase with ATP activation of the purinergic receptor (Figure 5.2.9C).

In Cos-7 cells, 15 µM CPA produced a 26.0 ± 6.0% decrease in the fluorescence signal of CatchER-T', and ATP produced a 13.0 ± 3.0% decrease in intensity (Figure 5.2.10). The basal fluorescence intensity returned to baseline when the cells were washed with 6 mL Ringer's buffer after treatment. We then looked at the response of CatchER-T' in HEK293 cells (Figure 5.2.11). SERCA pump inhibition with CPA produced a 21% decrease in fluorescence intensity (Figure 5.2.11C).

Table 5.2.2 Analysis of CatchER-T' response to different drugs in different cell types

	CatchER-T'											CatchER-JP45	
	C2C12					Cos-7		HEK293				C2C12	
	4-cmc	CPA	ATP	thaps	caffeine	CPA	ATP	4-cmc	CPA	ATP	caffeine	4-cmc	CPA
Time to peak (s)	97.1 ± 31.5	158.0 ± 58.5	182.5 ± 17.7	145.0 ± 26.0	116.5 ± 22.8	113.0 ± 2.7	202.5 ± 15.0	118.2 ± 5.0	148.7 ± 12.3	180.0 ± 36.6	344.0 ± 43.3	78.7 ± 8.5	195.0 ± 7.1
$\Delta F/F_0$ (%)	30.0 ± 7.0	21.3 ± 4.0	13.0 ± 2.5	5.4 ± 2.7	6.2 ± 2.0	26.0 ± 6.0	13.0 ± 3.0	12.0 ± 2.2	21.0 ± 3.0	6.0 ± 3.0	7.3 ± 0.6	13.2 ± 7.6	15.1 ± 2.8
# of cells	7	5	5	3	5	10	9	8	14	4	8	6	2

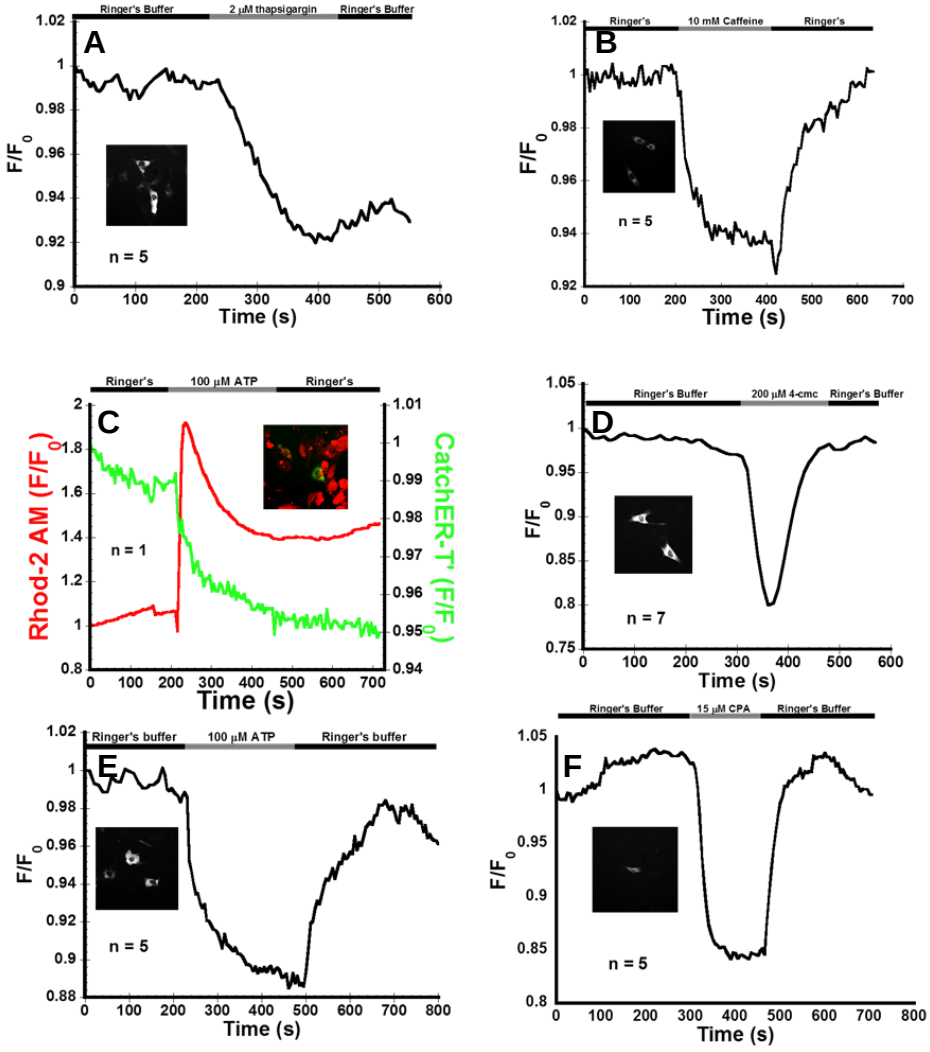

Figure 5.2.9 Monitoring changes in $[Ca^{2+}]_{ER/SR}$ induced by receptor agonists and antagonists in C2C12 cells with CatchER-T'

A-F) Cells were transfected with a 1:4 DNA to Effectene ratio (2 µg of DNA and 8 µL of Effectene) for 24 h in 3 mL of DMEM mixed with 2 mL of OPTI MEM at 37°C. Cells were imaged using a Leica DM6100B inverted microscope with a cooled EM-CCD camera. Cells were viewed through a 40X oil immersion objective with and exposure time of 0.07 s and a gain of 175. The fluorophore was excited at 488 nm with emission monitored at 510.A frame was taken every 5 s. Experiments were done in Ringer's buffer containing 10 mM glucose and 1.8 mM Ca^{2+}. n refers to the number of cells. Inset fluorescence images are representative of cells before treatment. A) Treatment with 2 µM thapsigargin in Ringer's buffer with 1.8 mM Ca^{2+}. B) Treatment with 10 mM caffeine. C) Treatment of cells with 100 µM ATP with cytosolic Ca^{2+} monitored with Rhodamine 2. D) Treatment with 200 µM 4-cmc. E) Treatment with 100 µM ATP. F) Treatment with 15 µM CPA.

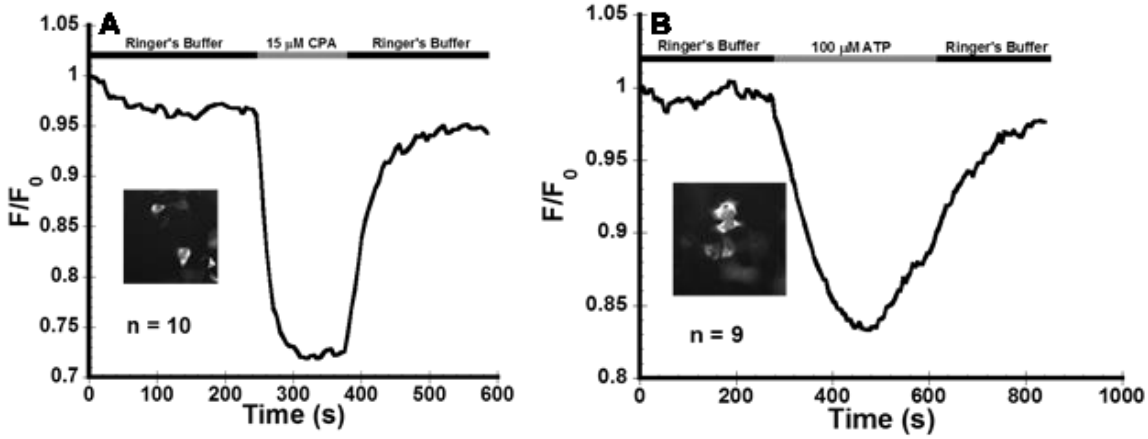

Figure 5.2.10 Monitoring changes in $[Ca^{2+}]_{ER/SR}$ induced by receptor agonists and antagonists in Cos-7 cells with CatchER-T'

Cells were transfected with a 1:4 DNA to Effectene ratio (2 µg of DNA and 8 µL of Effectene) for 4 h in 3 mL of DMEM mixed with 2 mL of OPTI MEM at 37˚C. Cells were imaged using a Leica DM6100B inverted microscope with a cooled EM-CCD camera. Cells were viewed through a 40X oil immersion objective with and exposure time of 0.07 s and a gain of 175. The fluorophore was excited at 488 nm with emission monitored at 510.A frame was taken every 5 s. Experiments were done in Ringer's buffer containing 10 mM glucose and 1.8 mM Ca^{2+}. n refers to the number of cells. Inset fluorescence images are representative of cells before treatment. A) Cells were treated with 15 µM of SERCA pump inhibitor CPA. B). Cells were treated with 100 µM of purinergic receptor agonist ATP.

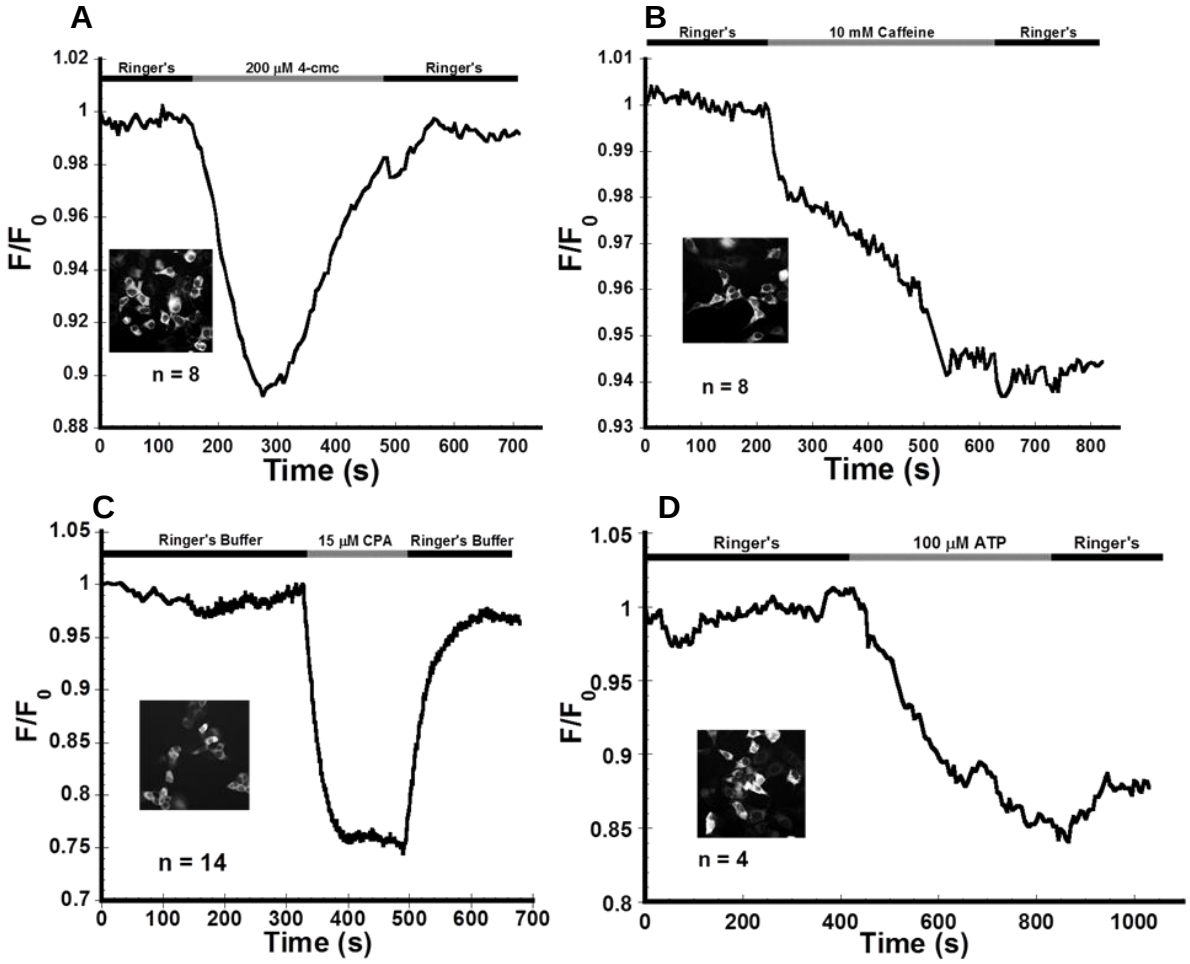

Figure 5.2.11 Monitoring changes in $[Ca^{2+}]_{ER/SR}$ induced by receptor agonists and antagonists in HEK293 cells with CatchER-T'

Cells were imaged using a Leica DM6100B inverted microscope with a cooled EM-CCD camera. Cells were viewed through a 40X oil immersion objective with and exposure time of 0.07 s and a gain of 175. The fluorophore was excited at 488 nm with emission monitored at 510.CatchER-T' was viewed through a 40X oil immersion objective and excited at 488 nm using the Till polychrome V light source with the gain set at 175 and an exposure time of 0.07 s. A frame was taken every 5 s. Experiments were done in Ringer's buffer containing 10 mM glucose and 1.8 mM Ca^{2+}. n refers to the number of cells. Inset fluorescence images are representative of cells before treatment. Cells were treated with A). 200 μM 4-cmc, B). 10 mM caffeine, C). 15 μM CPA, and D). 100 μM ATP.

5.2.5 Understanding local vs. global SR Ca^{2+} dynamics using JP45 targeted constructs

Local changes in luminal SR Ca^{2+} near the opening of the RyR1 effect the process of contraction in muscle cells as opposed to global levels of SR Ca^{2+} because of the buffering role of CASQ1[96]. To visualize the difference in Ca^{2+} release events near the junctional SR membrane and in the longitudinal SR, the CatchER-T' and CatchER-T'-JP45 constructs were both expressed in these regions of FDB fibers by Dr. Francesco Zorzato and colleagues in Switzerland. Table 5.2.3 lists the data comparing the amplitude changes, time to peak, half relaxation time, and Vmax for transients monitored with both constructs from nine cells. Figure 5.2.12A-C show the expression patterns for both Ca^{2+} probes in FDB fibers. Figure 5.2.12D shows the resulting Ca^{2+} transients from electrical stimulation with a 100 Hz pulse for 300 ms. The peak amplitude change is much larger for CatchER-T'-JP45 compared to CatchER-T'.

Table 5.2.3 Analysis of electrical stimulation of Ca^{2+} release from the SR of FDB fibers with CatchER-T' and CatchER-T'-JP45

	WT CatchER-T' n. of fibers 9	WT CatchER-T'-JP45 n. of fibers 9
Peak Amplitude (dF/F)	-0.48 ± 0.20	-0.80 ± 0.16 *°
Time to Peak (ms)	-236.7 ± 76.3	-201.8 ± 70.6
Half relaxation time (ms)	-135.7 ± 62.5	-562.2 ± 471.8 *
Vmax (dF/F)/s	1.61 ± 0.69	2.69 ± 0.54 *°

*Values are mean ± sd Student's unpaired t test P<0.05
°Mann-Whitney Test P<0.05
*Cells stimulated at 100 Hz with a 300 ms duration
Data collect by Dr. Francesco Zorzato and colleagues.

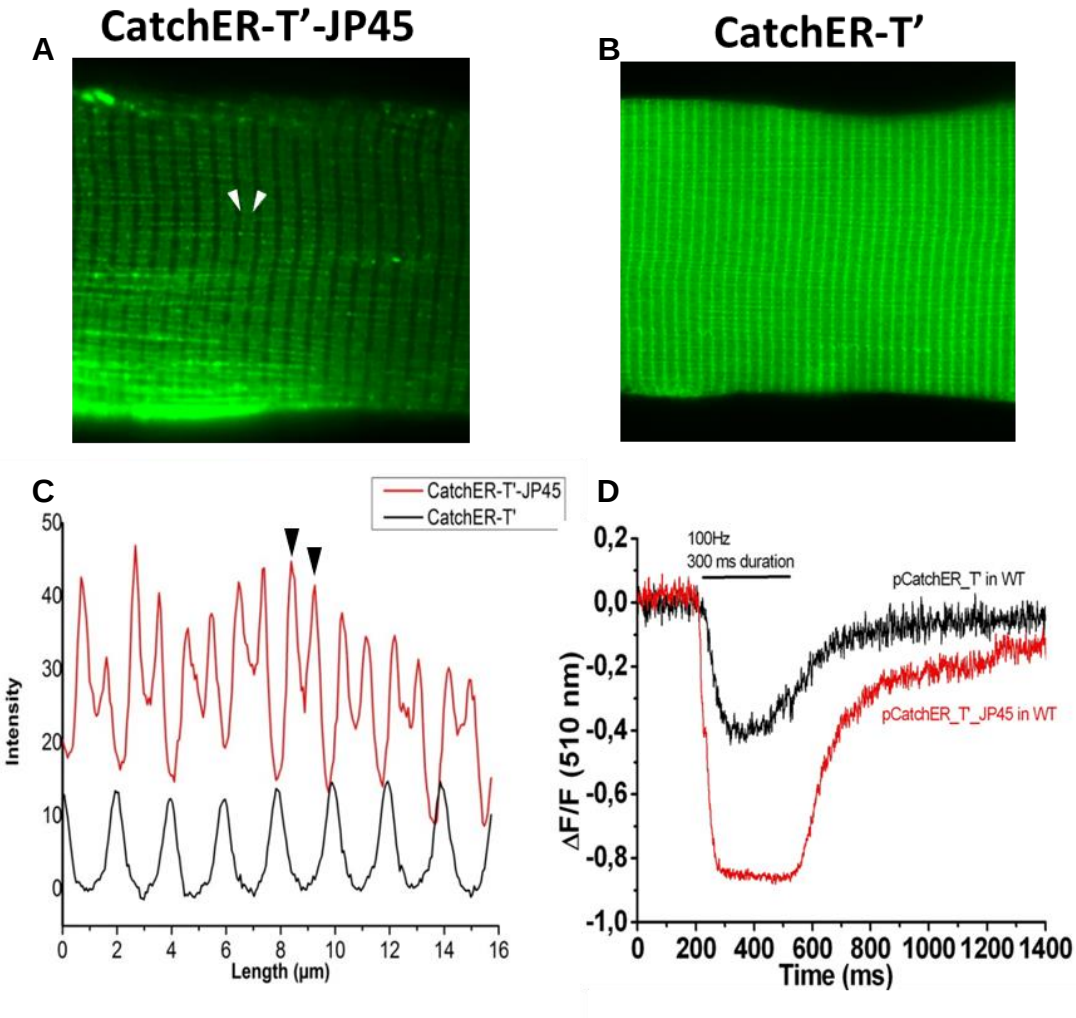

Figure 5.2.12 Monitoring the global vs. local changes in SR Ca^{2+} in electrically stimulated WT FDB fibers with CatchER-T' and CatchER-T'-JP45

(A and B) Wild-type FDB fibers were electroporated with CatchER-T'-JP45 and CatchER-T' constructs. Images were taken with a Nikon A1 confocal microscope and reveal different expression patterns for the targeted and un-targeted probe. C) Intensity change from CatchER-T' and CatchER-T'-JP45 fibers plotted against fiber length. Arrows correspond to arrows in A. A clear distinction is seen in the localization of CatchER-T'-JP45 and CatchER-T'. CatchER-T'-JP45 displays a double-row which results from pairs of T tubule-TC junctions flanking the Z lines (shallow deep) of mammalian skeletal muscle fibers. The double-row patterns are separated by deep valley which correspond to the M line localized in correspondence of the longitudinal SR. The distribution pattern of CatchER-T' is different from that of CatchER-T'-JP45. The superimposition of the intensity profile between different electroporated fibers indicates that CatchER-T' is localized in the longitudinal SR, i.e., in correspondence of deep valley which separates the double-row pattern of CatchER-T'-JP45. D) Ca^{2+} transients in FDB fibers were recorded upon stimulation with a 100 Hz electrical pulse

for 300 ms. Black trace is fluorescence intensity monitored with CatchER-T' expressed in the longitudinal SR and the red trace is CatchER-T'-JP45 located near the opening of RyR1 in the SR lumen. Large changes in peak amplitude were seen with targeted CatchER-T'-JP45 compared to those detected with CatchER-T'.

5.3 Discussion

5.3.1 Design of CatchER-T' and CatchER-T'-JP45

Although our Ca^{2+} probe CatchER has been extensively used in the Ca^{2+} imaging field and has good properties, it expresses poorly at 37°C. With this work, we successfully improved the fluorescence of CatchER at 37°C resulting in our new variant CatchER-T'. The loss of muscle strength has been directly linked to decreasing amounts of available Ca^{2+} released by the SR. In studies of JP45/CASQ1 double knockout mice, $Ca_v1.1$ activity was increased restoring Ca^{2+} and subsequently muscle strength[277]. To further understand the Ca^{2+} dynamics involved in E-C coupling at the junctional face membrane of skeletal muscle cells, we attempted to fuse our Ca^{2+} sensor CatchER to JP45 (Figure 5.2.1) in collaboration with Dr. Fransesco Zorzato and colleagues. We successfully designed the CatchER-JP45 construct and later incorporated the S175G, S30R, and Y39N mutations into the construct to create CatchER-T'-JP45 to monitor the local Ca^{2+} dynamics near the mouth of RyR1 in rat skeletal muscle FDB fibers.

5.3.2 Expression and purification of CatchER-T variants

The CatchER-T mutants were successfully expressed in BL21 (DE3) cells (Figure 5.2.2). SDS-PAGE gel analysis of the samples obtained from HisTag and gel filtration purification reveal sharp bands near the 26 kDa marker, representing pure

protein (Figures 5.2.3 and 5.2.4). A major band is seen between the 26 and 68 kDa marker and a smaller band is seen at 26 kDa. These bands may correspond to the dimer and monomer form of the sensors. GFP forms a weak dimer at the A206 interface, often appearing in crystal structures as a dimer[162]. The successful expression and purification of the bacterially expressed variants confirm that the three brightness mutations do not prevent proper folding of the protein.

5.3.3 In vitro and in situ K_d of CatchER-T'

The K_d of CatchER-T' obtained from both excitation wavelengths is similar to one another (1.1 and 1.3 mM, Table 5.2.1) suggesting that the three mutations made to create CatchER-T' made the populations of the two chromophore states similar. The *in vitro* Ca^{2+} K_d of CatchER is 0.3 ± 0.1 mM at 395 nm excitation and 0.2 ± 0.1 mM at 488 nm excitation. The Ca^{2+} K_d of CatchER-T' is ~3.6 fold weaker than CatchER (Table 5.2.1). CatchER has a higher population of the neutral chromophore which causes the K_d value at 395 nm to be high. Because our sensors are targeted to the ER/SR it is important to know how physiological concentrations of salts, like KCl, will influence the affinity of the sensors for Ca^{2+}. It is clear that the addition of 150 mM KCl during Ca^{2+} titration weakens the affinity of the sensors for Ca^{2+} (Table 5.2.1). In some cases, the Cl^- ion quenched fluorescence from one excitation wavelength (Appendix C, Figure C.1). At this salt concentration, the dynamic range of the sensors was reduced. Cl^- ions have been reported to quench the fluorescence of GFP proteins[173].

CatchER-T' has a seven times weaker K_d than CatchER *in vitro* and three times weaker K_d *in situ*. The *in vitro* and *in situ* K_ds for CatchER-T' differ. Inconsistencies

between *in vitro* and *in situ* K_ds are common among Ca^{2+} probes due to the molecular composition of intracellular fluid[275].

5.3.4 Monitoring drug effects on ER/SR receptor mediated pathways with CatchER-T'

Our improved ER-targeted Ca^{2+} probe CatchER-T' has significantly improved fluorescence at 37°C expression compared to the older probe CatchER. This is advantageous for mammalian cell application as cells grow healthier at 37°C. Several genetically-encoded Ca^{2+} probes have been created to monitor changes in ER/SR Ca^{2+}. The Cameleon probe D1ER, containing an altered version of calmodulin (CaM), was applied in breast cancer cells and showed that the antiapoptotic protein Bcl-2 decreases ER Ca^{2+} levels[207]. Recently, red genetically-encoded indicators for optical imaging (GECOs) were created by Robert Campbell and colleagues. The low affinity sensor LAR-GECO1 was used to monitor thapsigargin inhibition of ER refilling in HeLa, HEK293, and U2-OS cells co-transfected with CatchER[200]. In 2014, new low affinity, GECO-type indicators were created based on cfGCaMP2. This new variant termed Ca^{2+}-measuring organelle-Entrapped Protein IndicAtor 1 in the ER (CEPIA1*er*) was able to monitor ER Ca^{2+} dynamics in HeLa cells with thapsigargin and histamine treatment[201]. Our findings show that our optimized probe CatchER-T' can monitor receptor-mediated ER/SR Ca^{2+} transients in C2C12 myoblasts, HEK293 cells, and Cos-7 cells after applying different stimulating or inhibiting agents to the cells. The amplitude changes are indicative of ER/SR localization but must be confirmed further with confocal imaging.

5.3.5 Understanding the local and global changes in SR Ca^{2+} dynamics using JP45 targeted constructs

Here we investigated the difference in local Ca^{2+} transients generated near the luminal opening of RyR1 and the global Ca^{2+} transients generated in the longitudinal SR using CatchER-T' under fast electrical stimulation performed in collaboration with Dr. Fransesco Zorzato and colleagues. The SR in muscle cells is distinctly designed to distribute large amounts of Ca^{2+} into the cytosol, in response to electrical stimulation, for muscle contraction[269,92]. The SR TC functions as the Ca^{2+} release unit of the SR as this is where the junctional SR membrane and t tubule membrane face one another allowing the interaction of the DHPR with RyR1 causing Ca^{2+} release[270]. Concentrated in the longitudinal SR are SERCA pumps that are tasked with refilling the SR with Ca^{2+} [92]. Large amounts of the high capacity Ca^{2+} buffer protein CASQ1 exist as polymers near the luminal side of the junctional SR membrane where it interacts with JP45, RyR1, Junctin and triadin[96]. CASQ is reported to influence Ca^{2+} release during E-C coupling[98]. Figure 5.2.12A-C show the expression pattern of targeted and un-targeted CatchER-T'. A clear distinction is seen in the localization of CatchER-T'-JP45 and CatchER-T'. CatchER-T'-JP45 displays a double-row which results from pairs of T tubule-TC junctions flanking the Z lines (shallow deep) of mammalian skeletal muscle fibers. The double-row patterns are separated by deep valley which correspond to the M line localized in correspondence of the longitudinal SR. The distribution pattern of CatchER-T' is different from that of CatchER-T'-JP45. The superimposition of the intensity profile between different electroporated fibers indicates that CatchER-T' is localized in the longitudinal SR, i.e., in correspondence of deep valley which separates the double-row

pattern of CatchER-T'-JP45. Figure 5.2.12D shows the difference in the shape of the Ca^{2+} transients imaged with CatchER-T' and CatchER-T'-JP45. It is clear that electrical stimulation causes less SR Ca^{2+} release from the longitudinal SR detected with globally expressed CatchER-T' compared to the large amplitude decrease detected by the targeted construct. These findings suggest that a large local pool of Ca^{2+} exists around the luminal opening of RyR1 that is buffered by CASQ that differs from the global Ca^{2+} dynamics.

5.4 Conclusion

In this work, we exhibited our ability to improve the utility of CatchER for mammalian cell application by creating the CatchER-T series of variants. Of the new variants, CatchER-T' was the brightest at 37°C expression in C2C12 myoblast cells. Treatment of CatchER-T' transfected C2C12, Cos-7, and HEK293 cells with ER/SR receptor agonists and antagonists demonstrate the ability of our sensor to monitor Ca^{2+} changes in different ER/SR receptor-mediated pathways. In collaboration with Dr. Francesco Zorzato, we created the CatchER-T'-JP45 construct to compare the local versus global changes in luminal SR Ca^{2+}. Fusing CatchER-T' to the SR membrane protein JP45 allowed us to detect local changes in Ca^{2+} near the mouth of the RyR in FDB fibers. Our targeted construct proved that Ca^{2+} levels near the opening of the RyR are highly buffered, producing different Ca^{2+} transients compared to the probe expressed globally in the SR. Many skeletal muscle diseases are associated with mutations in junctional zone receptors and proteins. Our findings highlight the potential use of CatchER-T' as a diagnostic tool for deeper study and exploration of Ca^{2+} handling in normal and diseased skeletal muscle.

6 MONITORING MAGNESIUM SIGNALING IN T LYMPHOCYTES USING CATCHER VARIANTS

6.1 Introduction

The magnesium (Mg^{2+}) ion is found in high abundance in the human body. In healthy individuals, serum levels of Mg^{2+} are between 0.7-1.05 mM with tight regulation by absorption and excretion through the intestines and kidneys. Mg^{2+} in serum only accounts for 1% of the 24 g of total Mg^{2+} found in the body with the majority of it residing in muscle, bone, and other tissues[75]. Intracellularly, Mg^{2+} has an almost negligible electrochemical gradient unlike that of its counter ion Ca^{2+} (Ca^{2+}), leaving its speculated role as a second messenger unclear[77,78]. Intracellular levels of Mg^{2+} are maintained between 0.5-1.2 mM with levels at ~1 mM in the ER/SR and the high milli-molar range in the mitochondrion. Cytosolic Mg^{2+} only represents 5-10% of cellular Mg^{2+} [77]. Levels of free cytosolic Mg^{2+} are maintained through different membrane transporters such as TRPM7[79], MRS2[80], and MagT1[81]. The importance of MagT1 will be discussed later in this section. Mg^{2+} flows into the cell by diffusion. Extrusion of this ion occurs against an electrochemical gradient that is commonly coupled to Na^{+} exchange, where two Na^{+} ions are exchanged for one Mg^{2+} ion. In addition to its structural role in nucleic acids and its role as a cofactor and activator in many enzymatic reactions, Mg^{2+} also binds to ATP to stabilize its charge. Implicated in its function in ATP, the level of free cytosolic Mg^{2+} is affected by the rate of energy production occurring in the mitochondrion, where increases in ATP production lower $[Mg^{2+}]_i$[82]. Along with its function in energy metabolism, Mg^{2+} also plays an important role in bone formation and the proper function of the heart, brain, and skeletal muscle[75].

Hypomagnesemia, a clinical state in which serum Mg^{2+} levels fall below 0.5 mM, effects physiological processes involving Mg^{2+} adversely[83]. The pathological results of improper Mg^{2+} regulation include coronary artery disease, neurological disorders, asthma, vascular calcification, and muscle cramps, to name a few[75].

Mg^{2+} also plays a vital role in the immune response[278]. Many channels and receptors on the membranes of lymphocyte cells control cytosolic Mg^{2+} concentrations that modulate the function of these cells[279,278]. Of great importance is the MagT1 receptor found on the plasma membrane of T lymphocytes. MagT1 is a unique, ubiquitously expressed transporter with no sequence similarity to other well-studied transporters. MagT1 is selective for Mg^{2+} with no activation from other divalent ions. Knocking down MagT1 in yeast drastically reduced cytosolic Mg^{2+} levels[81,280]. The second messenger function of Mg^{2+} was clarified by studying MagT1 mutations in T lymphocytes. X-linked mutations in the MagT1 receptor of human T cells cause distinctive decreases in cytosolic Mg^{2+}, low CD4+ T cell numbers, and lingering Epstein-Barr virus infections. A deficiency or loss of function of MagT1 prevents the regular influx of Mg^{2+} in these cells with T-cell antigen receptor (TCR) stimulation, preventing Mg^{2+} activation of phospholipase C-ɣ1 that indirectly triggers IP_3-mediated Ca^{2+} release[278,281]. Dysfunction in the MagT1 transporter was also shown to cause impaired expression of the natural killer activating receptor, NKG2D, in CD8+ and killer T cells, preventing proper immune response to the Epstein-Barr virus[282]. Because of the vital role Mg^{2+} has in immune function, it is important to research further its ability to act as a second messenger in the immune response.

Even though Mg^{2+} is copious and important in physiology, visualizing Mg^{2+} movement in cells remains a challenge. Mg^{2+} probes are scarce, impeding the advancement of Mg^{2+} signaling research[283]. Methods for intracellular Mg^{2+} detection include the use of NMR[284] and microelectrodes[285], where the former technique is indirect, and the latter method is direct but harmful to cells. Synthetic dyes have also been used to study intracellular Mg^{2+} but suffer from selectivity issues since they bind Ca^{2+} as well[139,286,283]. Although several genetically-encoded Ca^{2+} probes exist for the study of Ca^{2+} signaling[177,203,200], MagFRET-1 is the only protein-based Mg^{2+} probe designed thus far[287]. MagFRET-1 was created using a portion of human centrin 3 (HsCen3) that binds Mg^{2+}, attaching the fluorescent proteins Cerulean and Citrine to the ends. When Mg^{2+} binds to HsCen3, the protein takes on a condensed conformation allowing FRET to occur. MagFRET-1 has a Mg^{2+} K_d of 148 µM and a Ca^{2+} K_d of 10 µM. However, MagFRET-1 can only detected changes in cytosolic [Mg^{2+}] in permeablized cells, not intact cells[287].

Here we report the *in vitro* Mg^{2+} binding affinity and application of cytosolic versions of CatchER variants to studying Mg^{2+} flux in Jurkat cells. Wild type and MagT1 knockout JurKat cells were studied via flow cytometry using CatchER and CatchER-T' by our collaborator Dr. Michael Lenardo at the NIH. Results show that CatchER variants can detect changes in cytosolic Mg^{2+} without interference from cytosolic Ca^{2+}. CatchERs can be a useful tool in future studies of Mg^{2+}-linked immunodeficiencies.

6.2 Results

6.2.1 Creation of cytosol-targeted CatchER variants

Since CatchER contains the calreticulin signal peptide and the KDEL ER/SR retention sequence for ER/SR localization, all the variants made from CatchER are targeted to the ER/SR. To remove the ER/SR localization sequences for cytosol targeting, primers were designed to remove the calreticulin signal peptide and the KDEL sequence through PCR. The calreticulin signal deletion primer for the forward direction was 5'- AGCTCGGATCCGGGCCCTCTAGAATGGTGAGCAAGGGC-3' and the reverse primer was 5'- GCCCGGATCCGAGCTCGGTACCAAGCTTAAGTTAAACGCTAG-3'. The deletion primers for the KDEL sequence were 5'-GCTGTACAAGTAAGAATTCTGCAGATATCCAGCACAGTGGCG-3' for the forward and 5'-GCAGAATTCTTACTTGTACAGCTCGTCCATGCCGAGAGTG-3' for the reverse. The PCR protocol was used for complimentary primer pairs with non-overlapping ends as outlined in Chapter 2 section 2.1. The resulting products were sent for sequencing and confirmed using the T7 promoter.

6.2.2 In vitro Mg^{2+} K_d of select CatchER variants via fluorescence spectroscopy

To determine the Mg^{2+} K_d of select CatchER variants for their use in measuring cytosolic Mg^{2+} levels, fluorescence titrations were done via fluorescence spectroscopy. The resulting Mg^{2+} affinities are listed in Table 6.2.1. Protein samples were prepared, in triplicate, in 10 mM Tris pH 7.4 with 5 µM of EGTA. A large increase in amplitude was seen in the absorbance and fluorescence spectra of CatchER in response to Mg^{2+} addition (Figure 6.2.1A-C) with calculated Mg^{2+} K_ds of 0.5 ± 0.1 mM and 0.7 ± 0.1 mM at 395 nm and 488 nm excitation, respectively. CatchER excited at 488 nm exhibited a

two-fold dynamic range over the basal intensity. Our improved CatchER variant, CatchER-T' (Figure 6.2.1D-F), had no fluorescence response with 395 nm excitation. The Mg^{2+} K_d at 488 nm excitation was 1.8 ± 0.4 mM. Like CatchER, saturating levels of Mg^{2+} had a profound effect on the absorbance spectrum of 149E S30R (Figure 6.2.1G-I), but like CatchER-T' there was no fluorescence response with increased addition of Mg^{2+} at 395 nm excitation. The resulting K_d for 149E S30R was 0.8 ± 0.1 mM.

Table 6.2.1 *In vitro* Mg^{2+} K_ds and dynamic range of select CatchER variants

	λ_{ex} (nm)	K_d (mM)	F_{max}/F_{min}
CatchER	**395**	0.5 ± 0.1	1.7 ± 0.1
	488	0.7 ± 0.1	2.4 ± 0.1
CatchER-T'	**395**	NR	NR
	488	1.8 ± 0.4	1.6 ± 0.1
149E S30R	**395**	NR	NR
	488	0.8 ± 0.1	1.9 ± 0.1

*Data represents mean ± stdev. K_d – dissociation constant, λ_{ex} – excitation wavelength, F_{max}/F_{min} – dynamic range in response to Mg^{2+} calculated using the fluorescence at maximal saturation divided by the fluorescence with no Mg^{2+} present. Data collected at room temperature. Samples prepared in 10 mM Tris pH 7.4.Fluorescence slit widths were 0.25 mm for excitation and emission. NR – no response.

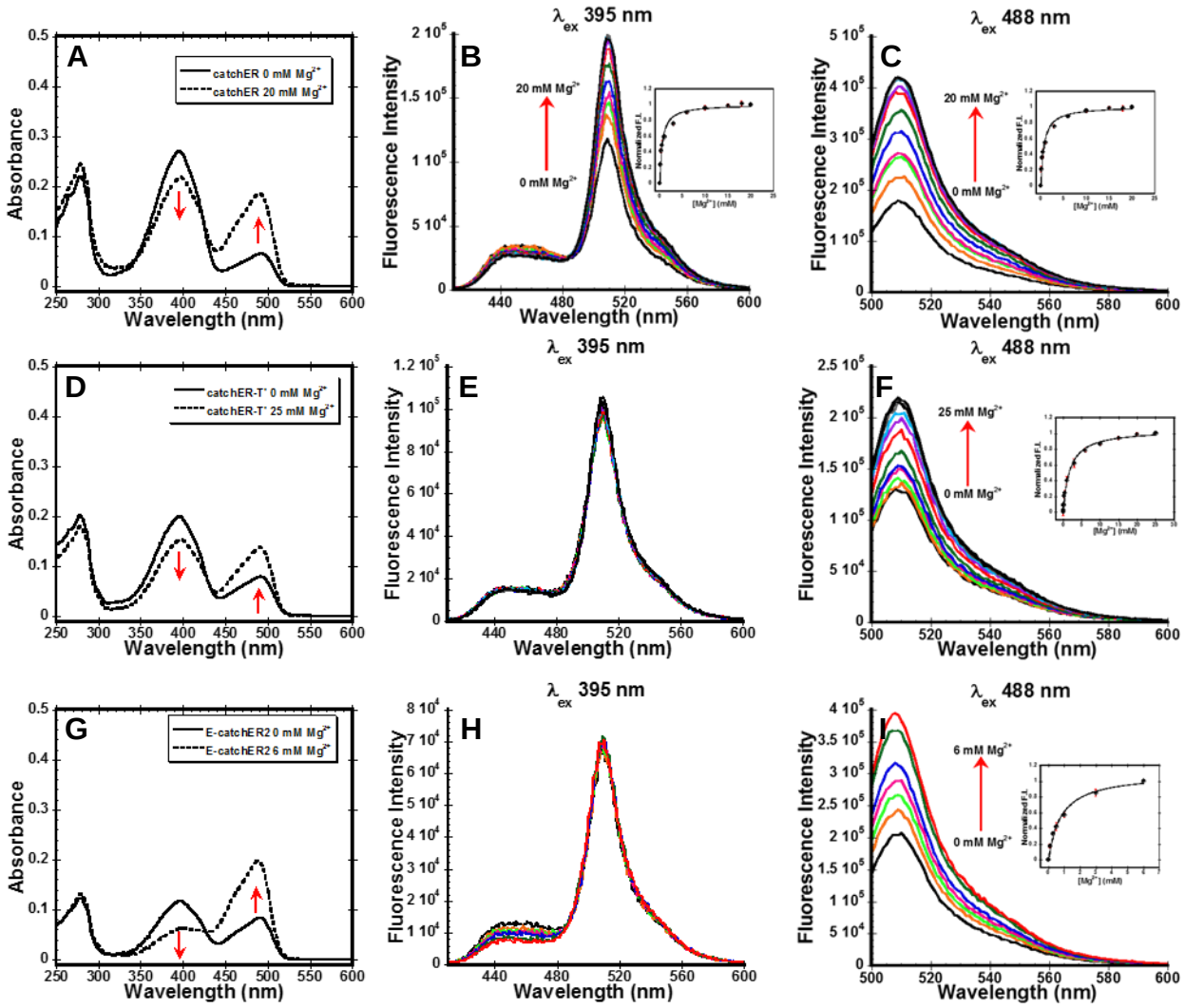

Figure 6.2.1 *In vitro* Mg^{2+} K_d of select CatchER variants

(A, D, and G) Absorbance spectrums of CatchER, CatchER-T', and 149E S30R in the absence (solid line) and presence (dotted line) of saturating levels of Mg^{2+}. Like Ca^{2+}, magnesium has the same effect on the absorbance spectrum of CatchER variants causing an increase in the 488 nm peak (increase in anionic chromophore) and a decrease in the 395 nm peak (decrease in neutral chromophore). The fluorescence of CatchER at 395 nm (B) and 488 nm (C) excitation increases with increasing Mg^{2+} concentrations reaching saturation at 20 mM Mg^{2+}. Inset binding curves were obtained by fitting the normalized data with a 1:1 binding equation resulting in K_ds of 0.5 ± 0.1 and 0.7 ± 0.1 mM. CatchER-T' (E) and 149E S30R (H) had no response to Mg^{2+} addition at 395 nm excitation. The Mg^{2+} K_d for CatchER-T' (F) and 149E S30R (I) were calculated to be 1.8 ± 0.4 mM and 0.8 ± 0.1 mM, respectively at 488 nm excitation.

6.2.3 Using CatchER variants to monitor Mg^{2+} flux in Jurkat cells with and without the MagT1 receptor

Magnesium plays an important role in the immune response[278]. Decreases in cytosolic Mg^{2+} due to deficiency in the MagT1 receptor of T lymphocytes has been linked to immune disorders in humans and promotes Mg^{2+} as a second messenger molecule in immune system function[281]. Jurkat cells, human leukaemic T cells that are consistently used by immunologists as a model system for the study of T cell receptor signaling[288], were employed to study the effect of MagT1 deletion on the Mg^{2+} transient. Wild type Jurkat cells and MagT1 knockout Jurkat cells were first transfected with CatchER and incubated in media supplemented with increasing concentrations of Mg^{2+}. The fluorescence response of CatchER to changes in cytosolic Mg^{2+} concentration was monitored using flow cytometry using FITC settings (Figure 6.2.2A and B). In a similar experiment, WT and MagT1 KO Jurkat cells were transfected with CatchER and CatchER-T'. All cells were co-transfected with mCherry as the fluorescent marker. Cells only expressing mCherry were used as the control. The results are found in Figure 6.2.3A-C.

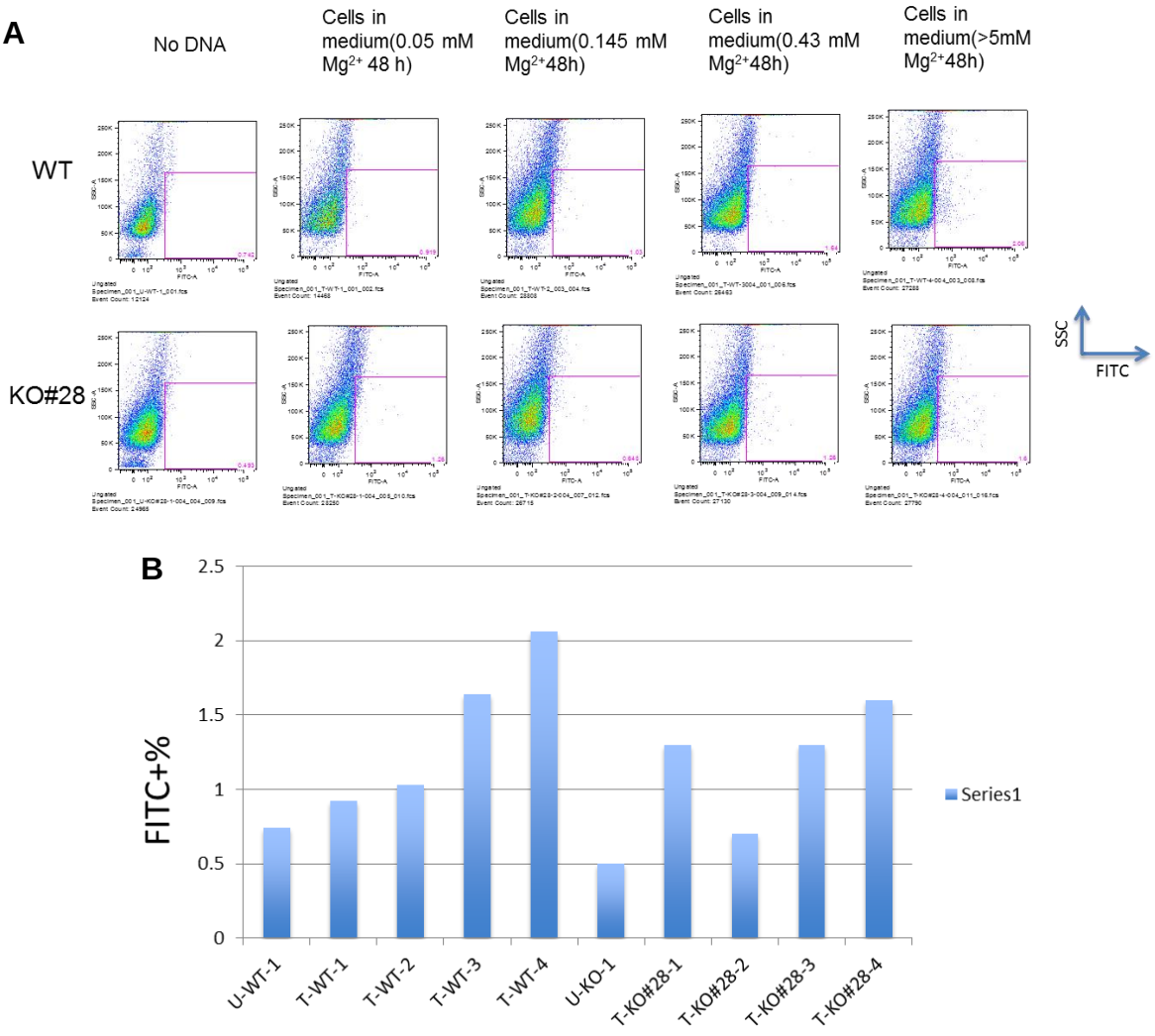

Figure 6.2.2 CatchER measurement of cytosolic Mg^{2+} in WT and MagT1 KO Jurkat cells using flow cytometry

WT and MagT1 KO Jurkat cells were transiently transfected with CatchER. The cell culture media was supplemented with 0.05, 0.145, 0.43, and >5 mM Mg^{2+} for 48 h. After Mg^{2+} supplementation, the cells were labeled with FITC and flow cytometry was used to analyze the fluorescence response of CatchER to changes in Mg^{2+} flux (A). Cells with no CatchER DNA were used as a control. The flow cytometry data was further processed as %FITC (B). Data collected by Dr. Michael Lenardo and colleagues.

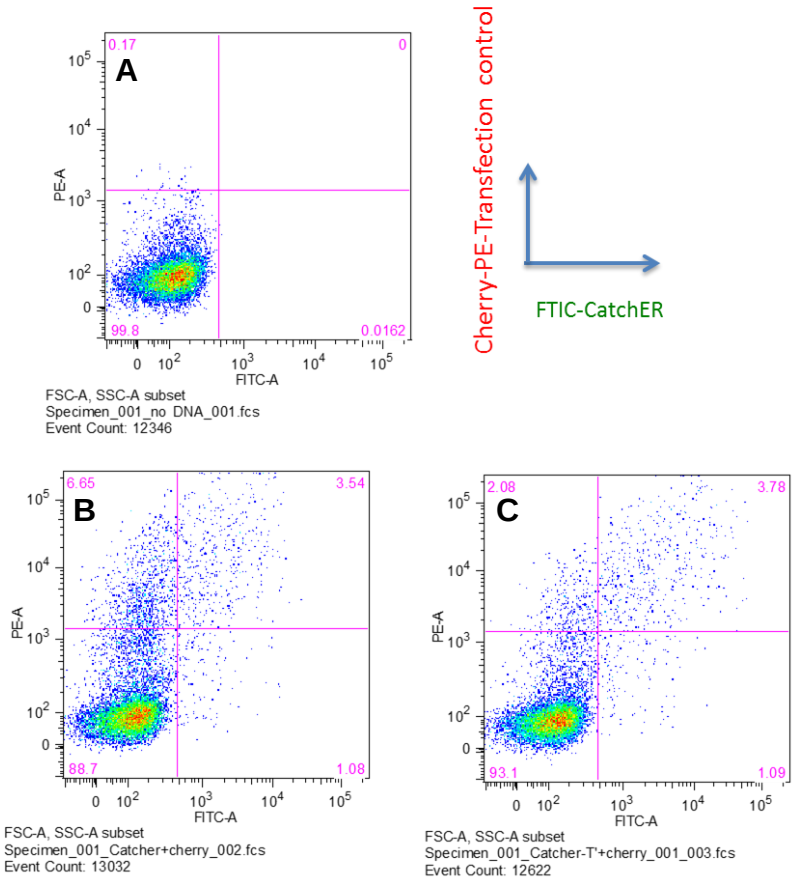

Figure 6.2.3 Monitoring cytosolic Mg^{2+} in Jurkat cells using CatchER and CatchER-T'

Jurkat cells were co-transfected with mCherry and CatchER or CatchER-T' and analyzed using flow cytometry. Cells transfected with only mCherry were used as the control (A) while data was collected for cells expressing mCherry+CatchER (B) and mCherry+CatchER-T' (C). Data collected by Dr. Michael Lenardo and colleagues.

6.3 Discussion

6.3.1 In vitro Mg^{2+} K_d of CatchER variants

Fluorescence titrations of CatchER, CatchER-T', and E-CatchER2 revealed that our weak affinity Ca^{2+} sensors also bind magnesium with high micromolar to low milli-molar dissociation constants (Table 6.2.1). The concentration of free Ca^{2+} in the cytosol

of most cells is between 0.1-1 μM[5], whereas the concentration of free magnesium is ~1000 fold greater at 0.5-1.2 mM[75]. Since cytosolic levels of Mg^{2+} are higher than that for Ca^{2+}, Ca^{2+} is not expected to interfere with the cytosolic application of our CatchER variants in the study of cytosolic Mg^{2+} transients. Mg^{2+} binding is an issue in CaBPs because of its high intracellular concentration and the similarities between the two ions[289]. The Ca^{2+} ion has an ionic radius of 0.99 Å and Mg^{2+} has an ionic radius of 0.65 Å. The metal coordination chemistry of Ca^{2+} in proteins is pentagonal bipyramidal with oxygen as the primary atom for its 6-8 coordinating ligands[212]. Mg^{2+} has octahedral coordination geometry in its inner shell with six coordinating ligands coming from strong interactions with water molecules[290]. Because magnesium binds water so tightly in its inner sphere, a large energy barrier exists for the release of a water molecule. Removal of an inner sphere water molecule from Mg^{2+} has an energetic cost of 20-80 kcal/mol, with the energy increasing when fewer water molecules are present[76]. Due to the large hydration energy, magnesium coordinates with proteins and other biological compounds through its outer sphere, pointing to the typical weak K_ds for proteins that bind magnesium[291,292,76]. In the case of our CatchER variants, the K_ds for Mg^{2+} are weak as expected.

6.3.2 Monitoring Mg^{2+} transients in Jurkat cells using CatchER variants

By applying the cytosolic versions of CatchER and CatchER-T' in WT and MagT1 KO Jurkat cells, we were able to see changes in cytosolic Mg^{2+}. After supplementing the cell culture media with different concentrations of Mg^{2+}, the cytosolic Mg^{2+} level decreases in MagT1 KO cells compared to WT cells (Figure 6.2.2B). MagT1 is found in great abundance in lymphocytes and selectively transports Mg^{2+} into the cytosol from

the extracellular environment[279]. The decrease in the CatchER fluorescence from flow cytometry analysis confirms impairment of the Mg^{2+} signal in MagT1 deficient cells.

6.4 Conclusion

In conclusion, Mg^{2+} is a significant ion that plays a pivotal role in the immune response. We have shown that our GECIs bind Mg^{2+} *in vitro* with K_d values appropriate for measuring changes in cytosolic Mg^{2+}. Cytosol-targeted CatchER variants can be expressed in human T lymphocytes to monitor variations in cytosolic free Mg^{2+}. Although the changes seen in flow cytometry were small, the preliminary results suggest that our probes can monitor fluctuations in cytosolic Mg^{2+} without interference from Ca^{2+}. This work and future research will help to unveil further the function of Mg^{2+} as a second messenger in biological processes and its compromised role in immunodeficiencies.

7 SIGNIFICANCE

The discovery of GFP and GFP-like proteins has revolutionized the field of Ca^{2+} imaging. The new protein-based Ca^{2+} indicators that have been developed incorporating GFP to translate the Ca^{2+} binding event into a measurable fluorescence response are easily targeted to organelles of interest through genetic manipulation. Because of the various probes available with different emission wavelengths, it is possible to monitor Ca^{2+} signaling events in various cellular compartments simultaneously. A limitation of widely used GECIs, like GCaMP and others, is their strong affinity for Ca^{2+} and their slow Ca^{2+} release kinetics due to their use of a native CaBP as the binding moiety. These limitations prevent the accurate measure of fast Ca^{2+} regulated events like E-C coupling in cardiac and skeletal muscle and the precise measurement of basal Ca^{2+} in high concentration organelles like the ER/SR. The ideal Ca^{2+} probe would use a single FP, as the scaffold, with a Ca^{2+} binding site designed on the surface via site-directed mutagenesis. It would have good selectivity for Ca^{2+}, an appropriate affinity, and proper binding and release kinetics to monitor Ca^{2+} dynamics in a particular subcellular location. The ideal Ca^{2+} probe would also have a substantial fluorescence change in response to Ca^{2+} with good fluorescence at 37°C for mammalian cell application. Inherent challenges exist in designing the aforementioned Ca^{2+} probe. The Ca^{2+} binding coordination geometry has to be created de novo. Once Ca^{2+} binds to the design site, the binding event must produce the appropriate change in the chromophore environment which will not perturb the overall folding but induce a fluorescence intensity change.

With much research, our lab created a design strategy for developing genetically-encoded Ca^{2+} probes using a single GFP. Over the years, our lab has analyzed the canonical binding geometry in E-F hand and non E-F hand CaBPs. We have used this information to create Ca^{2+} binding sites, through grafting or site-directed mutagenesis, on the surface of scaffold proteins like CD2 and parvalbumin. With this knowledge, we designed the EGFP-based Ca^{2+} probe CatchER with ER/SR targeting. CatchER has fast kinetics and a weak affinity for Ca^{2+}, making it suitable to measure fast Ca^{2+} transients associated with muscle contraction. However, CatchER has reduced fluorescence at 37°C. To better understand the structural changes in CatchER that are responsible for the fast kinetics, weak affinity, and absorbance spectrum changes, the Ca^{2+}-free, Ca^{2+}-bound, and gadolinium-bound crystal structures were determined at 1.66, 1.20, and 1.78 Å resolution. Both Ca^{2+} and gadolinium were found in the designed binding site with double occupancies of 0.5/0.5 and 0.7/0.3 for Ca^{2+} and Gd^{3+} respectively, even though CatchER binds both metals with 1:1 stoichiometry. Both ions have an overlapping occupancy site where the metals are primarily chelated by E147, D202, and E204. From these results, it was concluded that the multiple occupancies in the binding site for each metal make the binding event a dynamic process, directly causing the fast kinetics and weak affinity of CatchER. In all three CatchER structures, T203 has a flipped conformation resulting in a water-mediated bond between its main chain carbonyl group and the tyrosyl of the chromophore which is the same conformation found in wt-GFP providing the reason for the two excitation peaks in CatchER. E222 was shown to have alternate conformations in the crystal structures. The H-bond network formed by E222 through two water molecules to Q69, in the Ca^{2+}

and Gd3+ CatchER structures, are interrupted in the Ca^{2+} free structure. E222 stabilizes the negative charge of the anionic chromophore through H-bonding with T65 creating more of the anionic chromophore with the addition of Ca^{2+}. Obtaining the crystal structures of CatchER is significant for the development of future Ca^{2+} probes with fast kinetics.

Next, mutagenesis was employed to see if mutations could be introduced into CatchER to create variants with different K_ds, quantum yields, and extinction coefficients. The N149E mutation was incorporated into CatchER, creating the 149E mutant having six negatively charged residues in its binding site. Analysis of the absorbance spectrum of 149E showed that the mutation increased the 488 nm absorbance peak, increasing the amount of anionic chromophore present. Fluorescence titrations of 149E with Ca^{2+} confirmed the Ca^{2+} induced fluorescence change and revealed a weaker Ca^{2+} K_d for 149E compared to CatchER. Errors in the equilibrium dialysis measurement prevented accurate calculation of the Ca^{2+} K_d for the different variants analyzed. Compared to CatchER, 149E has a 3.7 fold increase in its extinction coefficient in the apo form, which is the largest increase of all the mutants analyzed. CatchER-T, containing the S175G mutation, also experiences an increase in its extinction coefficient in the apo form, 11.0 ± 0.1 $mM^{-1}cm^{-1}$ compared to 7.1 ± 0.1 $mM^{-1}cm^{-1}$ of CatchER. Through analysis of the 149E variants, the S30R and Y39N mutations decrease the extinction coefficients in the apo form. Only the quantum yield of 149E S30R has a slight increase over that of 149E, 0.7 ± 0.1 compared to 0.6 ± 0.1. Comparing the optical properties of all the variants with Ca^{2+}, metal binding increases the extinction coefficient and brightness, while slightly decreasing the quantum yield.

Compared to CatchER, 149E has less pH dependence. Kinetic analysis of 149E revealed slower kinetics compared to CatchER. As a result of this work, a less pH sensitive CatchER variant was made with a weaker affinity for Ca^{2+} and increased absorption ability, providing another tool that can be used to monitor Ca^{2+} dynamics in the ER/SR.

Although CatchER has been used in many different mammalian cell lines to monitor Ca^{2+} release dynamics in the ER/SR, its fluorescence is reduced at 37°C. CatchER only fluoresces when expressed at 30°C which is not the ideal temperature for mammalian cell growth. To improve the brightness of CatchER for mammalian cell application, we incorporated two key mutations from superfolder GFP that were deemed essential for improving the folding and subsequent fluorescence at 37°C: S30R and Y39N. We also made the S175G mutation that enhances thermostability of GFP at 37°C. With this work, we successfully improved the fluorescence of CatchER at 37°C resulting in the CatchER-T series of mutants with CatchER-T' having the largest improvement in fluorescence at 37°C. To further understand the Ca^{2+} dynamics involved in E-C coupling at the junctional face membrane of skeletal muscle cells, we attempted to fuse our Ca^{2+} sensor CatchER to JP45 in collaboration with Dr. Fransesco Zorzato and colleagues. We successfully designed the CatchER-JP45 construct and later incorporated the S175G, S30R, and Y39N mutations into the construct to create CatchER-T'-JP45 to monitor the local Ca^{2+} dynamics near the luminal opening of RyR1 in rat skeletal muscle FDB fibers. By applying the targeted CatchER-T'-JP45 construct in these muscle fibers, we were able to visualize the large pool of Ca^{2+} that exists, near the opening of the RyR1 in the SR lumen, to fuel the E-C coupling process necessary

for muscle function. Our probe can be used to monitor the Ca^{2+} flux in this region of muscle cells in neuromuscular diseases associated with dysfunctional proteins in this region of muscle cells.

The function of T lymphocytes is modified by cytosolic Mg^{2+} which is maintained at 1 mM. The influx of Mg^{2+} in these cells is primarily controlled by the MagT1 receptor. Mutations in the MagT1 receptor of human T cells cause decreases in cytosolic [Mg^{2+}] leading to lingering Epstein-Barr virus infections. Because the intracellular signaling role of Mg^{2+} has been unclear, little has been done to develop probes to monitor Mg^{2+} flux. Since Ca^{2+} and Mg^{2+} share similar metal coordination geometries, proteins that bind Ca^{2+} also bind Mg^{2+}. To probe the role of Mg^{2+} in the immune response, cytosolic versions of our ER/SR targeted probes were created and transfected into wild-type and MagT1 knockout Jurkat cells. We have shown that our GECIs bind Mg^{2+} *in vitro* with K_d values appropriate for measuring changes in cytosolic Mg^{2+}. Although the changes seen in flow cytometry were small, the preliminary results suggest that our weak affinity probes can monitor fluctuations in cytosolic Mg^{2+} without interference from Ca^{2+} since the cytosolic Ca^{2+} level is in the nanomolar range. This work and future research will help to unveil further the function of Mg^{2+} as a second messenger in biological processes and its compromised role in immunodeficiencies.

This work solidifies that our optimized Ca^{2+} probes can be applied in different cell types to monitor receptor-mediated ER/SR Ca^{2+} release and changes in cytosolic Mg^{2+}. We have also proved that our probes can be targeted to specific locations within the ER/SR to show the vastly different Ca^{2+} transients that exist compared to global Ca^{2+}

changes. Our findings will continue to push the fields of Ca^{2+} imaging and probe design forward to provide future tools for diagnosing Ca^{2+}-related diseases.

REFERENCES

1. Young, V.; Garza, C., Dietary Reference Intakes for Calcium, Phosphorus, Magnesium, Vitamin D and Fluoride. Standing Committee on the Scientific Evaluation of Dietary Reference Intakes, Food and Nutritional Board, Institute of Medicine. *Food and Nutrition Board, Institute of Medicine. National Academy Press: Washington, DC* **1997**.
2. Zhu, K.; Prince, R. L., Calcium and bone. *Clinical biochemistry* **2012,** *45* (12), 936-942.
3. Peacock, M., Calcium metabolism in health and disease. *Clin J Am Soc Nephrol* **2010,** *5 Suppl 1*, S23-30.
4. Moore, E. W., Ionized calcium in normal serum, ultrafiltrates, and whole blood determined by ion-exchange electrodes. *Journal of Clinical Investigation* **1970,** *49* (2), 318.
5. Berridge, M. J.; Lipp, P.; Bootman, M. D., The versatility and universality of calcium signalling. *Nat. Rev. Mol. Cell Biol.* **2000,** *1* (1), 11-21.
6. Hurwitz, S., Homeostatic control of plasma calcium concentration. *Crit. Rev. Biochem. Mol. Biol.* **1996,** *31* (1), 41-100.
7. Pin, J. P.; Galvez, T.; Prezeau, L., Evolution, structure, and activation mechanism of family 3/C G-protein-coupled receptors. *Pharmacol. Ther.* **2003,** *98* (3), 325-354.
8. Brown, E. M.; Gamba, G.; Riccardi, D.; Lombardi, M.; Butters, R.; Kifor, O.; Sun, A.; Hediger, M. A.; Lytton, J.; Hebert, S. C., CLONING AND CHARACTERIZATION OF AN EXTRACELLULAR CA2+-SENSING RECEPTOR FROM BOVINE PARATHYROID. *Nature* **1993,** *366* (6455), 575-580.
9. Zhang, C.; Miller, C. L.; Brown, E. M.; Yang, J. J., The calcium sensing receptor: from calcium sensing to signaling. *Sci. China-Life Sci.* **2015,** *58* (1), 14-27.
10. Ray, K.; Clapp, P.; Goldsmith, P. K.; Spiegel, A. M., Identification of the sites of N-linked glycosylation on the human calcium receptor and assessment of their role in cell surface expression and signal transduction. *J. Biol. Chem.* **1998,** *273* (51), 34558-34567.
11. Bai, M.; Trivedi, S.; Brown, E. M., Dimerization of the extracellular calcium-sensing receptor (CaR) on the cell surface of CaR-transfected HEK293 cells. *J. Biol. Chem.* **1998,** *273* (36), 23605-23610.
12. Ray, K.; Hauschild, B. C.; Steinbach, P. J.; Goldsmith, P. K.; Hauache, O.; Spiegel, A. M., Identification of the cysteine residues in the amino-terminal extracellular domain of the human Ca2+ receptor critical for dimerization - Implications for function of monomeric Ca2+ receptor. *J. Biol. Chem.* **1999,** *274* (39), 27642-27650.
13. Hofer, A. M.; Brown, E. M., Extracellular calcium sensing and signalling. *Nat. Rev. Mol. Cell Biol.* **2003,** *4* (7), 530-538.
14. Ferre, S.; Hoenderop, J. G. J.; Bindels, R. J. M., Sensing mechanisms involved in Ca2+ and Mg2+ homeostasis. *Kidney International* **2012,** *82* (11), 1157-1166.
15. Zhang, C.; Huang, Y.; Jiang, Y. S.; Mulpuri, N.; Wei, L.; Hamelberg, D.; Brown, E. M.; Yang, J. J., Identification of an L-Phenylalanine Binding Site Enhancing the Cooperative Responses of the Calcium-sensing Receptor to Calcium*. *J. Biol. Chem.* **2014,** *289* (8), 5296-5309.
16. Conigrave, A. D.; Quinn, S. J.; Brown, E. M., L-Amino acid sensing by the extracellular Ca2+-sensing receptor. *Proc. Natl. Acad. Sci. U. S. A.* **2000,** *97* (9), 4814-4819.
17. Zhang, C.; Zhuo, Y.; Moniz, H. A.; Wang, S.; Moremen, K. W.; Prestegard, J. H.; Brown, E. M.; Yang, J. J., Direct Determination of Multiple Ligand Interactions with the Extracellular Domain of the Calcium-sensing Receptor. *J. Biol. Chem.* **2014,** *289* (48), 33529-33542.
18. Brauner-Osborne, H.; Jensen, A. A.; Sheppard, P. O.; O'Hara, P.; Krogsgaard-Larsen, P., The agonist-binding domain of the calcium-sensing receptor is located at the amino-terminal domain. *J. Biol. Chem.* **1999,** *274* (26), 18382-18386.
19. Brown, E. M., The extracellular Ca2+-sensing receptor: Central mediator of systemic calcium homeostasis. *Annu. Rev. Nutr.* **2000,** *20*, 507-533.

20. Magno, A. L.; Ward, B. K.; Ratajczak, T., The Calcium-Sensing Receptor: A Molecular Perspective. *Endocr. Rev.* **2011,** *32* (1), 3-30.
21. Berridge, M. J.; Bootman, M. D.; Roderick, H. L., Calcium signalling: Dynamics, homeostasis and remodelling. *Nat. Rev. Mol. Cell Biol.* **2003,** *4* (7), 517-529.
22. Clapham, D. E., Calcium Signaling. *Cell* **2007,** *131* (6), 1047-1058.
23. Dolmetsch, R. E.; Xu, K.; Lewis, R. S., Calcium oscillations increase the efficiency and specificity of gene expression. *Nature* **1998,** *392* (6679), 933-936.
24. Berridge, M. J., Neuronal Calcium Signaling. *Neuron* **1998,** *21* (1), 13-26.
25. Berridge, M. J., Calcium signalling remodelling and disease. *Biochem. Soc. Trans.* **2012,** *40*, 297-309.
26. Strehler, E. E.; Filoteo, A. G.; Penniston, J. T.; Caride, A. J., Plasma-membrane Ca2+ pumps: structural diversity as the basis for functional versatility. *Biochem. Soc. Trans.* **2007,** *35*, 919-922.
27. Guerini, D., The significance of the isoforms of plasma membrane calcium ATPase. *Cell Tissue Res.* **1998,** *292* (2), 191-197.
28. Lopreiato, R.; Giacomello, M.; Carafoli, E., The Plasma Membrane Calcium Pump: New Ways to Look at an Old Enzyme. *J. Biol. Chem.* **2014,** *289* (15), 10261-10268.
29. Brini, M.; Carafoli, E., Calcium Pumps in Health and Disease. *Physiol. Rev.* **2009,** *89* (4), 1341-1378.
30. Grover, A. K.; Khan, I., CALCIUM-PUMP ISOFORMS - DIVERSITY, SELECTIVITY AND PLASTICITY. *Cell Calcium* **1992,** *13* (1), 9-17.
31. Periasamy, M.; Kalyanasundaram, A., SERCA pump isoforms: Their role in calcium transport and disease. *Muscle Nerve* **2007,** *35* (4), 430-442.
32. Toyoshima, C.; Nomura, H.; Sugita, Y., Crystal structures of Ca2+-ATPase in various physiological states. In *Na,K-Atpase and Related Cation Pumps: Structure, Function, and Regulatory Mechanisms*, Jorgensen, P. L.; Karlish, S. J. D.; Maunsbach, A. B., Eds. New York Acad Sciences: New York, 2003; Vol. 986, pp 1-8.
33. Toyoshima, C.; Nakasako, M.; Nomura, H.; Ogawa, H., Crystal structure of the calcium pump of sarcoplasmic reticulum at 2.6 [angst] resolution. *Nature* **2000,** *405* (6787), 647-655.
34. Michelangeli, F.; East, J. M., A diversity of SERCA Ca2+ pump inhibitors. *Biochem. Soc. Trans.* **2011,** *39* (3), 789-797.
35. Cai, X. J.; Lytton, J., The cation/Ca2+ exchanger superfamily: Phylogenetic analysis and structural implications. *Mol. Biol. Evol.* **2004,** *21* (9), 1692-1703.
36. Lytton, J., Na+/Ca2+ exchangers: three mammalian gene families control Ca2+ transport. *Biochem. J.* **2007,** *406*, 365-382.
37. Sharma, V.; O'Halloran, D. M., Recent Structural and Functional Insights into the Family of Sodium Calcium Exchangers. *Genesis* **2014,** *52* (2), 93-109.
38. Schnetkamp, P. P. M., The SLC24 gene family of Na+/Ca2+-K+ exchangers: From sight and smell to memory consolidation and skin pigmentation. *Mol. Asp. Med.* **2013,** *34* (2-3), 455-464.
39. Neumaier, F.; Dibue-Adjei, M.; Hescheler, J.; Schneider, T., Voltage-gated calcium channels: Determinants of channel function and modulation by inorganic cations. *Progress in neurobiology* **2015,** *129*, 1-36.
40. Catterall, W. A., Structure and regulation of voltage-gated Ca2+ channels. *Annu. Rev. Cell Dev. Biol.* **2000,** *16*, 521-555.
41. Perez Reyes, E.; Kim, H. S.; Lacerda, A. E.; Horne, W.; Wei, X.; Rampe, D.; Campbell, K. P.; Brown, A. M.; Birnbaumer, L., Induction of calcium currents by the expression of the α 1-subunit of the dihydropyridine receptor from skeletal muscle. *Nature* **1989,** *340* (6230), 233-236.

42. Catterall, W. A.; Perez-Reyes, E.; Snutch, T. P.; Striessnig, J., International Union of Pharmacology. XLVIII. Nomenclature and structure-function relationships of voltage-gated calcium channels. *Pharmacological reviews* **2005,** *57* (4), 411-425.
43. Ramsey, I. S.; Delling, M.; Clapham, D. E., An introduction to TRP channels. In *Annual Review of Physiology*, Annual Reviews: Palo Alto, 2006; Vol. 68, pp 619-647.
44. Hofmann, T.; Schaefer, M.; Schultz, G.; Gudermann, T., Subunit composition of mammalian transient receptor potential channels in living cells. *Proceedings of the National Academy of Sciences* **2002,** *99* (11), 7461-7466.
45. FranziniArmstrong, C.; Protasi, F., Ryanodine receptors of striated muscles: A complex channel capable of multiple interactions. *Physiol. Rev.* **1997,** *77* (3), 699-729.
46. Hakamata, Y.; Nakai, J.; Takeshima, H.; Imoto, K., Primary structure and distribution of a novel ryanodine receptor/calcium release channel from rabbit brain. *FEBS Lett.* **1992,** *312* (2-3), 229-235.
47. Zalk, R.; Clarke, O. B.; des Georges, A.; Grassucci, R. A.; Reiken, S.; Mancia, F.; Hendrickson, W. A.; Frank, J.; Marks, A. R., Structure of a mammalian ryanodine receptor. *Nature* **2015,** *517* (7532), 44-U90.
48. Yan, Z.; Bai, X. C.; Yan, C. Y.; Wu, J. P.; Li, Z. Q.; Xie, T.; Peng, W.; Yin, C. C.; Li, X. M.; Scheres, S. H. W.; Shi, Y. G.; Yan, N., Structure of the rabbit ryanodine receptor RyR1 at near-atomic resolution. *Nature* **2015,** *517* (7532), 50-+.
49. Capes, E. M.; Loaiza, R.; Valdivia, H. H., Ryanodine receptors. *Skeletal Muscle* **2011,** *1*.
50. Lanner, J. T.; Georgiou, D. K.; Joshi, A. D.; Hamilton, S. L., Ryanodine Receptors: Structure, Expression, Molecular Details, and Function in Calcium Release. *Cold Spring Harbor Perspect. Biol.* **2010,** *2* (11).
51. Lamb, G.; Stephenson, D., Effect of Mg2+ on the control of Ca2+ release in skeletal muscle fibres of the toad. *The Journal of Physiology* **1991,** *434*, 507.
52. Herrmann-Frank, A.; Lüttgau, H.-C.; Stephenson, D. G., Caffeine and excitation–contraction coupling in skeletal muscle: a stimulating story. *Journal of Muscle Research & Cell Motility* **1999,** *20* (2), 223-236.
53. HerrmannFrank, A.; Richter, M.; Sarkozi, S.; Mohr, U.; LehmannHorn, F., 4-chloro-m-cresol, a potent and specific activator of the skeletal muscle ryanodine receptor. *Biochim. Biophys. Acta-Gen. Subj.* **1996,** *1289* (1), 31-40.
54. Sorrentino, V., Sarcoplasmic reticulum: Structural determinants and protein dynamics. *Int. J. Biochem. Cell Biol.* **2011,** *43* (8), 1075-1078.
55. Nakai, J.; Sekiguchi, N.; Rando, T. A.; Allen, P. D.; Beam, K. G., Two Regions of the Ryanodine Receptor Involved in Coupling withl-Type Ca2+ Channels. *J. Biol. Chem.* **1998,** *273* (22), 13403-13406.
56. Perez, C. F.; Mukherjee, S.; Allen, P. D., Amino acids 1-1,680 of ryanodine receptor type 1 hold critical determinants of skeletal type for excitation-contraction coupling - Role of divergence domain D2. *J. Biol. Chem.* **2003,** *278* (41), 39644-39652.
57. Nakai, J.; Dirksen, R. T.; Nguyen, H. T.; Pessah, I. N.; Beam, K. G.; Allen, P. D., Enhanced dihydropyridine receptor channel activity in the presence of ryanodine receptor. *Nature* **1996,** *380* (6569), 72-75.
58. Divet, A.; Paesante, S.; Bleunven, C.; Anderson, A.; Treves, S.; Zorzato, F., Novel sarco(endo) plasmic reticulum proteins and calcium homeostasis in striated muscles. *J. Muscle Res. Cell Motil.* **2005,** *26* (1), 7-12.
59. Patterson, R. L.; Boehning, D.; Snyder, S. H., Inositol 1,4,5-trisphosphatereceptors as signal integrators. *Annu. Rev. Biochem.* **2004,** *73*, 437-465.
60. Zhu, H. P.; Bhattacharyya, B. J.; Lin, H.; Gomez, C. M., Skeletal Muscle IP3R1 Receptors Amplify Physiological and Pathological Synaptic Calcium Signals. *J. Neurosci.* **2011,** *31* (43), 15269-15283.

61. Mikoshiba, K., IP3 receptor/Ca2+ channel: from discovery to new signaling concepts. *J. Neurochem.* **2007,** *102* (5), 1426-1446.
62. Serysheva, II, Toward a high-resolution structure of IP3R channel. *Cell Calcium* **2014,** *56* (3), 125-132.
63. Bezprozvanny, I., The inositol 1,4,5-trisphosphate receptors. *Cell Calcium* **2005,** *38* (3–4), 261-272.
64. Ferris, C. D.; Huganir, R. L.; Bredt, D. S.; Cameron, A. M.; Snyder, S. H., Inositol trisphosphate receptor: phosphorylation by protein kinase C and calcium calmodulin-dependent protein kinases in reconstituted lipid vesicles. *Proceedings of the National Academy of Sciences* **1991,** *88* (6), 2232-2235.
65. Dubyak, G. R.; el-Moatassim, C., Signal transduction via P2-purinergic receptors for extracellular ATP and other nucleotides. *American Journal of Physiology - Cell Physiology* **1993,** *265* (3), C577-C606.
66. Song, Z.; Vijayaraghavan, S.; Sladek, C. D., ATP increases intracellular calcium in supraoptic neurons by activation of both P2X and P2Y purinergic receptors. *American Journal of Physiology - Regulatory, Integrative and Comparative Physiology* **2007,** *292* (1), R423-R431.
67. Heizmann, C. W.; Hunzlker, W., Intracellular calcium-binding proteins: more sites than insights. *Trends Biochem.Sci.* **1991,** *16*, 98-103.
68. Schwaller, B., Cytosolic Ca2+ Buffers. *Cold Spring Harbor Perspect. Biol.* **2010,** *2* (11).
69. Arif, S. H., A Ca2+-binding protein with numerous roles and uses: parvalbumin in molecular biology and physiology. *Bioessays* **2009,** *31* (4), 410-421.
70. Robertson, S. P.; Johnson, J. D.; Potter, J. D., The time-course of Ca2+ exchange with calmodulin, troponin, parvalbumin, and myosin in response to transient increases in Ca2+. *Biophys. J.* **1981,** *34* (3), 559-569.
71. Lewit-Bentley, A.; Réty, S., EF-hand calcium-binding proteins. *Curr. Opin. Struct. Biol.* **2000,** *10* (6), 637-643.
72. Grabarek, Z., Structural basis for diversity of the EF-hand calcium-binding proteins. *Journal of Molecular Biology* **2006,** *359* (3), 509-525.
73. Hoeflich, K. P.; Ikura, M., Calmodulin in action: diversity in target recognition and activation mechanisms. *Cell* **2002,** *108* (6), 739-742.
74. Chin, D.; Means, A. R., Calmodulin: a prototypical calcium sensor. *Trends Cell Biol.* **2000,** *10* (8), 322-328.
75. de Baaij, J. H. F.; Hoenderop, J. G. J.; Bindels, R. J. M., Magnesium in Man: Implications for Health and Disease. *Physiol. Rev.* **2015,** *95* (1), 1-46.
76. Dudev, T.; Cowan, J. A.; Lim, C., Competitive Binding in Magnesium Coordination Chemistry: Water versus Ligands of Biological Interest. *Journal of the American Chemical Society* **1999,** *121* (33), 7665-7673.
77. Murphy, E., Mysteries of magnesium homeostasis. *Circ.Res.* **2000,** *86* (3), 245-248.
78. Permyakov, E. A.; Kretsinger, R. H., Cell signaling, beyond cytosolic calcium in eukaryotes. *J. Inorg. Biochem.* **2009,** *103* (1), 77-86.
79. Li, M.; Jiang, J.; Yue, L., Functional Characterization of Homo- and Heteromeric Channel Kinases TRPM6 and TRPM7. *The Journal of General Physiology* **2006,** *127* (5), 525-537.
80. Piskacek, M.; Zotova, L.; Zsurka, G.; Schweyen, R. J., Conditional knockdown of hMRS2 results in loss of mitochondrial Mg + uptake and cell death. *Journal of Cellular and Molecular Medicine* **2009,** *13* (4), 693-700.
81. Goytain, A.; Quamme, G. A., Identification and characterization of a novel mammalian Mg2+ transporter with channel-like properties. *BMC Genomics* **2005,** *6*, 18.
82. Saris, N. E. L.; Mervaala, E.; Karppanen, H.; Khawaja, J. A.; Lewenstam, A., Magnesium - An update on physiological, clinical and analytical aspects. *Clin. Chim. Acta* **2000,** *294* (1-2), 1-26.

83. Pham, P.-C. T.; Pham, P.-A. T.; Pham, S. V.; Pham, P.-T. T.; Pham, P.-M. T.; Pham, P.-T. T., Hypomagnesemia: a clinical perspective. *International journal of nephrology and renovascular disease* **2014,** *7*, 219-30.
84. Berridge, M. J., The endoplasmic reticulum: a multifunctional signaling organelle. *Cell Calcium* **2002,** *32* (5-6), 235-249.
85. Bootman, M. D.; Rietdorf, K.; Hardy, H.; Dautova, Y.; Corps, E.; Pierro, C.; Stapleton, E.; Kang, E.; Proudfoot, D., Calcium signalling and regulation of cell function. *eLS* **2006**.
86. Rizzuto, R.; Pozzan, T., Microdomains of intracellular Ca2+: Molecular determinants and functional consequences. *Physiol. Rev.* **2006,** *86* (1), 369-408.
87. Zhang, L.; Kelley, J.; Schmeisser, G.; Kobayashi, Y. M.; Jones, L. R., Complex formation between junction, triadin, calsequestrin, and the ryanodine receptor - Proteins of the cardiac junctional sarcoplasmic reticulum membrane. *J. Biol. Chem.* **1997,** *272* (37), 23389-23397.
88. Sorrentino, V., Molecular determinants of the structural and functional organization of the sarcoplasmic reticulum. *Biochimica et Biophysica Acta (BBA) - Molecular Cell Research* **2004,** *1742* (1–3), 113-118.
89. Bootman, M. D.; Lipp, P.; Berridge, M. J., The organisation and functions of local Ca2+ signals. *J. Cell Sci.* **2001,** *114* (12), 2213-2222.
90. Pozzan, T.; Rizzuto, R.; Volpe, P.; Meldolesi, J., *Molecular and cellular physiology of intracellular calcium stores*. 1994; Vol. 74, p 595-636.
91. Lam, A. K. M.; Galione, A., The endoplasmic reticulum and junctional membrane communication during calcium signaling. *Biochimica et Biophysica Acta (BBA) - Molecular Cell Research* **2013,** *1833* (11), 2542-2559.
92. Rossi, D.; Barone, V.; Giacomello, E.; Cusimano, V.; Sorrentino, V., The sarcoplasmic reticulum: an organized patchwork of specialized domains. *Traffic* **2008,** *9* (7), 1044-1049.
93. Porter, K. R.; Palade, G. E., Studies on the endoplasmic reticulum III. Its form and distribution in striated muscle cells. *The Journal of biophysical and biochemical cytology* **1957,** *3* (2), 269-300.
94. Rossi, A. E.; Dirksen, R. T., Sarcoplasmic reticulum: The dynamic calcium governor of muscle. *Muscle Nerve* **2006,** *33* (6), 715-731.
95. Sanchez, E. J.; Lewis, K. M.; Danna, B. R.; Kang, C., High-capacity Ca2+ Binding of Human Skeletal Calsequestrin. *J. Biol. Chem.* **2012,** *287* (14), 11592-11601.
96. Royer, L.; Rios, E., Deconstructing calsequestrin. Complex buffering in the calcium store of skeletal muscle. *J. Physiol.-London* **2009,** *587* (13), 3101-3111.
97. Park, H.; Wu, S.; Dunker, A. K.; Kang, C., Polymerization of Calsequestrin: IMPLICATIONS FOR Ca2+ REGULATION. *J. Biol. Chem.* **2003,** *278* (18), 16176-16182.
98. Beard, N. A.; Laver, D. R.; Dulhunty, A. F., Calsequestrin and the calcium release channel of skeletal and cardiac muscle. *Progress in Biophysics and Molecular Biology* **2004,** *85* (1), 33-69.
99. Zorzato, F.; Anderson, A. A.; Ohlendieck, K.; Froemming, G.; Guerrini, R.; Treves, S., Identification of a novel 45 kDa protein (JP-45) from rabbit sarcoplasmic-reticulum junctional-face membrane. *Biochem. J.* **2000,** *351*, 537-543.
100. Anderson, A. A.; Treves, S.; Biral, D.; Betto, R.; Sandona, D.; Ronjat, M.; Zorzato, F., The novel skeletal muscle sarcoplasmic reticulum JP-45 protein - Molecular cloning, tissue distribution, developmental expression, and interaction with alpha 1.1 subunit of the voltage-gated calcium channel. *J. Biol. Chem.* **2003,** *278* (41), 39987-39992.
101. Delbono, O.; Xia, J. Y.; Treves, S.; Wang, Z. M.; Jimenez-Moreno, R.; Payne, A. M.; Messi, M. L.; Briguet, A.; Schaerer, F.; Nishi, M.; Takeshima, H.; Zorzato, F., Loss of skeletal muscle strength by ablation of the sarcoplasmic reticulum protein JP45. *Proc. Natl. Acad. Sci. U. S. A.* **2007,** *104* (50), 20108-20113.

102. Hernandez-Ochoa, E. O.; Pratt, S. J. P.; Lovering, R. M.; Schneider, M. F., Critical Role of Intracellular RyR1 Calcium Release Channels in Skeletal Muscle Function and Disease. *Front. Physiol.* **2016,** *6*, 11.
103. Seo, M. D.; Enomoto, M.; Ishiyama, N.; Stathopulos, P. B.; Ikura, M., Structural insights into endoplasmic reticulum stored calcium regulation by inositol 1,4,5-trisphosphate and ryanodine receptors. *Biochimica Et Biophysica Acta-Molecular Cell Research* **2015,** *1853* (9), 1980-1991.
104. Bers, D. M., Calcium Cycling and Signaling in Cardiac Myocytes. *Annual Review of Physiology* **2008,** *70* (1), 23-49.
105. Bers, D. M.; Guo, T., Calcium signaling in cardiac ventricular myocytes. In *Communicative Cardiac Cell*, Sideman, S.; Beyar, R.; Landesberg, A., Eds. New York Acad Sciences: New York, 2005; Vol. 1047, pp 86-98.
106. Ríos, E.; Figueroa, L.; Manno, C.; Kraeva, N.; Riazi, S., The couplonopathies: A comparative approach to a class of diseases of skeletal and cardiac muscle. *The Journal of General Physiology* **2015,** *145* (6), 459-474.
107. Leenhardt, A.; Denjoy, I.; Guicheney, P., Catecholaminergic Polymorphic Ventricular Tachycardia. *Circulation: Arrhythmia and Electrophysiology* **2012,** *5* (5), 1044-1052.
108. Jiang, D. W.; Xiao, B. L.; Zhang, L.; Chen, S. R. W., Enhanced basal activity of a cardiac Ca2+ release channel (Ryanodine receptor) mutant associated with ventricular tachycardia and sudden death. *Circ.Res.* **2002,** *91* (3), 218-225.
109. Yano, M.; Yamamoto, T.; Kobayashi, S.; Matsuzaki, M., Role of ryanodine receptor as a Ca2+ regulatory center in normal and failing hearts. *J. Cardiol.* **2009,** *53* (1), 1-7.
110. Bers, D. M.; Shannon, T. R., Calcium movements inside the sarcoplasmic reticulum of cardiac myocytes. *J. Mol. Cell. Cardiol.* **2013,** *58*, 59-66.
111. Robinson, R.; Carpenter, D.; Shaw, M. A.; Halsall, J.; Hopkins, P., Mutations in RYR1 in malignant hyperthermia and central core disease. *Hum. Mutat.* **2006,** *27* (10), 977-989.
112. Mickelson, J. R.; Louis, C. F., Malignant hyperthermia: Excitation-contraction coupling, Ca2+ release channel, and cell Ca2+ regulation defects. *Physiol. Rev.* **1996,** *76* (2), 537-592.
113. Rosenberg, H.; Pollock, N.; Schiemann, A.; Bulger, T.; Stowell, K., Malignant hyperthermia: a review. *Orphanet J. Rare Dis.* **2015,** *10*.
114. Betzenhauser, M. J.; Marks, A. R., Ryanodine receptor channelopathies. *Pflugers Arch.* **2010,** *460* (2), 467-480.
115. Monnier, N.; Procaccio, V.; Stieglitz, P.; Lunardi, J., Malignant-hyperthermia susceptibility is associated with a mutation of the alpha(1)-subunit of the human dihydropyridine-sensitive L-type voltage-dependent calcium-channel receptor in skeletal muscle. *Am. J. Hum. Genet.* **1997,** *60* (6), 1316-1325.
116. MacLennan, D. H., Ca2+ signalling and muscle disease. *Eur. J. Biochem.* **2000,** *267* (17), 5291-5297.
117. Krause, T.; Gerbershagen, M. U.; Fiege, M.; Weisshorn, R.; Wappler, F., Dantrolene - A review of its pharmacology, therapeutic use and new developments. *Anaesthesia* **2004,** *59* (4), 364-373.
118. Bannister, R. A., Dantrolene-Induced Inhibition of Skeletal L-Type Ca2+ Current Requires RyR1 Expression. *Biomed Res. Int.* **2013**.
119. LaFerla, F. M., Calcium dyshomeostasis and intracellular signalling in Alzheimer's disease. *Nat. Rev. Neurosci.* **2002,** *3* (11), 862-872.
120. Supnet, C.; Bezprozvanny, I., The dysregulation of intracellular calcium in Alzheimer disease. *Cell Calcium* **2010,** *47* (2), 183-189.
121. Wojda, U.; Salinska, E.; Kuznicki, J., Calcium ions in neuronal degeneration. *Iubmb Life* **2008,** *60* (9), 575-590.

122. Mattson, M. P.; Chan, S. L., Neuronal and glial calcium signaling in Alzheimer's disease. *Cell Calcium* **2003,** *34* (4-5), 385-397.
123. Liang, J. Y.; Kulasiri, D.; Samarasinghe, S., Ca2+ dysregulation in the endoplasmic reticulum related to Alzheimer's disease: A review on experimental progress and computational modeling. *Biosystems* **2015,** *134*, 1-15.
124. Lopez, J. R.; Lyckman, A.; Oddo, S.; LaFerla, F. M.; Querfurth, H. W.; Shtifman, A., Increased intraneuronal resting Ca2+ in adult Alzheimer's disease mice. *J. Neurochem.* **2008,** *105* (1), 262-271.
125. Cheung, K. H.; Shineman, D.; Muller, M.; Cardenas, C.; Mei, L. J.; Yang, J.; Tomita, T.; Iwatsubo, T.; Lee, V. M. Y.; Foskett, J. K., Mechanism of Ca2+ disruption in Alzheimer's disease by presenilin regulation of InsP(3) receptor channel gating. *Neuron* **2008,** *58* (6), 871-883.
126. Demuro, A.; Parker, I., Cytotoxicity of Intracellular A beta(42) Amyloid Oligomers Involves Ca2+ Release from the Endoplasmic Reticulum by Stimulated Production of Inositol Trisphosphate. *J. Neurosci.* **2013,** *33* (9), 3824-3833.
127. Shilling, D.; Muller, M.; Takano, H.; Mak, D. O. D.; Abel, T.; Coulter, D. A.; Foskett, J. K., Suppression of InsP(3) Receptor-Mediated Ca2+ Signaling Alleviates Mutant Presenilin-Linked Familial Alzheimer's Disease Pathogenesis. *J. Neurosci.* **2014,** *34* (20), 6910-6923.
128. Oules, B.; Del Prete, D.; Greco, B.; Zhang, X. X.; Lauritzen, I.; Sevalle, J.; Moreno, S.; Paterlini-Brechot, P.; Trebak, M.; Checler, F.; Benfenati, F.; Chami, M., Ryanodine Receptor Blockade Reduces Amyloid-beta Load and Memory Impairments in Tg2576 Mouse Model of Alzheimer Disease. *J. Neurosci.* **2012,** *32* (34), 11820-11834.
129. Paredes, R. M.; Etzler, J. C.; Watts, L. T.; Zheng, W.; Lechleiter, J. D., Chemical calcium indicators. *Methods* **2008,** *46* (3), 143-151.
130. Koldenkova, V. P.; Nagai, T., Genetically encoded Ca2+ indicators: Properties and evaluation. *Biochimica Et Biophysica Acta-Molecular Cell Research* **2013,** *1833* (7), 1787-1797.
131. Gerasimenko, J. V.; Petersen, O. H.; Gerasimenko, O. V., Monitoring of intra-ER free Ca2+. *Wiley Interdisciplinary Reviews: Membrane Transport and Signaling* **2014,** *3* (3), 63-71.
132. Tsien, R. Y., New calcium indicators and buffers with high selectivity against magnesium and protons: design, synthesis, and properties of prototype structures. *Biochemistry* **1980,** *19* (11), 2396-2404.
133. Grynkiewicz, G.; Poenie, M.; Tsien, R. Y., A new generation of Ca2+ indicators with greatly improved fluorescence properties. *J. Biol. Chem.* **1985,** *260* (6), 3440-3450.
134. Tsien, R. Y.; Pozzan, T.; Rink, T. J., Calcium homeostasis in intact lymphocytes: cytoplasmic free calcium monitored with a new, intracellularly trapped fluorescent indicator. *The Journal of cell biology* **1982,** *94* (2), 325-34.
135. Pethig, R.; Kuhn, M.; Payne, R.; Adler, E.; Chen, T. H.; Jaffe, L. F., On the dissociation constants of BAPTA-type calcium buffers. *Cell Calcium* **1989,** *10* (7), 491-498.
136. Hoth, M.; Penner, R., DEPLETION OF INTRACELLULAR CALCIUM STORES ACTIVATES A CALCIUM CURRENT IN MAST-CELLS. *Nature* **1992,** *355* (6358), 353-356.
137. Liu, G. L.; Honisch, S.; Liu, G. X.; Schmidt, S.; Alkahtani, S.; AlKahtane, A. A.; Stournaras, C.; Lang, F., Up-regulation of Orai1 expression and store operated Ca2+ entry following activation of membrane androgen receptors in MCF-7 breast tumor cells. *Bmc Cancer* **2015,** *15*, 10.
138. *A fluorescent indicator for measuring cytosolic free magnesium*. 1989; Vol. 256, p C540-C548.
139. Raju, B.; Murphy, E.; Levy, L. A.; Hall, R. D.; London, R. E., A fluorescent indicator for measuring cytosolic free magnesium. *American Journal of Physiology - Cell Physiology* **1989,** *256* (3), C540-C548.
140. Murphy, E.; Freudenrich, C. C.; Levy, L. A.; London, R. E.; Lieberman, M., MONITORING CYTOSOLIC FREE MAGNESIUM IN CULTURED CHICKEN HEART CELLS BY USE OF THE FLUORESCENT INDICATOR FURAPTRA. *Proc. Natl. Acad. Sci. U. S. A.* **1989,** *86* (8), 2981-2984.

141. Hofer, A. M.; Machen, T. E., TECHNIQUE FOR INSITU MEASUREMENT OF CALCIUM IN INTRACELLULAR INOSITOL 1,4,5-TRISPHOSPHATE-SENSITIVE STORES USING THE FLUORESCENT INDICATOR MAG-FURA-2. *Proc. Natl. Acad. Sci. U. S. A.* **1993,** *90* (7), 2598-2602.
142. Gee, K. R.; Brown, K. A.; Chen, W. N. U.; Bishop-Stewart, J.; Gray, D.; Johnson, I., Chemical and physiological characterization of fluo-4 Ca2+-indicator dyes. *Cell Calcium* **2000,** *27* (2), 97-106.
143. Minta, A.; Kao, J.; Tsien, R. Y., Fluorescent indicators for cytosolic calcium based on rhodamine and fluorescein chromophores. *J. Biol. Chem.* **1989,** *264* (14), 8171-8178.
144. Chudakov, D. M.; Lukyanov, S.; Lukyanov, K. A., Fluorescent proteins as a toolkit for in vivo imaging. *Trends in Biotechnology* **2005,** *23* (12), 605-613.
145. Chudakov, D. M.; Matz, M. V.; Lukyanov, S.; Lukyanov, K. A., Fluorescent Proteins and Their Applications in Imaging Living Cells and Tissues. *Physiol. Rev.* **2010,** *90* (3), 1103-1163.
146. Morise, H.; Shimomura, O.; Johnson, F. H.; Winant, J., Intermolecular energy transfer in the bioluminescent system of Aequorea. *Biochemistry* **1974,** *13* (12), 2656-2662.
147. Shimomura, O.; Johnson, F. H.; Saiga, Y., Extraction, Purification and Properties of Aequorin, a Bioluminescent Protein from the Luminous Hydromedusan, Aequorea. *Journal of Cellular and Comparative Physiology* **1962,** *59* (3), 223-239.
148. Head, J. F.; Inouye, S.; Teranishi, K.; Shimomura, O., The crystal structure of the photoprotein aequorin at 2.3 [angst] resolution. *Nature* **2000,** *405* (6784), 372-376.
149. Shimomura, O., Structure of the chromophore of Aequorea green fluorescent protein. *FEBS Lett.* **1979,** *104* (2), 220-222.
150. Prasher, D. C.; Eckenrode, V. K.; Ward, W. W.; Prendergast, F. G.; Cormier, M. J., PRIMARY STRUCTURE OF THE AEQUOREA-VICTORIA GREEN-FLUORESCENT PROTEIN. *Gene* **1992,** *111* (2), 229-233.
151. Chalfie, M.; Tu, Y.; Euskirchen, G.; Ward, W.; Prasher, D., Green fluorescent protein as a marker for gene expression. *Science* **1994,** *263* (5148), 802-805.
152. Heim, R.; Prasher, D. C.; Tsien, R. Y., WAVELENGTH MUTATIONS AND POSTTRANSLATIONAL AUTOXIDATION OF GREEN FLUORESCENT PROTEIN. *Proc. Natl. Acad. Sci. U. S. A.* **1994,** *91* (26), 12501-12504.
153. Ormö, M.; Cubitt, A. B.; Kallio, K.; Gross, L. A.; Tsien, R. Y.; Remington, S. J., Crystal Structure of the Aequorea victoria Green Fluorescent Protein. *Science* **1996,** *273* (5280), 1392-1395.
154. Yang, F.; Moss, L. G.; Phillips, G. N., The molecular structure of green fluorescent protein. *Nat. Biotechnol.* **1996,** *14* (10), 1246-1251.
155. Heim, R.; Tsien, R. Y., Engineering green fluorescent protein for improved brightness, longer wavelengths and fluorescence resonance energy transfer. *Curr. Biol.* **1996,** *6* (2), 178-182.
156. Baird, G. S.; Zacharias, D. A.; Tsien, R. Y., Biochemistry, mutagenesis, and oligomerization of DsRed, a red fluorescent protein from coral. *Proceedings of the National Academy of Sciences* **2000,** *97* (22), 11984-11989.
157. Gross, L. A.; Baird, G. S.; Hoffman, R. C.; Baldridge, K. K.; Tsien, R. Y., The structure of the chromophore within DsRed, a red fluorescent protein from coral. *Proc. Natl. Acad. Sci. U. S. A.* **2000,** *97* (22), 11990-11995.
158. Campbell, R. E.; Tour, O.; Palmer, A. E.; Steinbach, P. A.; Baird, G. S.; Zacharias, D. A.; Tsien, R. Y., A monomeric red fluorescent protein. *Proceedings of the National Academy of Sciences* **2002,** *99* (12), 7877-7882.
159. Shaner, N. C.; Campbell, R. E.; Steinbach, P. A.; Giepmans, B. N. G.; Palmer, A. E.; Tsien, R. Y., Improved monomeric red, orange and yellow fluorescent proteins derived from Discosoma sp. red fluorescent protein. *Nat Biotech* **2004,** *22* (12), 1567-1572.
160. Shu, X. K.; Shaner, N. C.; Yarbrough, C. A.; Tsien, R. Y.; Remington, S. J., Novel chromophores and buried charges control color in mFruits. *Biochemistry* **2006,** *45* (32), 9639-9647.

161. Dedecker, P.; De Schryver, F. C.; Hofkens, J., Fluorescent Proteins: Shine on, You Crazy Diamond. *Journal of the American Chemical Society* **2013,** *135* (7), 2387-2402.
162. Tsien, R. Y., The green fluorescent protein. *Annu. Rev. Biochem.* **1998,** *67*, 509-544.
163. Reid, B. G.; Flynn, G. C., Chromophore formation in green fluorescent protein. *Biochemistry* **1997,** *36* (22), 6786-6791.
164. Zimmer, M., Green fluorescent protein (GFP): Applications, structure, and related photophysical behavior. *Chem. Rev.* **2002,** *102* (3), 759-781.
165. Sample, V.; Newman, R. H.; Zhang, J., The structure and function of fluorescent proteins. *Chem. Soc. Rev.* **2009,** *38* (10), 2852-2864.
166. Shinobu, A.; Palm, G. J.; Schierbeek, A. J.; Agmon, N., Visualizing Proton Antenna in a High-Resolution Green Fluorescent Protein Structure. *Journal of the American Chemical Society* **2010,** *132* (32), 11093-11102.
167. Li, X. Q.; Zhang, G. H.; Ngo, N.; Zhao, X. N.; Kain, S. R.; Huang, C. C., Deletions of the Aequorea victoria green fluorescent protein define the minimal domain required for fluorescence. *J. Biol. Chem.* **1997,** *272* (45), 28545-28549.
168. Crameri, A.; Whitehorn, E. A.; Tate, E.; Stemmer, W. P. C., Improved Green Fluorescent Protein by Molecular Evolution Using DNA Shuffling. *Nat Biotech* **1996,** *14* (3), 315-319.
169. Pedelacq, J. D.; Cabantous, S.; Tran, T.; Terwilliger, T. C.; Waldo, G. S., Engineering and characterization of a superfolder green fluorescent protein. *Nat. Biotechnol.* **2006,** *24* (1), 79-88.
170. Arpino, J. A. J.; Rizkallah, P. J.; Jones, D. D., Crystal Structure of Enhanced Green Fluorescent Protein to 1.35 Å Resolution Reveals Alternative Conformations for Glu222. *PLoS One* **2012,** *7* (10), e47132.
171. Patterson, G. H.; Knobel, S. M.; Sharif, W. D.; Kain, S. R.; Piston, D. W., Use of the green fluorescent protein and its mutants in quantitative fluorescence microscopy. *Biophys. J.* **1997,** *73* (5), 2782-2790.
172. Wachter, R. M.; King, B. A.; Heim, R.; Kallio, K.; Tsien, R. Y.; Boxer, S. G.; Remington, S. J., Crystal Structure and Photodynamic Behavior of the Blue Emission Variant Y66H/Y145F of Green Fluorescent Protein. *Biochemistry* **1997,** *36* (32), 9759-9765.
173. Griesbeck, O.; Baird, G. S.; Campbell, R. E.; Zacharias, D. A.; Tsien, R. Y., Reducing the environmental sensitivity of yellow fluorescent protein - Mechanism and applications. *J. Biol. Chem.* **2001,** *276* (31), 29188-29194.
174. Rekas, A.; Alattia, J. R.; Nagai, T.; Miyawaki, A.; Ikura, M., Crystal structure of Venus, a yellow fluorescent protein with improved maturation and reduced environmental sensitivity. *J. Biol. Chem.* **2002,** *277* (52), 50573-50578.
175. Nagai, T.; Ibata, K.; Park, E. S.; Kubota, M.; Mikoshiba, K.; Miyawaki, A., A variant of yellow fluorescent protein with fast and efficient maturation for cell-biological applications. *Nat. Biotechnol.* **2002,** *20* (1), 87-90.
176. Kremers, G.-J.; Goedhart, J.; van Munster, E. B.; Gadella, T. W. J., Cyan and Yellow Super Fluorescent Proteins with Improved Brightness, Protein Folding, and FRET Förster Radius. *Biochemistry* **2006,** *45* (21), 6570-6580.
177. Miyawaki, A.; Llopis, J.; Heim, R.; McCaffery, J. M.; Adams, J. A.; Ikura, M.; Tsien, R. Y., Fluorescent indicators for Ca2+ based on green fluorescent proteins and calmodulin. *Nature* **1997,** *388* (6645), 882-887.
178. Whitaker, M., Genetically Encoded Probes for Measurement of Intracellular Calcium. In *Calcium in Living Cells*, Whitaker, M., Ed. Elsevier Academic Press Inc: San Diego, 2010; Vol. 99, pp 153-182.
179. Palmer, A. E.; Qin, Y.; Park, J. G.; McCombs, J. E., Design and application of genetically encoded biosensors. *Trends Biotechnol.* **2011,** *29* (3), 144-152.

180. Tang, S.; Wong, H. C.; Wang, Z. M.; Huang, Y.; Zou, J.; Zhuo, Y.; Pennati, A.; Gadda, G.; Delbono, O.; Yang, J. J., Design and application of a class of sensors to monitor Ca(2+) dynamics in high Ca(2+) concentration cellular compartments. *Proc. Natl. Acad. Sci. U. S. A.* **2011,** *108* (39), 16265-16270.
181. Zhang, Y.; Reddish, F.; Tang, S.; Zhuo, Y.; Wang, Y. F.; Yang, J. J.; Weber, I. T., Structural basis for a hand-like site in the calcium sensor CatchER with fast kinetics. *Acta Crystallographica Section D-Biological Crystallography* **2013,** *69*, 2309-2319.
182. Frommer, W. B.; Davidson, M. W.; Campbell, R. E., Genetically encoded biosensors based on engineered fluorescent proteins. *Chem. Soc. Rev.* **2009,** *38* (10), 2833-2841.
183. Newman, R. H.; Fosbrink, M. D.; Zhang, J., Genetically Encodable Fluorescent Biosensors for Tracking Signaling Dynamics in Living Cells. *Chem. Rev.* **2011,** *111* (5), 3614-3666.
184. Prasher, D.; McCann, R. O.; Cormier, M. J., Cloning and expression of the cDNA coding for aequorin, a bioluminescent calcium-binding protein. *Biochemical and Biophysical Research Communications* **1985,** *126* (3), 1259-1268.
185. Brini, M.; Marsault, R.; Bastianutto, C.; Alvarez, J.; Pozzan, T.; Rizzuto, R., Transfected Aequorin in the Measurement of Cytosolic Ca2+ Concentration ([Ca2+]c): A CRITICAL EVALUATION. *J. Biol. Chem.* **1995,** *270* (17), 9896-9903.
186. Rutter, G. A.; Burnett, P.; Rizzuto, R.; Brini, M.; Murgia, M.; Pozzan, T.; Tavare, J. M.; Denton, R. M., Subcellular imaging of intramitochondrial Ca2+ with recombinant targeted aequorin: Significance for the regulation of pyruvate dehydrogenase activity. *Proc. Natl. Acad. Sci. U. S. A.* **1996,** *93* (11), 5489-5494.
187. Baubet, V.; Le Mouellic, H.; Campbell, A. K.; Lucas-Meunier, E.; Fossier, P.; Brulet, P., Chimeric green fluorescent protein-aequorin as bioluminescent Ca2+ reporters at the single-cell level. *Proc. Natl. Acad. Sci. U. S. A.* **2000,** *97* (13), 7260-7265.
188. Curie, T.; Rogers, K. L.; Colasante, C.; Brulet, P., Red-shifted aequorin-based bioluminescent reporters for in vivo imaging of Ca2+ signaling. *Mol. Imaging* **2007,** *6* (1), 30-42.
189. Rodriguez-Garcia, A.; Rojo-Ruiz, J.; Navas-Navarro, P.; Aulestia, F. J.; Gallego-Sandin, S.; Garcia-Sancho, J.; Alonso, M. T., GAP, an aequorin-based fluorescent indicator for imaging Ca2+ in organelles. *Proc. Natl. Acad. Sci. U. S. A.* **2014,** *111* (7), 2584-2589.
190. Geoffrey, S. B.; David, A. Z.; Roger, Y. T., Circular Permutation and Receptor Insertion within Green Fluorescent Proteins. *Proc. Natl. Acad. Sci. U. S. A.* **1999,** *96* (20), 11241-11246.
191. Zou, J.; Hofer, A. M.; Lurtz, M. M.; Gadda, G.; Ellis, A. L.; Chen, N.; Huang, Y.; Holder, A.; Ye, Y.; Louis, C. F.; Welshhans, K.; Rehder, V.; Yang, J. J., Developing sensors for real-time measurement of high Ca2+ concentrations. *Biochemistry* **2007,** *46* (43), 12275-12288.
192. Waldeck-Weiermair, M.; Bischof, H.; Blass, S.; Deak, A.; Klec, C.; Graier, T.; Roller, C.; Rost, R.; Eroglu, E.; Gottschalk, B.; Hofmann, N.; Graier, W.; Malli, R., Generation of Red-Shifted Cameleons for Imaging Ca2+ Dynamics of the Endoplasmic Reticulum. *Sensors* **2015,** *15* (6), 13052.
193. Nakai, J.; Ohkura, M.; Imoto, K., A high signal-to-noise Ca2+ probe composed of a single green fluorescent protein. *Nat. Biotechnol.* **2001,** *19* (2), 137-141.
194. Akerboom, J.; Rivera, J. D. V.; Guilbe, M. M. R.; Malave, E. C. A.; Hernandez, H. H.; Tian, L.; Hires, S. A.; Marvin, J. S.; Looger, L. L.; Schreiter, E. R., Crystal Structures of the GCaMP Calcium Sensor Reveal the Mechanism of Fluorescence Signal Change and Aid Rational Design. *J. Biol. Chem.* **2009,** *284* (10), 6455-6464.
195. Tallini, Y. N.; Ohkura, M.; Choi, B. R.; Ji, G. J.; Imoto, K.; Doran, R.; Lee, J.; Plan, P.; Wilson, J.; Xin, H. B.; Sanbe, A.; Gulick, J.; Mathai, J.; Robbins, J.; Salama, G.; Nakai, J.; Kotlikoff, M. I., Imaging cellular signals in the heart in vivo: Cardiac expression of the high-signal Ca2+ indicator GCaMP2. *Proc. Natl. Acad. Sci. U. S. A.* **2006,** *103* (12), 4753-4758.
196. Tian, L.; Hires, S. A.; Mao, T.; Huber, D.; Chiappe, M. E.; Chalasani, S. H.; Petreanu, L.; Akerboom, J.; McKinney, S. A.; Schreiter, E. R.; Bargmann, C. I.; Jayaraman, V.; Svoboda, K.; Looger, L. L., Imaging

neural activity in worms, flies and mice with improved GCaMP calcium indicators. *Nat. Methods* **2009,** *6* (12), 875-881.
197. Akerboom, J.; Chen, T. W.; Wardill, T. J.; Tian, L.; Marvin, J. S.; Mutlu, S.; Calderon, N. C.; Esposti, F.; Borghuis, B. G.; Sun, X. R.; Gordus, A.; Orger, M. B.; Portugues, R.; Engert, F.; Macklin, J. J.; Filosa, A.; Aggarwal, A.; Kerr, R. A.; Takagi, R.; Kracun, S.; Shigetomi, E.; Khakh, B. S.; Baier, H.; Lagnado, L.; Wang, S. S. H.; Bargmann, C. I.; Kimmel, B. E.; Jayaraman, V.; Svoboda, K.; Kim, D. S.; Schreiter, E. R.; Looger, L. L., Optimization of a GCaMP Calcium Indicator for Neural Activity Imaging. *J. Neurosci.* **2012,** *32* (40), 13819-13840.
198. Shang, W.; Lu, F.; Sun, T.; Xu, J.; Li, L. L.; Wang, Y.; Wang, G.; Chen, L.; Wang, X.; Cannell, M. B.; Wang, S. Q.; Cheng, H., Imaging Ca2+ nanosparks in heart with a new targeted biosensor. *Circ Res* **2014,** *114* (3), 412-20.
199. Yamada, Y.; Mikoshiba, K., Quantitative comparison of novel GCaMP-type genetically encoded Ca2+ indicators in mammalian neurons. *Front. Cell. Neurosci.* **2012,** *6*.
200. Wu, J. H.; Prole, D. L.; Shen, Y.; Lin, Z. H.; Gnanasekaran, A.; Liu, Y. J.; Chen, L. D.; Zhou, H.; Cheng, S. R. W.; Usachev, Y. M.; Taylor, C. W.; Campbell, R. E., Red fluorescent genetically encoded Ca2+ indicators for use in mitochondria and endoplasmic reticulum. *Biochem. J.* **2014,** *464*, 13-22.
201. Suzuki, J.; Kanemaru, K.; Ishii, K.; Ohkura, M.; Okubo, Y.; Iino, M., Imaging intraorganellar Ca2+ at subcellular resolution using CEPIA. *Nat. Commun.* **2014,** *5*.
202. Heim, N.; Griesbeck, O., Genetically Encoded Indicators of Cellular Calcium Dynamics Based on Troponin C and Green Fluorescent Protein. *J. Biol. Chem.* **2004,** *279* (14), 14280-14286.
203. Nagai, T.; Sawano, A.; Park, E. S.; Miyawaki, A., Circularly permuted green fluorescent proteins engineered to sense Ca2+. *Proceedings of the National Academy of Sciences* **2001,** *98* (6), 3197-3202.
204. Nagai, T.; Yamada, S.; Tominaga, T.; Ichikawa, M.; Miyawaki, A., Expanded dynamic range of fluorescent indicators for Ca2+ by circularly permuted yellow fluorescent proteins. *Proc. Natl. Acad. Sci. U. S. A.* **2004,** *101* (29), 10554-10559.
205. Mank, M.; Reiff, D. F.; Heim, N.; Friedrich, M. W.; Borst, A.; Griesbeck, O., A FRET-based calcium biosensor with fast signal kinetics and high fluorescence change. *Biophys. J.* **2006,** *90* (5), 1790-1796.
206. Miyawaki, A.; Griesbeck, O.; Heim, R.; Tsien, R. Y., Dynamic and quantitative Ca2+ measurements using improved cameleons. *Proc. Natl. Acad. Sci. U. S. A.* **1999,** *96* (5), 2135-2140.
207. Palmer, A. E.; Jin, C.; Reed, J. C.; Tsien, R. Y., Bcl-2-mediated alterations in endoplasmic reticulum Ca2+ analyzed with an improved genetically encoded fluorescent sensor. *Proc. Natl. Acad. Sci. U. S. A.* **2004,** *101* (50), 17404-17409.
208. Yang, W.; Wilkins, A. L.; Ye, Y. M.; Liu, Z. R.; Li, S. Y.; Urbauer, J. L.; Hellinga, H. W.; Kearney, A.; van der Merwe, P. A.; Yang, J. J., Design of a calcium-binding protein with desired structure in a cell adhesion molecule. *Journal of the American Chemical Society* **2005,** *127* (7), 2085-2093.
209. Yang, W.; Jones, L. M.; Isley, L.; Ye, Y. M.; Lee, H. W.; Wilkins, A.; Liu, Z. R.; Hellinga, H. W.; Malchow, R.; Ghazi, M.; Yang, J. J., Rational design of a calcium-binding protein. *Journal of the American Chemical Society* **2003,** *125* (20), 6165-6171.
210. Maniccia, A. W.; Yang, W.; Li, S. Y.; Johnson, J. A.; Yang, J. J., Using protein design to dissect the effect of charged residues on metal binding and protein stability. *Biochemistry* **2006,** *45* (18), 5848-5856.
211. Maniccia, A. L. W.; Yang, W.; Johnson, J.; Li, S.; Harianto, T.; Zhou, H. X.; Shaket, L. A.; Yang, J. J., Inverse tuning of metal binding affinity and protein stability by altering charged coordination residues in designed calcium binding proteins. *PMC Biophysics* **2009,** *2* (11).
212. Kirberger, M.; Wang, X.; Deng, H.; Yang, W.; Chen, G. T.; Yang, J. J., Statistical analysis of structural characteristics of protein Ca(2+)-binding sites. *J. Biol. Inorg. Chem.* **2008,** *13* (7), 1169-1181.
213. Kirberger, M.; Wang, X.; Zhao, K.; Tang, S.; Chen, G. T.; Yang, J. J., Integration of Diverse Research Methods to Analyze and Engineer Ca(2+)-Binding Proteins: From Prediction to Production. *Curr. Bioinform.* **2010,** *5* (1), 68-80.

214. Zhuo, Y.; Solntsev, K. M.; Reddish, F.; Tang, S.; Yang, J. J., Effect of Ca2+ on the Steady-State and Time-Resolved Emission Properties of the Genetically Encoded Fluorescent Sensor CatchER. *The Journal of Physical Chemistry B* **2014**.
215. Liu, H.; Naismith, J. H., An efficient one-step site-directed deletion, insertion, single and multiple-site plasmid mutagenesis protocol. *BMC Biotechnology* **2008,** *8*, 91-91.
216. Hughes, D., A press for disrupting bacteria and other micro-organisms. *British journal of experimental pathology* **1951,** *32* (2), 97.
217. Huang, C. Y., [27] Determination of binding stoichiometry by the continuous variation method: The job plot. *Methods in enzymology* **1982,** *87*, 509-525.
218. Fery-Forgues, S.; Lavabre, D., Are fluorescence quantum yields so tricky to measure? A demonstration using familiar stationery products. *J. Chem. Educ* **1999,** *76* (9), 1260.
219. Escobedo, J.; Koh, T. J., Improved transfection technique for adherent cells using a commercial lipid reagent. *Biotechniques* **2003,** *35* (5), 936-+.
220. Berridge, M. J.; Bootman, M. D.; Lipp, P., Calcium - a life and death signal. *Nature* **1998,** *395* (6703), 645-648.
221. Zhang, X. C.; Joseph, S. K., Effect of mutation of a calmodulin binding site on Ca2+ regulation of inositol trisphosphate receptors. *Biochem. J.* **2001,** *360*, 395-400.
222. Persechini, A.; Lynch, J. A.; Romoser, V. A., Novel fluorescent indicator proteins for monitoring free intracellular Ca2+. *Cell Calcium* **1997,** *22* (3), 209-216.
223. Mank, M.; Griesbeck, O., Genetically encoded calcium indicators. *Chem. Rev.* **2008,** *108* (5), 1550-1564.
224. Romoser, V. A.; Hinkle, P. M.; Persechini, A., Detection in living cells of Ca2+-dependent changes in the fluorescence emission of an indicator composed of two green fluorescent protein variants linked by a calmodulin-binding sequence - A new class of fluorescent indicators. *J. Biol. Chem.* **1997,** *272* (20), 13270-13274.
225. Takahashi, A.; Camacho, P.; Lechleiter, J. D.; Herman, B., Measurement of intracellular calcium. *Physiol. Rev.* **1999,** *79* (4), 1089-1125.
226. Solovyova, N.; Verkhratsky, A., Monitoring of free calcium in the neuronal endoplasmic reticulum: an overview of modern approaches. *Journal of Neuroscience Methods* **2002,** *122* (1), 1-12.
227. Ohkura, M.; Matsuzaki, M.; Kasai, H.; Imoto, K.; Nakai, J., Genetically encoded bright Ca-2+ probe applicable for dynamic Ca-2+ imaging of dendritic spines. *Anal. Chem.* **2005,** *77* (18), 5861-5869.
228. Palmer, A. E.; Giacomello, M.; Kortemme, T.; Hires, S. A.; Lev-Ram, V.; Baker, D.; Tsien, R. Y., Ca2+ indicators based on computationally redesigned calmodulin-peptide pairs. *Chemistry & Biology* **2006,** *13* (5), 521-530.
229. Evanko, D. S.; Haydon, P. G., Elimination of environmental sensitivity in a cameleon FRET-based calcium sensor via replacement of the acceptor with Venus. *Cell Calcium* **2005,** *37* (4), 341-348.
230. Rudolf, R.; Magalhaes, P. J.; Pozzan, T., Direct in vivo monitoring of sarcoplasmic reticulum Ca2+ and cytosolic cAMP dynamics in mouse skeletal muscle. *Journal of Cell Biology* **2006,** *173* (2), 187-193.
231. Jimenez-Moreno, R.; Wang, Z.-M.; Messi, M. L.; Delbono, O., Sarcoplasmic reticulum Ca2+ depletion in adult skeletal muscle fibres measured with the biosensor D1ER. *Pflugers Arch.* **2010,** *459* (5), 725-735.
232. Ormo, M.; Cubitt, A. B.; Kallio, K.; Gross, L. A.; Tsien, R. Y.; Remington, S. J., Crystal structure of the Aequorea victoria green fluorescent protein. *Science* **1996,** *273* (5280), 1392-1395.
233. Arpino, J. A. J.; Rizkallah, P. J.; Jones, D. D., Crystal Structure of Enhanced Green Fluorescent Protein to 1.35 angstrom Resolution Reveals Alternative Conformations for Glu222. *PLoS One* **2012,** *7* (10).

234. Wang, Z.-M.; Tang, S.; Messi, M. L.; Yang, J. J.; Delbono, O., Residual sarcoplasmic reticulum Ca2+ concentration after Ca2+ release in skeletal myofibers from young adult and old mice. *Pflügers Archiv - European Journal of Physiology* **2012,** *463* (4), 615-624.
235. Tang, S.; Wong, H.-C.; Wang, Z.-M.; Huang, Y.; Zou, J.; Zhuo, Y.; Pennati, A.; Gadda, G.; Delbono, O.; Yang, J. J., Design and application of a class of sensors to monitor Ca2+ dynamics in high Ca2+ concentration cellular compartments. *Proc. Natl. Acad. Sci. U. S. A.* **2011,** *108* (39), 16265-16270.
236. Wang, Z.-M.; Tang, S.; Messi, M. L.; Yang, J. J.; Delbono, O., Residual sarcoplasmic reticulum Ca2+ concentration after Ca2+ release in skeletal myofibers from young adult and old mice. *Pflugers Arch.* **2012,** *463* (4), 615-624.
237. Rosenow, M. A.; Patel, H. N.; Wachter, R. M., Oxidative chemistry in the GFP active site leads to covalent cross-linking of a modified leucine side chain with a histidine imidazole: implications for the mechanism of chromophore formation. *Biochemistry* **2005,** *44* (23), 8303-8311.
238. Yarbrough, D.; Wachter, R. M.; Kallio, K.; Matz, M. V.; Remington, S. J., Refined crystal structure of DsRed, a red fluorescent protein from coral, at 2.0-Å resolution. *Proceedings of the National Academy of Sciences* **2001,** *98* (2), 462-467.
239. Malo, G. D.; Wang, M.; Wu, D.; Stelling, A. L.; Tonge, P. J.; Wachter, R. M., Crystal structure and Raman studies of dsFP483, a cyan fluorescent protein from Discosoma striata. *Journal of molecular biology* **2008,** *378* (4), 871-886.
240. Shu, X.; Wang, L.; Colip, L.; Kallio, K.; Remington, S. J., Unique interactions between the chromophore and glutamate 16 lead to far-red emission in a red fluorescent protein. *Protein Sci.* **2009,** *18* (2), 460-466.
241. Stiel, A. C.; Trowitzsch, S.; Weber, G.; Andresen, M.; Eggeling, C.; Hell, S. W.; Jakobs, S.; Wahl, M. C., 1.8 Å bright-state structure of the reversibly switchable fluorescent protein Dronpa guides the generation of fast switching variants. *Biochem. J.* **2007,** *402* (1), 35-42.
242. Tie, Y. F.; Boross, P. I.; Wang, Y. F.; Gaddis, L.; Liu, F. L.; Chen, X. F.; Tozser, J.; Harrison, R. W.; Weber, I. T., Molecular basis for substrate recognition and drug resistance from 1.1 to 1.6 angstrom resolution crystal structures of HIV-1 protease mutants with substrate analogs. *Febs J.* **2005,** *272* (20), 5265-5277.
243. Harding, M. M., Geometry of metal-ligand interactions in proteins. *Acta Crystallographica Section D-Biological Crystallography* **2001,** *57*, 401-411.
244. Brejc, K.; Sixma, T. K.; Kitts, P. A.; Kain, S. R.; Tsien, R. Y.; Ormo, M.; Remington, S. J., Structural basis for dual excitation and photoisomerization of the Aequorea victoria green fluorescent protein. *Proc. Natl. Acad. Sci. U. S. A.* **1997,** *94* (6), 2306-2311.
245. Royant, A.; Noirclerc-Savoye, M., Stabilizing role of glutamic acid 222 in the structure of Enhanced Green Fluorescent Protein. *Journal of Structural Biology* **2011,** *174* (2), 385-390.
246. Ehrig, T.; Okane, D. J.; Prendergast, F. G., GREEN-FLUORESCENT PROTEIN MUTANTS WITH ALTERED FLUORESCENCE EXCITATION-SPECTRA. *FEBS Lett.* **1995,** *367* (2), 163-166.
247. Chattoraj, M.; King, B. A.; Bublitz, G. U.; Boxer, S. G., Ultra-fast excited state dynamics in green fluorescent protein: Multiple states and proton transfer. *Proc. Natl. Acad. Sci. U. S. A.* **1996,** *93* (16), 8362-8367.
248. Hofer, A. M.; Landolfi, B.; Debellis, L.; Pozzan, T.; Curci, S., Free Ca2+ dynamics measured in agonist-sensitive stores of single living intact cells: a new look at the refilling process. *Embo J.* **1998,** *17* (7), 1986-1995.
249. Wang, Q.; Shui, B.; Kotlikoff, M. I.; Sondermann, H., Structural Basis for Calcium Sensing by GCaMP2. *Structure* **2008,** *16* (12), 1817-1827.
250. Carlson, H. J.; Campbell, R. E., Mutational Analysis of a Red Fluorescent Protein-Based Calcium Ion Indicator. *Sensors* **2013,** *13* (9), 11507-11521.

251. Garaschuk, O.; Griesbeck, O.; Konnerth, A., Troponin C-based biosensors: A new family of genetically encoded indicators for in vivo calcium imaging in the nervous system. *Cell Calcium* **2007,** *42* (4-5), 351-361.
252. Tang, S.; Reddish, F.; Zhuo, Y.; Yang, J. J., Fast kinetics of calcium signaling and sensor design. *Current opinion in chemical biology* **2015,** *27*, 90-7.
253. Vuignier, K.; Schappler, J.; Veuthey, J. L.; Carrupt, P. A.; Martel, S., Drug-protein binding: a critical review of analytical tools. *Anal. Bioanal. Chem.* **2010,** *398* (1), 53-66.
254. Agatemor, C.; Beauchemin, D., Towards the reduction of matrix effects in inductively coupled plasma mass spectrometry without compromising detection limits: The use of argon-nitrogen mixed-gas plasma. *Spectroc. Acta Pt. B-Atom. Spectr.* **2011,** *66* (1), 1-11.
255. Bings, N. H.; Bogaerts, A.; Broekaert, J. A. C., Atomic spectroscopy. *Anal. Chem.* **2006,** *78* (12), 3917-3945.
256. Hou, X., Jones, BT, Inductively coupled plasma/optical emission spectrometry. *Encyclopedia of Analytical Chemistry* **2000**, 9468-9485.
257. Kim, J. H.; Johannes, L.; Goud, B.; Antony, C.; Lingwood, C. A.; Daneman, R.; Grinstein, S., Noninvasive measurement of the pH of the endoplasmic reticulum at rest and during calcium release. *Proceedings of the National Academy of Sciences* **1998,** *95* (6), 2997-3002.
258. Demaurex, N., pH homeostasis of cellular organelles. *News in Physiological Sciences* **2002,** *17*, 1-5.
259. Kneen, M.; Farinas, J.; Li, Y. X.; Verkman, A. S., Green fluorescent protein as a noninvasive intracellular pH indicator. *Biophys. J.* **1998,** *74* (3), 1591-1599.
260. Sawano, A.; Miyawaki, A., Directed evolution of green fluorescent protein by a new versatile PCR strategy for site-directed and semi-random mutagenesis. *Nucleic Acids Research* **2000,** *28* (16), e78.
261. Torre, M.; Rodriguez, A. R.; Sauracalixto, F., STUDY OF THE INTERACTIONS OF CALCIUM-IONS WITH LIGNIN, CELLULOSE, AND PECTIN. *J. Agric. Food Chem.* **1992,** *40* (10), 1762-1766.
262. Oravcova, J.; Bohs, B.; Lindner, W., Drug-protein binding studies - New trends in analytical and experimental methodology. *J. Chromatogr. B-Biomed. Appl.* **1996,** *677* (1), 1-28.
263. Huang, J.-D., Errors in estimating the unbound fraction of drugs due to the volume shift in equilibrium dialysis. *J. Pharm. Sci.* **1983,** *72* (11), 1368-1369.
264. Lockwood, G. F.; Wagner, J. G., Plasma volume changes as a result of equilibrium dialysis. *Journal of Pharmacy and Pharmacology* **1983,** *35* (6), 387-388.
265. Donnan, F. G., The theory of membrane equilibria. *Chem. Rev.* **1924,** *1* (1), 73-90.
266. Desoye, G., Error analysis in equilibrium dialysis: evaluation of adsorption phenomena. *Journal of Biochemical and Biophysical Methods* **1988,** *17* (1), 3-15.
267. Papp, S.; Dziak, E.; Michalak, M.; Opas, M., Is all of the endoplasmic reticulum created equal? The effects of the heterogeneous distribution of endoplasmic reticulum Ca2+-handling proteins. *The Journal of cell biology* **2003,** *160* (4), 475-479.
268. Petersen, O. H.; Tepikin, A.; Park, M. K., The endoplasmic reticulum: one continuous or several separate Ca2+ stores? *Trends in Neurosciences* **2001,** *24* (5), 271-276.
269. Lamb, G. D., Excitation-contraction coupling in skeletal muscle: Comparisons with cardiac muscle. *Clin. Exp. Pharmacol. Physiol.* **2000,** *27* (3), 216-224.
270. Flucher, B. E.; Takekura, H.; Franzini-Armstrong, C., Development of the Excitation-Contraction Coupling Apparatus in Skeletal Muscle: Association of Sarcoplasmic Reticulum and Transverse Tubules with Myofibrils. *Developmental Biology* **1993,** *160* (1), 135-147.
271. Protasi, F.; Paolini, C.; Dainese, M., Calsequestrin-1: a new candidate gene for malignant hyperthermia and exertional/environmental heat stroke. *The Journal of physiology* **2009,** *587* (13), 3095-3100.

272. Dainese, M.; Quarta, M.; Lyfenko, A. D.; Paolini, C.; Canato, M.; Reggiani, C.; Dirksen, R. T.; Protasi, F., Anesthetic-and heat-induced sudden death in calsequestrin-1-knockout mice. *The FASEB Journal* **2009,** *23* (6), 1710-1720.
273. Lewis, K. M.; Ronish, L. A.; Rios, E.; Kang, C., Characterization of Two Human Skeletal Calsequestrin Mutants Implicated in Malignant Hyperthermia and Vacuolar Aggregate Myopathy. *J. Biol. Chem.* **2015,** *290* (48), 28665-28674.
274. Siemering, K. R.; Golbik, R.; Sever, R.; Haseloff, J., Mutations that suppress the thermosensitivity of green fluorescent protein. *Curr. Biol. 6* (12), 1653-1663.
275. Finney, L. A.; O'Halloran, T. V., Transition metal speciation in the cell: insights from the chemistry of metal ion receptors. *Science* **2003,** *300* (5621), 931-936.
276. Anderson, A. A.; Altafaj, X.; Zheng, Z. L.; Wang, Z. M.; Delbono, O.; Ronjat, M.; Treves, S.; Zorzato, F., The junctional SR protein JP-45 affects the functional expression of the voltage-dependent Ca2+ channel Ca(v)1.1. *J. Cell Sci.* **2006,** *119* (10), 2145-2155.
277. Mosca, B.; Delbono, O.; Messi, M. L.; Bergamelli, L.; Wang, Z. M.; Vukcevic, M.; Lopez, R.; Treves, S.; Nishi, M.; Takeshima, H.; Paolini, C.; Martini, M.; Rispoli, G.; Protasi, F.; Zorzato, F., Enhanced dihydropyridine receptor calcium channel activity restores muscle strength in JP45/CASQ1 double knockout mice. *Nat. Commun.* **2013,** *4*.
278. Chaigne-Delalande, B.; Lenardo, M. J., Divalent cation signaling in immune cells. *Trends Immunol.* **2014,** *35* (7), 332-344.
279. Feske, S.; Skolnik, E. Y.; Prakriya, M., Ion channels and transporters in lymphocyte function and immunity. *Nat. Rev. Immunol.* **2012,** *12* (7), 532-547.
280. Zhou, H.; Clapham, D. E., Mammalian MagT1 and TUSC3 are required for cellular magnesium uptake and vertebrate embryonic development. *Proc. Natl. Acad. Sci. U. S. A.* **2009,** *106* (37), 15750-15755.
281. Li, F. Y.; Chaigne-Delalande, B.; Kanellopoulou, C.; Davis, J. C.; Matthews, H. F.; Douek, D. C.; Cohen, J. I.; Uzel, G.; Su, H. C.; Lenardo, M. J., Second messenger role for Mg2+ revealed by human T-cell immunodeficiency. *Nature* **2011,** *475* (7357), 471-U63.
282. Chaigne-Delalande, B.; Li, F. Y.; O'Connor, G. M.; Lukacs, M. J.; Jiang, P.; Zheng, L. X.; Shatzer, A.; Biancalana, M.; Pittaluga, S.; Matthews, H. F.; Jancel, T. J.; Bleesing, J. J.; Marsh, R. A.; Kuijpers, T. W.; Nichols, K. E.; Lucas, C. L.; Nagpal, S.; Mehmet, H.; Su, H. C.; Cohen, J. I.; Uzel, G.; Lenardo, M. J., Mg2+ Regulates Cytotoxic Functions of NK and CD8 T Cells in Chronic EBV Infection Through NKG2D. *Science* **2013,** *341* (6142), 186-191.
283. Trapani, V.; Farruggia, G.; Marraccini, C.; Iotti, S.; Cittadini, A.; Wolf, F. I., Intracellular magnesium detection: imaging a brighter future. *Analyst* **2010,** *135* (8), 1855-1866.
284. Cohen, S. M.; Burt, C. T., 31P nuclear magnetic relaxation studies of phosphocreatine in intact muscle: determination of intracellular free magnesium. *Proceedings of the National Academy of Sciences* **1977,** *74* (10), 4271-4275.
285. Grubbs, R. D., Intracellular magnesium and magnesium buffering. *Biometals* **2002,** *15* (3), 251-259.
286. Kim, H. M.; Yang, P. R.; Seo, M. S.; Yi, J.-S.; Hong, J. H.; Jeon, S.-J.; Ko, Y.-G.; Lee, K. J.; Cho, B. R., Magnesium ion selective two-photon fluorescent probe based on a benzo [h] chromene derivative for in vivo imaging. *The Journal of organic chemistry* **2007,** *72* (6), 2088-2096.
287. Lindenburg, L. H.; Vinkenborg, J. L.; Oortwijn, J.; Aper, S. J. A.; Merkx, M., MagFRET: The First Genetically Encoded Fluorescent Mg2+ Sensor. *PLoS One* **2013,** *8* (12).
288. Abraham, R. T.; Weiss, A., Timeline - Jurkat T cells and development of the T-cell receptor signalling paradigm. *Nat. Rev. Immunol.* **2004,** *4* (4), 301-308.
289. Gifford, J. L.; Walsh, M. P.; Vogel, H. J., Structures and metal-ion-binding properties of the Ca2+-binding helix-loop-helix EF-hand motifs. *Biochem. J.* **2007,** *405*, 199-221.

290. Dudev, T.; Lim, C., Principles governing Mg, Ca, and Zn binding and selectivity in proteins. *Chem. Rev.* **2003,** *103* (3), 773-787.
291. Katz, A. K.; Glusker, J. P.; Beebe, S. A.; Bock, C. W., Calcium Ion Coordination: A Comparison with That of Beryllium, Magnesium, and Zinc. *Journal of the American Chemical Society* **1996,** *118* (24), 5752-5763.
292. Collins, K. D., Ion hydration: Implications for cellular function, polyelectrolytes, and protein crystallization. *Biophys. Chem.* **2006,** *119* (3), 271-281.

APPENDIX

Appendix A Crystal structure of CatchER supplemental data

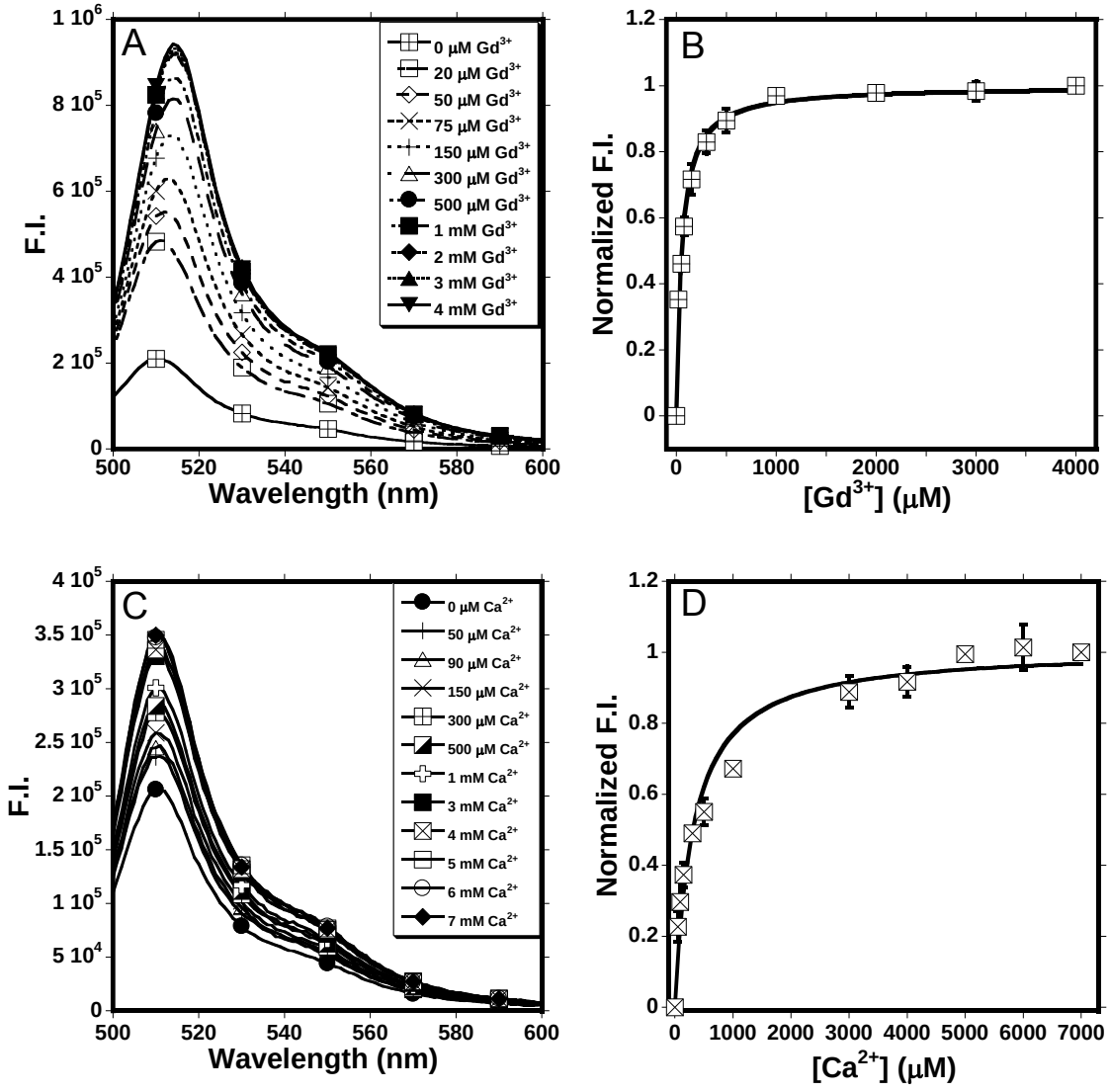

Figure A.1 Fluorescence response of CatchER to Gd^{3+} and Ca^{2+} excited at 395 nm (A and C) and fitted normalized intensity (B and D).

CatchER experiences a large fluorescence increase when titrated with Gd^{3+} and with Ca^{2+}. The normalized fluorescence was fitted with the 1:1 binding equation to give K_d values of 53.0 ± 4.0 μM for Gd^{3+} and 315.4 ± 40.0 μM for Ca^{2+}. Taken from Zhang, et al., *Acta Cryst*., 2013.

Table A.1 Data statistics vs. resolution

CatchER(apo)

Resolution Å							
Lower limit	Upper limit	Average I	Average error	Norm. stat	Linear Chi**2	Square R-fac	R-fac
50.00	3.34	5526.4	721.1	193.4	0.927	0.074	0.084
3.34	2.65	2331.2	342.5	61.5	0.987	0.092	0.098
2.65	2.32	1051.1	160.5	30.8	1.102	0.108	0.113
2.32	2.10	710.5	114.6	26.3	1.147	0.125	0.128
2.10	1.95	484.3	93.9	23.2	0.910	0.135	0.134
1.95	1.84	282.1	46.5	16.4	1.202	0.153	0.147
1.84	1.75	160.0	27.1	11.4	1.163	0.174	0.159
1.75	1.67	108.8	22.2	11.4	0.989	0.201	0.171
1.67	1.61	80.0	17.5	10.9	1.020	0.233	0.194
1.61	1.55	59.0	14.1	10.9	1.135	0.270	0.220
All reflections		1071.7	155.1	39.4	1.059	0.096	0.090

Table taken from Zhang, et al., *Acta Cryst*., 2013.

CatchER-Ca^{2+}

Resolution Å							
Lower limit	Upper limit	Average I	Average error	Norm. stat	Linear Chi**2	Square R-fac	R-fac
50.00	2.59	15117.6	803.1	245.3	0.901	0.060	0.071
2.59	2.05	4838.3	172.0	34.5	1.098	0.074	0.084
2.05	1.79	2084.5	106.1	23.6	0.955	0.098	0.110
1.79	1.63	811.5	39.3	11.3	1.094	0.128	0.147
1.63	1.51	448.4	23.4	9.4	1.124	0.157	0.175
1.51	1.42	262.5	16.1	8.6	1.122	0.210	0.224
1.42	1.35	163.4	12.6	8.5	1.077	0.281	0.295
1.35	1.29	120.5	11.3	8.8	1.108	0.317	0.331
1.29	1.24	87.4	10.7	9.2	1.063	0.351	0.370
1.24	1.20	64.1	10.5	9.5	1.013	0.392	0.408
All reflections		2389.8	119.8	36.6	1.061	0.081	0.076

Table taken from Zhang, et al., *Acta Cryst*., 2013.

CatchER-Gd^{3+}

Resolution Å							
Lower limit	Upper limit	Average I	Average error	Norm. stat	Linear Chi**2	Square R-fac	R-fac
50.00	3.83	2142.8	130.3	21.5	0.951	0.065	0.071
3.83	3.04	1484.5	109.5	15.9	0.980	0.086	0.088
3.04	2.66	611.6	47.1	8.3	0.951	0.091	0.094
2.66	2.42	379.2	29.5	6.3	0.912	0.093	0.092
2.42	2.24	283.8	22.6	5.9	0.930	0.102	0.101
2.24	2.11	217.9	16.8	5.3	1.048	0.115	0.107
2.11	2.00	171.4	13.7	5.0	0.973	0.118	0.108
2.00	1.92	122.6	10.2	4.7	0.989	0.131	0.114
1.92	1.84	78.8	7.1	4.4	1.004	0.162	0.149
1.84	1.78	52.8	6.1	4.7	1.008	0.185	0.156
All reflections		572.3	40.4	8.4	0.974	0.085	0.079

Table taken from Zhang, et al., *Acta Cryst*., 2013.

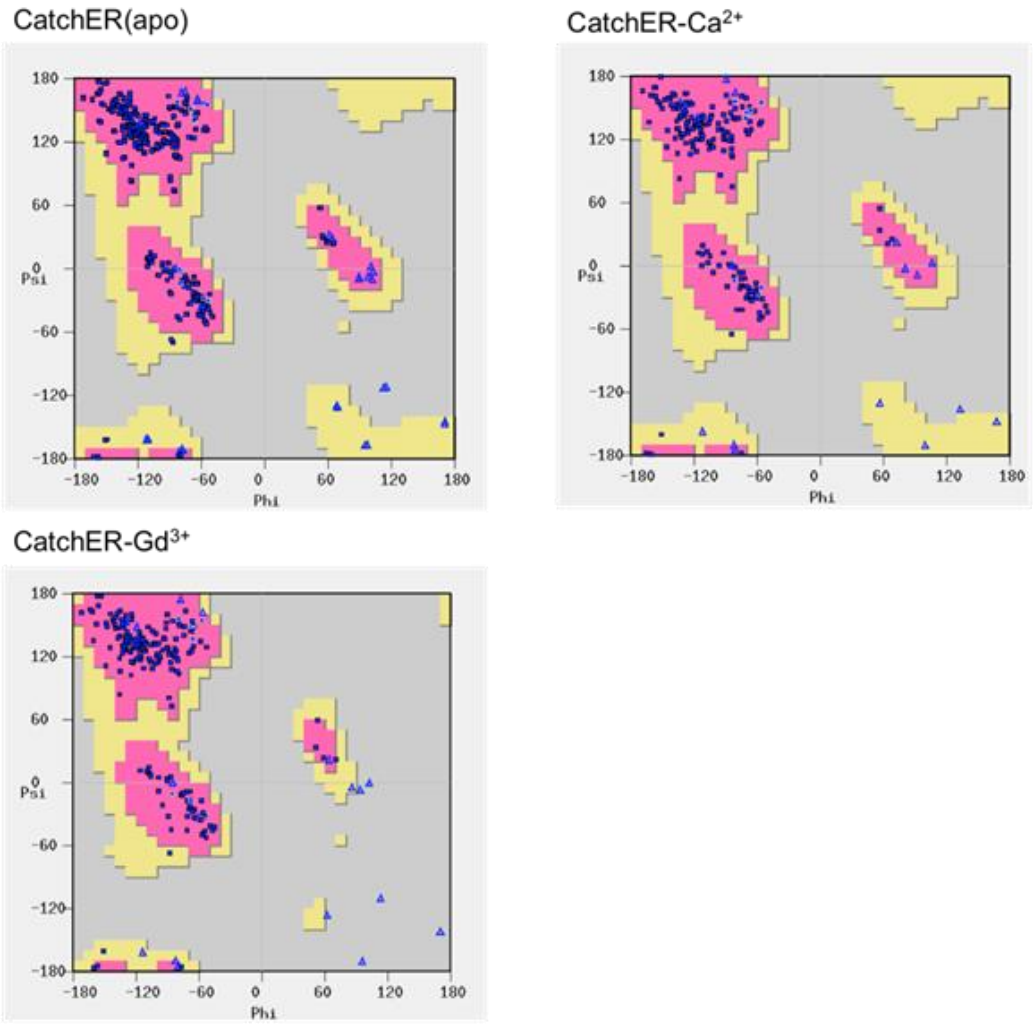

Figure A.2 Structure validation by Ramachandran plots for the three CatchER structures, as performed by Coot 0.5.2.

The residues analyzed in all three structures are within the allowed region. Taken from Zhang, et al., *Acta Cryst*., 2013.

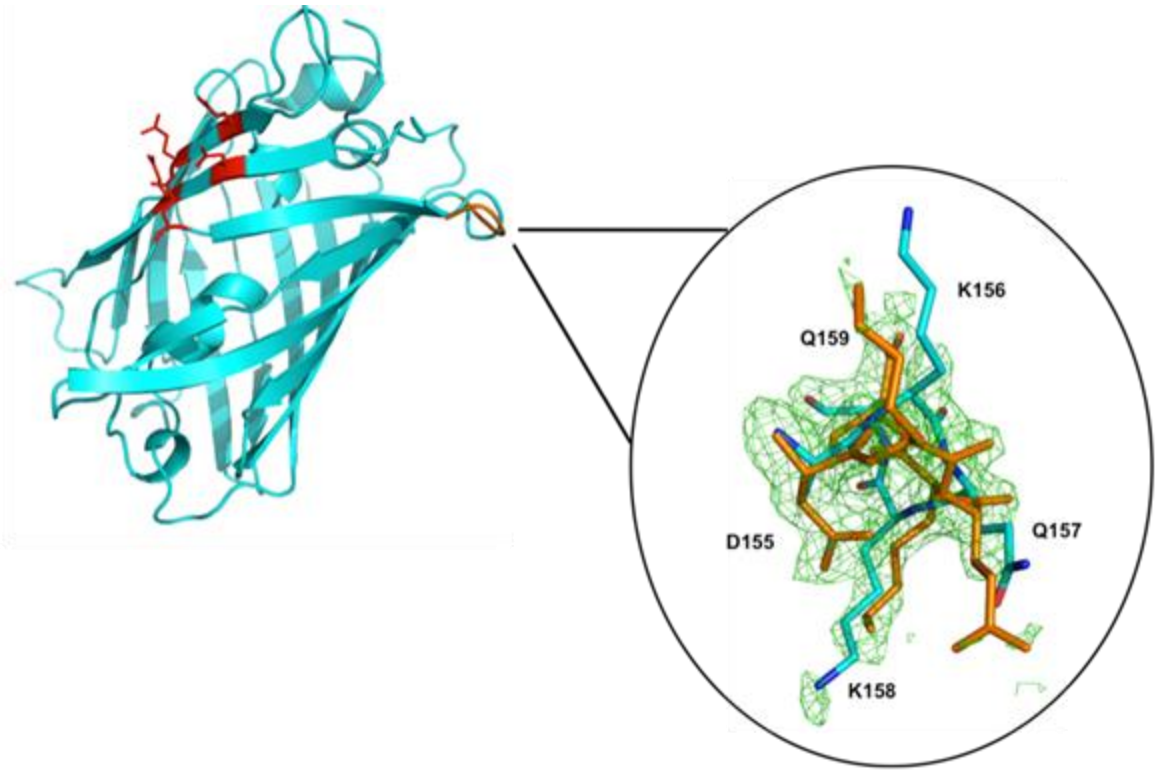

Figure A.3 Flexible loop region comprising residues 155-159.

CatchER-Gd^{3+} is shown in a cyan cartoon representation with the mutated residues of the designed Ca^{2+} binding site in red sticks. The alternative conformations of residues 155-159 are indicated in cyan and orange. (B) F_o-F_c omit map (in green) for the two conformations of residues 155-159 contoured at 2.0σ. In EGFP (PDB code: 4EUL) and GFP structure (PDB code: 2WUR), only the conformation in orange was observed. Table taken from Zhang, et al., *Acta Cryst*., 2013.

Appendix B Biophysical characterization of CatchER variants supplemental data

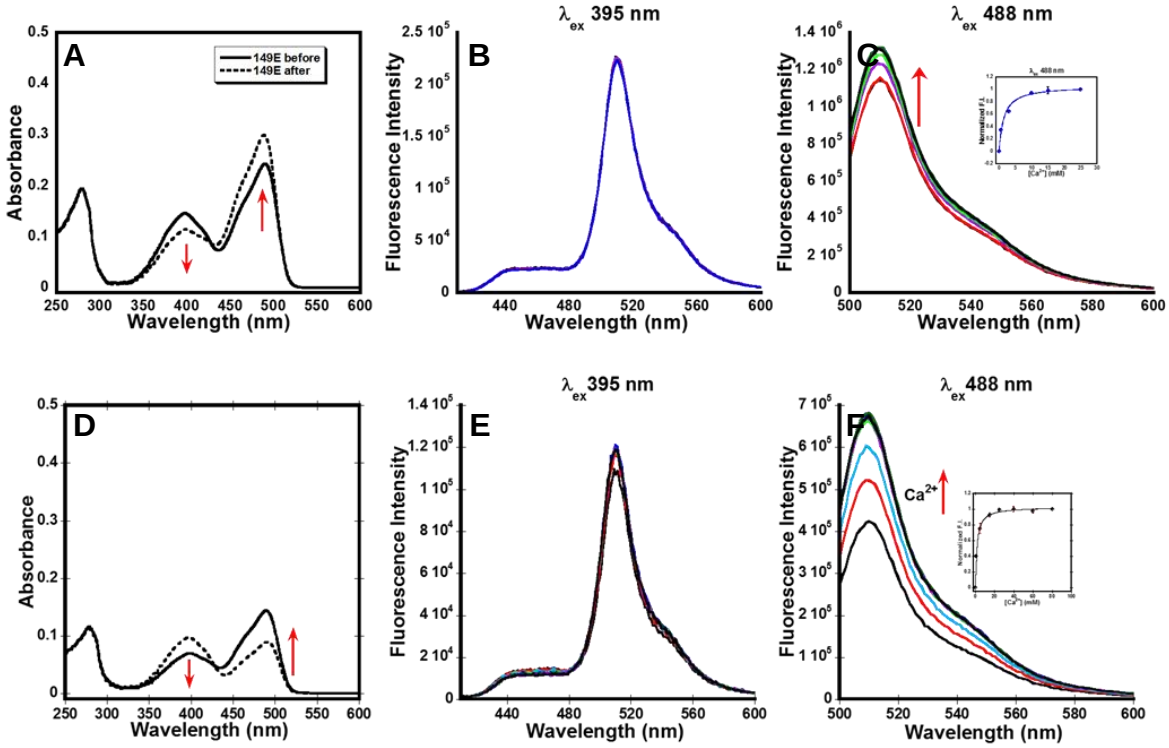

Figure B.1 *In vitro* Ca^{2+} K_d of 149E (A-C) and 149E S30R (D-F) in 10 mM Tris 150 mM KCl pH 7.4

(A and D) Absorbance spectrums of 149E (A) and 149E S30R (B) in the absence (solid line) and presence (dotted line) of saturating levels of Ca^{2+}. Ca^{2+} causes an increase in the 488 nm peak (increase in anionic chromophore) and a decrease in the 395 nm peak (decrease in neutral chromophore) in the presence of KCl. No fluorescence change occurs when excited at 395 nm (B and E). Inset binding curves were obtained by fitting the normalized data with a 1:1 binding equation.

Table B.1 Calculated amounts of Ca^{2+} in each dialysis bag from equilibrium dialysis experiment with 15 μM Ca^{2+} obtained from ICP-OES

λ (nm)	[Ca^{2+}] (μM)						
	T = 1 buffer	T = 2 buffer	blank	α-lactalbumin	149E	EGFP	Myoglobin
396.847	14.607	15.850	17.217	29.773	23.385	27.606	17.381
317.933	14.627	15.741	16.949	28.090	22.399	26.226	17.171
219.779	15.890	16.350	18.196	30.218	23.848	26.800	18.675
370.602	14.536	15.590	16.843	27.782	22.052	25.883	16.783
643.907	14.963	16.199	17.221	29.396	23.053	27.084	17.578
373.69	14.701	15.750	17.040	27.825	22.251	26.047	17.655
Average	14.887	15.914	17.244	28.848	22.831	26.608	17.540
Stdev	0.513	0.296	0.490	1.076	0.710	0.670	0.638

Table B.2 Calculated amounts of Ca^{2+} in each dialysis bag from equilibrium dialysis experiment with 20 μM Ca^{2+} obtained from ICP-OES

	[Ca^{2+}] (μM)								
λ (nm)	396.847	317.933	219.779	370.602	643.907	220.861	373.690	Avg	Stdev
Buffer 1	17.990	18.195	18.122	17.995	17.941	19.234	18.104	18.226	0.453
Buffer 2	22.617	22.346	24.015	21.911	22.371	22.541	22.081	22.554	0.689
α-lactalbumin	33.931	34.495	35.682	34.012	34.916	36.739	34.032	34.829	1.049
CatchER-T	32.425	32.858	35.255	32.439	33.712	34.293	32.433	33.345	1.112
EGFP	26.197	24.984	26.265	24.570	26.022	25.794	24.906	25.534	0.696
Myoglobin	24.995	24.052	25.085	23.492	24.767	24.934	24.339	24.523	0.590
Blank	24.094	23.205	24.064	22.944	23.606	23.498	23.121	23.505	0.451

Table B.3 Calculated amounts of Ca^{2+} in each dialysis bag from equilibrium dialysis experiment with 20 μM Ca^{2+} obtained from ICP-OES

λ (nm)	[Ca^{2+}] (μM)					
	T = 1 buffer	T = 2 buffer	blank	α-lactalbumin	CatchER	EGFP
396.847	19.017	20.198	20.681	35.549	32.239	22.300
317.933	18.679	19.897	22.720	35.553	31.464	21.459
219.779	18.726	21.651	25.087	36.715	33.714	23.133
370.602	18.589	19.660	22.065	35.360	31.634	21.700
643.907	18.850	20.101	21.618	36.683	33.285	22.176
220.861	19.464	20.831	23.193	37.470	32.500	22.881
373.69	18.840	20.013	22.226	35.450	31.675	21.802
Average	**18.881**	**20.336**	**22.513**	**36.112**	**32.359**	**22.207**
Stdev	**0.292**	**0.684**	**1.389**	**0.833**	**0.868**	**0.619**

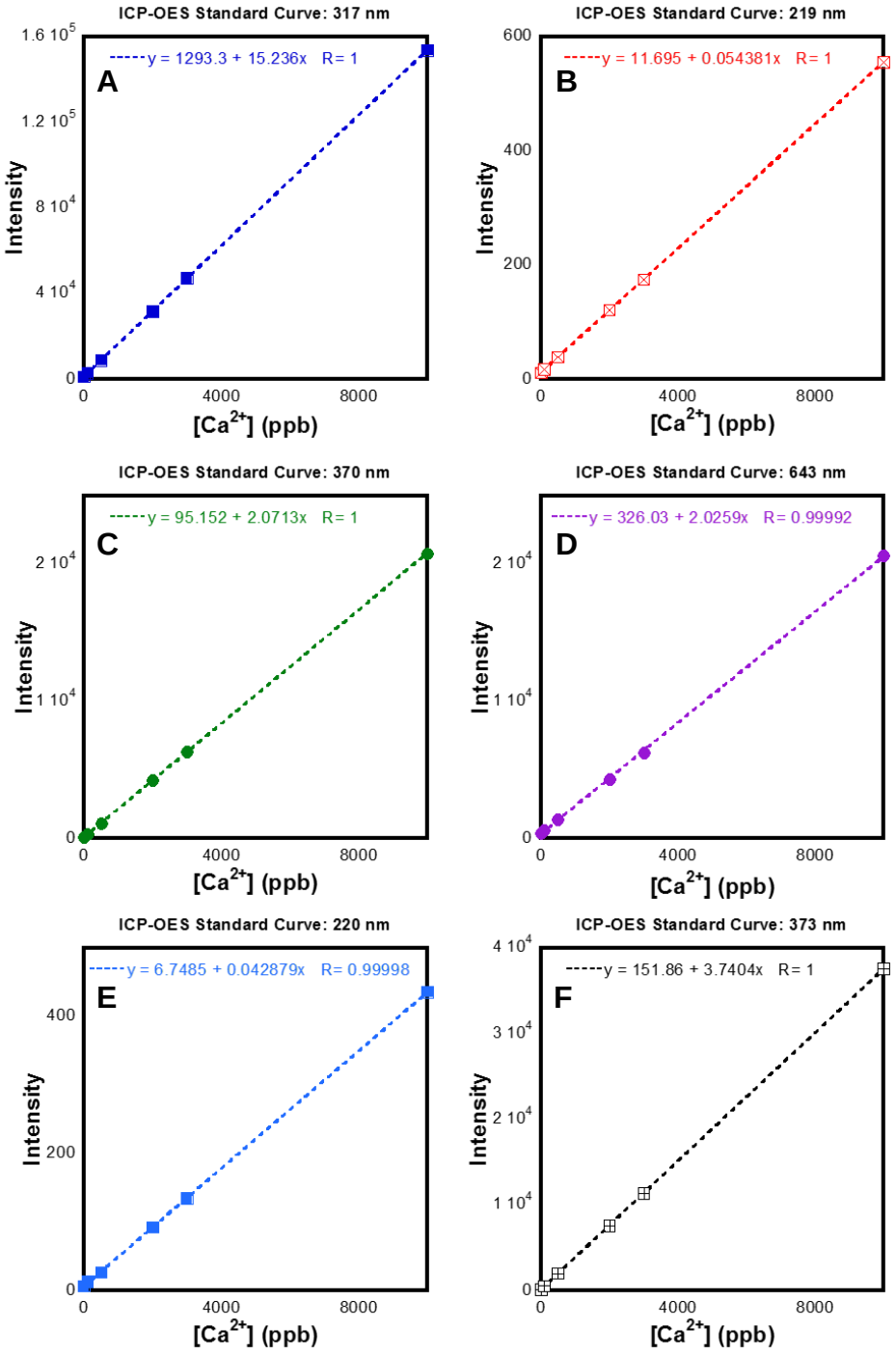

Figure B.2 ICP-OES standard curves for Ca^{2+} emission wavelengths

Appendix C Optimization of CatchER and its targeted subcellular application supplemental data

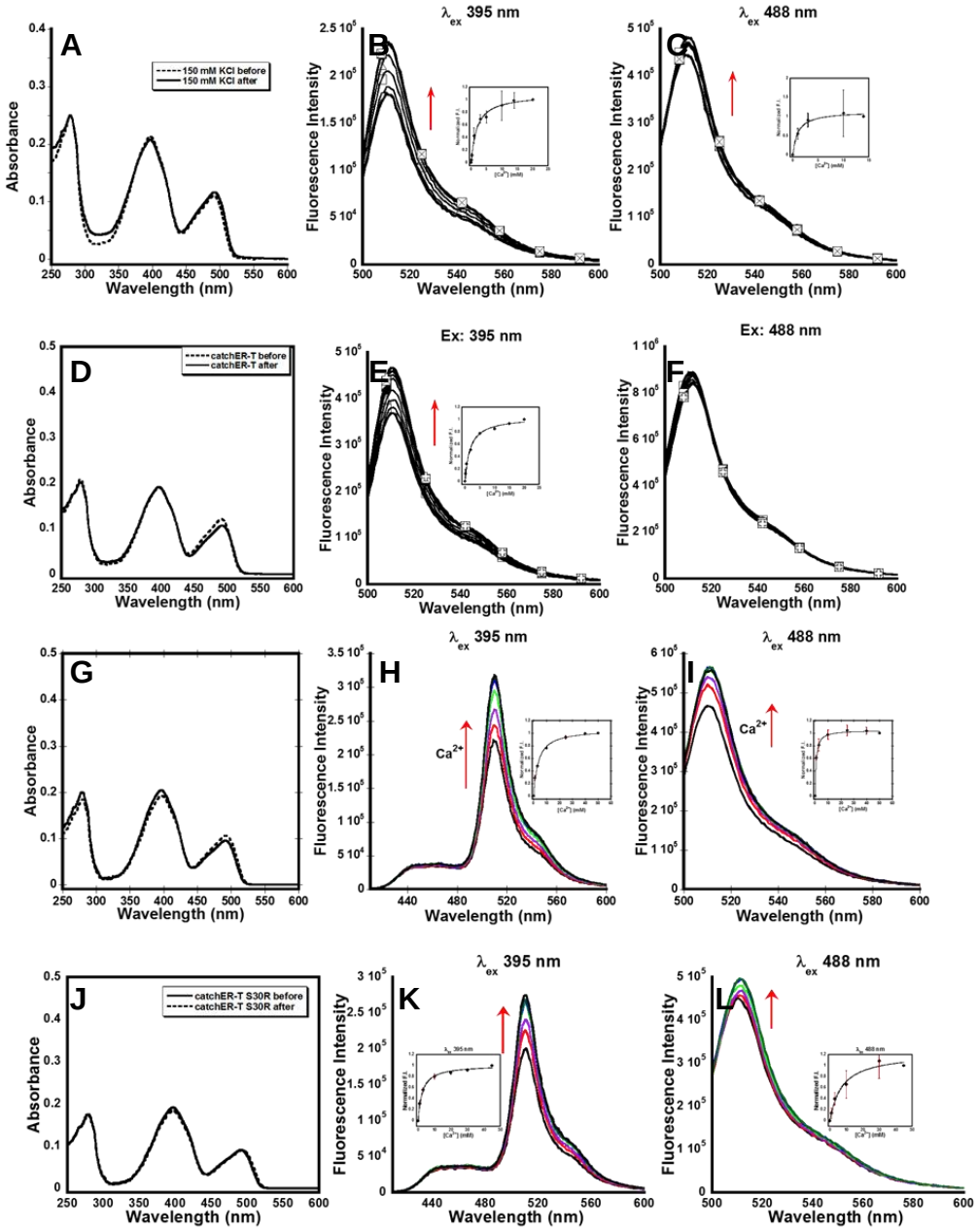

Figure C.1 *In vitro* Ca^{2+} K_d of CatchER variants in 10 mM Tris 150 mM KCl pH 7.4

(A, D, G, J) Absorbance spectra of 10 µM of the protein sample before titration with 5 µM EGTA (dashed line) and after with a saturating amount of Ca^{2+} (solid line). The absorbance peaks have no response to increasing Ca^{2+}. CatchER (A-C), CatchER-T

(D-F), CatchER-T Y39N (G-I), and CatchER-T S30R (J-L) have reduced responses to Ca^{2+} in 150 mM KCl. All samples were excited at 395 nm and 488 nm with emission scanned from 410-600 nm for 395 nm excitation and from 500-600 nm for 488 nm excitation. Slit widths for excitation and emission were 0.25 mm. Inset curves show the normalized fluorescence intensity data fit to the 1:1 binding equation to get the K_d.